In-situ exploration of Titan's atmosphere

Adapting SPEX for a balloon mission to Titan

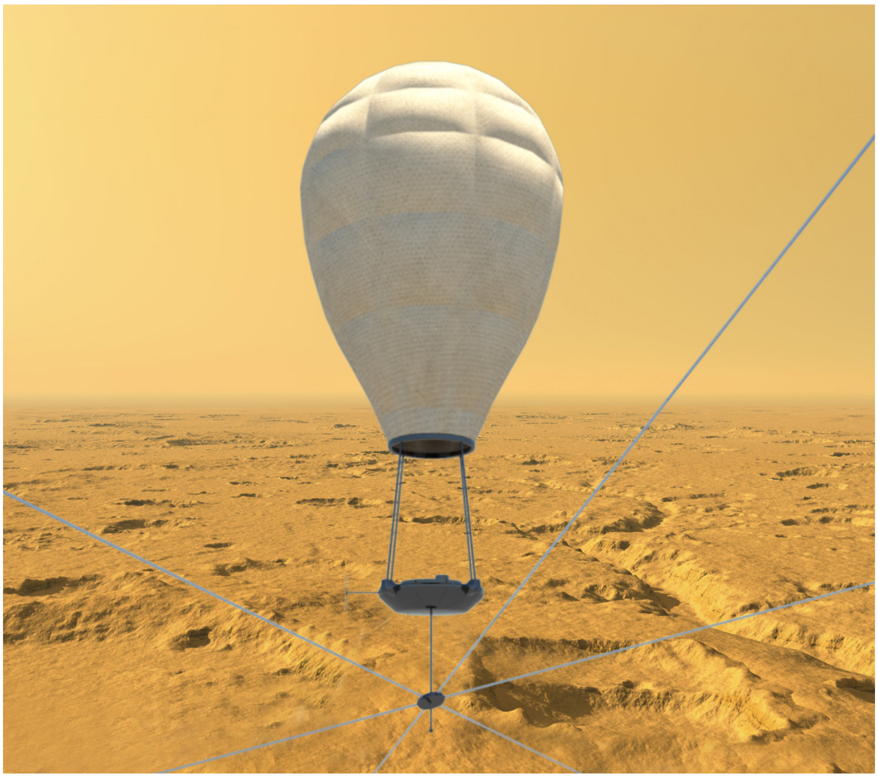

Nicoletta Silvestri

August 31, 2010

Faculty of Aerospace Engineering - Delft University of Technology

In-situ exploration of Titan's atmosphere

Adapting SPEX for a balloon mission to Titan

MASTER OF SCIENCE THESIS

Nicoletta Silvestri

Supervisor: dr. D.M. Stam
SRON - Netherlands Institute for Space Research
Sorbonnelaan 2, 3584 CA, Utrecht The Netherlands

Co-Supervisor: dr. L.L.A. Vermeersen
Astrodynamics & Space Missions
Faculty of Aerospace Engineering - TU Delft
Kluyverweg 1, 2628 CD Delft The Netherlands

Faculty of Aerospace Engineering - Delft University of Technology

Preface

The Aerospace Engineering Masters at the Delft University of Technology is concluded with the development of a final project. The research and the development of the project are documented in a thesis work. This report presents the thesis work of the author. The project hereby presented has been developed at SRON - Netherlands Institute of Space Research - in Utrecht at the division of Earth and Planetary Science. The last stage of this research has been carried out at the chair of Astrodynamics and Space Missions at the aforementioned faculty. The thesis is addressed to people who are interested in both atmospheric science and instrument engineering. This thesis will provide the reader with basic but thorough insight into the related disciplines of radiative transfer in planetary atmospheres and spectropolarimetry. The reader that will go through the report will read about how to characterize the microphysical properties of aerosol particles contained in the atmosphere of Titan by using the spectropolarimeter SPEX for in-situ exploration aboard a hot-air balloon. This thesis can serve as a means for broadening ones knowledge on the subject or as a start for further research.

The background knowledge on radiative transfer and light scattering phenomena is given by Chapters 4 to 6. Here, the single scattering and the multiple scattering taking place in the atmosphere of Titan are explained together with numerical simulations of radiative transfer. If the reader is more interested in spectropolarimetry, the author would recommend to take a look at Chapter 7. Here, SPEX (Spectropolarimeter for Planetary Exploration) and its novel spectropolarimetric technique is treated in detail. In this chapter, the advantages of its new method are compared to classical polarimetric techniques. In addition, the author would like to bring the attention of the reader to the content of appendix A. Here it is possible to find the article presented by the author at the 7^{th} edition of the International Planetary Probe Workshop (IPPW-7) held in Barcelona on June 14-18 2010. The article is a concise version of the thesis work. Together with the article, I would definitively recommend to read Chapter 1 where a detailed introduction to the whole project is given.

I would like to thank my thesis supervisor Dr. Daphne Stam in specific for her constant and fruitful guidance in the 'new world' of atmospheric radiative transfer. I would like to thank her for her help, patience and constant availability during the research. A special thanks goes to Dr. ir. Martijn Smit and Dr. ir. Jeroen Rietjens, without their help this thesis work would not have been possible. I would like thank my co-supervisor dr. Bert Vermeersen for his guidance during the last stage of the thesis work. A particular thank goes also to the EPS division members for the incredible year spent together at SRON. In particular I would like to thank Dinand Schepers, my desk-mate at SRON and friend in life. A special word of appreciation goes out to the students from the 9th floor for keeping me company during this work. Specifically, in random order, Guido Ridolfi, Antonio Pagano, Stefan van Doorn, Hermes Jara Orue, Tom de Groot, Mirjam Boere, Vivek Vittaldev. Moreover, I am particularly grateful to my'dutch family' and to Federica and Manuela for their precious friendship. Last but not least, the biggest thank goes to my boyfriend Bob who supported me during the IPPW-7 and during most of the thesis work. I would like to thank him for helping me out with drawing the new design of SPEX and making the movie about the Titan-balloon.

This thesis work is dedicated to my Family, who gave me the possibility to become who I am.

Nicoletta Silvestri
August 23, 2010

Summary

Titan is the biggest moon orbiting the planet Saturn. The peculiarity of Titan lies in its thick nitrogen atmosphere with a surface pressure of 1.5 bar. The atmosphere consists of two thick haze layers thought to be composed of fractal-shaped aerosols. Knowing the properties of the hazes is crucial for understanding the existence and evolution of Titan's atmosphere and the dynamical processes that take place therein. This work investigates how we can characterize the hazes in Titan's atmosphere using a balloon-borne spectropolarimeter SPEX, the Spectropolarimeter for Planetary EXploration. First, we focus on the haze particles: what is the knowledge that has been acquired so far and what more do we need to know about the aerosols? Next, we explain the concept of spectropolarimetry, which is the method we plan to use to get more information about the haze. Then, we explain how to measure the aerosol's properties. We describe the SPEX instrument and its novel polarimetric method, and compare it with classical polarimetric methods. SPEX measures simultaneously the radiance and the degree and direction of linear polarization of sunlight scattered inside a planetary atmosphere. We present numerical simulations of sunlight scattered inside Titan's atmosphere and numerical simulations of realistic performances of SPEX as payload on the hot-air balloon of the Titan Saturn System mission (TSSM) which was submitted for the ESA's Cosmic Vision Program. In its current design, SPEX has been optimized as payload for a Mars orbiter. For Titan we would prefer a higher spectral resolution to resolve the methane features that show up in the spectra of scattered sunlight inside the atmosphere. Moreover, compared to a Mars SPEX, we would prefer different viewing angles due to its placement on a balloon instead of on an orbiter. We conclude that if we increase the thickness of the birefringent crystals in the SPEX' pre-optic system from 4 mm (Mars design) to 16 mm, we can resolve the strong methane bands present in Titan's spectra, which will allow us to retrieve aerosol information contained in these bands. An interesting solution for the viewing angles would be to have a rotating disk placed on a boom beneath the balloon's gondola and inclined under an angle of 40° with respect to the vertical axis. The disk would contain a number of apertures looking outward along its rim. We conclude that SPEX on the TSSM balloon would be a powerful tool for characterizing Titan's haze.

Contents

List of Figures

List of Tables

List of Symbols

Latin Symbols

Al	Aluminium	[-]
a_n	Mie coefficient	[-]
A_s	Surface albedo	[-]
AU	Astronomical unit	[149ă598ă000 km]
A_v	Aerosol radius	[μm]
b_{a}	Aerosol optical thickness	[-]
b_{aabs}	Aerosols absorption optical thickness	[-]
b_{asca}	Aerosol scattering optical thickness	[-]
b_{m}	Molecule optical thickness	[-]
b_{mabs}	Molecule absorption optical thickness	[-]
b_{msca}	Molecule scattering optical thickness	[-]
b_n	Mie coefficient	[-]
CH_4	Methane	[-]
CO_2	Carbon dioxide	[-]
D	Fractal Dimension	[-]
F	Iron	[-]
$\mathbf{F}_{\mathrm{in}}$	Input vector for SPEX	$[W/\mu m\, m^2 sr]$
$\mathbf{F}_{\mathrm{out}}$	Output vector for SPEX	$[W/\mu m\, m^2 sr]$
I	Total radiance	$[W/\mu m\, m^2 sr]$
I_0	Incident radiance	$[W/\mu m\, m^2 sr]$
$\mathbf{I}$	Stokes vector	$[W/\mu m\, m^2 sr]$
k	Wavenumber	[cm^{-1}]
k_{abs}	Absorption coefficient	[μm^{-1}]
k_{ext}	Extinction coefficient	[μm^{-1}]
k_{sca}	Scattering coefficient	[μm^{-1}]
m	Cosine of the instrument zenith angle	[-]
m	Refractive index	[-]
$\mathbf{M}$	Mueller matrix	[-]
m_0	Cosine of the solar zenith angle	[-]
Mg	Magnesium	[-]
N	Number of monomers	[-]
N_2	Nitrogen	[-]
n_e	Extraordinary index of refraction	[-]
N_i	Number of molecules	[-]
n_i	Immaginary part of the refractive index	[-]

n_o	Ordinary index of refraction	[-]
n_r	Real part of the refractive index	[-]
O	Oxigen	[-]
P	Degree of linear polarization	[-]
p	Fractal dimension pre-factor	[-]
P^{11}	Phase function	[-]
$\mathbf{P}$	Phase matrix	[-]
$\mathbf{P}_a$	Phase matrix for aerosol	[-]
$\mathbf{P}_m$	Phase matrix for molecule	[-]
P_S	Single scattering degree of polarization	[-]
Q	Linear radiance	$[W/\mu m\, m^2 sr]$
R	Radius of gyration	$[m^{-2}]$
R	Scattering distance	[μm]
r_{eff}	Effective monomer radius	[μm]
$\mathbf{R}$	Reflection matrix	[-]
S	Output radiance spectrum	$[W/\mu m\, m^2 sr]$
S_0	Input radiance spectrum	$[W/\mu m\, m^2 sr]$
T	Temperature	[K]
$\mathbf{T}$	Transmission matrix	[-]
U	Linear radiance	$[W/\mu m\, m^2 sr]$
V	Circular radiance	$[W/\mu m\, m^2 sr]$
v_{eff}	Effective variance	[-]
x	Direction of perpendicular to z	[-]
x_m	Monomer size	[-]
X_v	Aerosol size	[-]
y	Direction of perpendicular to z	[-]
z	Altitude	[km]
z	Direction of propagation of light	[-]

Greek Symbols

α	Scattering angle	[deg]
χ	Angle of linear polarization	[deg]
δ	Retardance	[μm]
λ	Wavelength	[μm]
$\tilde{\omega}$	Single scattering albedo	[-]
Ω	Solid angle	[sr]
φ	Signal phase	[deg]
ϕ	Azimuth angle of scattered light	[deg]
ϕ_0	Azimuth angle of incoming light	[deg]
ρ	Density	[kg m^{-3}]
σ_{abs}	Absorption cross-section	[m^2]
σ_{ext}	Extinction cross-section	[m^2]
σ_{sca}	Scattering cross-section	[m^2]
τ	Optical depth	[-]
θ	Instrument zenith angle	[deg]

Θ	Total scattering angle	[deg]
θ_0	Solar zenith angle	[deg]

Acronyms and Abbreviations

ASI	Agenzia Spaziale Italiana (Italian Space Agency)
BPCA	Balistic Particle-Cluster Aggregation
DAM	Doubling Adding Method
DAP	Doubling Adding program
DLA	Diffusion Limited Aggregation
ESA	European Space Agency
HWP	Half-wave plate
IPPW	International Planetary Probe Workshop
NASA	National Aeronautic and Space Administration
QWP	Quarter-wave plate
SPEX	Spectropolarimeter for Planteray Exploration

1 Introduction

Titan is the largest moon in the Saturn system and it is the second in size in the whole Solar System after Ganymede. The average distance with respect to Earth is about 9.2 AU, for this reason it belongs to the outer part of the Solar System. The radius of the moon is 0.4 times the size of Earth, Titan revolves around Saturn in 16 Earth days and revolves (with Saturn) around the Sun in 29 Earth years. Since its discovery in 1655 by Christiaan Huygens, Titan has been the subject of many studies. The peculiarity of Titan lies in its extremely thick atmosphere and the important dynamical phenomena that take place inside the atmosphere. The vertical extension of Titan's atmosphere is 10 times that of the Earth's, up to 1000 km from its surface. Its vertical structure is similar to the atmospheric vertical profile we have on Earth as shown in Fig.1.1. Like Earth's, Titan's atmosphere is primarily composed by nitrogen (N_2), however, with methane (CH_4) and not oxygen (O_2) as the next most abundant constituent [Flasar et al., 2005; Raulin, 2007]. Haze and aerosols are CH_4 and N_2 byproducts resulting from photochemistry phenomena taking place in the upper layer of the atmosphere. Titan's atmosphere is a hot-topic nowadays because hydrocarbons (i.e. organic compounds consisting entirely of carbon and hydrogen) are building blocks for amino acids necessary for the formation of life [Raulin, 2007]. In fact Titan may offer the possibility of studying some of the prebiotic processes that were occurring on Earth when life was emerging. Eventually it has been claimed that Titan looks like an early frozen Earth and therefore could help in expanding the knowledge about the processes that took place on our planet at that early stage.

The first mission that performed a flyby around Titan was during the NASA Voyager Program in the '80s. The more recent Cassini-Huygens mission by NASA-ESA-ASI that was launched in 1997, is still studying Titan and the Saturnian system. The mission was equipped with ESA's Huygens probe that landed on Titan's surface in January 2005. The surface of the moon and the lower layers of its atmosphere were practically impossible to see before the Huygens descent inside Titan's atmosphere. The hampering is due to scattering of sunlight caused by the aerosols composing the haze layers, which makes optical remote sensing difficult from a spacecraft's altitude and from ground- and space-based telescopes. The Huygens probe was in fact, the first in-situ mission that explored the lower atmosphere and the surface of Titan. Several observations of Titan have been done using ground- and space-based telescopes, like the Very Large Telescope (VLT), the Keck telescope and Hubble Space Telescope. Observations made with telescopes are complementary to those obtained with an in-situ mission. As an example, the ground-based observations are of fundamental importance for the interpretation of results from the Huygens mission [Witasse et al., 2006].

Analyzing data coming from several missions, important information about the inner and outer structure of Titan has been obtained, which constrains the current models of both the interior and the atmosphere. Models of the interior are not yet well defined; they are mainly based on gravity data and not all the physical parameters are known. Atmospheric models strongly depend on the characterization of the aerosols contained in the haze layers which constrain the seasonal change and climate on Titan. Characterization of the aerosols is also fundamental to gain further knowledge on the so-called methane cycle, a cycle often compared to the water cycle present on Earth.

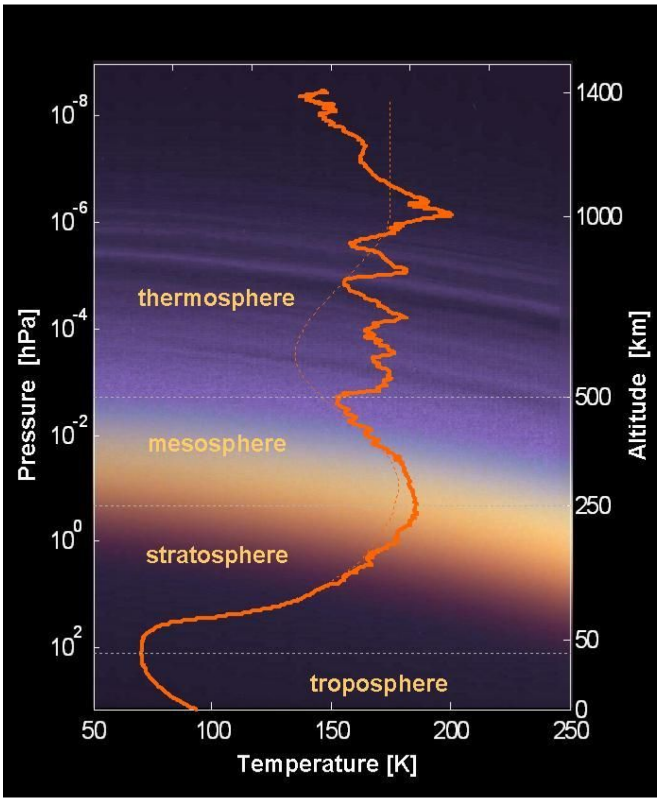

Figure 1.1: Titan's atmosphere temperature profile as retrieved during the Cassini-Huygens mission. *Credits of: L'Observatoire de Paris website* [1]

Methane is an amazingly active component that is present all over Titan. Despite the destruction by photochemical reactions in the upper layers, a loss in methane percentage in the atmosphere of Titan has never been observed: a reservoir of methane is probably present in the subsurface of the planet. Before the Huygens descent, people expected methane lakes or seas to cover the surface of Titan to explain the CH_4 source, but no ocean is present on the surface and lakes have been found only at the poles as observed by the Cassini orbiter (Fig.1.2). Nowadays scientists believe that methane is stored in clathrate form in the subsurface, and should replenish the atmospheric CH_4 by escaping from the surface. Several tectonic features in fact, have been observed all over the moon by both Huygens and, especially, Cassini radar instruments; these features, probably generated by the intense interaction between Titan and Saturn's gravity field, should allow the passage of methane by outgassing from the interior to the surface and therefore, to the atmosphere [Atreya et al., 2008; Coustenis, 2005; Niemann et al., 2005]. The methane cycle starts in the atmosphere.

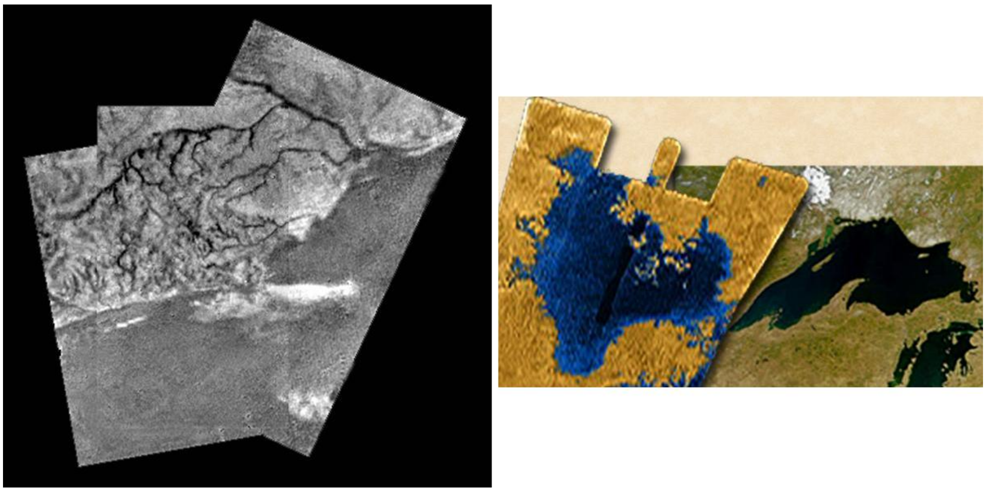

Figure 1.2: Liquid presence on Titan surface. On the left we have a mosaic of River Channel and Ridge Area on Titan. Picture taken with DISR instrument on the Huygens probe. On the right we have the Titan Sea and Lake Superior. Picture taken with Radar Mapper instrument on the Cassini orbiter (artificial colors). *Credits of NASA/JPL/ESA/University of Arizona*

The methane in the upper layers of the atmosphere is decomposed by UV radiation and recombines with nitrogen to form tiny haze particles, or monomers. In the middle layers of the atmosphere the collisions between these tiny haze particles produce fractal-shaped aerosols. The aerosols are nothing else than aggregates of hydrocarbons of different non-symmetrical shapes. This middle atmospheric haze layer reaches up to 200 km above the surface and prevents observing Titan's surface at visible wavelengths from an orbiter (e.g. the Voyagers or from Earth). Because of the obliquity of Saturn to its orbit (26.73°), Titan's atmospheres is characterized by a seasonal changes. Seasonal variations in haze and clouds present at different latitudes and altitudes suggest the presence of clouds and hazes is controlled by dynamical processes such as prevailing wind directions. But also the opposite is valid: the atmospheric dynamics together with the more global climate situation on Titan are driven by the presence of aerosols and its seasonal change. If methane evaporates from the surface and falls back as rain (not yet observed), the cycle can be considered as a closed cycle exactly as we have on Earth with water [Atreya et al., 2008; Coustenis, 2005; Hirtzig et al., 2009; Tomasko et al., 2005]. The atmospheric models are not yet fully constrained because of uncertainties in our knowledge of the aerosols microphysical properties, such as their vertical profile, size and shape.

This work is focused on a detailed investigation of the aerosols in Titan's atmosphere. Special attention is given to on gaining information on the number density, size, and shape of the haze particles as functions of the altitude, which is key to expand the knowledge of the atmosphere's complex hydrocarbon (methane) cycle and climate. One of the most valuable tools for analysis of clouds and aerosols is the sunlight these particles scatter due to its remarkable richness in information on planetary atmospheres. For this reason we will use spectropolarimetry to study the scattered sunlight inside the atmosphere of Titan expressed as total radiance I and degree of polarization P. In particular the degree of (linear) polarization is known to be very sensitive to the microphysical properties of the scattering particles, or aerosols in our case [Hansen and Travis, 1974].

If we measure the degree of polarization of scattered sunlight inside an atmosphere, we are able to deduce the size of the monomers (i.e. the aerosol components) at different altitudes and their variations along the vertical profile. From these observations it would become possible to understand in which form an atmospheric component is present at a certain altitude, whether the haze particles are small or big, have a compact shape or a fluffy shape, and so on. Differences in sizes, shapes or number density will influence the single scattering properties of the aerosol and of the multiple scattering of the solar radiation in the whole atmosphere (aerosols + gas molecules effects). This will influence the radiative flux and profile of solar heating and, consequently, it will give different constraints on atmospheric dynamics. This example gives an idea of the capabilities of polarization and the importance in determining size, shape and vertical profile of the aerosols as accurately as possible [Tomasko et al., 2009].

In the past decades there have been several missions to various planets that carried instruments with polarimetric capabilities such as Pioneers 10 and 11, Voyager 1 and 2, the Galileo and Cassini-Huygens mission. These instruments performed polarimetry using polarization filters in two or three positions. The total radiance and degree of polarization are then derived by combining measurements obtained with these different filters. We refer to this polarimetric method as a classic polarimetric method. An example of such classical polarimeter is the Descent Imager/Spectral Radiometer (DISR) instrument on the Huygens probe [Tomasko et al., 1997]. Thanks to its polarimetric capabilities DISR was able to obtain important information on the shape and size of the aerosols in Titan's atmosphere [Tomasko et al., 2008]. The DISR measurements were made using the classic polarimetric method applied only to two wavelength bands (i.e. blue and red). The disadvantage of this method is the necessity of combining different radiance measurements at a few wavelengths to obtain the total radiance and degree of polarization of scattered sunlight. This generates differential effects and errors that severely limit the capabilities of spectropolarimetry.

In order to expand our knowledge on Titan's aerosols it is important to measure the spatial and temporal variations of the aerosols' microphysical properties and their 3D distribution in Titan's atmosphere (note that the DISR measurements were local measurements constrained by the Huygens descent trajectory). The Titan Saturn System Mission (TSSM) that was submitted as part of ESA's Cosmic Vision Program, is a mission that might explore the orange moon and the Saturnian System in the future [TSSM Study Final Report, 2009]. The mission will be equipped with an hot-air balloon that will float underneath the lowest atmospheric haze layer of Titan with the specific intention, among others, to get more information on the aerosols and consequently on the climate on Titan.

SPEX (Spectropolarimeter for Planetary EXploration) is a new spectropolarimetric instrument which could improve the knowledge on the aerosols. SPEX as payload on the TSSM balloon, is designed to measure both the radiance and the degree of polarization of sunlight that is scattered in Titan's atmosphere and to retrieve size, shape and composition of the atmospheric particles and their vertical distribution[2]. In its current design, SPEX has been optimized as payload for a Mars orbiter to retrieve properties of the dust and ice particles in Mars' thin atmosphere. In this current design it works in the wavelength range between 350 to 800 nm and yields a spectral resolution between 2 nm (radiance) to 10 nm (polarization).

SPEX' spectropolarimetric method works by encoding the degree and the angle of (linear) polarization in a sinusoidal spectral modulation of the radiance spectrum. With a single measurement of the scattered sunlight we are able to determine the degree and the angle of linear polarization as function of the wavelength. In addition to being robust, SPEX is a small instrument (< 5 kg) with no moving parts, but is capable of full linear spectropolarimetry [Snik et al., 2009]. The polarimetric concept of SPEX is based on birefringent crystals and has been patented by Prof. Dr. C.U. Keller of the Astronomical Institute of the University of Utrecht, The Netherlands.

The goal of this report is to explore the versatility of the SPEX instrument. The question driving this research is: *can* SPEX*' design, now tailored for a mission orbiting Mars, be adapted for an in-situ mission to the moon Titan with the intention of retrieving the aerosols' microphysical properties?*

The difference with respect to a Mars mission lies in the features in the spectrum of the scattered sunlight and in the orientation of the viewing apertures. Mars' spectra are rich in information on the dust/ice particles' characteristics, but they have no strong absorption band features as Titan's: Mars spectra show no methane bands within SPEX wavelength range[3]. Titan's spectra, on the other hand, are characterized by strong methane absorption bands evident around 620nm, 730nm and 800nm, making the retrieval of the degree of polarization more complicated. These bands contain additional information on the aerosols such as vertical distribution. Spectrally resolving these bands would provide added value on the aerosols with respect to analyzing only the continuum. Moreover, Titan-SPEX needs to have different viewing angles due to its placement on a balloon instead of on a orbiter as planned for Mars-SPEX. The viewing angles for the Mars orbiter are mainly oriented downwards. For the Titan-SPEX we need to observe not only the surface underneath the balloon, but especially the haze layers.

In order to pursue the research goal it is necessary to first analyze the local atmospheric composition and structure that SPEX will face by describing the scattering and absorption taking place in Titan's atmosphere. Considering that there are almost no measurements for the scenarios we want to study (and certainly not with the required spectral and angular resolution), we performed numerical simulations of sunlight scattered inside the atmosphere of Titan. To verify the behavior of SPEX' current (Mars) design under the Titan conditions, a numerical instrument simulator that simulates the performances of SPEX (i.e. SPEX simulator) is supplied with the output obtained from the light scattering simulations. Already a quick analysis of SPEX' performance

---

[2] This study focuses on the retrieval of the size and shape of the aerosol particles, while the composition and the vertical distribution are considered as given.

[3] There can be absorption bands due to CO_2 in Mars' spectra, but they are not as pronounced as CH_4 absorption features in Titan's spectrum which are, therefore, more difficult to resolve spectrally.

shows that its current design is not optimal for Titan's exploration: it is not able to fully resolve the methane bands features. For this reason the SPEX' spectral resolution has to be increased to improve the instrument performance as we will show in this report. This can be achieved by increasing the size of the birefringent crystals in the SPEX pre-optics system from 4 mm to 16 mm. Additionally, an interesting solution to optimize SPEX' viewing angles would be to have a rotating disk placed on a boom beneath the balloon's gondola and inclined under an angle of 40° with respect to the vertical axis. A number of apertures looking outward would be positioned along the rim of the disk allowing observations both down and upwards but not interfering with the balloon itself.

The report is structured in the following way. Chapter 2 gives an introduction on the moon Titan, on its formation and its main physical characteristics starting by describing the moon's interior ending up to its atmosphere. Phenomena taking place inside the atmosphere are also described in this chapter. Chapter 3 describes the light scattering, the radiance and polarization generic concepts and formulations. The description and simulations of the single scattering of Titan's aerosols is given in Chapter 4. Chapter 5 takes care of the atmospheric radiative transfer: the aggregates described in the previous chapter are now placed in a "model atmosphere" to see how they macroscopically influence the light scattering. In this chapter there is a detailed description of the atmospheric model. In Chapter 6 we will describe which parameters are needed to model the atmosphere using the Doubling-Adding method (DAM). Several simulations and their results will be discussed in this chapter. SPEX is introduced in Chapter 7 as designed for the Mars orbiter. A description of how SPEX has to be adapted if placed on the TSSM balloon takes place in Chapter 8. The results of SPEX' simulator will be discussed. Chapter 9 presents the conclusion and recommendations.

This work has been presented at the 7^{th} International Planetary Probe Workshop (IPPW-7) that took place in Barcelona on June 14-18, 2010. I was selected to give an oral presentation (there were also poster presentations) and I won the first prize as "Outstanding student oral presentation". The article presented at the IPPW-7 can be found in Appendix A.

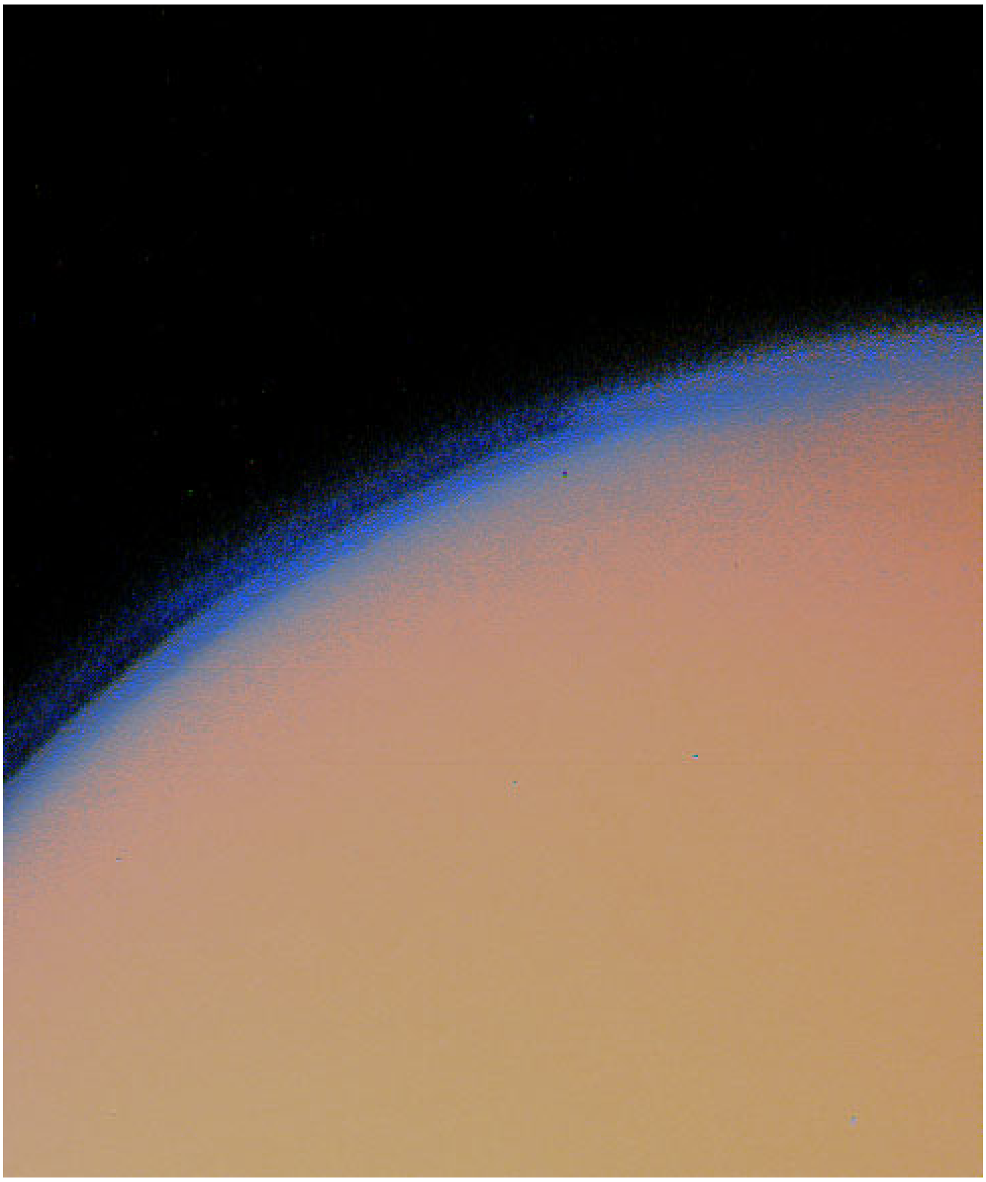

Figure 1.3: Titan haze layer. Picture taken on 12 November 1980 at 430000 km by Voyager I during the first flyby around Titan ever realized.
Image source: NASA website

2 Titan's structure

In this chapter a brief description on how Titan looks like from the interior part till the upper layer of the atmosphere will be drawn. In the first paragraph the interior of Titan will be analyzed together with the methane possible replenishment from it. In the second chapter the atmosphere structure is analyzed. A special attention is given to the aerosols and their seasonal cycle. In the last paragraph a comparison between Titan and two comparable Jovian moons is given to understand which reasons brought an atmosphere only on the Saturnian moon.

2.1 Titan's Interior and methane outgassing

The interior of Titan is extremely connected with the atmosphere content. A lot of studies have demonstrated that the content of methane we have nowadays of Titan is so high that has to be a replenishment coming from the interior of the planet. Part of the Nitrogen also could have come from the interior. Scientists are modeling the interior of Titan trying to understand how it is structured, where the methane reservoir is, how big it is and how the methane replenished the atmosphere content. One of the last model about the formation and the structure of Titan's interior has been validated by the mission Cassini-Huygens which confirmed some laboratory tests with pictures and data of the moon's surface .

As described in appendix B Titan has a mass just equal to the 2% of the Earth's one. It's main density is 1.88 g/cm^3 meaning that it's enterior is an ice/rock mixture [de Pater and Lissauer, 2001]. The actual structure of Titan has been confirmed as being a rocky core of silicate, an high-pressure ice layer, an ammonia enriched water layer and a methane-clathrate enriched icy layer as shown in Figure 2.1 [Tobie et al., 2009].

Most of the studies bring to the conclusion that 3 outgassing episodes took place during Titan's formation:

1. Accretion period (0,5 - 1 Gyr)
2. Core overturn (2 - 2,5 Gyr)
3. Thermal instabilities within outer ice crystallization (4 - 4,5 Gyr)

Let's look more in detail to see where and when was it possible to have methane outgassing during Titan's formation. During the accretion period the interior was mainly divided in 2 parts: the innermost part in which most of the volatiles (e.g. methane and ammonia) where trapped in while outwards there was probably a warm liquid water ocean with low solubility [Tobie et al., 2009].This means that methane

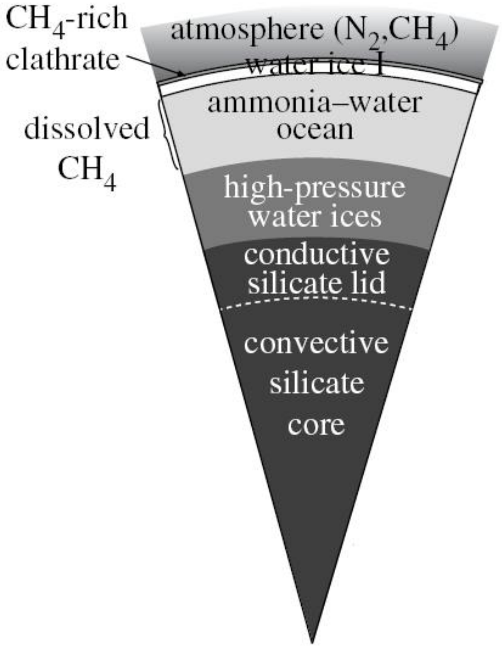

Figure 2.1: Titan's interior. [Tobie et al., 2009]

rapidly raised up the ocean with a probably first outgassing episode while ammonia got stuck in the ocean due to its high solubility. The few ammonia that reached the surface was converted into nitrogen. The next step of Titan's formation is the proto-core formation in which the few methane that did not escape in the previous step was stored in the undifferentiated proto-core in the form of methane clathrate. Methane clathrate is composed by methane and water molecules, this combination happens especially because of the temperature and pressure values on the cold Titan [Tobie et al., 2006]. Around 2,5 Gyr the differentiation of the core took place. During this period the core goes under overturn, meaning that all the light materials rose up at the edge of the core and the heavy materials (i.e. silicates) sank down forming the rocky core we still have now. Methane clathrates, being 2% less dense than water ammonia, reached the top of the outer liquid ammonia layer during differentiation. Another characteristic of methane clathrate is its strong stability, in fact while rising up into the the water ocean dissociation didn't happen and a layer of methane clatharate formed at the top of the water ammonia ocean. Once the differentiation is achieved the internal structure consist in the one showed in fig. 2.1 [Tobie et al., 2009].
What about outgassing?
Outgassing can happen only if the methane content in the liquid phase exceed the saturation solubility, in other words if the dissociation conditions were reached within the icy mantle. The methane clathrate layer influenced the thermal evolution after the differentiation. This layer actually acted as a insulator, the cooling rate of the interior was strongly slowed down. This is translated into a slower cooling down of the water ammonia ocean and in a slow crystallization of the bottom layer of this ocean. The latter phenomena led to a slow thickening of the high pressure layer. Around 3,5 Gyr the crystallization started from the top (ice I layer) slowly increasing the thermal

convective instabilities and tidal dissipations [Tobie et al., 2009]. The quantity of methane outgassed depends on the initial amount of methane in the proto-core and the convective activities in the silicate core. This amount puts boundaries to the total amount of methane storage inside Titan. In fact the model presented by Tobie *et al.* in 2006 proved that the amount of methane relative to water in the proto-core is between 0.15 and 0.25. The upper limit is a quite impossible choice since in that case we would have found a thick liquid methane and ethane layer on the surface, Cassini showed the opposite. The lower limit meas that outgassing took place quite recently. Most believe that the outgassing episode that replenished the atmosphere with methane took place around 4,5 Gyr when the surface heat flow was maximal. It was probably connected with thermal instabilities in the outer icy layer and upwelling icy plumes that penetrated the clathrate crust. Traces of cryovolcanism found by Cassini mission could be a proof of eruptive processes of outgassing.

A further proof of outgassing from the interior is the presence in the atmosphere of isotope ^{40}Ar a daughter of isotope ^{40}K connected with the rocky core. Potassium is one of the main constituent of a rocky core that decays into argon: the mole fraction of ^{40}Ar detect so far is about $4.32 \pm 0.1 \times 10^{-5}$ and it's an indication of long geological activity on Titan, i.e. cryovolcanism and tectonics [Niemann et al., 2005]. Argon could have been probably carried up by methane clathrate directly from the bottom of the ocean during the core overturn [Niemann et al., 2005; Tobie et al., 2009]. Maybe there was also a shorter episode around 2,5 Gyr (differentiation) but almost surely nothing around 1 Gyr.

2.2 Titan's atmosphere

2.2.1 Atmosphere's origin

From a scientific point of view Titan is a mystery since is the only moon in the Solar System with a thick atmosphere. In general most of the moons have a pretty faint atmosphere due to a lack in magnetic field, the force that keeps all the floating particles of a possible atmosphere linked to the planet they do belong (only exception is the planet Venus that has an atmosphere but no magnetic field). All the moons Titan included have a weak gravity field, their atmosphere scale height is large and thus is defined as faint atmosphere. But Titan is different, it has a weak gravity field but a thick atmosphere. Titan's atmosphere is the only one in the Solar System composed mainly of N_2 like on Earth; the other two main constituents are 2 % methane (CH_4) and 0.1% hydrogen (H_2) [Raulin, 2007]. Argon isotopes are also present. Several studies have been made to investigate and understand how this thick atmosphere formed. We have already mentioned methane outgassing, but let's go more inside out.

According to Coustenis [2005], Titan atmosphere could have had three different origins:

- Solar nebula
- Outgassing
- Impacting comets

Solar nebula - If the atmosphere would have been formed in the solar nebula at the same time Titan also formed, there should be traces of some noble gases that instead are completely absent like Ne. No traces of Ne have been found so far, thus this scenario is left out.

Outgassing & Impacting comets - Both these processes are considered as the ones directly related to the origin of Titan's atmosphere. The theory of outgassing comes from analysis of methane amount in Titan's atmosphere. Today, 4.5 Byr after the solar system origin, CH_4 on Titan should be exhausted due to the conversion of methane into hydrocarbons through photochemical processes. But we have already discovered in the previous chapter that the outgassing balances the photochemically loss rate rate, that's why atmospheric methane percentage did not see any drastic change within Titan's life.

To better understand the origin and evolution of chemical compounds like the ones we have here, some conclusions can be obtained with the D/H ratio analysis. The D/H ratio, called also deuterium enrichment, is the ratio between deuterium (D - an hydrogen isotope) and hydrogen (H), it's used to obtain information about origin and geologic history of any fluid. In our case in fact D/H ratio of methane on Titan is compared with the one of water on comets (supposed to be unchanged since the solar system formation). The D/H ratio calculated so far is $8.75^{+3.25}_{-2.25} \times 10^{-5}$ [Coustenis, 2005; Mousis et al., 2002a]. This value is an order of magnitude higher than the value in the solar nebula H_2, slightly less than 3.2×10^{-4} found for Oort-cloud comets [Niemann et al., 2005]. This leads to the conclusion that the contribution to Titan's atmosphere formation is not only due to impacting comets (we will discuss it better in the following chapter) otherwise the values of deuterium enrichment would have been the same. On the other side the actual value of D/H ratio for methane on Titan is important for outgassing. Mousis et al. [2002a] suggest that cryovolcanism episodes could have permitted escape of CH_4 from the interior of the planet. Latest news from Cassini-Huygens mission [*NASA official website*] is that the Cassini radar instrument showed clear traces of tectonic phenomena. This is the most valid proof of the outgassing theory of Mousis et al. [2002a] and Tobie et al. [2009]. In fact most of the science groups busy with Titan's interior structure believe there is a layer of clathrate methane possibly 100 km thick just above the NH_3 ocean [Coustenis, 2005; Mousis et al., 2002b; Tobie et al., 2009].

Nitrogen origin

Nitrogen's origin instead is analysed using ^{36}Ar another argon isotope present in the atmosphere. The question is if nitrogen came into the form of N_2 or in the form of nitrogen compounds like ammonia NH_3. Nitrogen atoms N_2 and argon atoms Ar are both in ice form around 75K [Coustenis, 2005], hence if they got trapped in ice at the same epoch, nowadays they should have the same abundance in the atmosphere . The value of ^{36}Ar abundance detected with GCMS instrument on Huygens probe at surface level is $2.8 \pm 0.3 \times 10^{-7}$, a value really low compared with N_2 ones. Nitrogen molar fraction value should be higher than the one of methane considering the abundance of methane and nitrogen in the atmosphere; if methane mole fraction is around 10^{-2} at

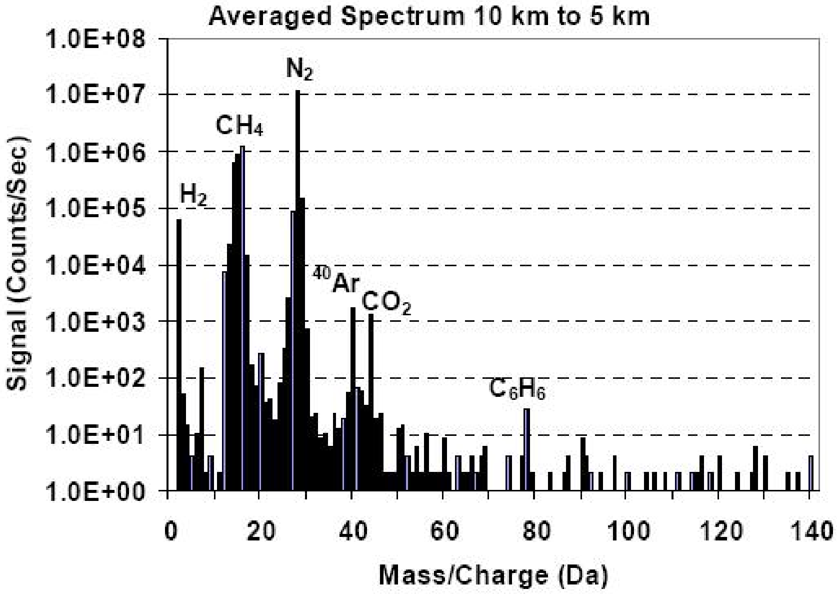

Figure 2.2: Average mass spectrum between 10km and 5km showing the major constituents of atmosphere:$H_2, CH_4, N_2,^{40}Ar$. The CO_2 is believed to be sensed background of the instrument.[Niemann et al., 2005]

the surface, nitrogen mole fraction should have at least the same order. Thus nitrogen was captured as ammonia NH_3 during the accretion period of Titan and then converted into N_2 through continuous photolysis [Niemann et al., 2005].

2.2.2 Hydrocarbon cycle

As discussed in the previous paragraph methane comes mainly from the inside of the planet through outgassing and apparently it goes back to the soil as hydrocarbon rain. Often it is referred to this photochemical-metereological-hydrogeochemical cycle as the Titan Methane cycle [Atreya et al., 2006].

The atmosphere of Titan is several kilometers more extended into space than Earth's one. It can be subdivided into three main regions: the first is the upper atmosphere where the photochemistry takes place, which includes the exosphere and the mesosphere; the second part is the middle atmosphere in which we have the aerosols growth and the haze layer formation, it includes stratosphere and troposphere; the third part is the lower atmosphere in contact with the surface where clouds and rain form letting the hydrocarbons accumulate on (replenish) the ground and probably close the cycle.

Photolysis

The presence of haze at lower altitudes suggests that there are chemical reactions converting small molecules into larger ones that form haze aerosols. The main sources of this process are Saturn's magnetosphere and the solar UV radiation. Titan spends most of its orbital time embedded into Saturn magnetosphere, but as soon as it gets

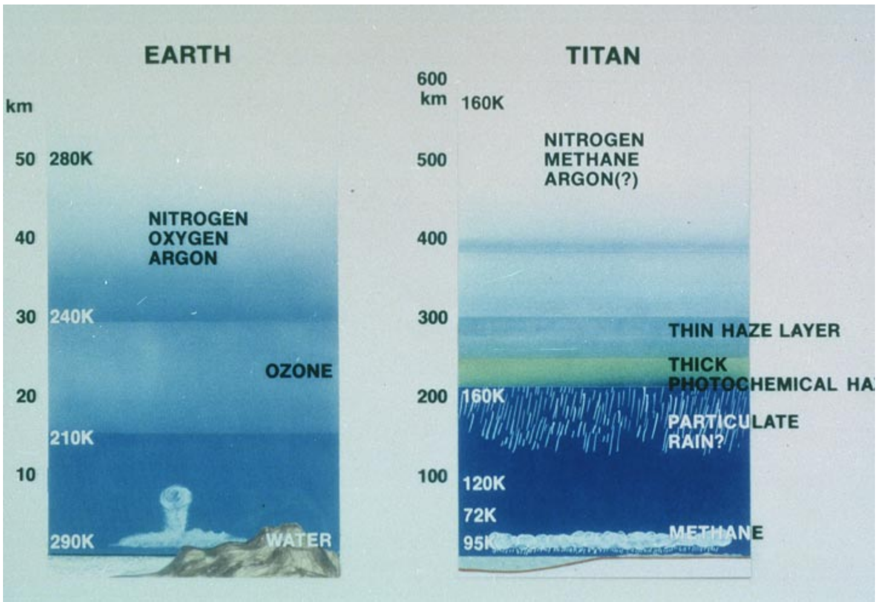

Figure 2.3: This graphic illustrates the differences in Titan's and Earth's atmospheres. Titan's atmosphere extends 10 times further into space than Earth's. *Credits: NASA/JPL*

out of it, the solar UV radiation increases about a factor of 20 [Fortes, 1997]. The flux due to magnetosphere electrons and protons is smaller by one order of magnitude than the flux due to solar EUV [Fortes, 1997; Tran et al., 2007]. Photolysis is a process that takes place in the upper atmosphere between 1400 km and 500 km (approximatively). It consists in the reaction between ions and protons, coming from the Sun or from the Saturn's magnetosphere, and the chemical molecules in the atmosphere; some of them get excited, some of them get charged other get expelled leading into a change in the composition of the atmosphere. Methane and nitrogen are broken down by UV absorption in the mesosphere forming hydrocarbon-nitrile compounds (C_xH_y and C-N-H respectively) while hydrogen is lost in space as a consequence of these reactions [Tran et al., 2007; Waite Jr et al., 2007]. The Ion Neutral Mass Spectrometer (INMS) experiment during the Cassini-Huygens mission revealed and confirmed that the atmosphere is filled mainly by N_2 and CH_4 accompanied by a rich mixture of polycyclic aromatic hydrocarbon (PAH - haze precursors) and haze. In particular polymers and nitriles form hazes in the upper atmosphere ($>$ 500 km), whereas PAH polymers condense to form hazes anly in the middle lower stratosphere ($<$ 200 km) [Atreya et al., 2006]. Ion-neutral chemistry also plays a central role in linking these organic units together to form more complex organics [Waite Jr et al., 2007].

During the Cassini mission it has been discovered that this complex molecules formation already takes place around 1000 km with a production rate of $1 \text{ x } 10^{-16}\, g\, cm^{-2} s^{-1}$. Supposing a spherical radius of the particles, with MIE scattering they estimated a radius of 0.0125 μm for the starting particles and a radius of 0.260 μm for the aerosols [Waite Jr et al., 2007] in accordance with what found in the lower part of the atmosphere.

The end product of photochemistry is then a conversion of methane to mainly ethane and hazes in comparable amounts. Contrary than on the giant planets, the small amount of hydrogen in Titan's relatively cold surface does not permit transforming the hydrocarbon products back to methane. [Atreya et al., 2006; Lunine and Atreya, 2008].

Haze formation and growth

The haze formation, growth and distribution throughout the atmosphere are the most discussed processes characterizing Titan's atmosphere. The process of formation is pretty complicated and scientists tried to analyze it implementing several different models. The main factors leading these processes have been pointed out by Bar-Nun et al. [2008] :

- temperature and pressure profile which influence the atmospheric density and then the velocity of the particle
- kinetic models describing the final composition of both the gaseous species and the aerosols materials
- nucleation index describing the number of initial particles (embryos)
- sedimentation index governed by gravity, nature of the particle and local environmental conditions
- condensation index directly related with the volatiles on the aerosols
- diffusion coefficient depending mainly on the nature of the transfer process (molecular and atmospheric motions)
- coagulation index that calculates the effective collisions depending mainly on the particles nature.

Just having a look at this list it's comprehensible how complicate is to model the formation of the aerosols and on how many parameters scientists can have a different opinion. The general process is that UV photolysis produces methane and nitrogens compounds (polymers) which condense at the exobase to form the so-called embryos of aerosols (nucleation). The size of these embryos is in the orders of nanometers, this explains also why we see them only from the bottom of the exobase: for the instrumentation state of art they are enough smaller to not be detectable at higher altitudes. The first stage of nucleation takes place between 850-550 km, below 550 km collisions lead the growth of the aerosols. Between 550 km and 100 km the size of the aggregates grows till reaching a size of 10^{-1} μm. Below 100 km we have mainly free fall trajectories bringing the aerosols to the ground, in this last stage the size is more or less stable because of the less probable successful collisions [Bar-Nun et al., 2008].

A curiosity studied by Rannou et al. [1993] is about the time span between the formation and the deposition of the particles on the ground. Rannou et al. [1993] together with Cabane et al. [1993] simulated the process of formation of aerosols in Titan's atmosphere reaching the conclusion that within one terrestrial day particles grow mainly through collisions with larger particles (below 550km according to Bar-Nun et al. [2008]). Between few terrestrial day till one terrestrial month evolve by collision with small particles and taking a spherical aerosol shape. While within thirty terrestrial years (one Titan year) they grow in the stratosphere by cluster-cluster aggregation reaching a final size of 0.4-0.5 μm (fractal model). According to their model the particles we find on Titan's surface have been created 300 years ago, this gives an

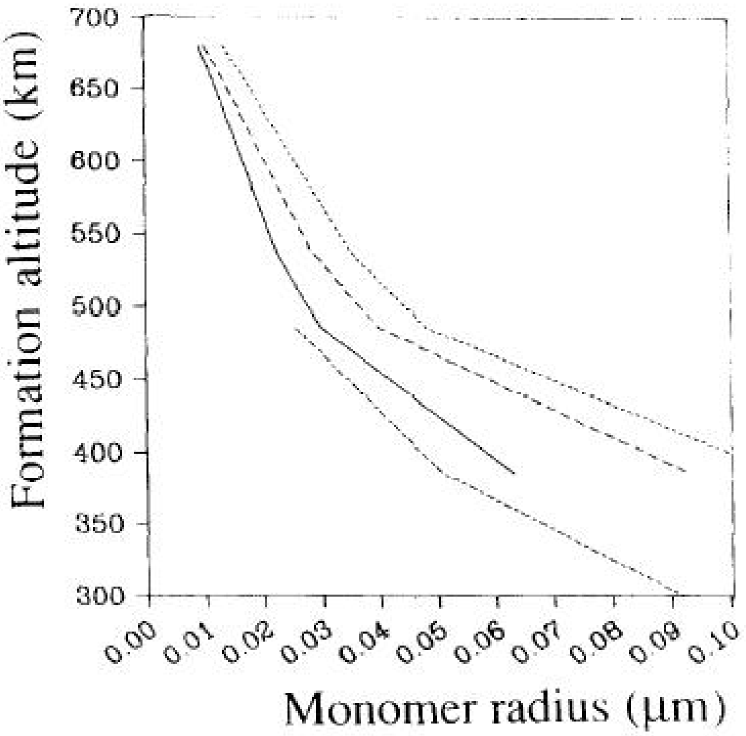

Figure 2.4: Vertical profile of the monomer radius as a function of the formation altitude for different mass production rates.M=$10^{-12}\,kg\,m^{-2}sec^{-1}$ (dotted line), M=3.5 x $10^{-13}\,kg\,m^{-2}sec^{-1}$ (dashed line), M=$10^{-13}\,kg\,m^{-2}sec^{-1}$ (solid line), M=3.5 x $10^{-14}\,kg\,m^{-2}sec^{-1}$ (lower dashed line) [Cabane et al., 1992].

idea on how slow is the process and how slow is the velocity of the particles in the atmosphere.

The choice of the monomer radius depends from the temperature and pressure profile and from the chosen mass production rate. The altitude of peak formation of the aerosols is settled between 200 and 700 km in the literature. The way to check which is the most probable altitude is fitting the measured extinction profile with the modeled one; being the aerosols absorbing, the extinction increases in their presence. This fitting has been done since after the Voyager mission that had the first global look at the atmosphere. In figure 2.4 we can see that increasing the mass production rate the altitude of the radius gets lower and lower. For a radius of 0.05 μm the mass production is between 3.5 x $10^{-13}\,kg\,m^{-2}sec^{-1}$ and $10^{-13}\,kg\,m^{-2}sec^{-1}$ for a production altitude between 500 km and 400 km [Cabane et al., 1992]. Lately Tomasko et al. [2009] and Lavvas et al. [2009] pointed out the possibility to have monomer radii of 0.04±0.01 μm with a production rate of 2.7-4.6 x $10^{-13}\,kg\,m^{-2}sec^{-1}$ for a production altitude around 500 km. They are in accordance with Cabane et al. [1992].

The processes leading the aerosol aggregation are of two kinds: ballistic and diffusion-limited (DLA). In the first case the particle moves along a straight line, while during DLA the particle undergoes Brownian motion. As soon as a particle collides and sticks to another particle or to a cluster of particles the process ends. The ballistic process takes place during the growth of the particle since the mean free path is bigger than the radius of the particle itself as it is at its early stage. DLA process takes place mostly in case the mean free path is smaller than the radius of the particle [McKay et al., 2001]. Thus ballistic processes are linked with the upper atmosphere when the particle is still small, while the DLA takes place when the particles are quite big and not easy in their movements as it is in the troposphere [Skorov et al., 2008]. Both the diffusive and ballistic process can produce compact and fluffy clusters. In case of ballistic mechanism it is possible to have particle-cluster aggregation (BPCA) and particle-particle aggregation (BCCA) respectively, the same is valid for DLA.

2.2.3 Seasonal haze circulation

In the past it was believed that the seasonal variations on Titan were driven by changes in haze production rate, but a re-analysis of the timescale has shown that haze seasonal variations are connected to dynamical effects. Rannou et al. [2002] and Rannou et al. [2006] studied the interaction between Titan's haze and dynamics taking into account latitudinal dissipations of the winds first and cloud microphysical models afterwards (for further informations than what mentioned here please see their articles and the references therein).

The model they got proves that also on Titan there is an Hadley cell type of circulation similar to the one we have on Earth. The main cell on Titan is a unique cell that goes from the summer pole to the winter pole for almost the 80% of the Titan's year (on Earth we have two Hadley cells). At the moment of the equinoxes this big cell weakens (for three terrestrial years [Rannou et al., 2006]), splitting in two transitory equator-to-pole cells. In the summer hemisphere there will be the ascending branch between the equator and the pole, while the winter hemisphere will have the descending branch of the Hedley cell. A secondary cell forms in the summer hemisphere between 50 and 200 km but it turns in the opposite direction in such a way to not let go all the haze in the other hemisphere (it is less strong than the principal one) [Rannou et al., 2006]. Inside the main Hadley cell there are two smaller ones between the equator where air starts rising, and latitude 60° where the air sinks. These two smaller cells are produced because of the strong temperature contrast between the mid-latitude regions and the polar regions. Therefore there are three paths: a main pole-to-pole cell, a secondary summer hood and the double tropospheric cells. The description will focus mainly on the pole-to-pole Hadley cell.

The haze starts forming around 400 km below which the aerosols mass mixing ratio decreases with altitude. The summer branch takes particles from the lower layers of the atmosphere and carries them up to the stratosphere, the aerosols then move horizontally [1] towards the winter hemisphere producing a detached haze layer, and then following the downwelling Hadley branch they sink in the troposphere at the winter pole. The passage stratosphere to troposphere reduces the temperature of the aerosols than condense around the coldest point (tropopause) producing a thick cloud everywhere below 60 km. This cloud well mixed with polar haze is referred to as the polar hood. The secondary cell has the same effect on the summer pole but in a less massive way than at the winter pole.

Basically the circulation takes most of the aerosols from the summer hemisphere

---

[1] The velocity of the meridional winds is two orders faster than the settling velocity. At the Voyager time the south pole was in summer. [Rannou et al., 2002]

to enrich the winter hemisphere. The poles are the richest parts in aerosols, the haze accumulation and cloud formation is stronger at the winter pole than at the summer pole. For this reason the poles, and especially the winter pole, will appear colder than the rest of the planet because of the antigreenhouse effect induced by the haze.

If the observations are made in the VIS range, then the less rich summer hemisphere will appear brighter, while if we are in the NIR-IR range the winter hemisphere appears brighter because the haze becomes brighter than the gaseous molecules (clouds become visible!). The size of the aerosols will also change with latitude, but this does not affect the optical properties of the haze, in particular the polarization does not depend on the aerosols size.

The Cassini Huygens mission and ground based observations of Titan had evidence of clouds presence on Titan at different latitudes. During the Cassini-Huygens mission clouds appeared around 16±5 km and around 27±3 km. With the VIMS and the Keck telescopes clouds have been observed at mid-southern latitudes of 37-44° S in 2005 (due to the tropospheric ascending branch, the south pole was in summer) around 20-46 km by Griffith et al. [2005] and Roe [2009] respectively. During the Huygens descent instead, sparse and transient clouds have been seen around 16-20 km (equatorial area, 10° S) by the GCMS and the DISR instruments.

Rannou et al. [2006], in their one-Titan-year circulation modeling, predicted presence of methane clouds around the equator between $\pm 50^\circ$ and near the poles where the cloud is thicker. On the other side the big polar cloud appearing at latitudes $> 60^\circ$ is mainly made of ethane. Around equinoxes equatorial cloud activity should decrease because of the weaker Hadley cell (less aerosols in the air at those latitudes) [Rannou et al., 2006].

The different altitudes where the clouds appear can be explained also by some physics insight on the methane-nitrogen compound.

The temperature gradient in Titan's troposphere is around 1.3 K km^{-1} while on Earth is 9.8 K km^{-1}. This gets translated into a layer near the surface of Titan where convection takes place thinner than the one on Earth [Lunine and Atreya, 2008], for this reason it's almost impossible to observe high stratospheric clouds.

The explanation for the clouds altitude lies in the triple-phase curve for methane-nitrogen compounds in Figure 2.5. Nitrogen works as an antifreeze for methane: the freezing point (boiling point) for the compound will be at lower temperatures (higher temperatures) than for pure methane depending on the pressure values of the surrounding environment. In Figure 2.5 there are two lines representing the temperature curve: the dashed is for polar areas with a surface temperature of $89°K$ and the dotted is for equatorial areas with a surface temperature of $93°K$. Both reach a tropopause temperature of $71°K$. The solid line represents the triple-phase curve above which liquid and vapor coexist, beneath only solid will be present. The intersection point between the two temperature lines and the curve represents the point in which methane will change state, it represents the freezing/melting point. In other words from there on liquid and vapor phases can coexist and condensation[2] can take place: clouds can

---

[2] Condensation is the passage from vapor to liquid and takes place if the air is supersaturated: if the ratio between the existing vapor pressure to the saturation vapor pressure is > 1. A nucleus for each condensed droplet is necessary. Aerosols are used as condensation nuclei for the clouds [Wallace and Hobbs, 2006].

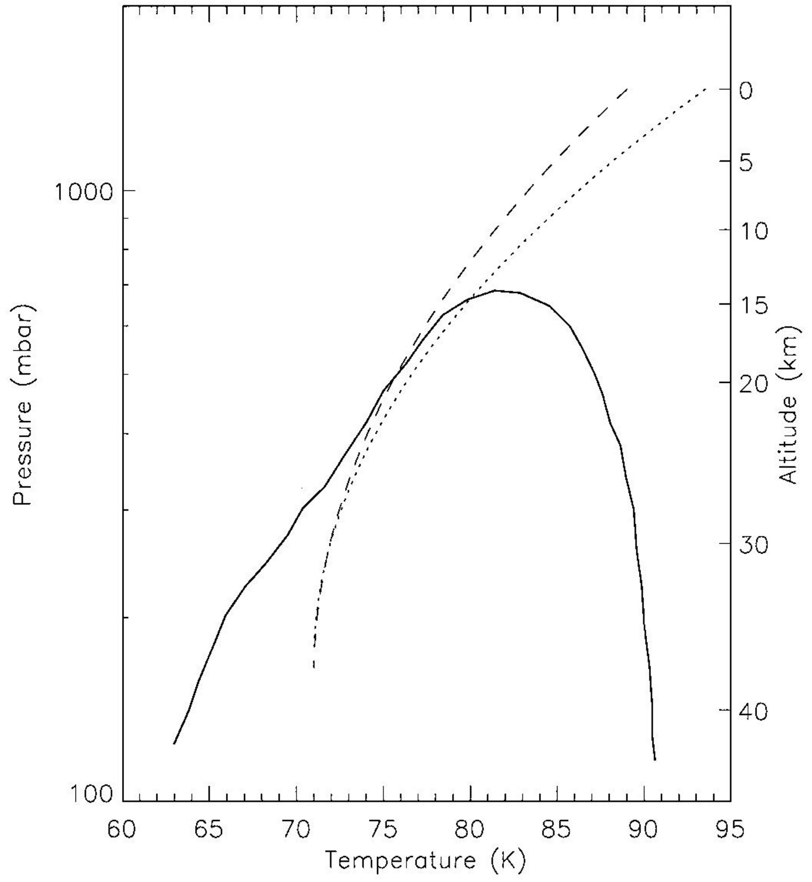

Figure 2.5: Melting point for a methane-nitrogen compound for equatorial and polar temperature profiles. The solid line is the triple-phase line for the compound, above it there will be liquid/vapor phase, beneath solid phase. The dashed line represents the polar temperature profile, while the dotted line represents the equatorial profile. The melting point for the methane-nitrogen compound will take place at higher altitudes for higher latitudes [Lorenz and Lunine, 2002]. See text for discussion.

form. For the equatorial curve the freezing point is reached at 14 km, while for the polar curve it is reached at 20 km. This means that if there is methane-nitrogen ice in the upper atmosphere, it will melt sooner at the poles than at the equator: the change-in-state altitude is higher at higher latitudes. That's why we could see higher clouds at the poles. Furthermore since this compound condenses and rains out at lower temperatures at the poles, it is then easier to see liquid presence at the polar surfaces as demonstrated by Cassini-orbiter (see Figure 1.2).

The average amount of rain is anyway expected to be very small because of the distance from the Sun, for the stratospheric haze block and for the lack in humidity. On Titan there is only the 45% of humidity at the equator, while for having a methane storm it is needed at least the 80% for the small amount of sunlight that gets there [Lunine and Atreya, 2008]. Even if liquid methane is present on the surface the evaporation will also be negligible. The triple point of pure methane is at $90.68°K$ really close to the surface temperature of $93.8°K$, so at the surface methane can be present

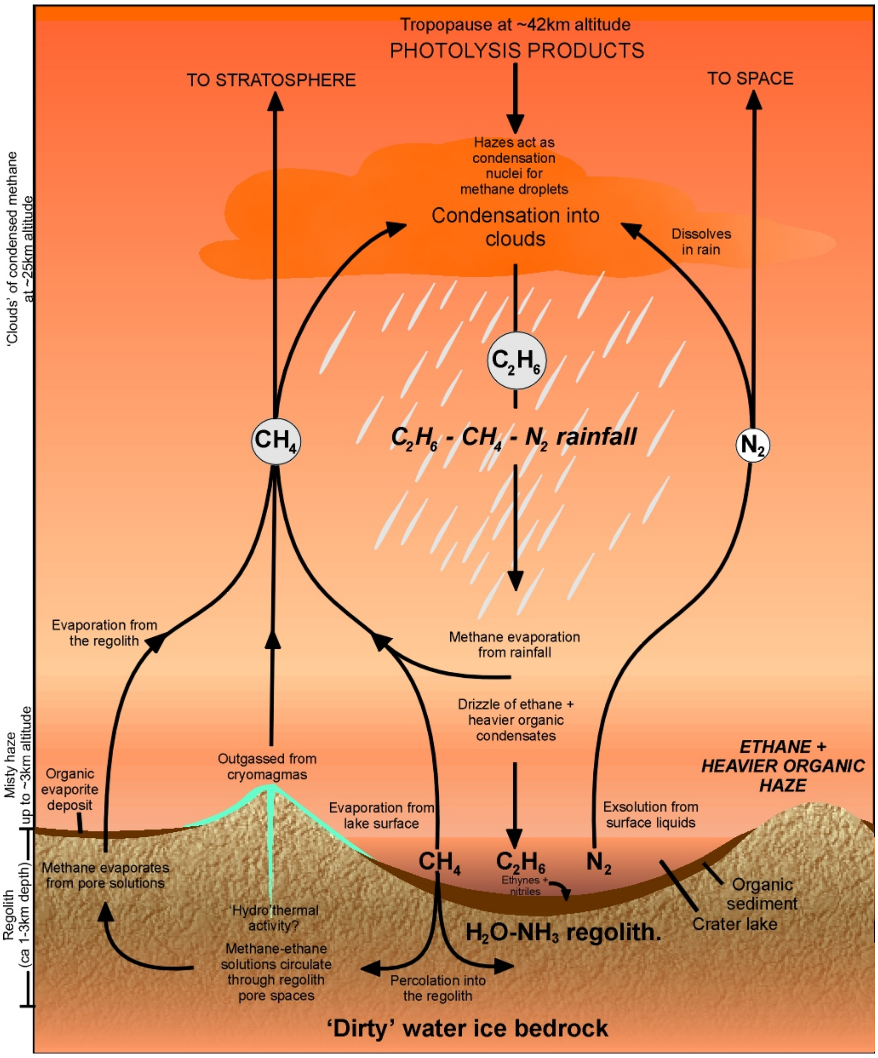

Figure 2.6: Overview of the phenomena taking place in Titan's atmosphere generally named as Methane cycle. [Fortes, 1997]

in its three forms.

According to Rannou et al. [2006] methane cycle is a balance between surface evaporation and precipitation, it evaporates between the tropics (±30°) and precipitates near the poles but evaporates before touching the ground. Generally the evaporation before reaching the ground depends on the height of the cloud and on the relative saturation below the cloud [Berry et al., 1945].

In any case the surface of Titan is rich in geological features as fluvial dendritic outflow channels, cryovolcanoes etc. indicating a possible interaction between the lower part of the atmosphere and the subsurface. In case of methane rain, the droplets could reach the subsurface through these openings and could be stored as icy regolith till being re-released into the atmosphere. To backup this assumption Atreya et al. [2006] compared the average resurfacing rate due to e.g. cryovolcanism to the rate at which methane is destroyed by phototchemistry with a final positive result. Current data are still inadequate to evaluate with accuracy if all the methane that eventually seeps from the surface in the interior is recirculated again into the atmosphere in such a way to have a closed cycle as we have for water here on Earth [Atreya et al., 2006].

3 Light scattering

Reflected sunlight is remarkably rich in potential information on planetary atmospheres and is one of the most valuable tools for analysis of clouds and aerosols [Hansen and Travis, 1974]. In this chapter we describe the flux/radiance and the status of polarization of light that SPEX will use to retrieve information on the atmospheric aerosols. An easy explanation of the light scattering concept is given in the first section. Description of the relationship between the radiation characteristics, such as radiance and polarization, and the physical properties of the scattering particles is given in the last two sections.

3.1 Why is the sky blue?

The answer to one of the most common questions of all the times is "Light scattering".

The sunlight travels in space in a straight line as long as nothing disturbs it. As soon as it enters the Earth's atmosphere it bumps into dust or gas molecule. Then what happens to the light depends on its wavelength and the size of the thing it hits. The white light from the sun is a mixture of all colors of the rainbow, each color is characterized by its own wavelength, frequency and energy. Longer is the wavelength, less is the frequency, higher is the energy. The light appears white because all the colors are in it.

When the light bumps in a big particle (e.g dust or water droplet, bigger than the wavelength of visible light), the different colors of the light are reflected in different directions but all in the same way, therefore the light keeps appearing white. If it bumps in a smaller particle (i.e. gas molecule, smaller than the wavelength of the visible light) some of its energy gets absorbed. It means that not all the wavelengths are still present in the light and only the remnant ones are radiated in a different direction. The color that is radiated back is the same color that was absorbed.

This absorption process is not random, it depends from the color wavelength: smaller is the wavelength more it gets absorbed. this means that blue tone gets more absorbed (thus more radiated back) than the red tone. This process is called Rayleigh scattering, named after Lord John Rayleigh, an English physicist, who first described it in the 1870's. He showed that the amount of light scattered is inversely proportional to the fourth power of wavelength for sufficiently small particles. That's why we see the sky blue.

This simple explanation about the blue sky gives a taste about the amount of informations on the particles in a atmosphere hidden inside the light scattering process. In order to be able to retrieve informations about the particles it is necessary to describe

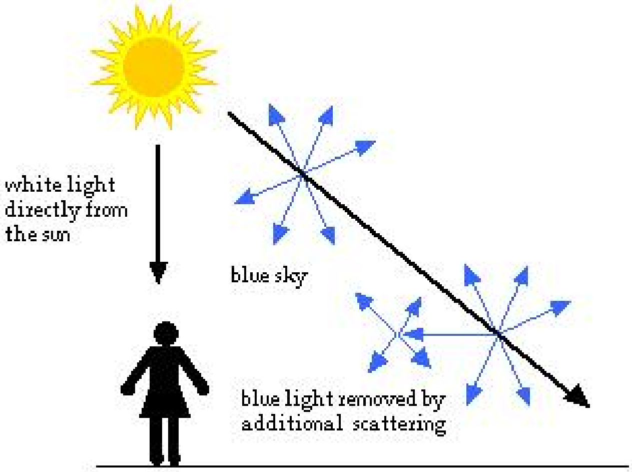

Figure 3.1: Scattering of blue light [1].

the relationship between the light radiation and the physical properties of the scattering particle from a more mathematical point of view.

3.2 Describing radiation and polarization

The observed quantities measured by a spectropolarimeter are the intensity, the degree of linear polarization and its direction, the degree of circular polarization. They are all measured as a function of wavelength, scattering geometry (the position of the source of light with respect to the observer - i.e. sun, instrument) and of course as a function of time and location on the planet. The introduction to this chapter has been adapted from Hansen and Travis [1974]

The **intensity** is the most common measured quantity. Its variation is an indication of the thickness of the atmosphere and can also reveal the presence of clouds. The low spectral resolution intensity is used to determine the composition of planetary surfaces and cloud layers, the high resolution instead can provide informations about the gaseous components of the atmosphere. Obviously it's always better to accompany the information gained with the intensity with information obtained through other means.

The **linear polarization** is less used than the intensity, probably because there is still some work to do in interpreting the polarization lines compared to the interpretation of intensity. On the other side it results more reliable and with higher accuracy with respect to intensity values. This is the reason why most of the atmospheric works are trying to study and apply this phenomena. The linear polarization is used in particular to determine the nature of clouds and aerosols particles. This is the quantity that will be modeled and analyzed in this work.

The **circular polarization** of reflected sunlight has been found to be very small, for this reason it has become an additional means for remote investigations. For SPEX we assume that the incoming light has no circular polarization.

3.2.1 Stokes vector

Before introducing the Stokes vector formalism, it is useful to clarify the terminology used for the observed quantities.

Unfortunately in literature an enormous variety of names is used to indicate the same quantity. In particular the radiance is also called intensity or, from an 'observer' point of view, (surface) brightness. The SI units for these quantities are $\mathrm{W}/\mu\mathrm{m}\,\mathrm{m}^2\,\mathrm{sr}$. The flux instead, which is the energy transmitted through an imagined surface, is called also irradiance or flux density and has SI units of $\mathrm{W}/\mu\mathrm{m}\,\mathrm{m}^2$. The difference between the two is that the flux integration extends over all the solid angles and I generally is a function of direction ('per solid angle'). Intensity is the most used quantity to describe the energy flow in a radiation field [Hovenier et al., 2004].

In 1864 J.C. Maxwell published his Electromagnetic theory in *"A dynamical theory of the electromagnetic field"* in which he proposed for the first time that light propagates in vacuum in form of electromagnetic waves. The electromagnetic wave equations are the solution of his (the so-called Maxwell's) differential equations. They represent the electric and magnetic plane waves that fluctuate perpendicularly to each other and perpendicularly to a common direction of propagation. Since we are dealing only with 'displacements' caused mainly by electric field variances, we can derive the sinusoidal plane wave solution [2] of the Maxwell's equations:

$$\mathbf{E}(\mathbf{r},t) = \mathrm{Re}\left\{\mathbf{E}(\mathbf{r})e^{j\omega t}\right\} \tag{3.1}$$

where $\omega = 2\pi f$ is the angular frequency, t represents the time, $\mathbf{r} = (x, y, z)$ is the position vector that varies with time. Graphically $\mathbf{E}(\mathbf{r})$ can be seen as a rotating vector with a phase φ that changes amplitude with time while moving along the direction of propagation z:

$$\mathbf{E}(\mathbf{r}) = E \cdot e^{j(\varphi - kz)}. \tag{3.2}$$

In 1852 G.G. Stokes described in one vector the time averages of the electric plane wave, this vector is called Stokes vector:

$$\begin{aligned}
I &= \left\langle E_{\parallel}^2 + E_{\perp}^2 \right\rangle \\
Q &= \left\langle E_{\parallel}^2 - E_{\perp}^2 \right\rangle \\
U &= 2\left\langle E_{\parallel}E_{\perp}\cos\delta \right\rangle \\
V &= 2\left\langle E_{\parallel}E_{\perp}\sin\delta \right\rangle
\end{aligned} \tag{3.3}$$

where $E_{\parallel}$ and $E_{\perp}$ are the components of the electric vector E , they represent the amplitudes of the electric wave; $\delta = \varphi_{\parallel} - \varphi_{\perp}$ is the difference in phase between the two components; I represents the total radiance of the scattered electric wave, Q, U and V have the same dimensions as I.

If we suppose that $I(\theta, \varphi)$ is the intensity due to vibrations of the light beam in the direction making an angle θ with the direction of propagation (orthogonal to the incident plane), and if we suppose also that $E_{\perp}$ has a phase delay φ with respect to $E_{\parallel}$, we can write:

---

[2] A plane wave is always fully polarized.

$$\begin{aligned} I &= I(0^\circ,0) + I(90^\circ,0) = I_\parallel + I\perp \\ Q &= I(0^\circ,0) - I(90^\circ,0) = I_\parallel - I\perp \\ U &= I(45^\circ,0) - I(135^\circ,0) \\ V &= I(45^\circ,\pi/2) - I(135^\circ,\pi/2). \end{aligned} \tag{3.4}$$

where I represents the total intensity of the EM wave; Q is the excess in intensity along the parallel direction ($y-$axis) with respect to the intensity along the perpendicular axis ($x-$axis), it represents the linear polarization; U is the same as Q only with a different angle. V is the only component that shows a phase delay, it represents the excess in intensity connected with circular polarization [Hansen and Travis, 1974]. Therefore the radiance (intensity) and the state of polarization of a beam of light can be fully described by a Stokes vector $\boldsymbol{I}$ [Chandrasekhar, 1950; Hovenier and Van der Mee, 1983]. All the Stokes parameters have the dimension of spectral radiance $\left[Watt/\mu m\, m^2\, sr\right]$ [3], are functions of the wavelength of the radiation, and are defined with respect to the scattering plane [Hansen and Travis, 1974; Stam et al., 2000].

The following should be valid for a Stokes vector:

$$\begin{aligned} &I(\lambda) > 0 \\ &I^2(\lambda) \geqslant Q^2(\lambda) + U^2(\lambda) + V^2(\lambda) \end{aligned} \tag{3.5}$$

The total intensity $\mathrm{I_{tot}}$ of the reflected sunlight can be considered as made up by two components, a polarized one and an unpolarized one:

$$I_{\text{tot}} = I_{\text{unpol}} + I_{\text{pol}} \tag{3.6}$$

where the intensity of the polarized light is:

$$I_{\text{pol}}(\lambda) = \left(Q(\lambda)^2 + U(\lambda)^2 + V(\lambda)^2\right) \tag{3.7}$$

and, assuming $V(\lambda) = 0$ due to its negligible value for planetary atmospheres, the degree of linear polarization is:

$$P = \frac{I_{\text{pol}}(\lambda)}{I(\lambda)} = \frac{\sqrt{Q^2(\lambda) + U^2(\lambda)}}{I(\lambda)}. \tag{3.8}$$

Moreover, if the incoming light is unpolarized ($I^0_{pol} = 0$), the light single-scattered by a sample of aerosols will have $U = 0$, and we will use the following definition of linear polarization:

$$P_s = -\frac{Q}{I} \tag{3.9}$$

Equation 3.9 contains information on the direction of polarization: if $P_s > 0$ then the polarization is perpendicular to the scattering plane, while if $P_s < 0$ it is parallel to the scattering plane [Stam, 2008].

---

[3] The spectral radiance is defined as the flux (power) emitted by a surface and received by an optical system from a certain specific direction. It is the power over a surface per unit solid angle per wavelength (or frequency). These dimensions are valid for a spectral radiance wavelength dependent, with the wavelength measured in μm. The radiance instead is the integration of the spectral radiance over all the directions.

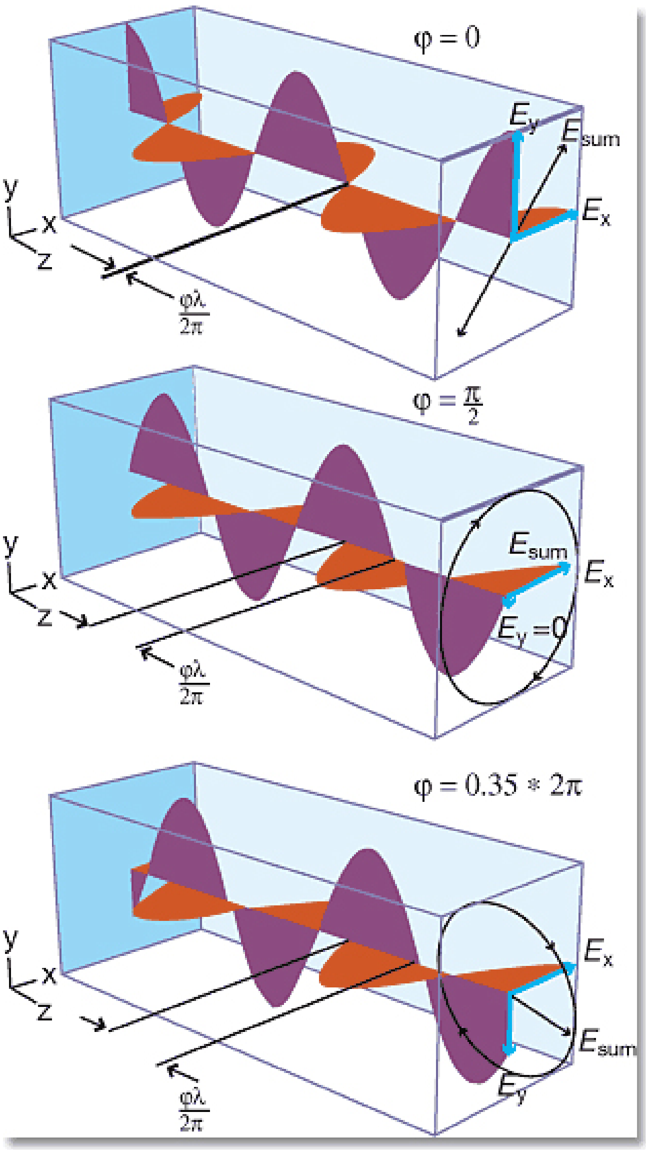

Figure 3.2: The vectors E_x and E_y represent the electric wave components on the scattering plane while the wave moves along the z direction. A difference in phase between the two components results in a different polarization status. See text for discussion [4].

In general we deal with electrical plane waves that are fully polarized by definition. This means that the resulting polarized light emission will be the vector sum of the two polarized components as shown in Fig.3.2. The two components of the electric field E_x and E_y, corresponding to $E_{\|}$ and $E_{\perp}$ in Equation 3.3, are moving along the $z-$axis. The sum vector of the electric components assumes different shapes in accordance to the difference in phase between the two components (see Eq. 3.3). In the top image of Fig.3.2 the components are in phase ($\varphi = 0$), the sum vector gives as result a linear polarized light. The following two images show a circular polarization for a difference in phase equal to $\varphi = \pi/2$, and an elliptical polarization for any other difference in phase $0 < \varphi < \pi/2$. To be more specific, the linear and circular polarization are two extreme cases of elliptical polarization [Hovenier et al., 2004].

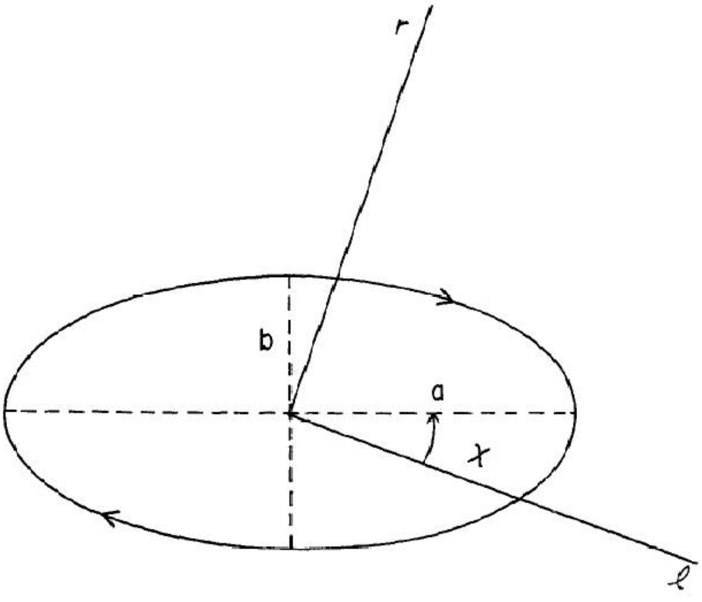

Figure 3.3: Illustration of the polarization ellipse. The direction of propagation z is into the page. l represents the parallel component of the electric wave while r represents the perpendicular one [Hansen and Travis, 1974].

Figure 3.3 shows the polarization ellipse, or, in other words, the 'track' left in time by the end point of the electric vector while it moves along the z direction. The direction of propagation z is into the page, l is the direction where $E_{\|}$ lies, r is the direction where the component $E_{\perp}$ lies. The ellipticity can be defined as $\tan\beta = \pm b/a$. For $\beta > 0$ we are dealing with a right-handed circular polarization, with $\beta < 0$ we are dealing with a left-handed circular polarization, with $\beta = 0$ we are dealing with linear polarization[5]. Therefore β defines the *shape* of the polarization ellipse.

The angle:

$$\chi = \frac{1}{2} \arctan \frac{U(\lambda)}{Q(\lambda)} \tag{3.10}$$

represents the orientation of the ellipse of polarization. It can also be seen as the amount of intensity in excess along the parallel or perpendicular direction with respect to the amount along the diagonal direction. Actually when $\chi = 90°$ ($\chi = 0°$), Q is negative (Q is positive), and the direction of polarization is perpendicular (parallel) to the scattering plane [Hansen and Travis, 1974].

---

[5] A right-handed polarization is when the observer (instrument), which is looking in the direction of propagation, sees the end of the electric vector moving in a clockwise sense [Hansen and Travis, 1974]

3.3 Mueller matrix and Poincaré sphere

A Mueller matrix is a matrix that describes the response of an instrument to the incident light when the latter is defined using the Stokes formalism. In a more mathematical way, the Mueller matrix is a matrix that allows the transformation from the incident Stokes vector to the measured Stokes vector:

$$\begin{pmatrix} I' \\ Q' \\ U' \\ V' \end{pmatrix} = \begin{pmatrix} M_{00} & M_{01} & M_{02} & M_{03} \\ M_{10} & M_{11} & M_{12} & M_{13} \\ M_{20} & M_{21} & M_{22} & M_{23} \\ M_{30} & M_{31} & M_{32} & M_{33} \end{pmatrix} \cdot \begin{pmatrix} I \\ Q \\ U \\ V \end{pmatrix} \tag{3.11}$$

From now on the wavelength dependency of the Stokes vector will be omitted just for a practical graphical representation.

Since for Stokes vector we have to met the requirements shown in Equation 3.5, it is a logic consequence that for the Mueller matrix we have to meet the same requirements:

$$\begin{aligned} &M_{00} > 0 \\ &M_{00}^2 \geqslant M_{01}^2 + M_{02}^2 + M_{03}^2 \end{aligned} \tag{3.12}$$

In this way the physical meaning of the Stokes vector has been preserved. Each optical device inside an instrument can be described by an unique Mueller matrix. If we have to describe the response of of a complex instrument, we must take into account the Mueller matrix of each component of the instrument. In Chapter 7 we will provide more details exploiting the Mueller matrices for the SPEX pre-optics components.

Another conversion that has to be modeled concerns the reference plane. The Stokes vector of the incoming light are referred to the scattering plane, but the reference plane of e.g. an instrument (observer) has a different orientation. In order to relate the two planes, a rotation matrix $\mathbf{M}_{\mathrm{rot}}$ has been defined[6]:

$$\mathbf{M}_{\mathrm{rot}}(\beta) = \begin{pmatrix} 1 & 0 & 0 & 0 \\ 0 & \cos 2\beta & \sin 2\beta & 0 \\ 0 & -\sin 2\beta & \cos 2\beta & 0 \\ 0 & 0 & 0 & 1 \end{pmatrix} \tag{3.13}$$

where the angle β is the angle between the two reference planes measured counter-clockwise from the old to the new plane looking in the direction of propagation of light ($\beta \geqslant 0$) [Stam, 2008].

Another way to describe the polarization status of the light is by using the Poincaré sphere. Each point on the surface and/or inside the sphere represents an unique status of polarization.

In order to prove the validity of this representation we have to take into account the equality for fully polarized waves in Eq.3.5. Dividing it by I^2 we get:

$$\begin{gathered} I^2 = Q^2 + U^2 + V^2 \\ 1 - \frac{Q^2}{I^2} - \frac{U^2}{I^2} - \frac{V^2}{I^2} = 0 \quad \Leftrightarrow \quad \frac{Q^2}{I^2} + \frac{U^2}{I^2} + \frac{V^2}{I^2} = 1 \end{gathered} \tag{3.14}$$

---

[6] For further details see Hovenier et al. [2004]

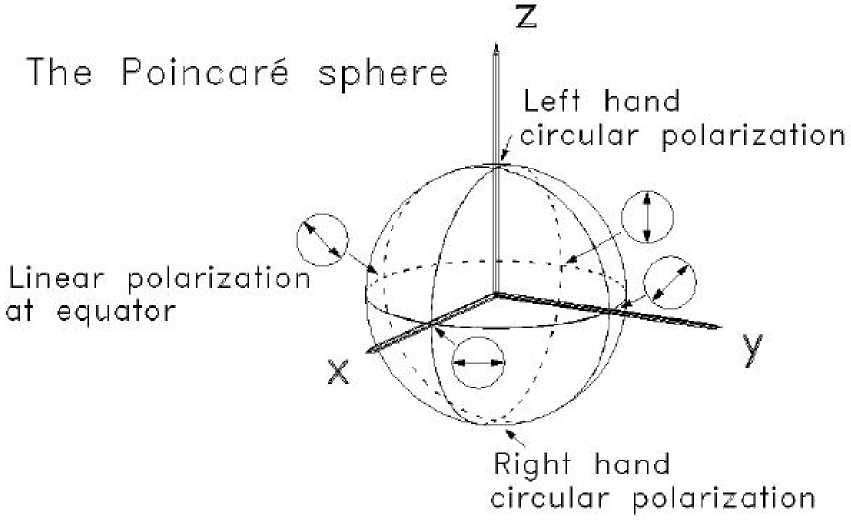

Figure 3.4: The Poincaré sphere. Each point on the surface represents one polarization status. At the equator we have linear polarization, at the poles we have circular polarization. All the other points are for elliptical polarization [Dahl, 2001].

which is the equation of a sphere with radius $r = 1$ and axes $x \equiv \frac{Q}{I}$, $y \equiv \frac{U}{I}$ and $z \equiv \frac{V}{I}$. In this way it is possible to have an immediate sense of the action of the different polarization components identifying the Stokes parameters with the Poincaré sphere coordinates [Dahl, 2001]. In particular, the center of the sphere represents the natural unpolarized light ($Q = U = V = 0 \leftrightarrow x = y = z = 0$), the points within the sphere represent the partially polarized light and the points on the surface of the sphere represent the fully polarized light.

4 Single scattering

The theoretical modeling of light scattering in planetary atmospheres requires two steps: the single scattering and the multiple scattering. The division between single and multiple scattering can take place only under the assumption that the particles are sufficiently separated (i.e. by a few times their radius [Van de Hulst, 1957]) that they may be treated as independent scatterers; this condition is met in planetary atmospheres [Hansen and Travis, 1974].

In this section single scattering is treated.

4.1 Analytic representation

We describe the radiance and state of polarization of a beam of radiation by a Stokes vector **I**, as follows [Chandrasekhar, 1950; Hovenier and Van der Mee, 1983]:

$$\mathbf{I_0} = \begin{bmatrix} I_0 \\ Q_0 \\ U_0 \\ V_0 \end{bmatrix} \tag{4.1}$$

where the pedix 0 refers to an incident beam of radiation. If the source of light is in the far-field and if this distance is several times bigger than the wavelength ($R \gg \lambda$), the scattered radiance is equal to:

$$\mathbf{I}_{sca} = k_{sca}\,\mathbf{P}(\alpha)\,\mathbf{I_0}\,\frac{dv}{4\pi R^2} \tag{4.2}$$

where dv is a small volume that contains small monomers. The quantities that influence the scattering properties of dv, which is characterized by no specific shape or orientation, are the scattering coefficient k_{sca} and the phase matrix $P(\alpha)$. The scattering coefficient is often referred as scattering cross-section but actually it holds that:

$$k_{\text{sca}} = \sigma_{\text{sca}}\,\rho \tag{4.3}$$

where σ_{sca} is the effective scattering cross section (dimension of an area) and ρ represents the volume density. Furthermore, k_{sca} (dimension length^{-1}) represents the sum of the cross sections of all the particles in the volume. Since in the atmosphere there is not only scattering but also absorption, k_{abs} represents the absorption coefficient and it holds that $k_{\text{ext}} = k_{\text{abs}} + k_{\text{sca}}$, where *ext* stands for extinction (of the energy of the incoming beam due to these phenomena). In terms of these quantities it is possible to define the single scattering albedo as:

$$\tilde{\omega} = \frac{k_{\text{sca}}}{k_{\text{ext}}} = \frac{\sigma_{\text{sca}}}{\sigma_{\text{ext}}} \tag{4.4}$$

where σ_{ext} is the extinction cross section. The dimensionless $\tilde{\omega}$ indicates the fraction scattered of the total energy removed from the incident beam, if $\tilde{\omega} = 0$ the extinction is due to complete absorption, if $\tilde{\omega} = 1$ there is no absorption but pure scattering[1].

The $\mathbf{P}(\alpha)$ matrix is a 4×4 matrix of dimensionless coefficients, it's called phase matrix. Its elements represent the radiance and the polarization variations with respect to the scattering angle α [Hansen and Travis, 1974]:

$$\mathbf{P}(\alpha) = \begin{pmatrix} P^{11} & P^{21} & 0 & 0 \\ P^{21} & P^{22} & 0 & 0 \\ 0 & 0 & P^{33} & P^{34} \\ 0 & 0 & -P^{34} & P^{44} \end{pmatrix} \tag{4.5}$$

This formulation for the phase matrix is valid only for:

1. randomly oriented particles, each of which has a plane of symmetry (microscopically symmetric level)
2. randomly oriented asymmetric particles, if half of the particles are mirror images of the others (macroscopically symmetric level)
3. more artificial cases are indicated in Van de Hulst [1957].

In case one of the conditions listed above is valid , it also holds that [De Rooij and Van der Stap, 1984]:

$$\text{if } \alpha = 0 \ \mapsto \begin{cases} P^{22} = P^{33} \\ P^{21} = P^{34} = 0 \end{cases} \tag{4.6}$$

$$\text{if } \alpha = \pi \ \mapsto \begin{cases} P^{22} = -P^{33} \\ P^{21} = P^{34} = 0 \end{cases} \tag{4.7}$$

Since we assume a macroscopic symmetrical atmosphere, the scattering matrix does not depend on the choice of the scattering plane but only on the scattering angle. For this reason we will refer to the phase matrix also as scattering matrix (they they are directly proportional to each other). The first element of the matrix in Eq.4.5 is called phase function and is normalized in such a way that:

$$\int_{4\pi} P^{11} \frac{d\Omega}{4\pi} = 1 \tag{4.8}$$

where $d\Omega$ is the solid angle and P^{11} is the first element of the phase matrix which describes the angular distribution of light reflected from a volume when illuminated from a specific direction (i.e. from the solid angle in figure 4.1) [Hansen and Travis, 1974].

To measure the symmetry of the phase function we use the anisotropy parameter:

---

[1] If the volume dv would be characterized by a certain shape, k_{sca} and $\tilde{\omega}$ would depend also on the orientation of the small volume dv to the direction of incidence (solid angle, see Figure 4.1).

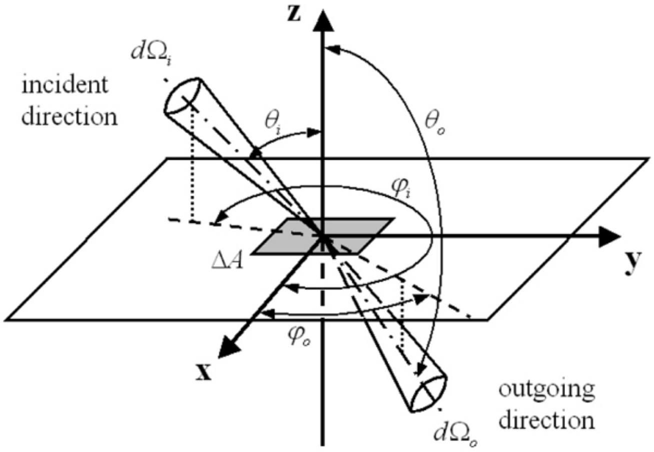

Figure 4.1: Geometry for scattered light. The angle θ represents the angle of the incoming and outgoing light. It is shown here the solid angle which represents the opening angle of the incident beam $d\Omega_i$, and of the transmitted (outgoing) beam $d\Omega_o$. *Image source*: `http://www.jvrb.org/5.2008/1498/figure01.jpg`.

$$\langle \cos\alpha \rangle = \int_{4\pi} \cos\alpha \, P^{11} \frac{d\Omega}{4\pi} \tag{4.9}$$

where α is the scattering angle. The anisotropy parameter varies from -1 (i.e. all radiation is backward scattered like a "mirror", $\alpha = 180°$) to 1 (for pure forward scattering, $\alpha = 0°$). In particular if a particle scatters more light toward the forward direction, $\langle \cos\alpha \rangle > 0$; $\langle \cos\alpha \rangle < 0$ if the scattering is directed more toward the back direction; $\langle \cos\alpha \rangle = 0$ if it scatters light isotropically (e.g. small grains in the Rayleigh regime - particle size smaller than the wavelength) or if the scattering is symmetric with respect to $\alpha = 90°$ (i.e. the scattered radiation is azimuthal independent and symmetric with respect to the plane perpendicular to the incident radiation) [2].

With single scattering calculations, we can obtain k_{sca}, $\tilde{\omega}$, and $\mathbf{P}$ for different types of particles. The ultimate goal is to understand how scattered radiation depends on the nature of the particle, i.e. shape, size distribution and optical properties [Hansen and Travis, 1974].

4.2 Mie theory

Geometric optics, Rayleigh scattering and Mie theory are the most common theoretical computations for single scattering of particles. Rayleigh scattering deals with particles having dimensions $x \ll \lambda$, where $x = \frac{2\pi r}{\lambda}$ with r the radius of the particle and λ the wavelength. In our model atmosphere, for example, the light scattering by the gas molecules is described by Rayleigh scattering. Geometric optics deals with particles having a size $x \gg \lambda$, but does not adequately describe the interactions of particles with light when the particle size is comparable to the wavelength of the light. Mie theory instead addresses the full range of complex interaction between electromagnetic

---

[2] *http://nedwww.ipac.caltech.edu/level5/Sept07/Li1/Li3.html*

quantities and the particle. In our model atmosphere in fact, the light scattering by the monomers is described by using Mie theory. In this chapter only Mie theory will be treated, for further reading about geometric optics and Rayleigh scattering please consult Hansen and Travis [1974].

Mie theory (also Lorentz-Mie theory) is a complete analytical solution of Maxwell's equations for the scattering of electromagnetic radiation by spherical particles. Often people also refer to it as Mie scattering. The following description of the Mie theory is following Van de Hulst [1957] and is described by De Rooij and Van der Stap [1984] and Hansen and Travis [1974].

Let's suppose that a spherical particle is illuminated by a plane wave[3] traveling in the z direction. The electric field components of the outgoing beam in the far field ($R \gg \lambda$) in the direction perpendicular and parallel to the scattering plane are:

$$\begin{pmatrix} E'_\perp \\ E'_\parallel \end{pmatrix} = \begin{pmatrix} S_1(\alpha) & 0 \\ 0 & S_2(\alpha) \end{pmatrix} \cdot \frac{e^{-ikR+ikz}}{ikR} \begin{pmatrix} E_\perp \\ E_\parallel \end{pmatrix} \tag{4.10}$$

where R is the distance to the particle, α is the scattering angle and $S(\alpha)$ are the amplitude functions described as:

$$\begin{aligned} S_1(\alpha) &= \sum_{n=1}^{\infty} \frac{2n+1}{n(n+1)} \left[a_n\, \pi_n(\cos\alpha) + b_n\, \tau_n(\cos\alpha)\right] \\ S_2(\alpha) &= \sum_{n=1}^{\infty} \frac{2n+1}{n(n+1)} \left[b_n\, \pi_n(\cos\alpha) + a_n\, \tau_n(\cos\alpha)\right] \end{aligned} \tag{4.11}$$

The computation of the scattering matrix $\mathbf{S}$ is the primary goal of the single scattering since from this matrix it is possible to obtain k_{sca}, $\tilde{\omega}$ and $\mathbf{P}$. The matrix is diagonal because we are considering isotropic homogeneous spheres [Hansen and Travis, 1974].

The angular functions are expressed in terms of associated Legendre functions and depend only on the scattering angle:

$$\begin{aligned} \pi_n(\cos\alpha) &= \frac{1}{\cos\alpha} P_n^1(\cos\alpha) \\ \tau_n(\cos\alpha) &= \frac{d}{d\alpha} P_n^1(\cos\alpha). \end{aligned} \tag{4.12}$$

The Mie coefficients a_n and b_n are the most important parameters in the Mie scattering problem:

$$\begin{aligned} a_n &= \frac{\left[\frac{D_n(z)}{m} + \frac{n}{x}\right] \psi_n(x) - \psi_{n-1}(x)}{\left[\frac{D_n(z)}{m} + \frac{n}{x}\right] \zeta_n(x) - \zeta_{n-1}(x)} \\ b_n &= \frac{\left[m\, D_n(z) + \frac{n}{x}\right] \psi_n(x) - \psi_{n-1}(x)}{\left[m\, D_n(z) + \frac{n}{x}\right] \zeta_n(x) - \zeta_{n-1}(x)} \end{aligned} \tag{4.13}$$

---

[3] A plane wave is a constant-frequency wave whose wavefronts (surfaces of constant phase) are infinite parallel planes of constant amplitude normal to the phase velocity vector (J. D. Jackson, Classical Electrodynamics, 1998)

where $m = n_r + in_i$ is the complex refractive index of the particle, $x = kr = 2\pi r/\lambda$ is the particle size parameter and r is its radius, k is the wavenumber. The Mie coefficients are function of the spherical Bessel functions of the first and second kind, $j_n(x)$ and $y_n(x)$ respectively:

$$\begin{aligned} \psi_n(x) &= x\, j_n(x) \\ \zeta_n(x) &= \psi_n(x) + i\,\chi_n(x) \end{aligned} \tag{4.14}$$

with $\chi_n(x) = -x\, y_n(x)$.

In order to be able to use the Stokes vector for the incident and scattering beam we need a transformation matrix $\mathbf{T}(\alpha)$:

$$\mathbf{I}' = \frac{1}{k^2\, R^2}\mathbf{T}(\alpha)\mathbf{I}. \tag{4.15}$$

In case of Mie scattering in addition to equation 4.6, another identity is valid:

$$\begin{aligned} P^{11}(\alpha) &= P^{22}(\alpha) \\ P^{33}(\alpha) &= P^{44}(\alpha) \end{aligned} \tag{4.16}$$

The normalized scattering matrix $\mathbf{P}(\alpha)$ is also proportional to the transformation matrix:

$$P^{ij}(\alpha) = \frac{4\pi}{k^2\, k_{\text{sca}}} T^{ij}(\alpha). \tag{4.17}$$

For the single scattering a small volume dv is considered containing N independently scattering particles. Eq.4.15 should then be replaced by:

$$\mathbf{I}' = \frac{1}{k^2\, R^2}\sum_{i=1}^{N}\mathbf{T}_i(\alpha)\mathbf{I} \tag{4.18}$$

where i in this case indicates the various particles. The transformation matrix per unit volume is given by:

$$T^{ij}(\alpha) = \int_{r_1}^{r_2} T^{ij}(\alpha, r) n(r) dr \tag{4.19}$$

where r_1 and r_2 are the smallest and the largest particles in the size distribution, $n(r)dr$ is the number pf particles per unit volume with radius between r and $r + dr$.

The size distribution of the particles in the volume plays an important role. Since we need to get properties of the scattering particle from measurements, it is handy to describe the size distribution with the minimum number of parameters. For this purpose we define an effective radius r_{eff} and an effective variance v_{eff}:

$$r_{\text{eff}} = \frac{1}{G}\int_{r_1}^{r_2} r\pi r^2 n(r) dr \tag{4.20}$$

$$v_{\text{eff}} = \frac{1}{G\, r_{\text{eff}}^2}\int_{r_1}^{r_2} (r - r_{\text{eff}})^2\, \pi r^2 n(r) dr \tag{4.21}$$

where $G = \int_{r_1}^{r_2} \pi r^2 n(r) dr$ is the geometric cross section area of particles per unit volume, the effective variance v_{eff} is a measure of the width of the distribution and is dimensionless. The particle effective size can be expressed as $x_{\text{m}} = 2\pi r_{\text{eff}}/\lambda$.

A useful standard analytic size distribution is:

$$n(r) = \text{constant}\, r^{\frac{(1-3b)}{b}}\, e^{\frac{-r}{ab}} \tag{4.22}$$

where the constant = 1 if the scattering matrix is normalized and:

$$\begin{aligned} a &= r_{\text{eff}} \\ b &= v_{\text{eff}}. \end{aligned} \tag{4.23}$$

The most common size distributions are the standard gamma distribution, the bimodal gamma distribution, the log-normal distribution and the power law distribution.

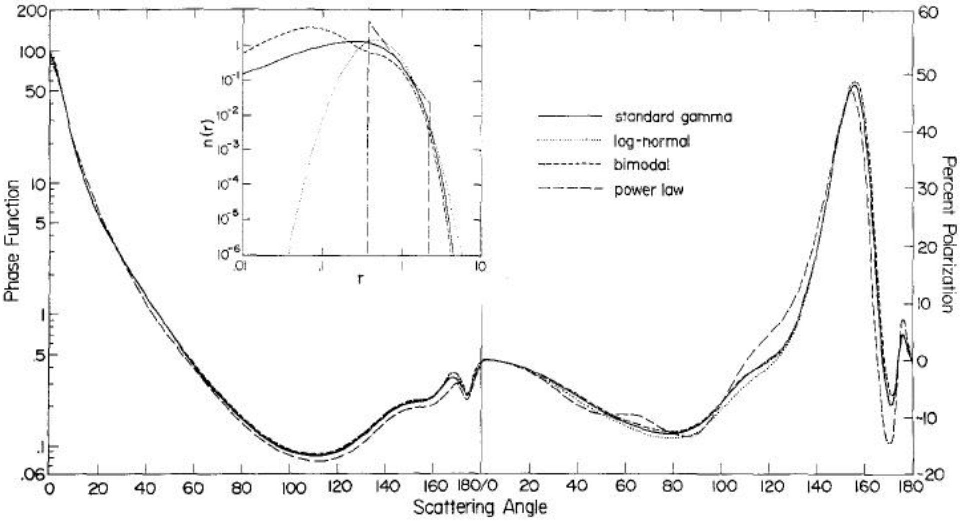

Figure 4.2: Phase function P^{11} and percent polarization,$-100\frac{P^{21}}{P^{11}}$, for single scattering of unpolarized light. Results are shown for the four size distributions shown in the inset [Hansen and Travis, 1974]. See text for discussion.

Detailed description of the parametrization of the size distribution functions can be found in Hansen and Travis [1974]. Here only a generic comparison among the four is done. In Figure 4.2 both the phase function and the percent polarization of the four different distribution is shown. All of them have the same value for $r_{\text{eff}} = 1\mu m$ and $v_{\text{eff}} = 0.25$, while $\lambda = 0.55\mu m$ and $n_r = 1.33$ (water). The behavior of the different distributions are almost equivalent except for the power law that show some differences for the polarization.

In our model we did not use a size distribution for our monomers. They are spehrical and all have the same radius equal to $r_{\text{eff}} = 0.04\mu$m or 0.05μm.

In case of scattering within a macroscopically symmetric medium it is possible to expand the elements of the scattering matrix [De Haan et al., 1987]:

$$
\begin{aligned}
a_1(\alpha) &= \sum_{s=0}^{s_{\max}} \alpha_1^s P_{00}^s(\cos\alpha) \\
a_2(\alpha) + a_3(\alpha) &= \sum_{s=0}^{s_{\max}} (\alpha_1^s + \alpha_3^s) P_{22}^s(\cos\alpha) \\
a_2(\alpha) - a_3(\alpha) &= \sum_{s=0}^{s_{\max}} (\alpha_1^s - \alpha_3^s) P_{22}^s(\cos\alpha) \\
a_4(\alpha) &= \sum_{s=0}^{s_{\max}} \alpha_4^s P_{00}^s(\cos\alpha) \\
b_1(\alpha) &= \sum_{s=2}^{s_{\max}} \beta_1^s P_{02}^s(\cos\alpha) \\
b_2(\alpha) &= \sum_{s=2}^{s_{\max}} \beta_2^s P_{02}^s(\cos\alpha)
\end{aligned}
\tag{4.24}
$$

where the $P_{nm}^s(\cos\alpha)$ are generalized spherical functions and $s_{\max}$ depends of the desired numerical accuracy. If the expansion coefficients are known, the elements of the scattering matrix can be calculated for any number of scattering angles [Mishchenko et al., 2000].

4.3 T-matrix

In Titan atmosphere the representation of an atmosphere by only spherical particles is not realistic: it is known that in nature there are more possibilities to have random shapes than all identical ones. Therefore non spherical particles have to be taken into account. Since the scattering properties between non spherical particles and their spherical-shaped equivalents differ a lot, an alternative to Mie theory has to be used to understand the effects of particle non sphericity on scattering patterns.

The choice went to the T-matrix method (TMM) that is one of the several equivalent methods of the Mie theory. The method was first introduced by Waterman in 1971 for single homogeneous scatterers and was then generalized to multi layered scatterers and arbitrary clusters of non spherical particles by Peterson and Strom in 1973 and 1974. Thanks to the updates by Mishchenko and Mackowski in 1991 and 1996 the T-matrix method is an analytical orientation-averaging procedure for arbitrary clusters of spheres randomly oriented, leaving thus complete freedom to the choice of shape (i.e. spheroids, cylinders) and orientation of the particle or cluster of these types of particles.

The main and only difference with the Mie theory is that, inside the scattering matrix, the identities showed in Eq.4.16 are not valid for non-spherical particles.

The code first calculates the cluster T-matrix through an iterative process described in the article by Mackowski and Mishchenko [1996], then it calculates the orientation averaged matrix elements for the cluster using a generalized spherical function formulation. In the T-matrix code we used, the only analytical part is the averaging over the orientations, the rest of the code is numerical.

The T-matrix code used for this work is the "*Double precision superposition codes for multi-sphere clusters in fixed and random orientation*" and can be downloaded at: `http://www.giss.nasa.gov/staff/mmishchenko/t_matrix.html`. For more details about the development and the structure of the T-matrix method, please consult Mackowski and Mishchenko [1996]; Mishchenko et al. [2000] and the references therein.

4.4 Single scattering properties of Titan aerosols

The polarization of the scattered light depends on the properties of the particles in Titan's atmosphere. In this section, we present and discuss the single scattering properties of the aggregate particles that we use in our model atmospheres. Our aggregate particles consist of clusters of monomers.

4.4.1 Complex refractive index

The choice of the complex refractive index depends on the wavelength range that is going to be observed. Since we have the intention to adapt the SPEX instrument to be able to perform within Titan's environment, it is reasonable to choose the visible range (VIS range) of wavelengths which is what the current design of SPEX is now tuned for. The shortest wavelength we use is at $0.400\mu m$ (blue) while the longest one is at $0.830\mu m$ (red). Based on this choice, the most recent refractive index for the VIS range is the one computed by Ramirez et al. [2002]. They presented a set of values for refractive index n_r and extinction coefficient n_i [4] calculated using laboratory measurements of tholins. Tholins are artificial analogues of Titan's aerosols reproduced in several laboratories around the world using different techniques and theories. Ramirez et al. [2002] made use of the values of transmittance and absorbance[5] in the $200 - 900\,nm$ range for a starting mixing ratio of N_2:CH_4 (98:2) for their tholins. Their resulting values are shown in Fig.4.3, on the left side we have the real part of the refractive index n_r, while the imaginary part n_i is shown on the right side.

4.4.2 Influence of monomer size

In this section we calculate the single scattering properties of monomers with a radius of $0.04 \pm 0.01\mu m$ in accordance to the results recently presented by Tomasko et al. [2009] and Lavvas et al. [2009]. The choice of the monomer radius depends from the temperature and pressure profile and from the chosen mass production rate. The monomer radius they believe to be representative of monomers in the atmosphere of Titan, is obtained for a production rate of 2.7-4.6 x $10^{-13}\,kg\,m^{-2}sec^{-1}$ and for a production altitude around 500 km (see Section 2.2.2 for further explanations).

Here, we show the changes in phase function and degree of polarization for a change in monomer radius equal to ±0.01 using Mie-calculations.

Figure 4.4 and 4.5 show the single scattering radiance and degree of polarization for a monomer effective radius of $r_{\text{eff}} = 0.05\mu m$ as function of the scattering angle, and for three different wavelengths. The size distribution for the monomers is the two

---

[4] The refractive index is a complex parameter represented by a real part and an imaginary part: $m = n_r + in_i$

[5] Fraction of light transmitted or absorbed by a sample of tholins at a specified wavelength.

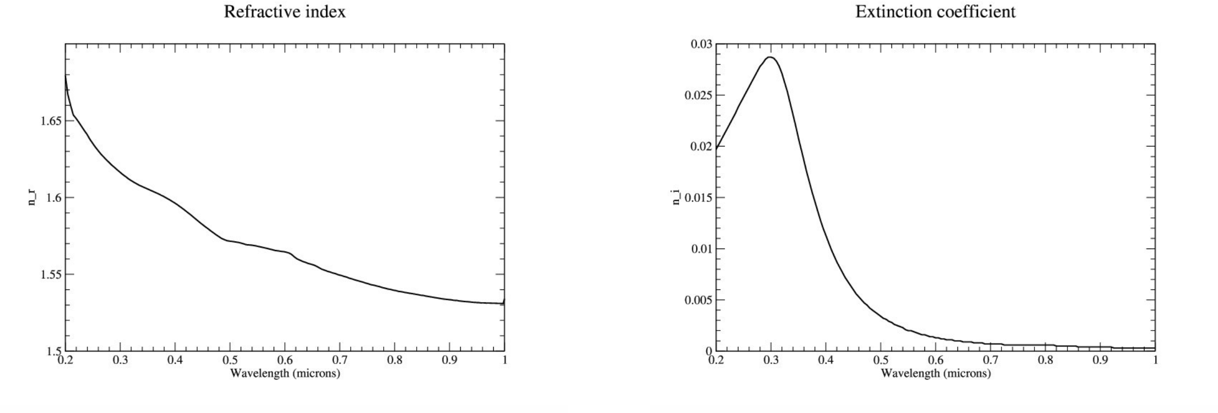

Figure 4.3: Dependency of complex refractive index on the wavelength: on the left we have the real part of the refractive index, while on the right side there is the imaginary part.

parameter gamma with $v_{\text{eff}} = 0.07$. A larger value of v_{eff} would give a higher peak in the degree of polarization, but would also increase the size-distribution width which is not recommendable. Therefore, we choose a small value for the effective variance in order to keep the size-distribution concentrated around its mean value.

In Fig. 4.4 it is possible to see that the peak of the degree of polarization moves towards smaller scattering angles as soon as the wavelength increases. This is due to the passage from a Mie regime ($x_{\text{m}} \simeq \lambda$) to a Rayleigh regime ($x_{\text{m}} \ll \lambda$), or in other words, to the fact that the particle will 'look' smaller for a longer wavelength. In Rayleigh regime the particles reach 100% polarization at $\alpha = 90°$ as shown in the plot.

In Fig.4.5 is shown the variation of radiance as function of the scattering angle for three different wavelengths. The radiance phase function shows a strong peak in the forward direction ($\alpha = 0°$) and a smaller one in the backscattering direction ($\alpha = 180°$). Increasing the wavelength, the forward peak diminishes because the particles 'look' smaller with respect to the wavelength, while the backscattering increases. The radiance value in forward scattering is usually used to determine the size of the particle: the smaller the particle with respect to the wavelength, the smaller the forward scattering peak. This is confirmed also in Fig. 4.6 where the phase function is plotted for $r_{\text{eff}} = 0.04\,\mu m$ and $r_{\text{eff}} = 0.05\,\mu m$ for $\lambda = 0.6\,\mu m$. Figure 4.7 shows the difference between the degree of polarization for the same particles. The difference between the degree of polarization curves of the two particles is $\sim 10\%$.

4.4.3 Influence of aerosol size

Observations of Titan indicate that the haze aerosols should consist of fractal-shaped, aggregates of small individual particles. The general process about aerosols growth has been already explained in Section 2.2.2. Just as a reminder, the aggregation processes follow ballistic or diffusive mechanisms and can involve a particle-cluster aggregation or a cluster-cluster aggregation. Thus we can have BPCA (ballistic particle-cluster aggregation) BCCA (ballistic cluster-cluster aggregation) and the

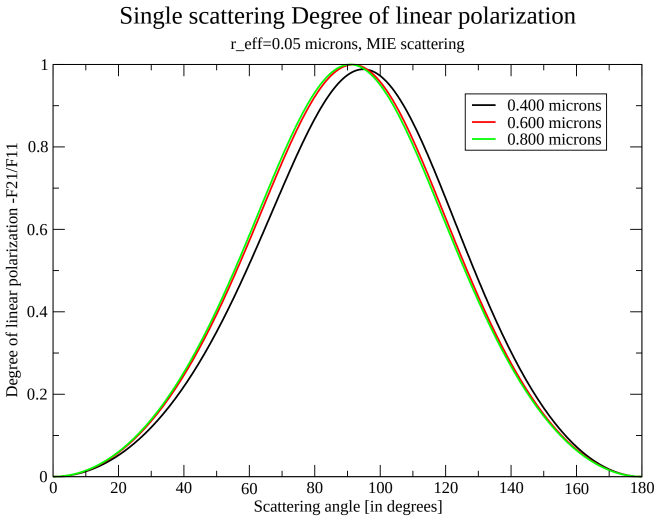

Figure 4.4: Single scattering degree of polarization P_S for spherical particle with $r_{\text{eff}} = 0.05\,\mu m,\ \ v_{\text{eff}} = 0.07$ as function of scattering angle, and for three different wavelengths.

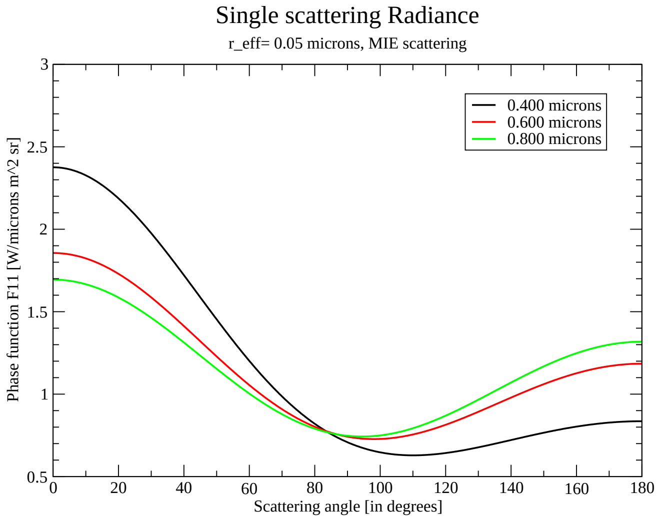

Figure 4.5: Phase function P^{11} for spherical particle with $r_{\text{eff}} = 0.05\,\mu m,\ \ v_{\text{eff}} = 0.07$ as function of the scattering angle, and for three different wavelengths.

same for DLA-PC and DLA-CC (diffusion-limited aggregation). Here we are going to explain how to model such aggregates.

The monomer size parameter is equal to: $x_{\text{m}} = 2\pi a/\lambda$ where $a \equiv r_{\text{eff}}$. The size parameter of the aggregate is equivalently calculated as:

$$X_v = 2\pi A_v/\lambda \qquad A_v = N^{1/3}a \tag{4.25}$$

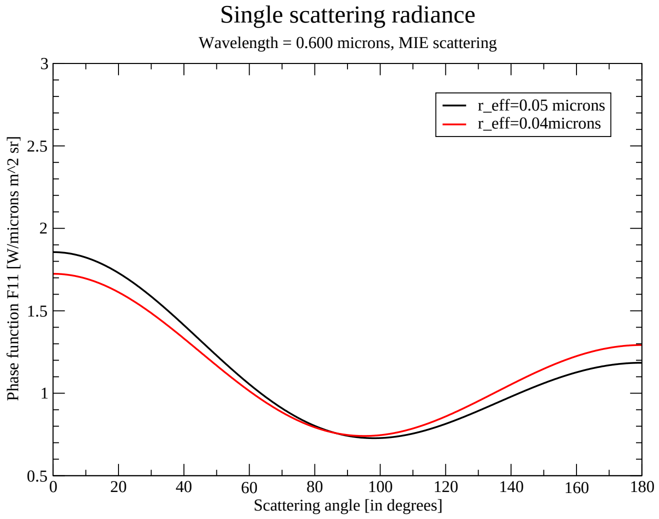

Figure 4.6: Phase function for spherical particles with $r_{\text{eff}} = 0.05\,\mu m$ and $r_{\text{eff}} = 0.04\,\mu m$ at a wavelength of $\lambda = 0.6\,\mu m$.

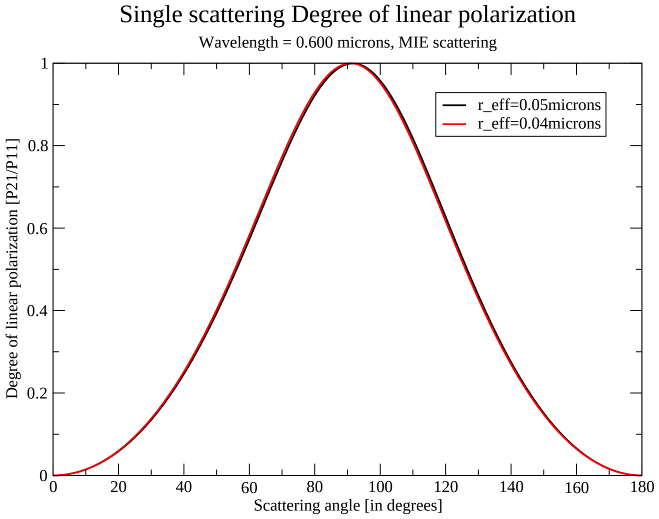

Figure 4.7: Degree of polarization for spherical particles with $r_{\text{eff}} = 0.05\,\mu m$ and $r_{\text{eff}} = 0.04\,\mu m$ at a wavelength of $\lambda = 0.6\,\mu m$.

where N is the monomer number, and A_v is the radius of a sphere of equal volume which contains monomers packed together. DLA-particles can be described by their fractal dimension D:

$$N = p \cdot \left(\frac{R}{2a}\right)^D \tag{4.26}$$

where a is the monomer effective radius, p is a constant pre-factor and R is the radius of gyration [6] of the cluster. To have compact structures it is assumed to have $D = 3$ and p from 7 to 9, for more fluffy clusters instead $D \simeq 2$ and p from 5 to 7. In case of diffusive behavior the fractal dimension is smaller than for the ballistic case [Skorov et al., 2008].

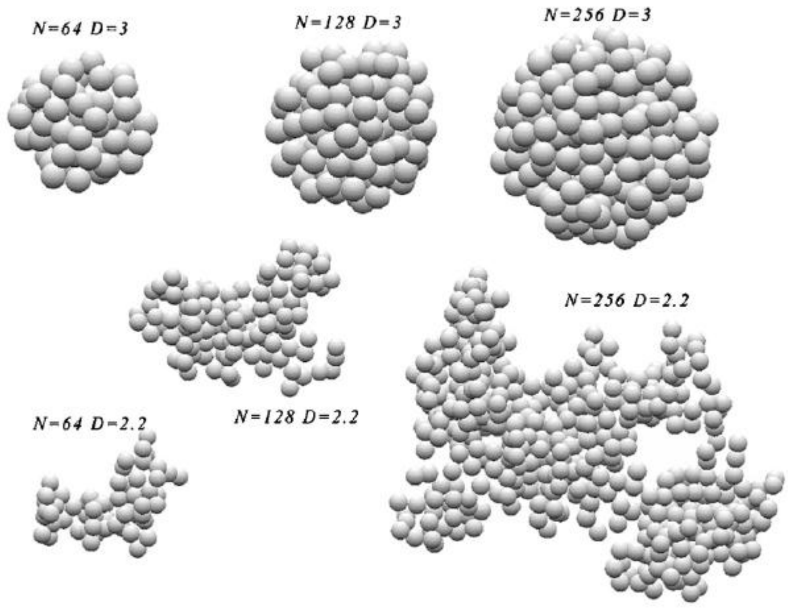

Figure 4.8: Samples of compact and fluffy spherical aggregates used by Skorov et al. [2008] during their simulations.

The aggregates considered in this report undergo the diffusion-limited aggregation (DLA) process or ballistic particle-cluster aggregation (BPCA). These aggregates are composed by 128 or 256 monomers and are monodisperse, e.g. they consist of monomers with one size. The monomer radius is equal to $r_{\text{eff}} = 0.05\,\mu m$. The files with the geometric position in space of the monomers forming these aggregates have been kindly provided by dr. Yu.V. Skorov from the *Max-Planck Institute for Solar System Research* in Lindau, Germany.

When particles form in Titan's atmosphere, we expect symmetric conditions, thus for every fractal shaped aggregate particle, there will be a mirror particle. We calculated the geometrical position in space of the monomers of the mirror particle simply inverting the geometric position of the monomers of the corresponding 'twin' particle. Since the aggregation process is supposed to be random, it is reasonable to consider the possibility to have two identical particles but with opposite geometrical disposition in space of their monomers. Under this assumption the phase matrix (or scattering matrix) is represented as in Eq. 4.5.

To show the general scattering characteristics of fractal aggregates, the compact DLA-particles with $N = 256$, $D = 2.2$ and $p = 8$ have been used as reference. Figure 4.9 shows the scattered radiance of these particles as function of the scattering angle for three different wavelengths in the VIS range.

---

[6] It is calculated as the root mean square distance of the objects' parts from either its center of gravity or an axis, or in other words as the square root of the moment of inertia of the cluster divided

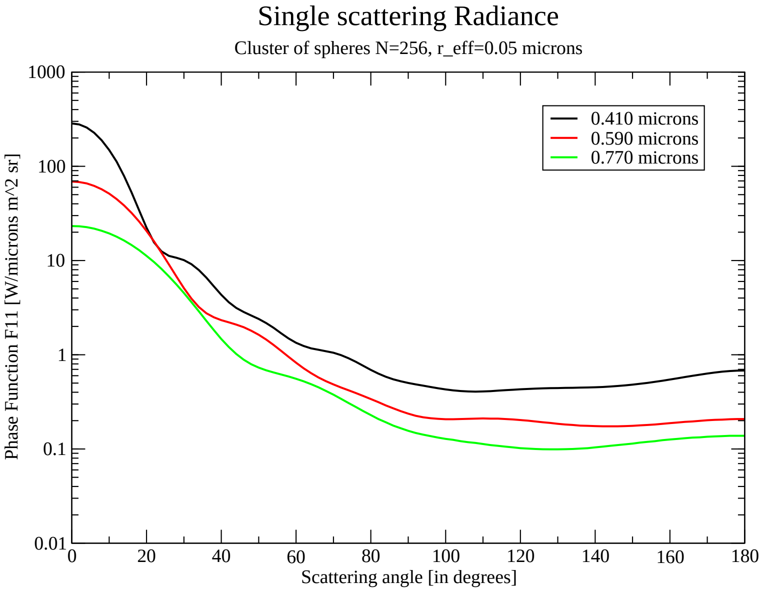

Figure 4.9: Radiance for $N = 256$ and $r_{\text{eff}} = 0.05\,\mu m$ as function of scattering angle. It has been plotted for several wavelengths in the VIS range. See text for discussion

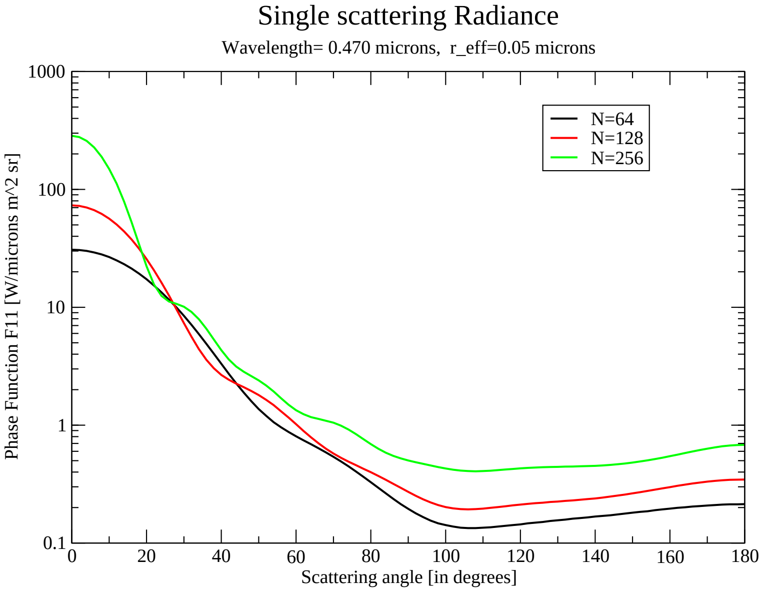

Figure 4.10: Radiance for $N = 64, 128, 256$ as function of scattering angle. The wavelength of reference is $\lambda = 0.470\,\mu m$.

In Fig. 4.9 we can notice that an increase in wavelength is comparable to having

---

by its mass.

a smaller aggregate size with a smaller forward scattering (at $\alpha = 0°$). The longer the wavelength the smaller the backscattering peak, as we can notice comparing the curve for $\lambda = 0.770\,\mu m$ to the curve for $\lambda = 0.410\,\mu m$. Apparently, in Fig. 4.9 the shorter the wavelength, the bigger appears the cluster, the more the oscillations in its phase function. In order to have a clearer picture of what just observed, in Fig.4.10 it has been plotted the radiance phase function for $\lambda = 0.470\,\mu m$ for particles with $N = 64, 128, 256$. It is clearly visible that as soon as the cluster grows in size the forward peak increases and the oscillations get more visible.

Figure 4.11 presents the degree of polarization for a cluster of 256 monodispersed monomers. It plotted as function of the scattering angle for three different wavelengths. As soon as the cluster 'looks' smaller (increase in wavelength) the polarization curve moves towards the Rayleigh regime. A smaller particle will have an higher peak for a smaller scattering angle: the highest peak will be reached at $\alpha = 90°$, a characteristic of the Rayleigh regime. The multiple scattering effects will diminish resulting in an increase in polarization maximum. Furthermore the smaller the cluster the smoother the curve.

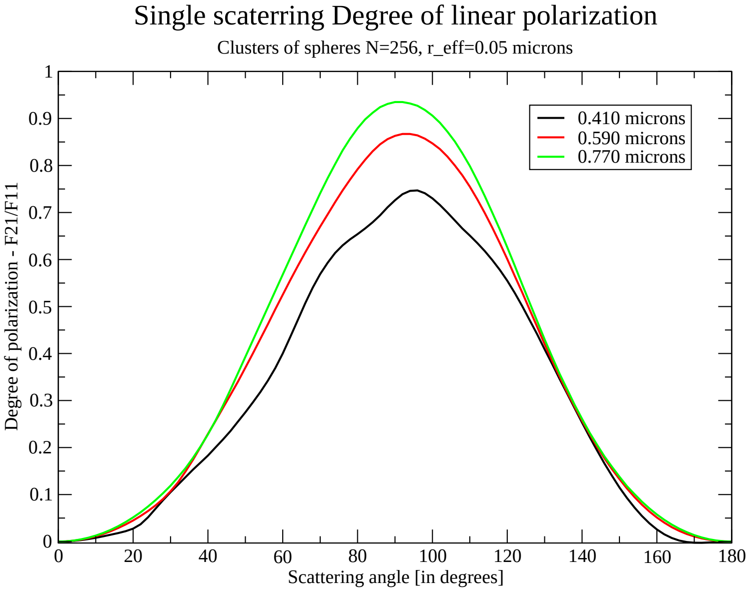

Figure 4.11: Degree of linear polarization $N = 256$ and $r_{\text{eff}} = 0.05\,\mu m$ with respect to scattering angle variation. It has been plotted for several wavelengths in the VIS range. The bigger is the aggregate, the higher is the scattering angle for the polarization maximum .

If we compare Fig.4.12 with Fig.4.14 [Skorov et al., 2008] for compact DLA particles at $\lambda = 0.410\,\mu m$, we can notice that the degree of linear polarization curves have the same behavior as soon as the number of monomers diminishes, in other words, as soon as the aggregate size parameters decreases. On the other hand, there is a completely different behavior regarding the scattering angle shift connected to an increase in polarization. In fact in Fig.4.14 the scattering angle corresponding with the peak in polarization bounces to smaller values for $N = 8$ and $N = 16$, while it goes to higher

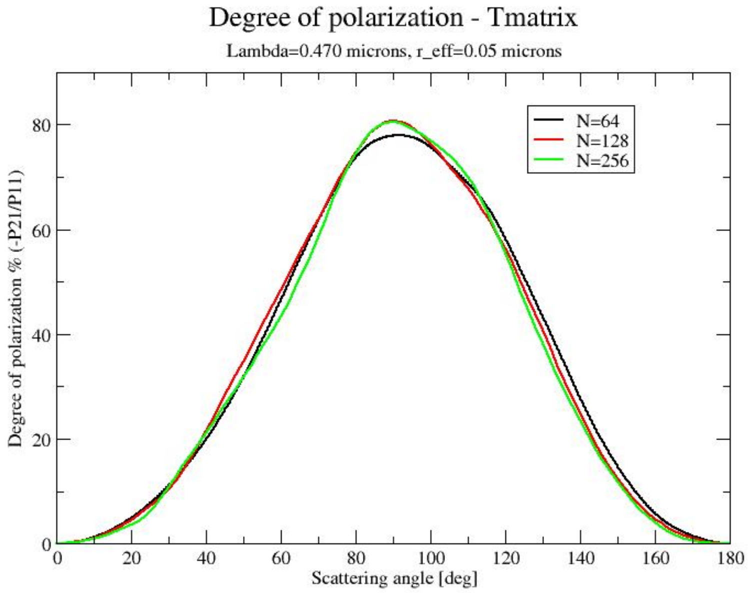

Figure 4.12: Degree of linear polarization for aggregates with monomer number of 64, 128 and 256 and $r_{\text{eff}} = 0.05\,\mu m$ with respect to scattering angle variation. It has been plotted for a wavelength of $\lambda = 0.41\mu$m. See text for discussion.

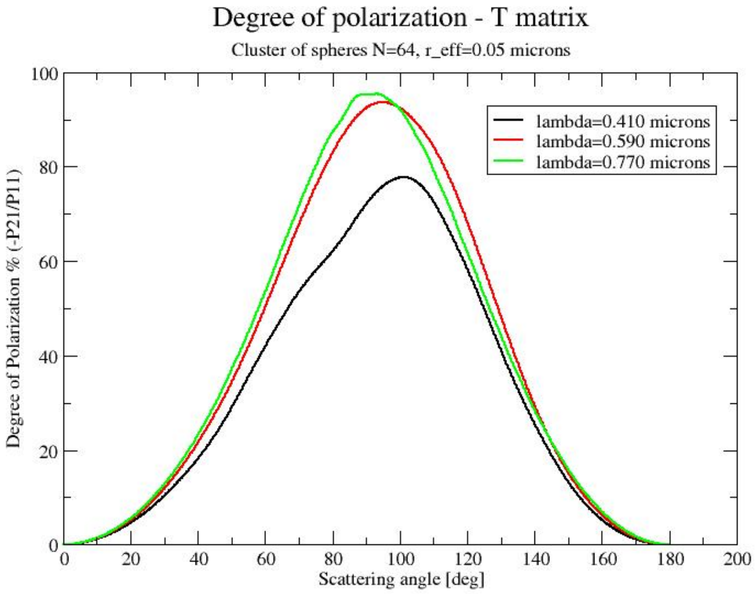

Figure 4.13: Degree of linear polarization $N = 64$ and $r_{\text{eff}} = 0.05\,\mu m$ with respect to scattering angle variation. It has been plotted for several wavelengths in the VIS range. No negative branch is present in the forward scattering in accordance to what has been observed on Titan by Tomasko et al. [2008]. See text for discussion.

values for $N = 32$ and again to smaller values for $N = 64$. In case of Fig.4.12 we notice that as soon as the aggregate size diminishes, the scattering angle shift is towards a smaller angle for an increase in polarization as demonstrated also for the degree of polarization of the monomers.

Moreover the polarization curve for $N = 64$ in Fig. 4.14 is different from what shown in Fig. 4.13 where no negative branch is present in the forward scattering. As mentioned also by Skorov et al. [2008], this behavior is totally different from what has been observed on Titan by Tomasko et al. [2008]. Skorov et al. [2008] suggest to solve this issue using a distribution of cluster sizes. The polarization phase functions that we calculated do not show such a negative branch. The reason for this is that we included particles and their mirror particles[7]. Apparently Titan's atmosphere is better represented by a macroscopically symmetric structure. Under this assumption the polarization curve has a trend similar to the one derived by Cassini-Huygens measurements and presented by Tomasko et al. [2008]. Furthermore during the simulations, it appeared that the particles that we received from dr. Y.V. Skorov were somewhat more compact than those used in the paper Skorov et al. [2008].

Compact aerosol versus Fluffy aerosol

As previously mentioned in this section, the particles that undergo Diffusion-Limited Aggregation process are more compact in structure and more probable to exist in the more dense layers of the atmosphere. The aerosols which formed in the Ballistic Particle-Cluster Aggregation process have a more fluffy structure and are more probable to exist in the less dense layers of the atmosphere. Figure 4.15 shows a 3D representation of the DLA- and BPCA-particle shape. The difference between the two particles stands in the outside layer of the structure. The BPCA-particle on the left of Fig.4.15 is characterized by a compact core that is surrounded by 'arms' of monomers; the DLA-particle lacks the extended 'arms' of monomers. According to Tishkovets et al. [2004], the different shapes of the two types of particles yield different scattering behaviors. In Fig.4.16 we show the phase function and degree of polarization P_S of singly scattered light by the BPCA-particle and DLA-particle that we calculated for $\lambda = 0.47\mu$m and $\lambda = 0.83$ μm. The phase functions for both types of particles clearly show forward scattering behaviour (see Fig. 4.16). The strength of the forward scattering peak at the shorter wavelength ($\lambda = 0.47$ μm) is significantly stronger for the BPCA-particle too. The size of the aggregates, calculated using Eq.4.25, is equal to 4.24 for $\lambda = 0.47\mu$m and 2.40 for $\lambda = 0.83\mu$m. With the shorter wavelength, the phase functions for both types of particles also show more angular features. These angular features are much less obvious for $\lambda = 0.83$ μm. Such features are usually due to interference between light that has been scattered by different, similarly sized particles Hansen and Travis [1974]. Apparently, when the light has a short wavelength compared to the fractal particles size, the light scattered by the different monomers that make up the fractal particle will interfere and give rise to the angular features Tishkovets et al. [2004]. With increasing λ, the light will increasingly be scattered by the fractal particle as a whole, and the interference patterns disappear due to the different scales of the macroscopic particle. Since the DLA-particle is more compact

---

[7] This allows us to have a scattering matrix as presented in Eq. 4.5, which is not valid without the macroscopically symmetric atmosphere assumption.

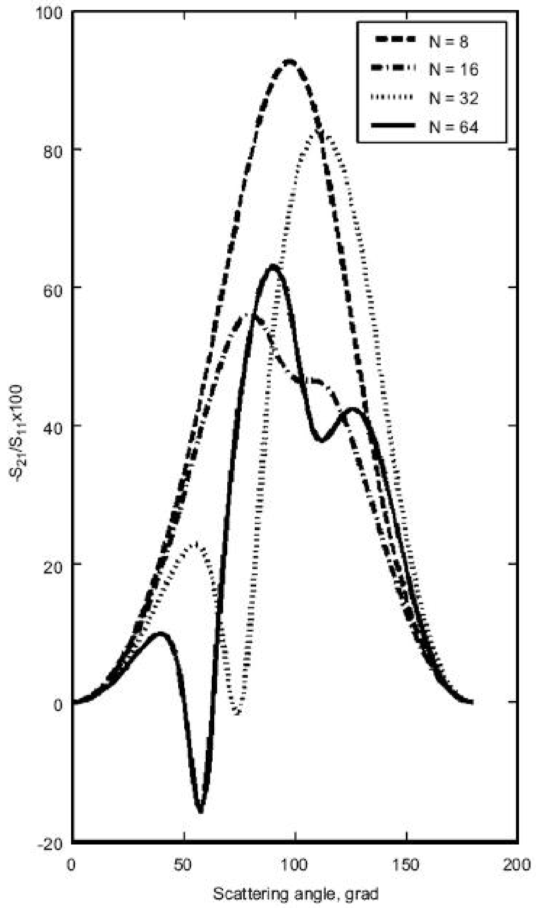

Figure 4.14: Degree of linear polarization for $N = 8, 16, 32, 64$ with respect to scattering angle variation for DLA's compact particles with $D = 3$. The wavelength of reference is $\lambda = 0.410\,\mu m$. Source: Skorov et al. [2008].

and thus somewhat smaller than the BPCA-particle, its phase function is the more symmetric one at $\lambda = 0.83$ μm.

The degree of linear polarization P_S of the light that is singly scattered by the BPCA-particle (see Fig. 4.16) shows the same bell-shape as the DLA-particle, which is characteristic for light that is scattered by particles that are small with respect to the wavelength Hansen and Travis [1974]. Apparently, this polarization signal is dominated by that of light that is scattered by the monomers. An effect of the macroscopic shape of the particles on P_S is found in the strength of the maximum of the polarization curve: with increasing λ, the maximum P_S increases more for the compact DLA-particles than for the fluffier BCPA-particles and moves toward smaller scattering angles in accordance with Petrova et al. [2004].

In conclusion of the single scattering analysis of the monomers and aggregates, we can say that:

- if N increases and/or if monomer size x_m increases, intensity will increase while polarization will decrease;

Figure 4.15: DLA aerosol particle (on the right) versus BPCA aerosol particle (on the left) with N=256.

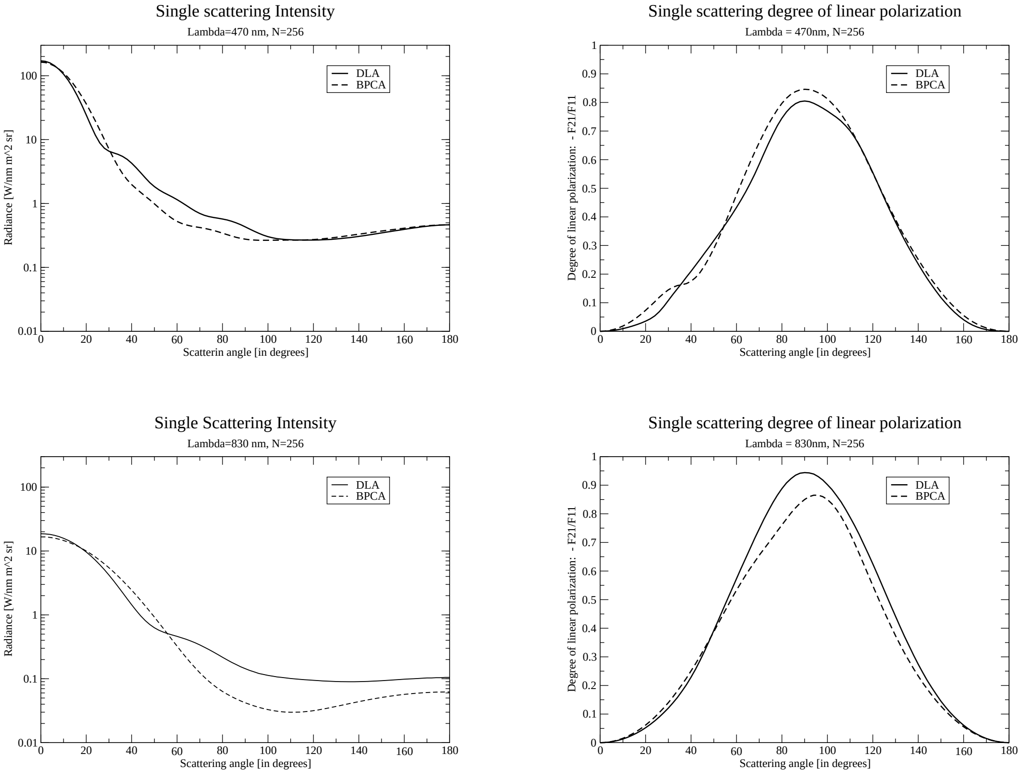

Figure 4.16: The phase function (left) and degree of linear polarization P_{S} (right) of unpolarized incident light that is singly scattered by the BPCA-particles (dashed lines) and the DLA-particles (solid lines) as functions of the single scattering angle Θ, for $\lambda = 0.47$ μm (top) and $\lambda = 0.83$ μm (bottom).

- if n_i increases (λ decreases) the intensity decreases while the polarization increases, it has a stronger effect on the intensity[8];
- if n_r increases the intensity increases while the polarization increases, it has a

---

[8] Valid only in this study, for our refractive indices and our wavelength range

stronger effect on polarization;

- if particle size (both X_v and x_m) grows oscillations will appear in both intensity and polarization;
- polarization depends more on the monomers and their radius than on the aggregate internal structure, in fact the outside layer of monomers is the one that will affect the most the scattering characteristics of the aggregate.

5 Modeling Titan's atmosphere

Titan's atmosphere extends up to 1000 km from its surface: it is ten times higher than Earth's atmosphere. The vertical structure of the atmosphere is similarly divided into troposphere (temperature decrease), stratosphere (temperature increase), mesosphere (temperature decrease), thermosphere and, the last stage, ionosphere as on Earth, as shown already in Fig. 1.1 and Fig. 2.3. Among the several phenomena that take place in the atmosphere, particular attention is given to the aerosols production and growth as explained in Section 2.2. In order to understand how the methane cycle works, it can be useful to describe not only the scattering behavior of the individual aerosols as done in Chapter 4, but also the interaction among the aerosols embedded in the whole atmosphere. As mentioned in Chapter 4, multiple scattering describes the scattering effects of an increase in aggregates number within a medium (atmosphere) causing multiple orders of scattering. The description of these multiple orders of scattering will take place in the first part of this chapter together with the description of the method used to model it. In the second part there will be an accurate description of Titan's atmosphere parametrization used in the model. The analytic representation of the multiple scattering problem and of the doubling-adding method have been adapted from De Haan et al. [1987], Hansen and Travis [1974] and Chandrasekhar [1950] respectively. For further details please consult their articles and the references therein.

5.1 Analytic representation

Most of the multiple scattering problems assumes that a vertically inhomogeneous atmosphere can be modeled using plane-parallel geometry: the atmosphere is supposed to be divided in several homogeneous plane-parallel layers of infinite horizontal length. This formulation works if the solar zenith angle (θ_0, measured with respect to the local vertical) is smaller than 75° and if the measurement is taken not at horizontal viewing directions[1] [Salinas et al., 2003]. Moreover no internal light sources are considered and the surface at the bottom is treated as a Lambertian surface.

In order to describe the complex scattering process, we should be able to describe the exact position of a point within the atmosphere. Using the atmosphere geometry, the atmospheric height measured from the bottom is represented by the z axis. Directions in the atmosphere are specified using the angles θ and ϕ, where the incident (indicated also as zenith) angle θ is measured from the positive z-direction. The azimuth position ϕ is measured clockwise when looking at the positive z-direction starting

---

[1] In case of higher solar zenith angles or limb observations, the plane-parallel is not applicable and the spherical model is used instead. See Salinas et al. [2003] for extra explanations.

from some plane containing the z axis. Since rotation is symmetric with respect to the z axis, only the difference in azimuth is relevant $(\phi - \phi_0)$. This geometry has been

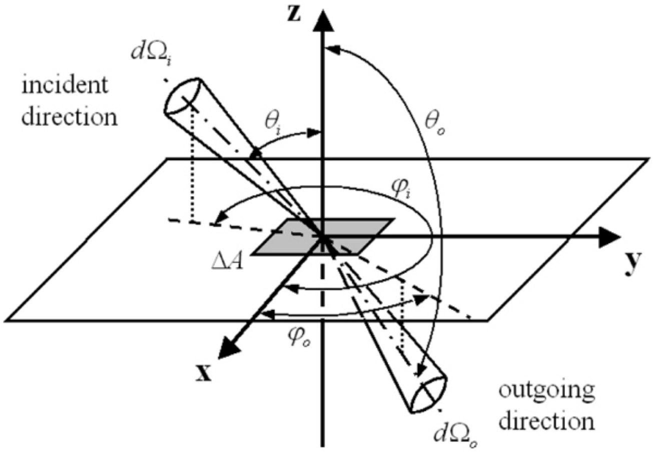

Figure 5.1: Geometry for scattered light. The same as in Figure 4.1. z represents the positive atmospheric height. Solar zenith (incident) angle θ is measured from the positive z axis. Azimuthal angle ϕ determines the position of the scattering plane from the positive x axis. These angles are measured both for ingoing and outgoing rays. The outgoing ray could represent the instrument position. Contrary to here, in the text the pedix 0 indicates the solar incoming parameters. *Image source*: `http://www.jvrb.org/5.2008/1498/figure01.jpg`.

already used and described in Chapter 4, except that the angle $\phi - \phi_0$ it is not used in the single-scattering representation. The geometry for scattered light in Fig.4.1 has been repeated for clarity in Fig.5.1.

Thanks to the use of the plane parallel geometry, the height of a specific location inside the atmosphere can be described through the *optical depth*:

$$\tau(z) = \int_z^\infty k_{\text{ext}} \rho \, dz' \tag{5.1}$$

where k_{ext} is the extinction coefficient per unit mass and ρ is the atmospheric density at height z'. According to Fig.5.2 we indicate the top of the atmosphere with $\tau = 0$ and the bottom with $\tau = b$. Any intermediate layer is characterized by a specific finite value of optical depth indicated as $\tau_i = b_i$ and referred to as *optical thickness*. For this assumption, the atmosphere can be seen also as a combination of several optical thicknesses b_i each characterizing a different layer. It is important to not confuse the terms optical depth and optical thickness: the optical thickness is the distance between two locations z_1 and z_2, it is a property of an atmospheric layer, while the optical depth is the distance that it has been covered to go from the location at height "z_1" to the location at height "z_2" (the distance τ can be different than the distance b). According to these assumptions, the single scattering albedo $\tilde{\omega}$ shown in Eq.4.4 and the scattering matrix $\mathbf{P}(\alpha)$ in Eq. 4.5 can only be function of the optical depth τ for a plane-parallel model [Hovenier et al., 2004].

According to the plane-parallel model, the optical depth is measured with respect to the positive direction of the local vertical using the zenith angle θ. Hansen and Travis [1974] uses two systems to specify the zenith angle shown in Fig. 5.2:

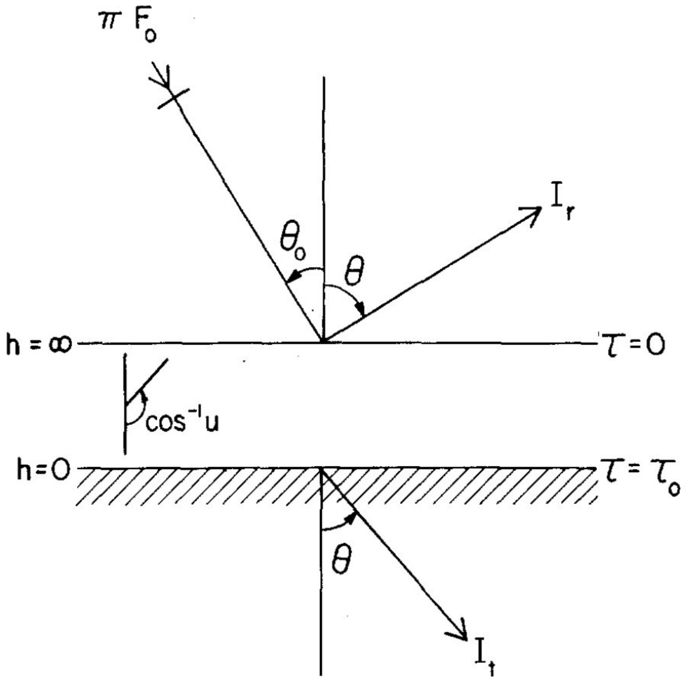

Figure 5.2: Geometry inside the atmosphere, the zenith angles and the optical depth are represented for a random layer inside the atmosphere. The vertical axis corresponds to the z axis in Figure 5.1. The solar incoming flux is equal to πF_0, the reflected ray is indicated by I_r, while the transmitted by I_t. h is the atmosphere altitude, τ is the optical depth. θ_0 is the solar zenith angle, θ is the instrument zenith angle. The image has been adapted from Hansen and Travis [1974].

- u equal to the cosine of angle with respect to direction of increasing τ (downward). Its value goes from +1 for the downward direction to -1 for the upward direction;

- $\mu = |u|$ equal to the cosine of angle with respect to the outward normal (local vertical) and it ranges from +1, for the normal direction, to 0 for the grazing direction.

The first system is used for internal radiation field inside the atmosphere, the second is used for reflected and transmitted radiation outside the atmosphere. In particular, in Fig.5.2 we have $\mu = \cos\theta$ for the reflected-transmitted radiation inside the atmosphere and $\mu_0 = \cos\theta_0$ for the zenith angle of solar incident radiation [De Haan et al., 1987].

After having described the atmosphere's internal geometry, it is important to point out that the radiance of an internal radiation field is strictly dependent on this geometry, or, in other words, on the location τ inside the atmosphere. This location is expressed by the azimuth angle ϕ, measured counterclockwise looking downward and by the zenith angle θ or its cosine μ. The intensities $I_r(\mu, \phi)$ and $I_t(\mu, \phi)$ of the light respectively reflected and transmitted in Fig. 5.2, are nothing else than two Stokes parameters of an internal radiation field (see Eq.4.1). For the multiple scattering problem 4×4 reflection and transmission matrices, **R** and **T**, have to be defined in such a way that:

$$I_r(\mu,\phi) = \frac{1}{\pi}\int_0^1 \mu_0\, d\mu_0 \int_0^{2\pi} d\phi_0\, \mathbf{R}(\mu,\mu_0,\phi-\phi_0)\mathbf{I_0}(\mu_0,\phi_0)$$
$$I_t(\mu,\phi) = \frac{1}{\pi}\int_0^1 \mu_0\, d\mu_0 \int_0^{2\pi} d\phi_0\, \mathbf{T}(\mu,\mu_0,\phi-\phi_0)\mathbf{I_0}(\mu_0,\phi_0) \tag{5.2}$$

The net flux of sunlight radiation can be expressed as:

$$\pi\mathbf{F} = \int_0^{2\pi}\int_{-1}^1 I(u,\phi)u\, du\, d\phi = 2\pi\int_{-1}^1 {}^0\mathbf{I}(u)\, u\, du \tag{5.3}$$

where ${}^0\mathbf{I}(u)$ is the azimuth-independent term of $\mathbf{I}(u,\phi)$ in a Fourier expansion. The net flux represents the amount of energy that is flowing at a certain point in space in all directions per unit of frequency interval, of surface area and of time [Hovenier et al., 2004].

If the incident sunlight is monodirectional:

$$\mathbf{I_0} = \delta(\mu-\mu_0)\,\delta(\phi-\phi_0)\pi\mathbf{F_0} \tag{5.4}$$

where δ is the Dirac-delta function and $\mathbf{F_0}$ is the Stokes vector of the incoming solar radiation with πF_0 the solar flux at the top of the atmosphere measured perpendicularly to the direction of incidence. Since it is assumed to be monodirectional and unpolarized, the solar radiation is given by $\mathbf{F}_0 = F_0\mathbf{1}$, with $\mathbf{1}$ the unit vector. This means that the direction of light is known and that the flux intensity can be modeled as one unique ray focused in a specific direction. It is fundamental to point out that both the degree of polarization P (Eq.3.9) and its direction χ (Eq.3.10) are independent of F_0.

Using Eq. 5.4, we can get a simpler formulation of the reflected and transmitted intensities:

$$\mathbf{I_r}(\mu,\phi) = \mu_0\mathbf{R}(\mu,\mu_0,\phi-\phi_0)\mathbf{F_0}$$
$$\mathbf{I_t}(\mu,\phi) = \mu_0\mathbf{T}(\mu,\mu_0,\phi-\phi_0)\mathbf{F_0} \tag{5.5}$$

Once the reflected and transmitted matrices $\mathbf{R}$ and $\mathbf{T}$ have been determined, we have to consider that a layer can be illuminated from above or below (we suppose to be inside the atmosphere) before being able to calculate the reflected and transmitted intensities for a generic layer. In case the layer is illuminated from above we use Eq. 5.5, if it is illuminated from below the reflected and transmitted intensities will be indicated as:

$$\mathbf{I_r^*}(\mu,\phi) = \mu_0\mathbf{R}^*(\mu,\mu_0,\phi-\phi_0)\mathbf{F_0}$$
$$\mathbf{I_t^*}(\mu,\phi) = \mu_0\mathbf{T}^*(\mu,\mu_0,\phi-\phi_0)\mathbf{F_0} \tag{5.6}$$

The fraction of incident flux that gets reflected by a plane-parallel atmosphere is called *local* (plane) *albedo* and is measured as:

$$A(\mu_0) = 2\int_0^1 {}^0R^{11}(\mu,\mu_0)\,\mu\, d\mu \tag{5.7}$$

where ${}^0R^{11}$ is the azimuth-independent part of the first element of the reflecting matrix $\mathbf{R}$. Being a ratio, the albedo is dimensionless. If, instead, we have to calculate the fraction of incident light that gets reflected in all directions by a plane-parallel atmosphere, we have to measure the *bond albedo*:

$$A = 2\int_0^1 A(\mu_0)\mu_0\, d\mu_0 = 4\int_0^1 \int_0^1 {}^0R^{11}(\mu,\mu_0)\,\mu\, d\mu \quad \mu_0\, d\mu_0 \tag{5.8}$$

Radiative transfer inside the atmosphere and, therefore, multiple scattering, is automatically connected with a continuous change in scattering plane. In Eq.4.5 the phase matrix $\mathbf{P}(\alpha)$ was defined with respect to one plane of scattering, the same as for the Stokes parameters. It is now necessary to choose a new plane common to all the multiple scattering problems. This new reference plane is the *local meridian plane* defined by the local normal ($u = 1$) and the direction of emergence of light (u, ϕ). Appropriate rotations can transform the old scattering matrix $\mathbf{P}(\alpha)$ in Eq.4.5 to the new phase matrix $\mathbf{Z}(u, u_0, \phi - \phi_0)$:

$$\mathbf{Z}(u, u_0, \phi - \phi_0) = \mathbf{M}_{\mathrm{rot}}(\pi - i_2)\mathbf{P}(\alpha)\mathbf{M}_{\mathrm{rot}}(-i_1) \tag{5.9}$$

where $\mathbf{M}_{\mathrm{rot}}$ is a simple rotation matrix used to rotate reference planes while i_1, i_2 are the angles between the scattering plane[2] and the meridian plane of the incident beam in case of i_1, and between the scattering plane and the meridian plane of the scattered beam in case of i_2 [De Haan et al., 1987; Hovenier et al., 2004]. For the complete transformation see Chandrasekhar [1950] and Hansen and Travis [1974].

As already mentioned in Chapter 4, we assume to have a macroscopic symmetrical atmosphere, therefore the scattering matrix $\mathbf{P}(\alpha)$ does not depend on the choice of the scattering plane, but only on the scattering angle (i.e. $\alpha = u$). Phase matrix and scattering matrix are directly proportional to each other:

$$\mathbf{P}(\alpha) = \frac{4\pi}{\sigma_{\mathrm{sca}}}\langle \mathbf{Z}(u, 0, 0)\rangle \tag{5.10}$$

where σ_{sca} represents the scattering cross section. We will refer to the matrices in the same way without making any difference between them.

After the transformation we obtain a phase matrix for both the transmitted and reflected intensities and for illumination from above or below:

$$\begin{aligned}
\mathbf{P_r}\,(\mu, \mu_0, \phi - \phi_0) &\equiv \mathbf{P}(-\mu, \mu_0, \phi - \phi_0)\\
\mathbf{P_t}\,(\mu, \mu_0, \phi - \phi_0) &\equiv \mathbf{P}(\mu, \mu_0, \phi - \phi_0)\\
\mathbf{P_r}^*(\mu, \mu_0, \phi - \phi_0) &\equiv \mathbf{P}(\mu, -\mu_0, \phi - \phi_0)\\
\mathbf{P_t}^*(\mu, \mu_0, \phi - \phi_0) &\equiv \mathbf{P}(-\mu, -\mu_0, \phi - \phi_0)
\end{aligned} \tag{5.11}$$

The * stands for illumination from below as in Eq. 5.6. If the sign of the cosine of the solar zenith angle (μ_0) and of the instrument zenith angle (μ) is the same, it means that the ray of light does not change direction as it happens in case of transmission through the layer. In case μ_0 shows a negative sign, it means that the layer is illuminated from below. If the phase matrix is of the form shown in Eq. 4.5, the symmetry relationships are valid also in case of multiple scattering. In particular we have:

$$\begin{aligned}
\mathbf{P_r}^*(\mu, \mu_0, \phi - \phi_0) &= \mathbf{P_r}\,(\mu, \mu_0, \phi_0 - \phi)\\
\mathbf{P_t}^*(\mu, \mu_0, \phi - \phi_0) &= \mathbf{P_t}\,(\mu, \mu_0, \phi_0 - \phi)
\end{aligned} \tag{5.12}$$

---

[2] The scattering plane is the plane between the incident and scattered beam.

These relations are valid also for the **R** and **T** matrices and have the advantage to reduce the number of quantities computed.

5.2 The Doubling-Adding method

Few methods examine the contribution of successive order of scattering to the radiance and the polarization for vertically inhomogeneous atmospheres. We use the Doubling-Adding method developed by De Haan et al. [1987] and successively adapted for application to various types of planetary atmospheres by Stam [2008]. The principle of the Adding method has been introduced by Van de Hulst [1957] and it belongs to the class of the 'exact' methods. The Doubling method, that computes scattering properties of homogeneous atmospheres, is an important application of the Adding method. According to De Haan et al. [1987], dividing the atmosphere in homogeneous layers allows to use a combination of adding and doubling method to obtain the radiance and polarization of the light emerging at the top and the bottom of the atmosphere. In particular, a homogeneous layer is a layer in which the optical thickness b_i does not vary and, therefore, the scattering matrix $\mathbf{P}(\alpha)$ and the single scattering albedo $\tilde{\omega}$ do not depend on b, but only on the global optical depth τ. The general problem is now to determine the matrices **R** and **T** from the known single scattering albedo $\tilde{\omega}(\tau)$ and the phase matrix $\mathbf{P}(\tau, u, u', \phi - \phi_0)$. If these quantities are known, the radiation field can be solved for all the possible distributions of incident light using Equations 5.5 and 5.6.

In order to better understand how the adding method and doubling method contribute to each other when combined together, it could be useful to describe them separately.

Adding method - With this method we can calculate the combined radiation properties of two layers of optical thickness b_a and b_b one on top of the other. The two layers are plane-parallel. The incident light $\pi\mathbf{F_0}$ travels through the upper layer and hits the bottom layer as shown in Fig. 5.3. Part of it will be reflected back (R-rays), part of it will be transmitted through the layer and emerge at the end of the combined layers (T-rays) while the rest can be partly absorbed and partly reflected. The interesting part is the interface between the two layers where the rays get reflected repeatedly (U and D rays - upward and downward direction). The sum of the transmitted intensities emerging at the end of the bottom layer together with the sum of the reflected intensities emerging above the upper layer, represents the total intensity emerging from the combined layer. If we want to have polarization measurements, we have to be sure to consider the intensity Stokes parameters. If the two starting layers are homogeneous, the combined layer is also homogeneous (i.e. scattering matrix and single scattering albedo still independent of $\tau_i = b_i$). Once the properties of the combined layer are found, a new layer can be added in the same way.

Doubling method - With this method it is possible to calculate the scattering properties of two identical homogeneous layers. The only requirement is to know *a priori* the reflection and transmission properties of the layer. With the doubling method we can calculate the properties of a layer with the same composition, but with double optical thickness. It is important then, to choose an appropriate

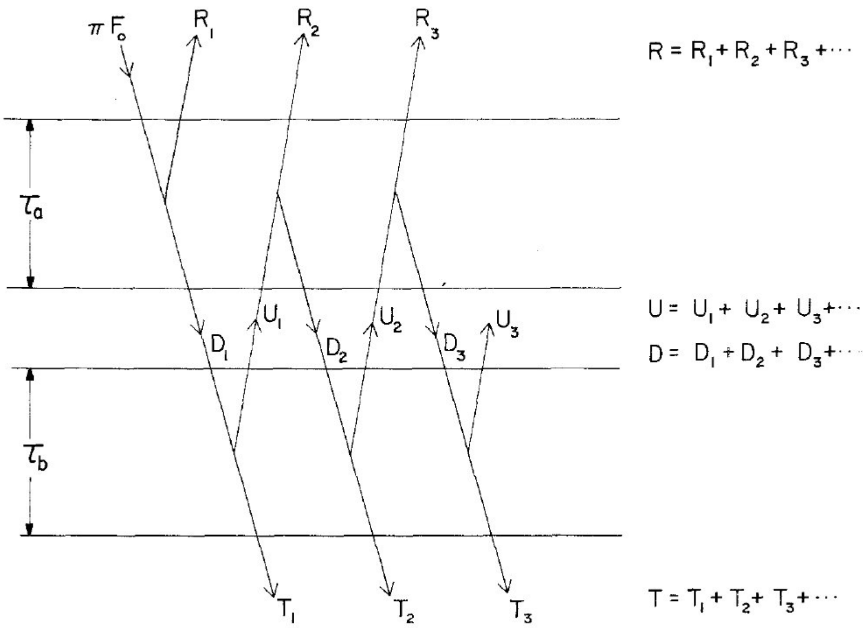

Figure 5.3: Schematic representation of the adding method.The two layers of optical thickness $\tau_a \equiv b_a$ and $\tau_b \equiv b_b$ are for convenience physically separated, but in reality they are on top of each other. The image has been adapted from Hansen and Travis [1974].

initial optical thickness in order to not repeat the process too many times and then loose in accuracy. In general, the initial τ is chosen in such a way that only single-scattering takes place in it and its scattering properties can be expressed directly in the phase matrix.

In conclusion, the reliability of the adding-doubling method depends on the accuracy with which we determine the phase matrix of the first thin layer at the beginning of the doubling method. Since the azimuth angle ϕ varies between $[-\pi, \pi]$ we can use the Fourier series expansion to handle in an efficient way the adding equations and avoid data overflow. In fact by expanding each function of azimuthal angle in a Fourier series in $\phi - \phi_0$, the number of integrations in the adding scheme is drastically reduced. Results of the Doubling-Adding method are thus for all values of azimuthal angles $\phi - \phi_0$ and for discrete values of zenith angles θ and θ_0 (or their cosines μ and μ_0). The number of zenith angles depends on the desired accuracy.

To determine the Fourier coefficients for the phase matrix, we used the expansion method described by De Haan et al. [1987]. The expansion of the elements of the scattering matrix in generalized spherical functions has been already shown in Eq. 4.24 for the Mie theory as described by De Rooij and Van der Stap [1984].

5.3 DAP input parameters

With the intention to simulate the radiative transfer within Titan's atmosphere using the Doubling-Adding method, some parameters have to be accurately selected.

With this we are referring to the main characteristics of an atmosphere such as the surface albedo, the optical depth (i.e. the vertical profile), pressure and temperature, gaseous absorption, aerosols or clouds. In our case Titan's atmosphere is considered as cloud-free, all the other parameters that influence the atmospheric scattering are hereby described.

We model Titan's atmosphere from 0 km to 400 km with 34 horizontally homogeneous layers. Each atmospheric layer contains gaseous molecules and, optionally, aerosols particles. For each atmospheric layer, we have to specify for each type of particle, their column number density and, for each wavelength λ, their extinction cross section σ, single scattering albedo $\tilde{\omega}$ and single scattering phase matrix $\mathbf{P}$. In Eq.5.13, b_{msca} and b_{asca} indicate the optical thickness due to molecules and aerosols scattering respectively, and both depend on the single scattering albedo as $b_{\mathrm{msca}} = \tilde{\omega}_m b_{\mathrm{m}}$ and $b_{\mathrm{asca}} = \tilde{\omega}_a b_{\mathrm{a}}$. The single scattering albedo $\tilde{\omega}$ of a certain layer can be defined as:

$$\tilde{\omega}(\lambda) = \frac{b_{\mathrm{msca}(\lambda)} + b_{\mathrm{asca}}(\lambda)}{b_{\mathrm{m}} + b_{\mathrm{aer}}} \tag{5.13}$$

The single scattering phase matrix of the gases and particles in a layer is given by:

$$\mathbf{P}(\Theta, \lambda) = \frac{b_{\mathrm{msca}}(\lambda)\mathbf{P}_m(\Theta, \lambda) + b_{\mathrm{asca}}(\lambda)\mathbf{P}_a(\Theta, \lambda)}{b_{\mathrm{msca}} + b_{\mathrm{asca}}} \tag{5.14}$$

where Θ is the total single scattering angle ($0^\circ \leq \Theta \leq 180^\circ$, $\Theta = 0^\circ$ implies forward scattering), and $\mathbf{P}_m$ and $\mathbf{P}_a$ are the single scattering matrices of the gaseous molecules and the aerosols particles respectively [Stam et al., 1999]. The atmosphere is bounded by an horizontally homogeneous Lambertian surface characterized by a wavelength dependent albedo A_S. Being Lambertian, the surface is isotropic and depolarizing.

Beside the atmospheric and surface properties, the radiative transfer depends on the illumination and viewing geometries. We specify the solar zenith angle θ_0 (the angle between the direction towards the sun and the upward vertical), the instrument zenith viewing angle θ (the angle between the direction of propagation of the observed light and the downward vertical), and the azimuthal angles ϕ_0 and ϕ that are measured between an arbitrary vertical plane and the directions of propagation of, respectively, the incoming and observed beams of radiation. Since our model atmosphere and surface are horizontally homogeneous, only $\phi - \phi_0$ is relevant. When $\phi - \phi_0 = 0^\circ$, the instrument is looking in the direction towards the sun. When $\phi - \phi_0 = 180^\circ$, it has the sun 'in its back.'

Since we assume that SPEX will be payload on a airborne platform floating below Titan's lowest haze layer, it will observe sunlight that has been transmitted through the atmosphere. With our adding-doubling algorithm, we calculate the transmission matrix $\mathbf{T}$ of the atmosphere-surface system, and obtain the Stokes vector of the transmitted light using [Hansen and Travis, 1974]:

$$\mathbf{I}(\lambda, \theta_0, \theta, \phi - \phi_0) = \cos\theta_0 \mathbf{T}(\lambda, \theta_0, \theta, \phi - \phi_0)\mathbf{F}_0(\lambda), \tag{5.15}$$

where $\mathbf{F}_0$ is the Stokes vector of the incoming solar radiation, with πF_0 the solar flux at the top of the atmosphere, measured perpendicularly to the direction of incidence as described in Eq. 5.4.

5.4 Setting up the atmospheric scenario

In this section a generic up-to-date Titan's atmospheric scenario is set up. We describe which realistic parameters we choose to use in the Doubling Adding Program (DAP) to simulate the radiative transfer taking place inside the atmosphere of Titan. The description starts with the surface parameters and continues with the atmospheric parameters.

5.4.1 Surface albedo

According to the Doubling-adding method, we assumed that both the top and the bottom of the atmosphere are illuminated in the downward and upward direction respectively. Light incident on the top layer is clearly due to solar radiation, the one incident on the bottom layer instead depends on the surface's properties. If the surface is treated as a black body (completely absorbing) no light hits the bottom layer. We will treat the surface as a Lambertian surface (totally reflecting).

The surface albedo is calculated as the ratio of the observed intensity I to $1/\pi$ of the incoming solar radiation πF [Gibbard et al., 2004; McCord et al., 2006] as presented in Eq. 5.2 and 5.8. Using other words, the surface albedo can be seen as the ratio of reflected light to incident light at the surface level.

For an optical depth of τ between 0.1 and 0.3 and at a wavelength of $2\mu m$, the surface albedo on Titan is equal to:

$$\begin{aligned} I/F &= 0.15 \div 0.20 \quad \text{for bright matter} \\ I/F &= 0.04 \div 0.08 \quad \text{for dark matter} \end{aligned} \tag{5.16}$$

The difference in the bright and dark features is probably due to water ice presence as bigger grains because of their lower reflectance. Optical imaging showed that 25% of the known equatorial area is covered by dark material [Keller et al., 2008; McCord et al., 2006]. The difference in optical depth τ between 0.1 and 0.3 for $\lambda = 2\,\mu$m [Gibbard et al., 2004; McCord et al., 2006] depends on latitude and seasonal variations. Regarding the latitude, at the poles there are more lakes and liquids than at the equator, that's why the poles appear generally more bright; seasonal because of thermal reasons, the summer hemisphere has the most hazes[3] due to slightly higher temperatures and therefore appears darker (i.e. $\tau = 0.2$ for the southern hemisphere between 2000 and 2005 [Gibbard et al., 2004], cfr appendix B.).

Tomasko et al. [2005] measured the ground reflectivity at the Huygens landing site (10.3° S) thanks to the ULIS [4] instrument on the Huygens probe. The values they found are 0.13 at $\lambda = 531\,nm$ and 0.19 at $\lambda = 829\,nm$. The latter is in agreement with the value measured by the Infrared Spectrometer (0.18) and with the value of surface albedo of 0.04 retrieved by McCord et al. [2006] for the dark terrain[5]. These values

---

[3] It has to be mentioned that the highest concentration of haze is near 40° latitude in both hemispheres [Rannou et al., 2006].

[4] Upward-Looking Infrared Spectrometers. Together with the DLIS (Downward-Looking) is part of the DISR instruments on board of Huygens. See Appendix C for the Cassini-Huygens instrumentation description.

[5] Ground reflectivity is the incident radiant energy reflected by a surface when illuminated directly from above. The albedo (reflectance) is the square of the magnitude of the reflectivity. Lambertian surfaces have an albedo equal to unity (pure reflecting), black bodies equal to zero (pure absorbing).

of dark and bright terrain are in accordance between Coustenis et al. [1995]; Gibbard et al. [2004]; McCord et al. [2006] and Tomasko et al. [2005]. On the other hand, the bright values of McCord et al. [2006] are different from the values retrieved by Keller et al. [2008], while their dark terrain values do agree, although a detailed comparison is not possible due to the different resolution of the observations made by VIMS and DLIS instruments. For this reason we used the albedo values for the bright and dark terrain presented in Eq.5.16 [McCord et al., 2006] because they are not wavelength dependent.

It would be recommendable to implement a more realistic wavelength dependent surface albedo in future simulations of radiative transfer inside the atmosphere of Titan.

5.4.2 Atmospheric pressure and temperature

The pressure and temperature of Titan's atmosphere have been retrieved from Cassini orbiter observations made by the CIRS instrument during the early southern summer in the second half of 2004. The data have been published by Flasar et al. [2005].

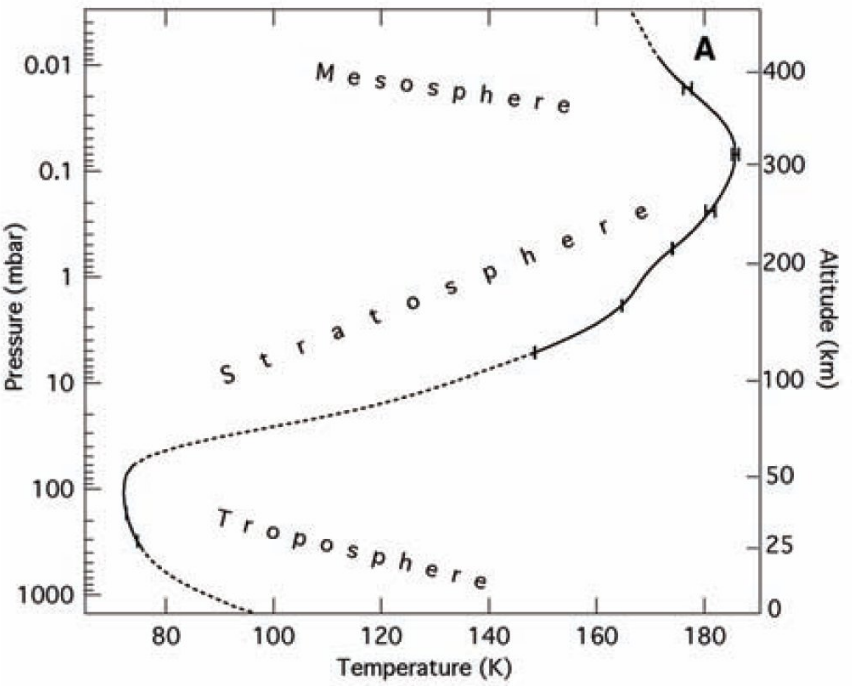

Figure 5.4: Temperature and pressure in Titan's atmosphere. The profile was retrieved at 15° S from a combination of nadir- and limb- observation of the CIRS instrument up to 400 km. The image has been adapted from Flasar et al. [2005].

Figure 5.4 shows the temperature and pressure altitude variations for a location at 15° S (close to Huygens site). At the surface the temperature is 96 K for a pressure of 1.4383 bar. The collisions taking place in the troposphere control its temperature; these collisions generate absorption and consequently a warming greenhouse effect. Above the tropopause, which is located at 44 km with a temperature of 72 K, the temperature increase depends on the haze extinction profile and thus on the haze layer model. Above the stratopause, at 320 km with a temperature of 186 K, the temperature drops due to the IR cooling by methane (antigreenhouse effect). The top layers of the atmosphere are warmed up by solar radiation and UV photodissociation [Lavvas et al., 2008]. A complete atmospheric thermal profile is shown in Fig. 1.1. For further informations about the temperature retrieval please consult Flasar et al. [2005].

We use CIRS-based dataset instead of HASI-based values with the intention to have a more global temperature profile. The HASI-based dataset are in-situ measurements relative only to the Huygens landing site. There are in fact several differences between the two retrievals that are still unexplained. The HASI in-situ measurements suggest a hotter stratosphere compared to the CIRS profile. The stratopause for the HASI measurements is at about 250 km with a temperature around 185 K [Fulchignoni et al., 2005], 70 km and 1 K higher than what retrieved from CIRS-measurements [Flasar et al., 2005].

We divided the atmosphere in 34 horizontally homogeneous layers up to 400 km above surface each with constant temperature and pressure values. We based the spacing between two consecutive layers on a logarithmic variation of pressure between two layers. On this logarithmic variation, we applied an exponential decrease of $1/e$ to determine the pressure at the new levels. Once the pressure variation with altitude was obtained, we could calculate the temperature and altitude values of the relative layers through interpolation. The original pressure and temperature values used for our interpolation are the one published by Flasar et al. [2005]. The interpolated temperature and pressure profiles are shown in Fig.5.5 and 5.6 respectively.

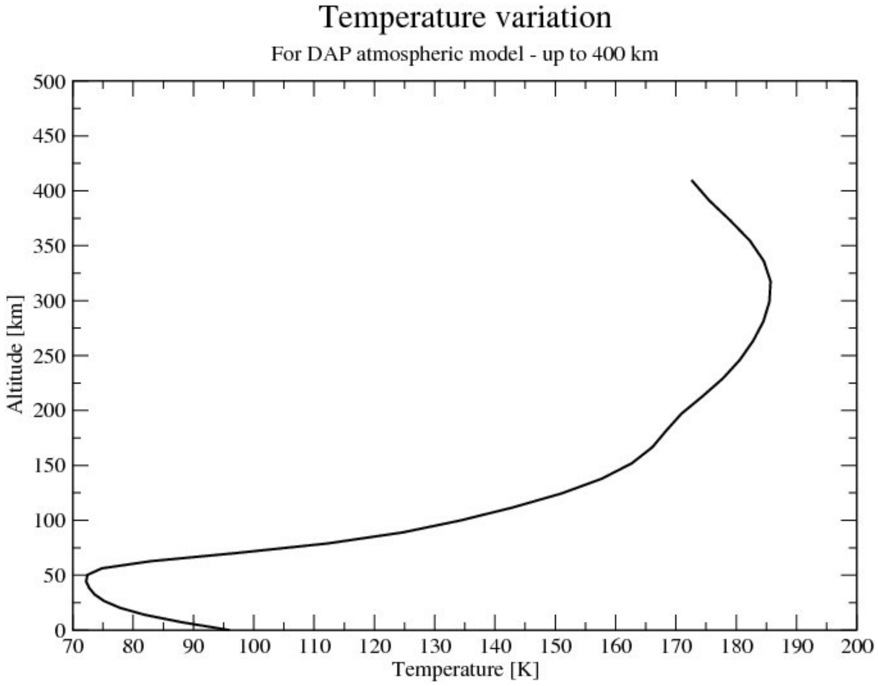

Figure 5.5: Temperature profile in Titan's atmosphere up to 400 km. The profile was obtained interpolating data retrieved by Flasar et al. [2005].

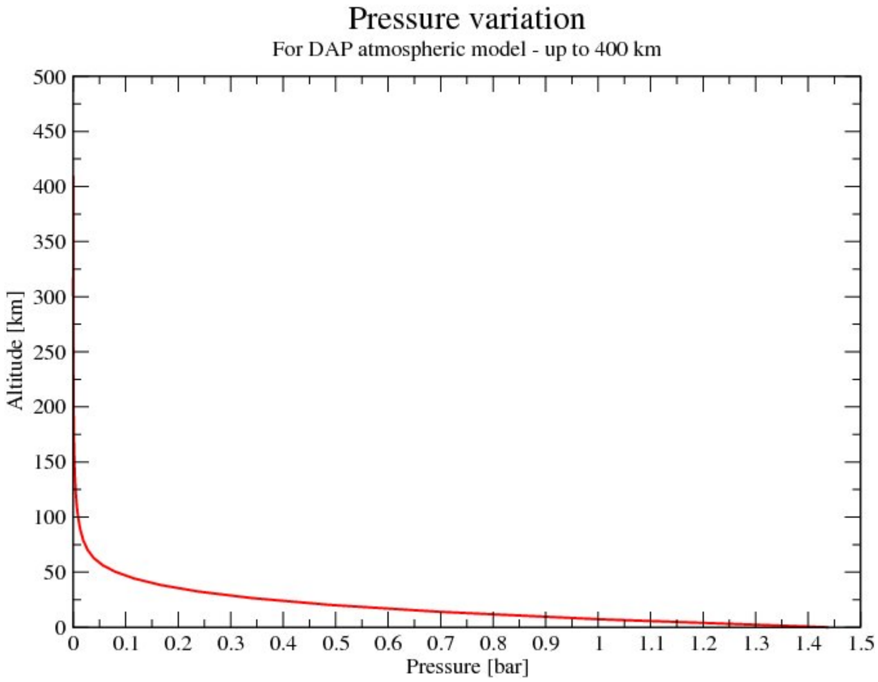

Figure 5.6: Pressure profile in Titan's atmosphere up to 400 km. The profile was obtained interpolating data retrieved by Flasar et al. [2005].

5.4.3 Aerosols' Refractive index

Now that the thermal profile of the atmosphere has been chosen, we have to define the aerosols characteristic parameters. The first thing to do is to choose the composition of the aerosols and therefore, their refractive index.

We used the complex refractive indices published by Ramirez et al. [2002]. They presented a set of values based on tholins' laboratory measurements which are the laboratory version of Titan's aerosols. The tholins mixing ratio is N_2:CH_4 (98:2). All the other possible aerosols components like hydrogen, carbon monoxide, hydrocarbons and nitriles are considered negligible. If we would like to take into account also one of the last mentioned components we should get a different refractive index with an appropriate extinction coefficient (imaginary part) for the new mixture. So far the Ramirez et al. [2002] is the most recent and up to date dataset. A more detailed description of the refractive index choice can be found in Section 4.4.

5.4.4 Methane absorption

Scattering and absorption are due to the presence of gaseous molecules and aerosol particles in the air. Absorption on Titan is mainly due to gaseous molecules. They play such an important role in the radiative transfer that their absorbing effect has to be taken into account for a complete and accurate modeling. In Titan's atmosphere, among the main gaseous components, methane is the most absorbing one. While traveling through the atmosphere, the light intensity gets attenuated: the longer is the path covered by the light, the more is the energy lost due to scattering and absorption processes. Consequently, a change in the vertical profile of CH_4 could influence the absorption (polarization) and lead to a completely different result and analysis.

We calculate the effect of absorption due to gas molecules as:

$$b_{\text{mabs}} = \sigma_{\text{abs}} \frac{\#\text{molecules}}{m^2} \tag{5.17}$$

where the second term on the right side represents the number of molecules in a vertical column through the layer with a cross section of 1 m^2, while σ_{abs} represents the absorption cross section $[\frac{m^2}{\#\text{molecules}}]$. The molecules absorption optical thickness b_{mabs} is dimensionless.

We determine the number of molecules present in each layer from the ratio of the difference in pressure between two consecutive layers and the product of the gravitational constant times the molecular mass of the air:

$$N_i = \frac{p_1 - p_2}{\text{molecular mass} \cdot \text{gravitational constant}} \tag{5.18}$$

where N_i represents the number of molecule in a layer $[\frac{\#\text{molecules}}{m^2}]$, while p_1 and p_2 represent the pressure values of two consecutive layers. Taking the difference between the pressure values of two consecutive layers from the bottom to the top of the atmosphere (Eq.5.18) is equivalent of taking into account the height variation dz in Eq. 5.19.

Since the molecular mass shown in Eq.5.18 varies with the altitude according to the vertical profile of the methane mole fraction, a detailed description of the atmospheric components vertical profiles is necessary. Niemann et al. [2005] analyzed the results obtained by the Gas Chromatograph Mass Spectrometer (GCSM) on board the Huygens probe. The GCMS instrument was designed to study the abundances of constituents of Titan's atmosphere and, so far, are the most updated values for the methane profile. As an example, Fig. 5.7 presents the species detected by the GCMS on the surface of Titan once the probe landed.

As we can see from Fig. 5.7, CH_4 and N_2 are the most common species not only at the surface level but in the whole atmosphere spectrum, all the others are compounds generated by the photolysis process in the upper atmosphere (see Section 2.2.2). The only noble gas detected is ^{40}Ar due to outgassing from the interior (see Section 2.1). The GCMS measured methane by monitoring the mass peak at m/z=16 (i.e. the molecular mass of CH_4). Comparing the counting rates at m/z=16 with those at m/z=28 (i.e. the molecular mass of N_2), the GCMS was able to detect the methane mole fraction X_{CH_4} shown in Fig. 5.8. Despite the difficulties created by the lack of knowledge of many factors, errors are not yet fully evaluated. Only the systematic errors due to calibration are estimated to be less than 5% [Niemann et al., 2005].

Figure 5.8 shows that the methane mole fraction X_{CH_4} is constant in the stratosphere with a value of 1.41×10^{-2}. This value has been confirmed also by the CIRS instrument mounted on the Cassini orbiter [Flasar et al., 2005]. Around 32 km the mole fraction increases gradually till 8 km where it reaches again a constant value of 4.92×10^{-2}. Having a constant mole fraction beneath 8 km means that methane is saturated and reached its condensation limit, therefore some haze could appear also at this altitude [Niemann et al., 2005]. Using a spline interpolation, we retrieved the distribution of methane mole fraction at the interesting altitudes. The interpolated values are shown in Fig. 5.9. Since the mole fraction represents the percentage of a

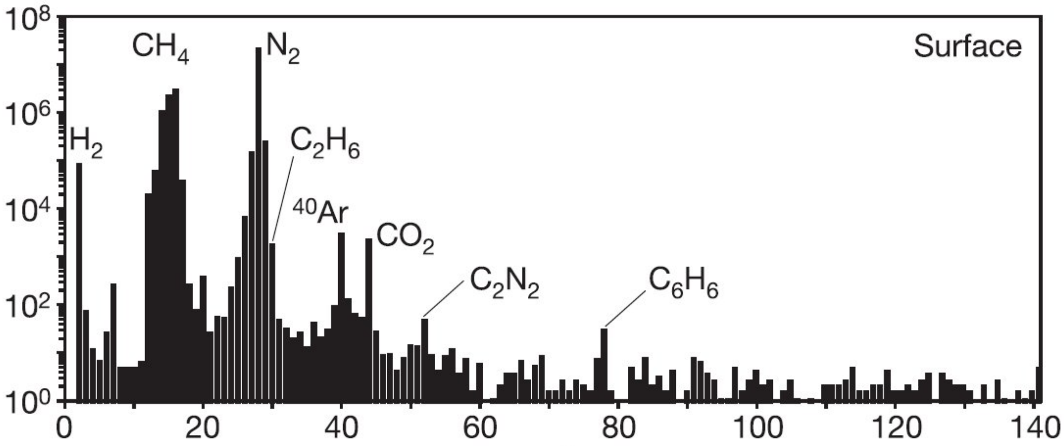

Figure 5.7: A surface mass spectrum from the Gas Chromatograph Mass Spectrometer (GCSM) adapted from Niemann et al. [2005]. It gives and idea about the atmospheric components at the Huygens landing site. Methane and Nitrogen are the most aboundant ones. There is no trace of noble gases. From the GCSM retrieval it is possible to obtaine the methane vertical profile.

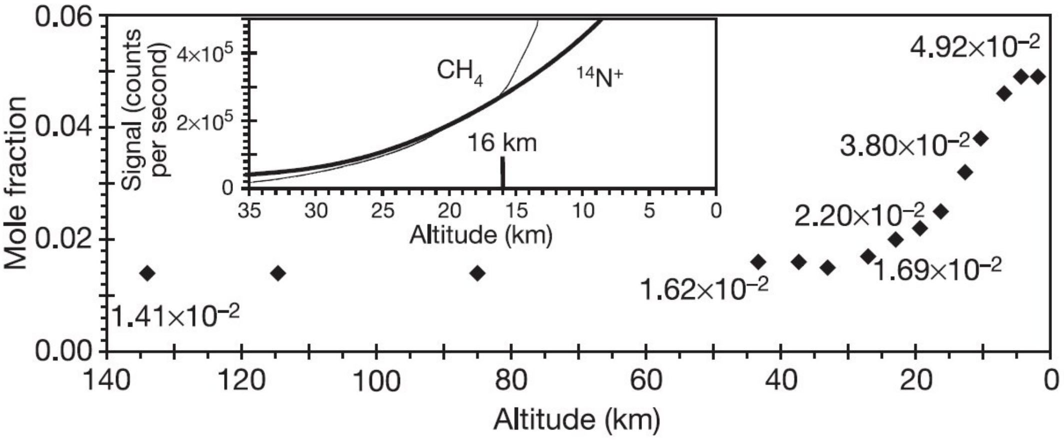

Figure 5.8: Methane mole fraction from the Gas Chromatograph Mass Spectrometer (GCSM) adapted from Niemann et al. [2005].

certain component at a specific altitude with respect to the general composition of the atmosphere, the sum of the different mole fraction has to be equal to 1. Therefore we are able to obtain also the nitrogen mole fraction profile directly from the methane values. The other components are neglected because their retrieved values are several orders of difference smaller.

Going back to how-to calculate the molecular absorption optical thickness in Eq.5.17, it is necessary to describe the meaning of other term on the right side of the equation, σ_{abs}. The absorption cross section σ_{abs} indicates a representative absorbing surface within an air column $[\frac{m^2}{\#\text{molecules}}]$. In other words, it is the section of a representative column of air indicating how much of this area (surface) is absorbing per molecules.

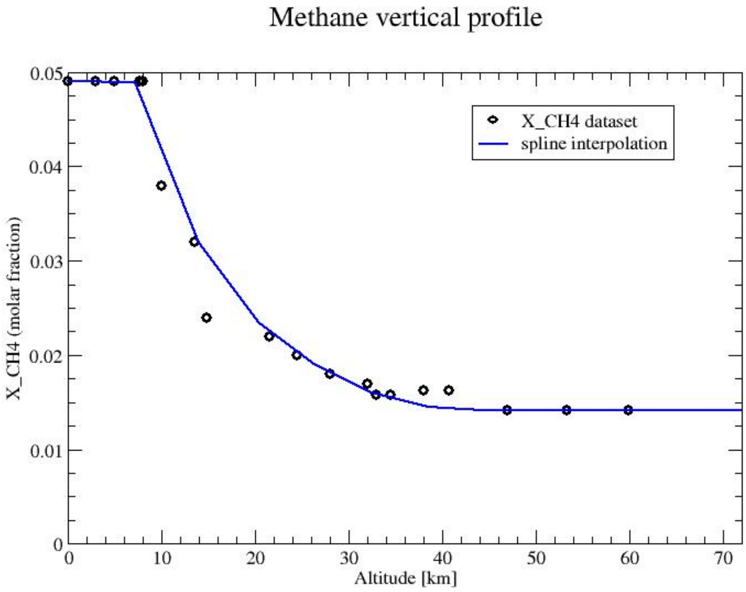

Figure 5.9: The distribution of methane mole fraction from the Gas Chromatograph Mass Spectrometer (GCSM) was interpolated using a spline function. The interpolated values are the ones used by the DAP.

Sometimes there is confusion between the term absorption cross section and the term absorption coefficient, but, looking at the dimensions, they represent the same value. The absorption coefficients for the visible wavelength range have been calculated by Karkoschka [1998] through observations of Titan from the European Southern Observatory situated in Chile. The values provided by Karkoschka [1998] have units of 1/km-amagat. In order to obtain a dimensionless optical thickness $b_m abs$ of the molecular methane, we need to convert the molecular column density of CH_4 measured in molecules over square meter into km-amagat.

The amagat of a gas is the ratio of the actual number of molecules per unit volume at standard temperature and pressure (STP) to Loschmidt's number. The thickness of an equivalent atmospheric column at standard temperature and pressure is referred as cm-amagat or km-amagat:

$$Z = \frac{1}{N_0} \int N_i(z) \cdot dz \tag{5.19}$$

The km-amagat it's just a pure indication on how the coefficient has been calculated. Dimensionally it represents an altitude, a thickness, practically it says which is the 'altitude resolution' this number of molecules has been found at. For example, if for a specific layer the optical thickness is 0.544 km-amagat, it means that its thickness would shrink to 0.544 km if the whole layer of methane under consideration would be cooled down to the STP. The Loschmidt's number we used in Eq. 5.19 is $N_0 = 2.54743 \times 10^{25}\, 1/m^3$ and it has been calculated at a STP of 288 K and 1013.25 hPa. N_i indicates the number density, dz indicates the vertical coordinates of the equivalent atmospheric column. Their product gives the atmospheric column density and it's basically what has to be converted from m^{-2} to km-amagat. Using some basic physics relations and taking care of the dimensions of the factors, we obtain the following conversion:

$$\begin{aligned} N_i \quad &\rightarrow \quad \left[\frac{\#molecules}{m^2}\right] \\ \frac{N_i}{Av} \quad &\rightarrow \quad \left[\frac{moles}{m^2}\right] \\ X_{\mathrm{CH_4}}\frac{N_i}{Av} \quad &\rightarrow \quad [moles_{\mathrm{CH_4}}] \\ X_{\mathrm{CH_4}}\frac{N_i}{Av}\cdot Av &\equiv X_{\mathrm{CH_4}}N_i \\ \rho = X_{\mathrm{CH_4}}N_i \quad &\rightarrow \quad \left[\frac{\#molecules_{\mathrm{CH_4}}}{m^2}\right] \\ Z = \frac{\rho}{Loschmidt} \quad &\rightarrow \quad [km - amagat] \end{aligned} \tag{5.20}$$

In these formulas Av stands for Avogadro's number and $X_{\mathrm{CH_4}}$ stands for methane mole fraction. The density of the absorber or, more appropriately, the column density of methane ρ is nothing else that the number of methane molecules present in the atmospheric column and it is given by the product of the methane mole fraction times the total number of molecules in each layer of the column. Once we obtained the column density, we had to divide it by the Loschmidt number giving as result the km-amagat coefficient as shown in Eq. 5.20.

To check the goodness of both the interpolation and the calculated absorption coefficients, we successfully compared the absorption depth in the total radiance curve with the absorption depth in the Karkoschka [1998] plot of the Full-Disk albedo of Titan. Karkoschka [1998] did some observation of Titan from the European Southern Observatory in Chile. The full disk albedo data have a resolution of 1nm. In order to compare the results, the same observing conditions have to be replicated. To observe Titan from Earth, the Sun and the Earth and Titan (Saturn) have to be aligned. For the DAP program it gets translated in having our instrument looking at Titan at the same angular position of the Sun. Choosing four different positions for the Sun and the instrument, we are able to obtain a sampled full-disk-equivalent result. The change in angle is connected to the amount of light that will reach eventually the ground.

5.4.5 Aerosol optical thickness

As described in Section 5.2, our model atmosphere consists of plane-parallel layers. In that section we introduced the concept of optical depth τ and optical thickness b. As a reminder, the optical thickness b is the distance between two locations z_1 and z_2, it is a property of an atmospheric layer, while the optical depth is the distance that it has been covered to go from the location at height "z_1" to the location at height "z_2" (the distance τ can be different than the distance b). In order to calculate the total optical thickness of a layer, we need to take into account the scattering and the absorption of both gaseous molecules and aerosol particles:

$$\begin{aligned} b(\lambda) &= b_{\mathrm{aer}}(\lambda) + b_{\mathrm{m}}(\lambda) = \\ &= \left(b_{\mathrm{sca}}(\lambda) + b_{\mathrm{abs}}(\lambda)\right)_{\mathrm{aer}} + \left(b_{\mathrm{sca}}(\lambda) + b_{\mathrm{abs}}(\lambda)\right)_{\mathrm{m}} \end{aligned} \tag{5.21}$$

where the subscript *sca* and *abs* indicate respectively the scattering and absorption components of the optical thickness for the gaseous molecules (m) and the aerosol particles (aer). Equation 5.21 represents the cumulative extinction optical thickness. It is calculated at a given wavelength by multiplying the column number density (vertical profile per layer) of the particles with their extinction cross-section[6] at the given wavelength. The aerosol optical thickness b_{aer} in Eq. 5.21 is determined by the aerosols vertical profile and by the wavelength. For our atmospheric model, we adopt the aerosols vertical profile of Tomasko et al. [2008]. From the DISR observations, Tomasko et al. [2008] derived that the wavelength dependence of the aerosol extinction optical thickness varies with altitude as shown in Fig.5.10. The solid curve indicates the wavelength dependence of the aerosol optical thickness b_{a} above an altitude of 80 km, the thick dashed curve is for an altitude between 80 km and 30 km, while the thin dashed curve is the wavelength dependence for an altitude below 30 km. The curves have

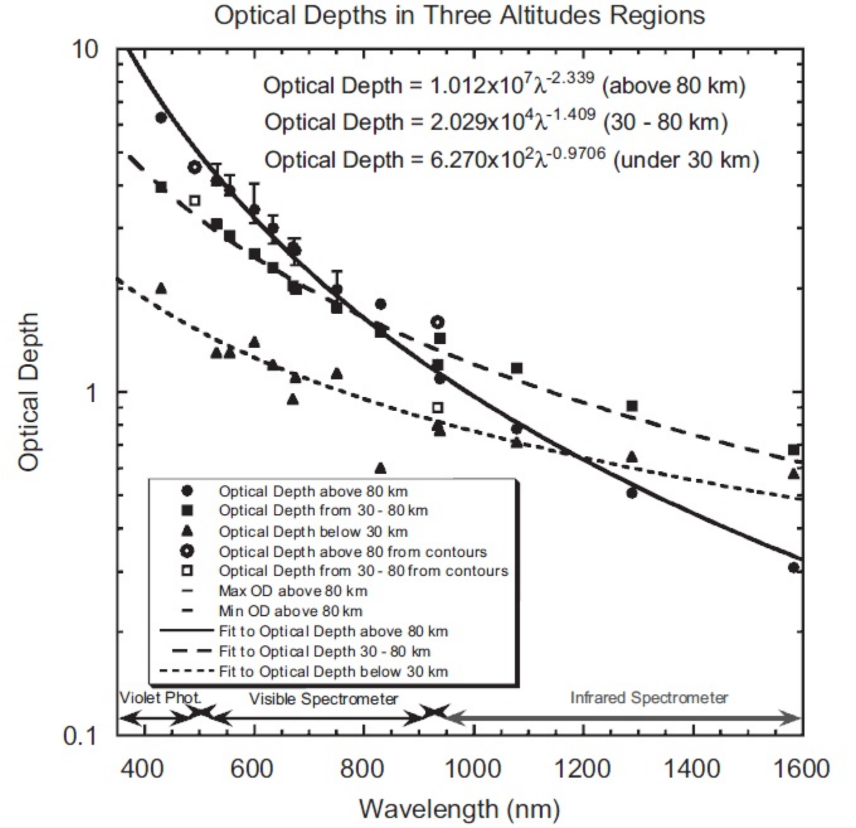

Figure 5.10: Aerosols extinction optical thickness at three different altitudes as function of the wavelength. The three altitude regions and the relative wavelength dependence are labeled in the figure. See text for discussion. The image has been adapted from Tomasko et al. [2008].

---

[6] As a reminder: $\sigma_{\mathrm{ext}} = \sigma_{\mathrm{sca}} + \sigma_{\mathrm{abs}}$. See Eq.4.3 and the explanation therein.

been obtained with power-law fits (as labeled in the top area of Fig.5.10) to match the observations of the DISR on board of the Huygens probe [Tomasko et al., 2008]. The cumulative aerosol extinction optical thickness decreases with increasing altitude above 80 km with a scale height of 65 km. Between 80 km and 30 km the altitude dependence of the cumulative optical thickness is linear as it is also below 30 km. In the lowest regions the linear dependence has a different slope as can be seen in Fig.5.11 adapted from Tomasko et al. [2008].

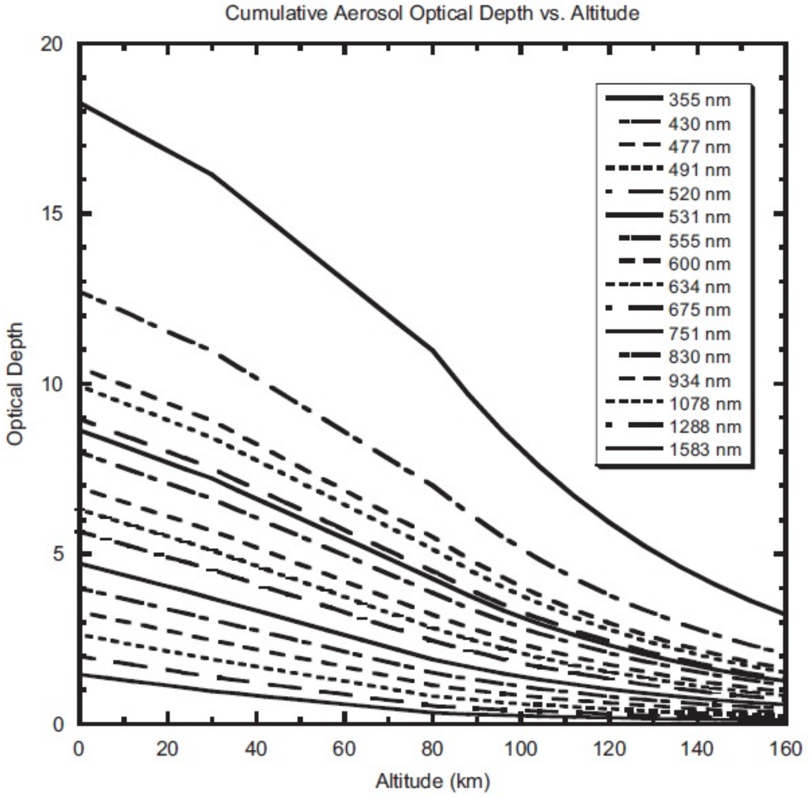

Figure 5.11: Cumulative aerosols extinction optical thickness for various wavelengths. Above 80 km the cumulative optical thickness decreases with a scale height of 65 km. Below 80 km there is a linear dependence with altitude but with two different slopes between 30 and 80km and below 30 km. See text for discussion. The image has been adapted from Tomasko et al. [2008].

We calculated the cumulative aerosol optical optical thickness of the atmospheric layers in Titan's atmosphere taking into account the wavelength dependence of Fig. 5.10 and the vertical profile of Fig. 5.11. In order to obtain the aerosols optical thickness b_{aer} for each of 34 layers in the atmosphere, we applied the power-law wavelength dependence for the three altitude regions as Tomasko et al. [2008] suggest:

$$\begin{array}{ll} 1.012 \times 10^{7} \lambda^{-2.334} & \mathrm{z} > 80 \mathrm{~km} \\ 2.029 \times 10^{4} \lambda^{-1.409} & 80 \mathrm{~km} > \mathrm{z} > 30 \mathrm{~km} \\ 6.270 \times 10^{2} \lambda^{-0.971} & \mathrm{z} < 30 \mathrm{~km} \end{array} \tag{5.22}$$

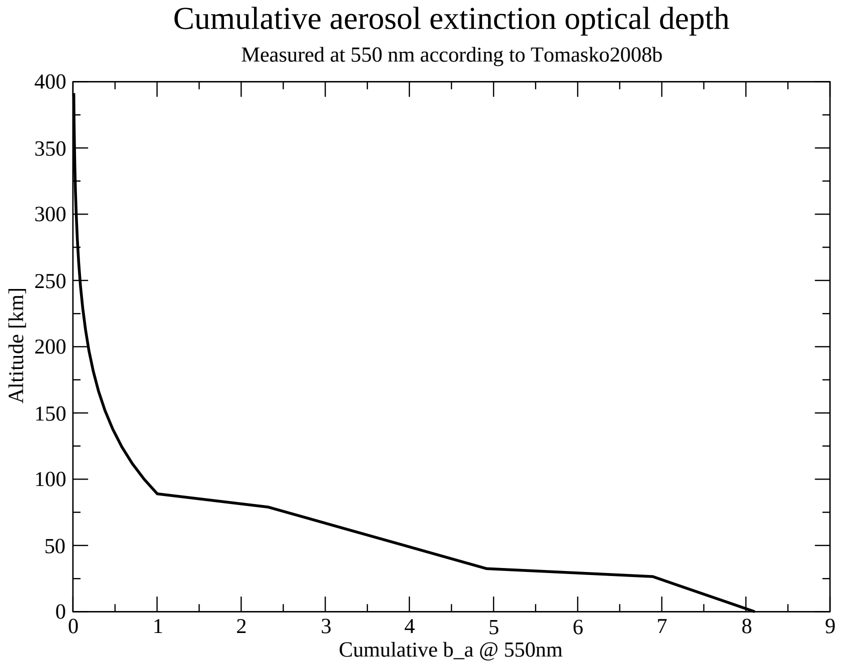

Figure 5.12: Cumulative aerosols extinction optical thickness as function of the altitude. Above 80 km the cumulative optical thickness decreases with a scale height of 65 km. Below 80 km there is a linear dependence with altitude but with two different slopes between 30 and 80km and below 30 km. See text for discussion.

with $\lambda = 0.55\mu$m. This gave us the value of the cumulative optical thickness at the bottom of each of the three regions. Taking into account the different altitude dependences (Fig. 5.11) and the spacing between the layers of our model, we calculated the aerosols optical thickness b_{aer} for each of the 34 layers. Figure 5.12 presents our interpolation of cumulative optical thickness at a wavelength of 0.55 μm. The three different altitude regions are clearly visible and comparable to what shown in Fig.5.11 (note that the vertical and horizontal axes are inverted). To test the validity of our calculations, we summed the b_{aer} of each layer to obtain the cumulative optical thickness. As presented in Fig: 5.12, at surface level we reached a cumulative aerosol optical thickness of 8.1 in complete accordance to Tomasko et al. [2008] and Fig. 5.11.

5.5 Sensitivity tests

During the simulations, we tried to simulate the single scattering properties of aggregates with $N = 2048$ but severe computational problems arose. This was because the T-matrix code used for the single scattering simulations is programmed to deal with aggregates formed by N<1000. As soon as we tried to increase the number of monomers the computation time and the memory usage grew exponentially. In order to reduce the memory problem, we had to decrease the accuracy of the calculations.

After a week we got a T-matrix result with this low-accuracy settings for the original particle with $N = 2048$ for only one wavelength. Still we had to run the code for the mirror particle for the same wavelength and then move to all the other wavelengths in the SPEX range. It could have taken several months. Therefore we decided to test only small aggregates up to $N = 256$.

Another parameter that affects the computational time is the Gaussian points: the higher it is, the longer is the computational time required by the DAP. In single scattering, the number of Gaussian points determines the accuracy with which the single scattering results are taken into account before being processed to map the multiple scattering events. If the number of Gaussian points is too low, the single scattering curve is scarcely sampled resulting in a not representable multiple scattering phenomena. They depend on the scattering geometry, thus they can vary between one simulation and another. For the single scattering the ideal number was found for GP=100. Gaussian points is also used in the multiple scattering calculations; it is used for the integration over all scattering angles. The ideal situation is to have the lowest Gaussian number possible without affecting the sampling rate, especially for the multiple scattering simulations. For the latter, tests have been done for GP=6,10,20,40,60. Already between GP=10 and GP=20 the results were completely identical proving that the sampling is correct. The number of Gaussian points that will be used for most of the simulation is GP=20, if not mentioned otherwise.

At this point the simulations can start.

6 Spectropolarimetry on Titan - Radiative transfer results

In this section we present the numerical simulation of the radiance I and the degree of linear polarization P of sunlight that has been scattered inside the atmosphere of Titan. The first simulation refers to what we call 'the atmospheric reference model'. We start describing the main characteristics of this atmospheric model and its total radiance and degree of polarization scattering functions. Then we change one model parameter per time to see what affects the scattering inside the atmosphere of Titan and what we can derive from these changes. The program used to simulate the radiative transfer is the Doubling-Adding program (DAP).

6.1 Reference atmospheric model

We calculate the molecular scattering optical thickness b_{msca} of each layer as described in Stam et al. [1999], using the values of Flasar et al. [2005] for the ambient pressure and temperature at the bottom and top of each layer. Across SPEX' wavelength region, the main gaseous absorption bands are due to methane. We calculate the molecular absorption optical thickness b_{mabs} of each layer as described in Stam et al. [1999], using the methane mixing ratio profile from Niemann et al. [2005] and the methane absorption coefficients from Karkoschka [1998]. We use the same type of aerosol throughout the atmosphere. We assume that the aerosol optical thickness b_{a} varies with altitude as described by Tomasko et al. [2008], with the cumulative atmospheric b_{a} at $\lambda = 550$ nm, equal to 8.10 and shown in Fig. 5.12. The actual wavelength dependence of b_{a}, as well as $\tilde{\omega}_{\mathrm{a}}$ and $\mathbf{F}_{\mathrm{a}}$ of the aerosol particles depends on the particles' microphysical properties (size, shape, composition). As described in Section 4.4.3, we assume aggregate, fractal-type particles that consist of clusters of spherical monomers. Our reference aerosol particle has been formed with Diffusion Limited Aggregation (DLA), is a compact particle with 256 spherical monomers each with a radius of 0.05μm [Skorov et al., 2008]. We assume that the incoming solar flux equals π, i.e. $F_0 = 1$ in Eq. 5.15. To describe the reflection of sunlight by Titan's surface, we use a wavelength independent surface albedo equal to 0.04, which is representative for Titan's dark terrain in accordance to McCord et al. [2006].

Figure 6.1 and 6.2 show, respectively, I and P as functions of the wavelength λ from 0.3 to 0.9 μm (SPEX' spectral range is somewhat shorter, namely from 0.4 to 0.8 μm). The solar zenith angle θ_0 is 0° (the sun is thus in the zenith), and the viewing angle θ ranges from 0° (looking towards the zenith) to 60°. For $\theta_0 = 0°$, the azimuthal angle $\phi - \phi_0$ is undefined.

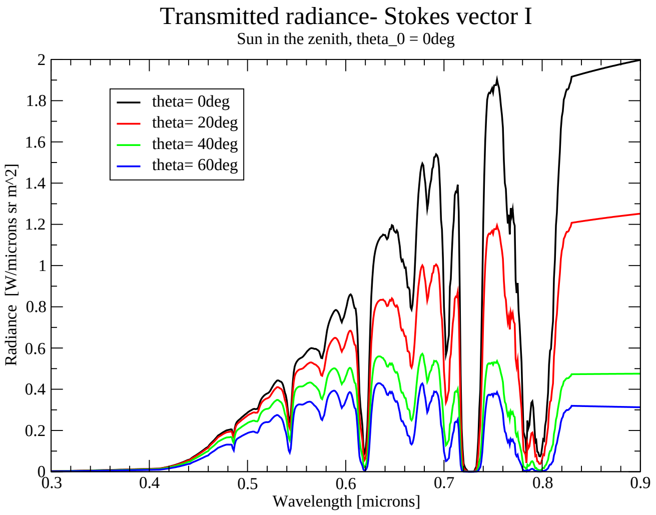

Figure 6.1: Numerically calculated radiance spectra of sunlight that is scattered in and transmitted through Titan's atmosphere. The solar zenith angle $\theta_0 = 0°$, and the viewing zenith angles are: 0° (black), 20° (red), 40° (green), and 60° (blue). The aerosol profile is shown in Fig. 5.12 and the aerosol particles are of the DLA-type.

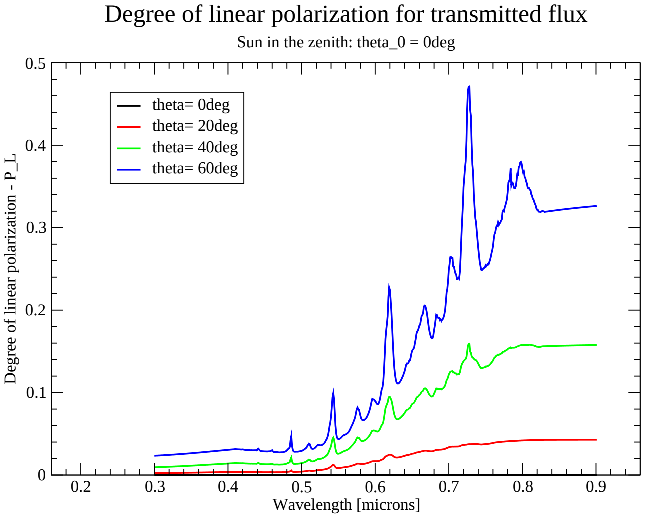

Figure 6.2: Numerically calculated degree of polarization for the same atmospheric model as described in Fig.6.1. Note that for $\theta = 0°$, P equals zero at all wavelengths.

As can be seen in Fig. 6.1, the scattered radiance spectra show strong absorption lines that are due to the methane in the atmosphere. With increasing λ, the continuum radiance of each spectrum increases steadily because of the decrease of the atmospheric optical thickness (gas + aerosol). The continuum radiance is highest for $\theta = 0°$ and decreases with increasing θ, because of the forward scattering behaviour of the phase function of the aerosol particles (see Fig. 4.9), and because of the increase of the effective atmospheric optical thickness with increasing θ (the sun is in the zenith). Increasing the instrument zenith angle θ, the sunlight scattered inside the atmosphere has to cover a longer distance than when the instrument is aligned just underneath the light source (both sun and instrument in the zenith). When the path is longer, the sunlight is more affected by scattering and absorption giving as result a lower amount of transmitted radiance.

The scattered polarization spectra (Fig. 6.2) can, like the radiance spectra, be thought of as to consist of a continuum with super-imposed spectral features that are due to absorption of light by methane. The continuum degree of polarization is small at the smallest wavelengths, because at those wavelengths, the optical thickness b of the atmosphere is relatively large. The multiple scattering of light in an optically thick atmosphere will usually decrease P. With increasing λ, b decreases, the multiple scattering decreases, and the continuum P increases. The continuum P will also depend on the single scattering P_S of the gas molecules and aerosol particles in the atmosphere. For example, at the longest wavelengths, P will be mostly determined by low order scattering by aerosol particles. The values of the continuum P at $\lambda = 0.9$ μm for each value of θ compare very well with those in Fig. 4.9 for the corresponding single scattering values of Θ (i.e. $\theta_0 = 0°$ and $\theta = 60°$ correspond to $\Theta = 60°$).

From $\lambda \approx 0.4$ to 0.5 μm, the continuum P is low for all values of θ. This is called a 'neutral' point of polarization, and it is due to the combination of the polarization signatures of single and second or higher order scattered light.

In the methane absorption bands instead, P generally increases with increasing absorption band strength. This is explained by a decrease of multiple scattering with increasing absorption, and hence an increase of P. However, to fully explain the changing shape of P across gaseous absorption bands, one also has to take into account the single scattering properties of the atmospheric molecules and aerosol particles. In the different parts of the absorption band, the transmitted light has been scattered in different regions of the atmosphere, and will carry the polarization signature of the mixture of aerosol particles and gases in those regions.

In the following sections we will change one atmospheric variable per time and compare the resulting scattering functions to those of the reference model.

6.2 Aerosol vertical profile

With respect to the reference model, here we keep all the parameters constant except the aerosols vertical profile. Here we discuss the changes due to doubling the aerosol optical thickness b_a obtained from Tomasko et al. [2008].

Comparing the radiance spectra in Fig.6.3 and Fig.6.1, we see that doubling the aerosol optical thickness b_a leaves the general shape of the radiance spectra untouched, while it decreases the total radiance for each illumination configuration and for the whole wavelength range. It has to be noticed that for $\theta = 40°, 60°$ and $\lambda > 0.72\mu$m, the continuum I is slightly increased with respect to the reference model. It looks like as if increasing b_a from 8.1 to 16.2 (at $\lambda = 0.55\mu$m) makes the sky brightness more

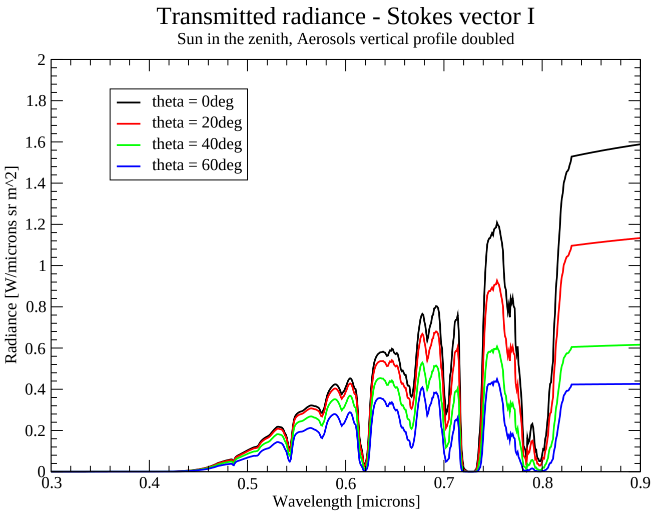

Figure 6.3: Numerically calculated radiance spectra of sunlight that is scattered in and transmitted through Titan's atmosphere. With respect to Fig.6.1, the aerosol optical thickness has been doubled. All the other parameters are the same as for Fig.6.1.

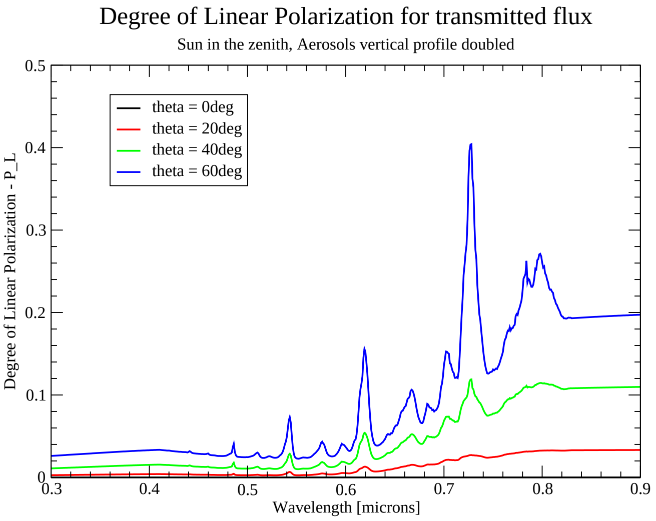

Figure 6.4: Numerically calculated degree of polarization for the same atmospheric model as described in Fig.6.3.

homogeneous.

The polarization spectra in Fig. 6.4 are very similar in shape to those in Fig. 6.2. For $\theta = 0°$ the polarization is zero for the whole wavelength range as for the reference model. The only difference is at the longer wavelengths where doubling b_{a} has led to a significant decrease of the continuum P because of an increase of multiple scattering.

At the shorter wavelengths, the amount of multiple scattering hasn't changed much and P seems rather insensitive to the doubling of b_{a} from 8.1 to 16.2 (at $\lambda = 0.55\ \mu$m), probably because scattering of light by the gas molecules is the most important process at those wavelengths. Interestingly, the neutral points of polarization seem to have shifted towards longer wavelengths with the increase of b_{a}: for $\lambda \approx 0.4$ to $0.6\ \mu$m the polarization is low especially for $\theta = 20°$.

6.3 Surface albedo

We modify the surface albedo from 0.04, which is representative for Titan's dark terrain, to 0.2 which is representative for bright terrain still according McCord et al. [2006]. These surface albedo values are wavelength independent.

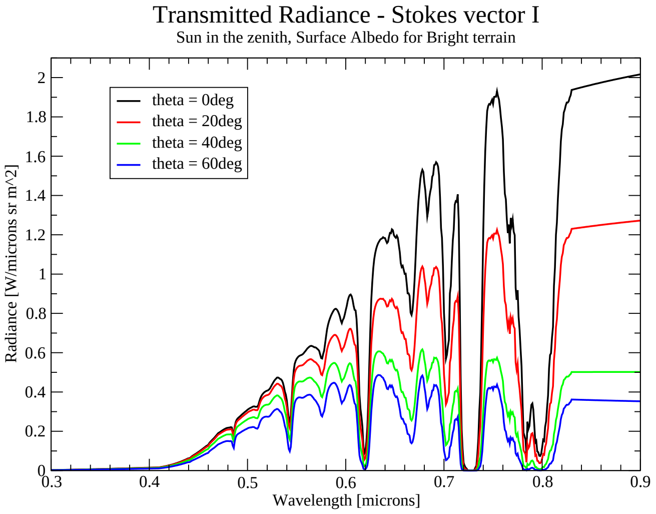

Figure 6.5: The same as in Fig.6.1, except that the surface albedo value changed from 0.04 (dark terrain) to 0.2 which is representative of bright terrain. All the other parameters are the same as for Fig.6.1.

Comparing the radiance in Fig.6.5 to Fig.6.1, we can see that a change from dark reflecting surface to bright reflecting surface, does not change the shape of I, but slightly modifies its absolute value especially at higher θ. The change is less than 10% as shown in Fig.6.7 for P. The same is valid for the degree of polarization in Fig.6.6 if compared to the P spectra in Fig.6.2. The difference in both I and P spectra is less than 10% when we change from a dark terrain to a bright terrain surface albedo.

6.4 Sun zenith angle

For the reference model, the Sun is positioned along the local vertical, the sun zenith angle is in fact $\theta_0 = 0°$. Here we move the Sun off zenith, to an angle of 30° and 60° with respect to the local vertical. As soon as the sun is off zenith, the azimuthal

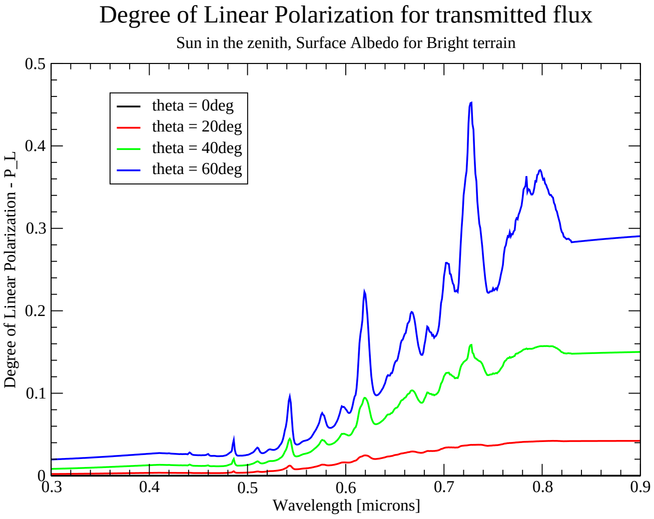

Figure 6.6: Numerically calculated degree of polarization for the same atmospheric model as described in Fig.6.5.

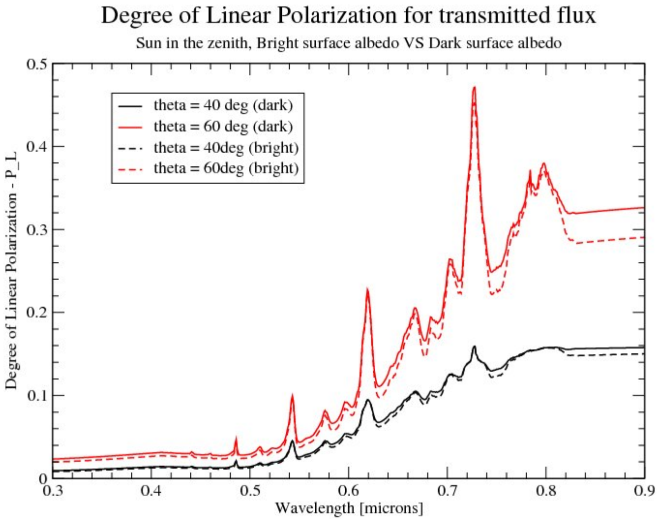

Figure 6.7: Difference in degree of polarization P between simulations with bright terrain (Fig.6.6) and dark terrain (Fig.6.2) values of surface albedo for $\theta = 40°$ and $60°$.

angle has to be defined. The results presented hereby are for $\phi - \phi_0 = 0°$, which means that SPEX is looking in the direction toward the Sun.

In Fig.6.8 the viewing angles $\theta = 20°$ and $40°$ are close to looking into the direction of the sun, which results in a large continuum radiance at the longest wavelengths, where the forward scattering by the aerosol particles is important. The size of the aerosols is comparable to the longest wavelengths and results in a stronger scattering effect than the one produced by the smaller gas molecules. Moreover, at the longer wavelengths, the aerosols scattering optical thickness b_{asca} is larger that the molecular

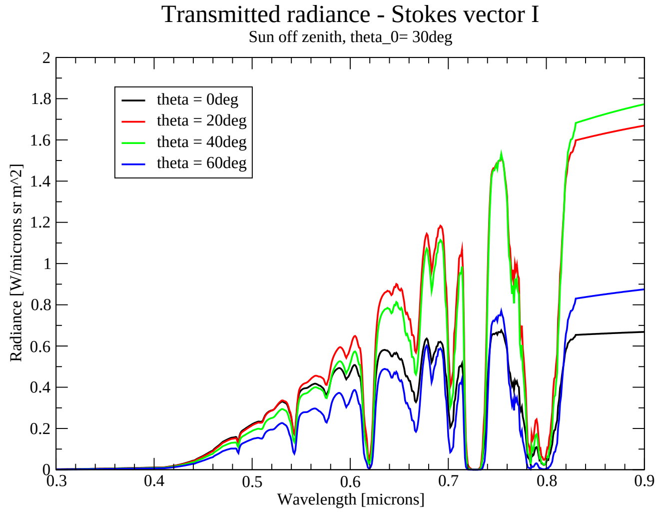

Figure 6.8: The same as in Fig.6.1, except that the Sun is now off zenith: the sun zenith angle is $\theta_0 = 30°$. The azimuth angle is $\phi - \phi_0 = 0°$ which means that the instrument is looking in the direction of the Sun. All the other parameters are the same as for Fig.6.1.

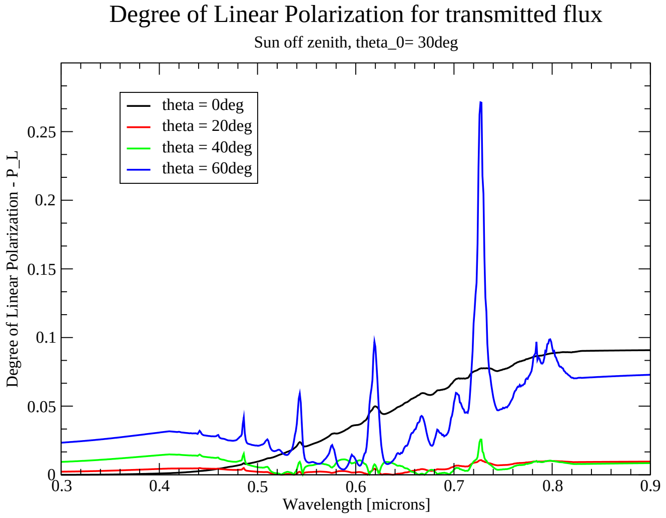

Figure 6.9: Numerically calculated degree of polarization for the same atmospheric model as described in Fig.6.8.

scattering optical thickness b_{msca} as shown in Fig.6.10. At the longest wavelengths and for $\theta = 60°$, the scattered continuum radiance is larger than for $\theta = 0°$, which means that in the red, the horizon is brighter than the zenith sky. At the shortest wavelengths, where scattering by gas molecules is most important, the horizon ($\theta = 60°$) is darker

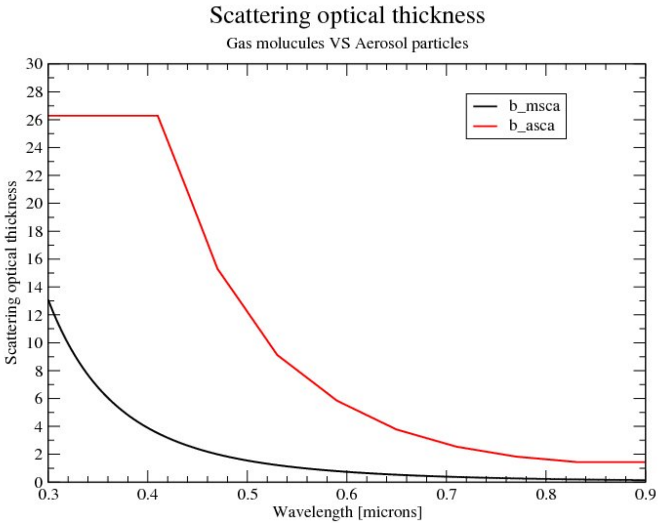

Figure 6.10: Scattering optical thickness for the simulation presented in Fig.6.8 and 6.9. The aerosol particles scattering (b_{asca}) is higher than the gaseous molecules scattering (b_{bsca}). The horizontal part of the b_{asca} curve is due to the fact that the aerosol's scattering is modeled starting from $\lambda = 0.410\mu$m.

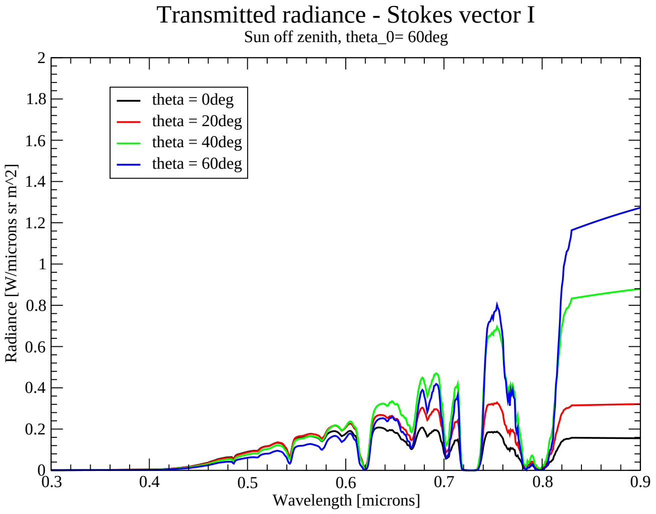

Figure 6.11: The same as in Fig. 6.8, but for $\theta_0 = 60°$.

than the zenith sky ($\theta = 0°$). Similarly as in Fig.6.3, an increase in solar zenith angle θ_0 makes the sky brightness more homogeneous. Moving the Sun closer to the horizon, $\theta_0 = 60°$, gives as result in the total radiance spectra of Fig.6.11. This time the viewing angle $\theta = 60°$ is looking straight into the direction of the Sun. At the longest wavelengths, the forward scattering by aerosols makes this direction of the sky very bright (note that the spectra only include the scattered light), while the zenith sky ($\theta = 0°$) is darkest. At the shortest wavelengths, the direction towards the sun is

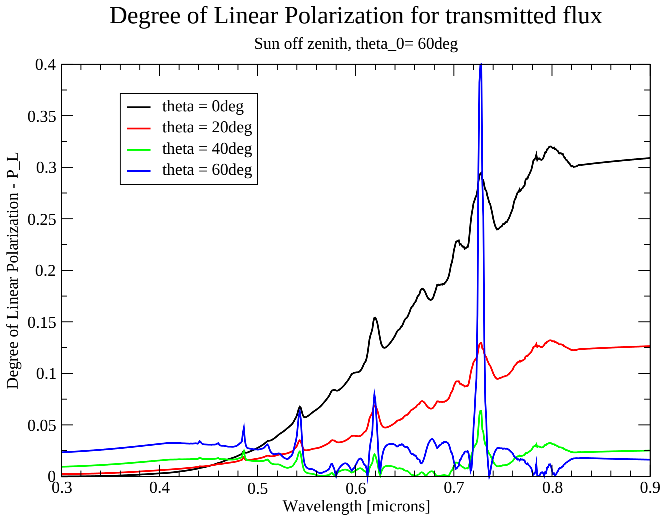

Figure 6.12: Numerically calculated degree of polarization for the same atmospheric model as described in Fig.6.11.

darkest. The absolute value of I is lower due to the longer path the scattered light has to cover inside the atmosphere to reach the instrument.

In Fig.6.9, the continuum P for $\theta_0 = 30^\circ$ looks very different from that when $\theta_0 = 0^\circ$ (Fig.6.2). In particular, the viewing directions $\theta = 20^\circ$ and 40°, which are closest (10° [1]) to looking directly into the sun yield very low degrees of polarization ($< 2\%$), because this is mostly forward scattered light which has a low degree of polarization (see Fig. 4.9 and 4.11 for $\Theta \leq 40^\circ$). It is important to notice the presence of neutral points for both $\theta = 20^\circ$ and 40° between $\lambda = 0.5$ and 0.7μm. The curves for $\theta = 0^\circ$ and 60° pertain to different single scattering angles (i.e. $\Theta = 30^\circ$ and $\Theta = 90^\circ$), and therefore their shapes are quite different. The curve for $\theta = 60^\circ$ shows a higher degree of polarization at longer wavelengths because of the stronger aerosols scattering in this wavelength region and because the single scattering angle is $\Theta = 90^\circ$. At this angle the spherical monomers on the outer layer of the particle, which can be considered to be Rayleigh scatterers, produce the highest scattering possible that influences strongly the scattering of the whole aerosol. The difference in shape between $\theta = 0^\circ$ and 60° is also because of the interplay between the degree of polarization of singly scattered light at these (single scattering) angles and the ratio of single to multiple scattering. The latter depends strongly on the effective atmospheric optical thickness, which increases with the viewing angle (i.e. scattered light has to cover a longer path through the atmosphere). In particular, for $\theta = 60^\circ$, this results in a broad region where P is about zero (a neutral point), which is absent for $\theta = 0^\circ$. Moreover, comparing Fig.6.9 to Fig.6.2, we notice a decrease in absolute value of P in the whole wavelength range for the various illumination geometries. This is connected with the increase in solar zenith

---

[1] If the instrument zenith angle would have been $\theta = 30^\circ$, then the instrument would have been looking directly into the sun. Every time that $\theta = \theta_0$ in case of transmitted light, the sun and the instrument are aligned along the same direction.

angle (i.e. the scattered light has to cover a longer path through the atmosphere) and the consequent increase in multiple scattering which, in turn, lowers the polarization P.

For $\theta_0 = 60°$ (Fig. 6.12), neutral points appear for $\theta = 60°$, and for $\theta = 40°$, which is close towards the direction of the sun. The highest continuum P is seen for smaller viewing angles due to the longer distance between the sun and the instrument, which produces stronger scattering and absorption, and therefore, causes higher polarization. Comparing Fig.6.9 and 6.12, we can see that when the viewing angle is close towards the direction of the Sun, the degree of polarization is lower than for other geometries (i.e. $\theta = 20°$ and $40°$ in Fig.6.9 and $\theta = 40°$ and $60°$ in Fig.6.12). Neutral points appear in these conditions.

6.5 Azimuthal angle

In the previous section we have described the results for a change in Sun zenith angle to $\theta_0 = 30°$. For this off zenith solar position, we had to define the azimuth angle as $\phi - \phi_0 = 0°$ which means that SPEX is looking in the direction toward the Sun. Here we keep the sun off zenith, but change the azimuth to $\phi - \phi_0 = 180°$, which means that SPEX has the Sun in 'its back'. For $\phi - \phi_0 = 0°$, SPEX is looking at the forward scattered light, while for $\phi - \phi_0 = 180°$ it is looking at the backward scattered light.

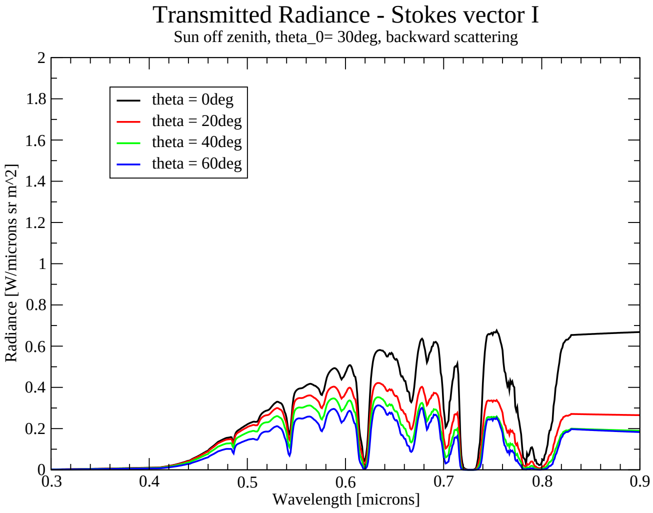

Figure 6.13: The same as in Fig.6.8, except that the instrument has now the sun in 'its back': the azimuth angle is $\phi - \phi_0 = 180°$.

The radiance spectra in Fig.6.13 have the same shape as the spectra in Fig.6.8, but the absolute value of I is almost halved for the whole wavelength range. This effect depends on the particles single scattering shown in Fig. 4.9. At higher single scattering angles the aerosol particles have a low backward scattering phase function.

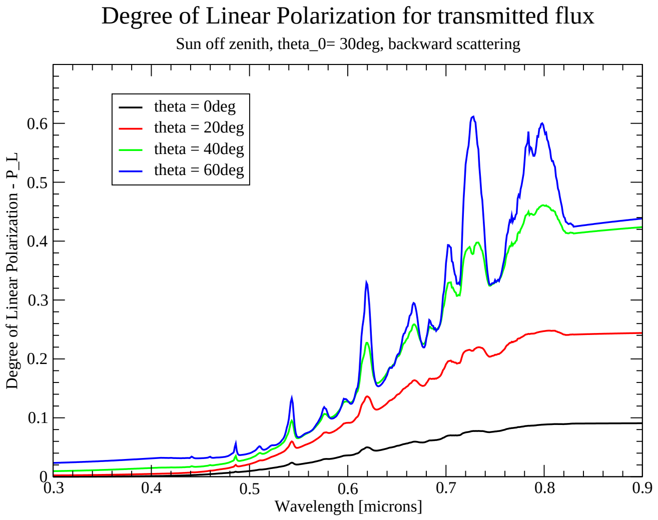

Figure 6.14: Numerically calculated degree of polarization for the same atmospheric model as described in Fig.6.13.

In the backward direction, $\phi - \phi_0 = 180°$, the effects of the single scattering of the aerosols is stronger than the multiple scattering effects.

Figure 6.14 presents a doubled degree of polarization spectra with respect to Fig.6.9. The effects of the single scattering angle Θ are more visible when the instrument is looking in the backward direction. The higher the instrument zenith angle, the closer to the monomers polarization peak at $\Theta = 90°$, as for $\theta = 60°$. Even though the multiple scattering should decrease the polarization, it looks like as if the aerosol single scattering P_S plays a stronger role than multiple scattering in backward direction. When looking away from the Sun, the neutral points for $\theta = 20°$ and $40°$ disappear. The only points where P is close to zero are for $\lambda \approx 0.4$ to 0.5μm as for Fig.6.2.

6.6 Aerosol particles

So far the atmosphere contained DLA aerosol particles with N=256 as explained in Section 6.1. We now try to see the effects in total radiance and degree of polarization spectra if we decrease the aerosol size to N=128 or if we change the aerosol structure from compact (DLA) to fluffy (BPCA).

6.6.1 Aerosol size

The continuum I decreases if we decrease the number of monomers forming an aerosol from N=256 (see Fig.6.1) to N=128 as done for Fig.6.15. This decrease is mainly due to the lower forward scattering in the single scattering phase function for a particle with N=128 with respect to N=256, which is visible in Fig. 4.10 for $\Theta \leq 30°$. Furthermore, a decrease in aerosol size produces a small change in the wavelength dependence of the aerosol optical thickness $b_a(\lambda)$. Fig.6.17 in fact, shows

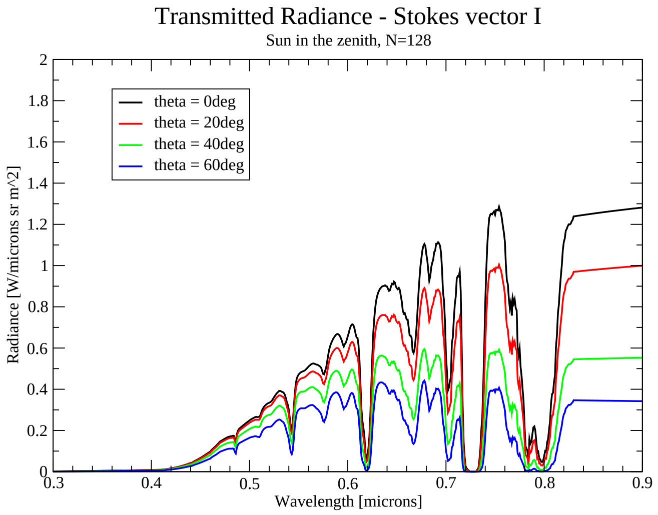

Figure 6.15: The same as in Fig.6.1, except that the number of monomers that form the aerosol particles in the atmosphere decreased from N=256 to N=128. All the other parameters are the same as in Fig. 6.1.

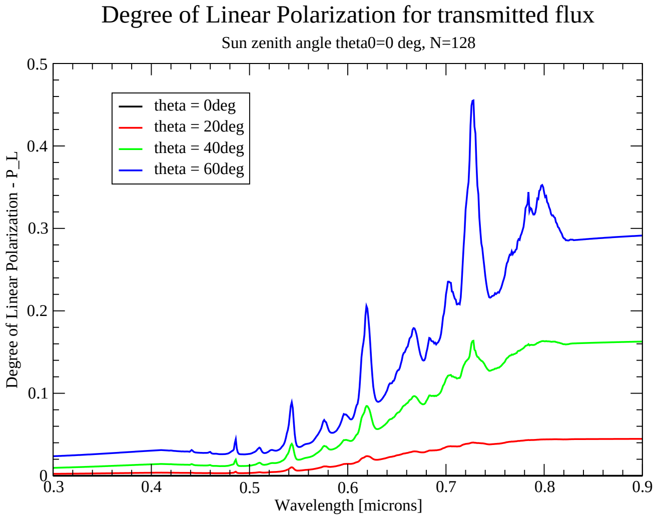

Figure 6.16: Numerically calculated degree of polarization for the same atmospheric model as described in Fig.6.15.

that if we reduce the number of monomers in each particle from N=256 to 128 or 64, the wavelength dependency of the aerosol optical thickness increases (especially for shorter λ) in order to keep the number of aerosol per layer and the atmospheric mass constant: the cumulative optical thickness of the aerosols has to stay constant. This can be verified with the formula of aerosol size (Eq.4.25): being the particle's size

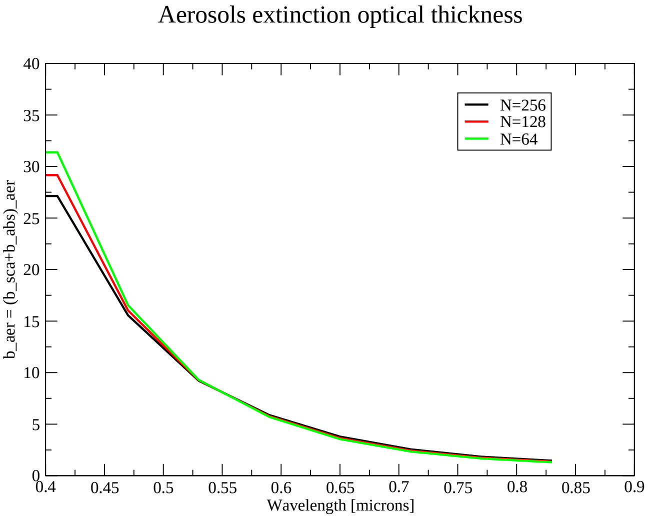

Figure 6.17: Aerosol extinction optical thickness as function of the wavelength for a decrease in particle size. Since the amount of aerosol per layer has to be constant, as soon as we decrease the particle size, the number of aerosol particles has to increase resulting in a less steep wavelength dependency of the extinction optical thickness $b_{\mathrm{a}}(\lambda)$.

smaller, each layer has to contain more aerosols to have the same cumulative optical thickness as for a bigger size (Fig.5.12). The decrease in monomer number size should increase the degree of polarization (i.e. the size of the aerosol particle is smaller). But looking at Fig. 6.16 and comparing it to Fig.6.2 there is almost no difference. It looks like as if the decrease in aerosol size is counterbalanced by the increase in multiple scattering due to an increase in aerosol optical depth $b_{\mathrm{a}}(\lambda)$ resulting in no visible change in the continuum P.

6.6.2 Aerosol inner structure: compact versus fluffy

If we keep the number of monomer constant (N=256) but change the inner structure of the aerosol from compact (DLA) to fluffy (BPCA) some changes in the scattering functions spectra are visible.

Figures 6.18 and 6.19 show the effects on the transmitted radiance and degree of polarization for when we have BPCA instead of DLA-particles in the atmosphere of Titan, with the same aerosol optical thickness at 0.55 μm. The solar zenith angle is 0° (Fig. 6.18) or 60° (Fig. 6.19) and results are shown for $\theta = 0°$ and 60° (with $\phi - \phi_0 = 0°$). As can be seen from the radiance spectra in Fig. 6.18, the DLA-particles show a stronger forward scattering behaviour than the BPCA-particles (at longer wavelengths). For the polarization, and $\theta = 60°$, we see in Fig. 6.18 that at the shorter wavelengths, there is little difference between DLA and BPCA, while at the longer wavelengths, there is a large difference (just like we would expect based on Fig. 4.16). The continuum P in Fig.6.18 is zero for $\theta = 0°$: for both the particles type looking directly into the sun produces high radiance spectra and low polarization.

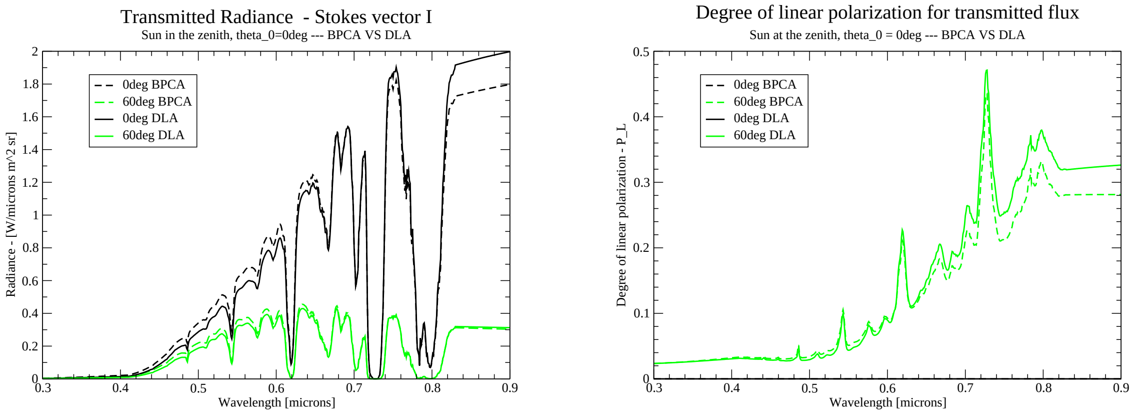

Figure 6.18: Similar to Fig. 6.1 and 6.2, except only for the viewing angles $\theta = 0°$ and 60°, and it also includes curves for BPCA-particles instead of DLA-particles (b_{a} at 0.55 μm is 8.1 for both aerosol types). Note that at $\theta = 0°$, $P = 0$ at all the wavelengths for both BPCA-particle and DLA-particle (see Fig. 6.1 and 6.2).

Moreover, the DLA-particle shows higher degree of polarization for $\theta = 60°$ at longer wavelengths because it looks 'smaller' than the BPCA type due to its compactness (see Fig.4.16 for $\lambda = 0.83\mu$m). It has to be pointed out that the DLA-particle could also look bigger because it is compact; the BPCA-particle, on the other side, can be viewed as consisting of only Rayleigh scattering particles (i.e. considering the monomer "arms" described in Section 4.4.3). With the sun at 60° (Fig. 6.19), we can again see the single scattering polarization features (Fig. 4.16) back in the multiple scattering behaviour. In this geometry, both the DLA- and the BPCA-particles give rise to neutral points at certain wavelengths, especially the DLA-particles. What permits to discern the two spectra, is the location of the neutral points. In Fig.6.20, which is a zoom-in of Fig.6.19, for a viewing zenith angle of 60°, the DLA-particle presents neutral points at $\lambda \approx 0.55$ μm and $\lambda \approx 0.57$ μm that the BPCA-particle does not show. The DLA-particles also give rise to inverted polarization in some of the methane absorption bands.

From the spectra we showed, it is clear that the spectral dependence of the degree of linear polarization of sunlight that is transmitted through Titan's atmosphere shows a stronger variation on the particle-type, than the radiance of this light. The latter does show variations, but the general shape of the spectra remains the same, while the continuum radiance is very dependent on the aerosol optical thickness and would thus not constrain particle type [Mishchenko and Travis, 1997]. Obviously, preferably, both the radiance and the polarization are measured.

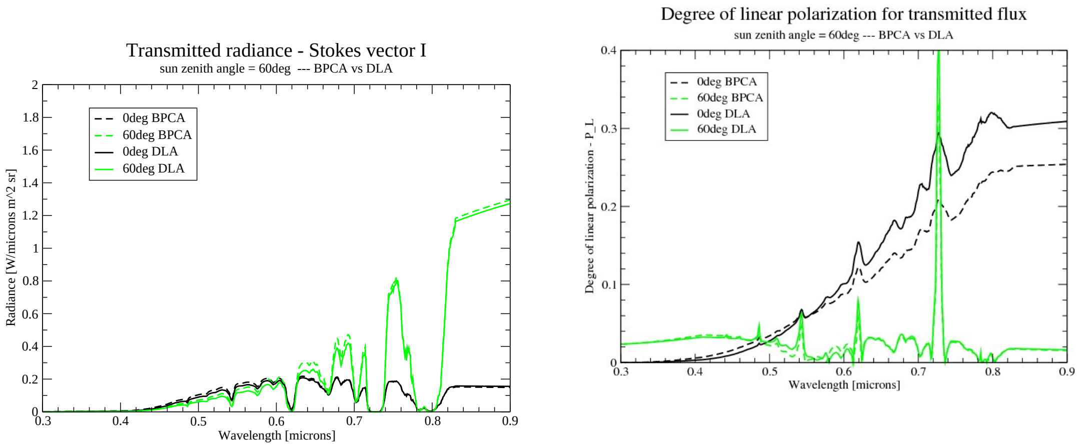

Figure 6.19: Same as for Fig.6.18, except for $\theta_0 = 60°$.

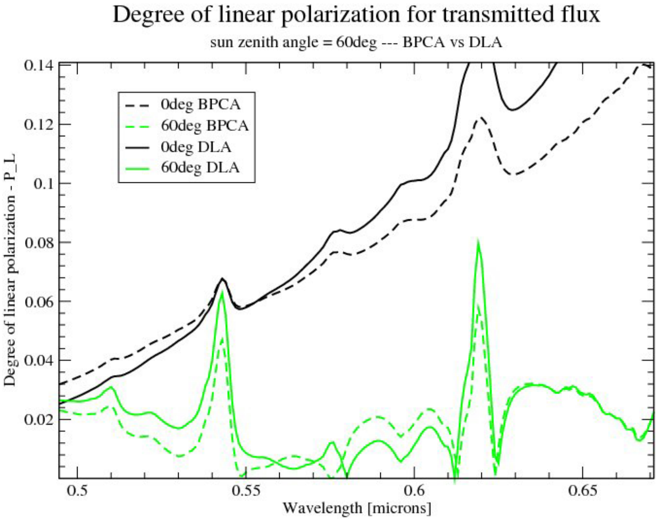

Figure 6.20: The same as the degree of polarization in Fig.6.19, but focused on the neutral points present between $\lambda \approx 0.55$ μm and $\lambda \approx 0.57$ μm for the DLA-particle.

7 SPEX - Spectropolarimeter for Planetary EXploration

In this chapter SPEX - Spectropolarimeter for Planetary EXploration will be introduced. In the first part a short description of conventional polarimetry is provided. SPEX' innovative polarimetric spectral intensity modulation concept will follow in the second section. A description of the optical design and the actual configuration of the instrument will conclude the chapter. For further information about SPEX please visit the SRON web page at: `http://www.sron.nl/spexinstrument`

7.1 The classical method of polarization measurements

The complete information on the linear polarization properties of the light is generally obtained from four independent intensity measurements. The four spectra can be formulated as:

$$\begin{aligned} s_1 &= t\left(I(\lambda) + Q(\lambda)\right), \qquad & s_2 &= t\left(I(\lambda) - Q(\lambda)\right), \\ s_3 &= t\left(I(\lambda) + U(\lambda)\right), \qquad & s_4 &= t\left(I(\lambda) - U(\lambda)\right). \end{aligned} \tag{7.1}$$

where $I(\lambda), Q(\lambda)$ and $U(\lambda)$ represent the Stokes parameters introduced in Section 3.2.1 and t is the transmission factor ideally identical for the four measurements. From the measured spectra s_i (with $i = 1, 4$) we determine the normalized parameters Q/I and U/I that are independent of t [Snik et al., 2009]. The conventional techniques used to retrieve the normalized parameters are spatial and temporal modulation:

Spatial modulation - the light is split into four beams, two oriented at 0° and 90° to detect the linear polarization along the Q direction, and two oriented at ±45° to detect the linear polarization along the U direction. Therefore four different optical paths and four detectors are needed. Different alignment and transmission of the four beams is critical and could lead to a not precise detection of the Stokes vectors.

Temporal modulation - the four measurements are obtained sequentially with a single beam by using an active component such as rotating a polarizer or a half-wave plate in front of a fixed polarizer. It requires power for the rotation and it may fail during the life of the polarimeter. Moreover since it uses sequential measurements (and not simultaneous), the observed scene might change in the mean time and random vibrations of the system could affect the outcome.

There are further drawbacks related to both classical methods: the more beams per viewing angle (i.e. four) the bigger the size of the instrument, the mechanical complexity is generally increased, time variations of the source or of the instrument's pointing could introduce extra differential effects. Last but not least, these methods are sensitive to random noise in the independent four spectra s_i especially if the measured degree of linear polarization is very low [Snik et al., 2008, 2009].

In the past decades there have been several missions that carried instruments with polarimetric capabilities such as Pioneers 10 and 11, Voyager 1 and 2 and the Galileo mission. Those polarimeters were able to detect the only intensity of the scattered light (using a combination of spatial and temporal modulation).

SPEX uses a novel approach: the linear polarization is mapped neither in the temporal, nor in the spatial but in the spectral domain. This method is called polarimetric spectral intensity modulation. Thanks to spectral modulation, SPEX can sample both the intensity and the polarization scattering phase functions of scattered light with one single measurement without using moving parts. As explained in the following section, differential effects and sensitivity to noise are therefore drastically reduced [Snik et al., 2009].

The polarimetric concept of SPEX based on birefringent crystals has been patented by Prof. Dr. C.U. Keller of the Astronomical Institute of the University of Utrecht, The Netherlands.

7.2 Spectral modulation and optical design

SPEX' spectropolarimetry works by encoding the degree and the angle of linear polarization in a sinusoidal spectral modulation of the flux spectrum. With a single measurement of the reflected sunlight we are able to determine the degree and the angle of linear polarization as function of the wavelength.

$$S_{\pm}(\lambda) = \frac{1}{2} S_0(\lambda) \left[1 \pm P(\lambda) \cos\varphi(\lambda)\right] \tag{7.2}$$

where the phase is given by

$$\varphi(\lambda) = \frac{2\pi\delta(\lambda)}{\lambda} + 2\chi(\lambda), \tag{7.3}$$

Equation 7.2 represents SPEX' output spectrum, i.e. the modulated spectrum. The amplitude variation of the signal is connected with the degree of linear polarization P while its phase variation $\varphi(\lambda)$ is connected with the angle of linear polarization χ. The ± sign depends on the orientation of the polarizer in the instrument's pre-optics and δ represents the retardance[1] (phase shift) of the multiple order retarder. With SPEX, we detect both the S_+ ('positive' modulated) and the S_- ('negative' modulate) spectrum, and it is clear that by adding these two modulated spectra, the incoming radiance spectrum S_0 (i.e. I) is obtained with the spectral resolution with which $S_{\pm}$

---

[1] The retardance δ depends strictly on wavelength and temperature, it should be indicated as $\delta(\lambda, T)$. In the text this dependency will be symbolically omitted for graphical clarity; it is treated in more details in Section 7.2.3.

are measured. Furthermore, S_0 represents the input spectrum and it corresponds to $S_0(\lambda) = I_0(\lambda)t(\lambda)$ [Snik et al., 2009]. From the degree of linear polarization P (Eq.3.9) and its orientation χ (Eq.3.10), we can derive the linear polarization Stokes parameters for describing the linear polarization Q and U (see Section 3.2.1).

The polarimetric spectral modulation, or simply spectral modulation, takes place inside the instrument thanks to a train of passive optical components (pre-optics):

- Achromatic quarter-wave retarder (Fresnel Rhomb)
- Athermal multiple-order retarder
- Polarizer (Wollaston Prism)

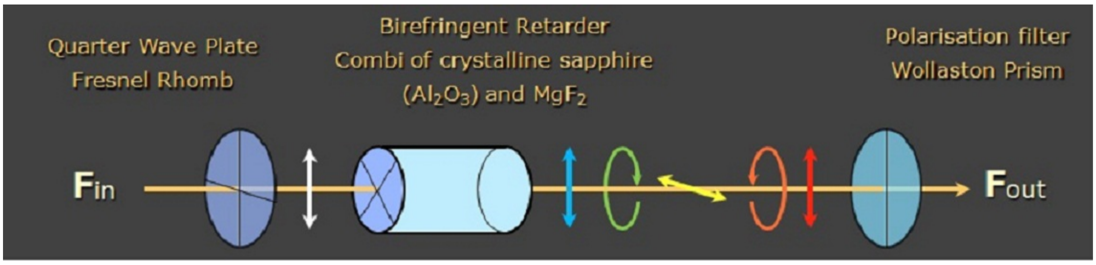

Figure 7.1: SPEX pre-optics, spectral modulator. The Fresnel Rhomb and the Wallaston prism are a retarder and a polarizers. The retarder placed between them will produce a sinusoidal modulation.
Image source: SRON presentation on the 24 Nov. 2009.

Figure 7.1 shows the sequence of retarders and polarizers used in SPEX. The vectors $\mathbf{F}_{\text{in}}$ and $\mathbf{F}_{\text{out}}$ are the input and output vectors and correspond respectively to the intensity I_0 and I inside $\mathbf{S}_0$ and $\mathbf{S}$ in Eq.7.2 [2]. Thanks to this instruments sequence and orientation, it is possible to retrieve the linear polarization[3] parameters from one single measurement, from one unique modulated spectrum.

The advantages with respect to the classical spatial and temporal modulations are:

- differential effects are eliminated - the polarization parameters are obtained from one single beam per viewing angle,
- noise is reduced - there is one single retarder and detector, P and χ are obtained through a simple curve fit of the sinusoidal spectral modulation,
- risk of failure is reduced - movable parts are not needed in this configuration.

In order to retrieve the properties on a single spectrum the original intensity spectrum needs to have features that are all broader than the modulation periodicity as determined by $\delta(\lambda, T)$ [Snik et al., 2009]. If this is not the case the curve fitting of both

---

[2] The flux indicated as F is the intensity, the energy I imagined over a surface. See Section 3.2.1.

[3] SPEX can retrieve, through a specific retrieval algorithm, only linear polarization, the circular polarization it is assumed to be zero.

the degree of linear polarization and of its angle does not accurately follow a sinusoidal shape resulting in a not precise retrieval of the polarization parameters.

With the intention to derive the formula of the modulated spectrum, it is necessary to understand how each pre-optics component works and how they act on the light wave.

7.2.1 Retarders

A **retarder** is a device that splits the light wave into two orthogonal linear polarization components and produces a phase shift between them giving as result a wave with a different polarization status. This does not mean that the wave gets polarized or is subject to a change in intensity: the change is only in the polarization form (i.e. linear to circular and viceversa)[4].

A birefringent retarder is formed by an anisotropic crystal which has different refractive indexes for different polarization directions [Snik, 2008]. If a material is anisotropic it means that the inner structure will look different if we look up in the crystal or at its side for example. Bi-refringent means that there are two directions of anisotropy each represented by its anisotropy axis (called also optical axis of the crystal). In Figure 7.2 we are looking at a section of the birefringent crystal: the two optical axes positioned at 45° with the $x-$ axis[5] are representative of the two different areas with two different indexes of refraction indicated as n_e (extraordinary) and n_o (ordinary). If $n_e > n_o$ the extraordinary axis will be the slow axis while the ordinary will be the fast axis. The velocities of the wave's components will be respectively c/n_e on the slow axis (larger index of refraction) and c/n_o on the fast axis (smaller index of refraction). The optical axes of the crystal in Fig.7.2 are parallel to the page in the e direction. The light is propagating along the z axis, orthogonal to the page toward the reader.

Let's assume now that the incident light is linearly polarized and it is decomposed into two orthogonal components as soon as it strikes the retarder's plate. The light plane wave will encounter two different areas of the crystal, the wavelength will change according to the index of refraction, so will the velocity. This change will affect the rays in a different way resulting in a phase difference at the crystal's exit in B as shown in Fig.7.3:

$$\lambda_o = \frac{\lambda}{n_o} \quad \longrightarrow \quad \varphi_{B,o} = \varphi_A + 2\pi\frac{d}{\lambda_o} \tag{7.4}$$

$$\lambda_e = \frac{\lambda}{n_e} \quad \longrightarrow \quad \varphi_{B,e} = \varphi_A + 2\pi\frac{d}{\lambda_e} \tag{7.5}$$

where d represents the crystal's thickness. The difference between the two phases is the total phase shift $\Delta\varphi_B$:

$$\Delta\varphi_B = \varphi_{B,o} - \varphi_{B,e} = 2\pi\frac{d}{\lambda}\left(n_o - n_e\right) \tag{7.6}$$

---

[4] `http://www.meadowlark.com/Products/RetardersLanding.php`

[5] This is valid for any angle the the retarder optical axis forms with the plane of incident light. For a 45° configuration the slow and fast components will have different velocity but the same amplitude. *Source*: SRON presentation on the 24 Nov. 2009.

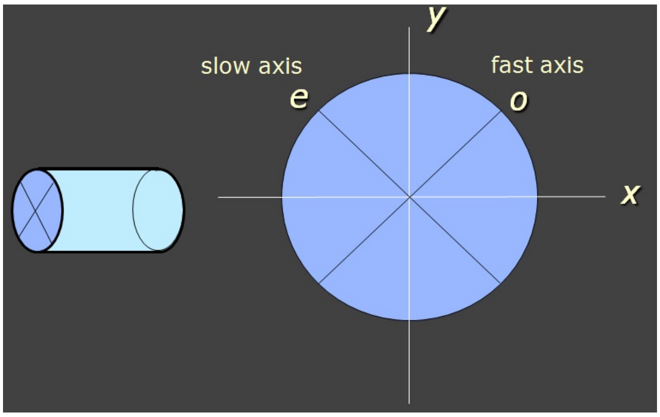

Figure 7.2: Retarder birefringence features. The extraordinary axis is parallel to the crystal optic axis, while the ordinary axis is perpendicular. The slow axis and the fast axis have two different refractive indices and therefore two different velocities. A ray of light traveling through the crystal will be subject to a phase shift due to this difference. See text for discussion.
Image source: SRON presentation on the 24 Nov. 2009.

The retardance (i.e. delay between ordinary and extraordinary ray) is given by:

$$\delta = N\lambda = d\ (n_o - n_e) \tag{7.7}$$

where N is the retardance expressed in waves. For a quarter-wave plate for example, $N = m + \frac{1}{4}$ where m is an integer. If $m = 0$ we have a *zero-order* retarder, if $m > 0$ we have a *multiple-order* retarder. Taking into consideration Eq.7.7, we can rewrite Eq.7.6 as:

$$\Delta\varphi_B = 2\pi\frac{\delta}{\lambda} \tag{7.8}$$

From Eq.7.8 it is evident that the total phase shift is directly dependent on the retardance and inversely dependent on the wavelength variation. The thicker the retarder becomes (increase of d), the faster the retardance changes as a function of the wavelength, the larger is the total phase shift [Keller, 2002].

Suppose that we have a quarter-wave *zero-order* retarder which means that $\Delta\varphi_B = \frac{\lambda}{4} \equiv 90°$. From a pragmatic point of view it means that the $e-$wave is slower, it will be retarded by 90° and will fall behind the $o-$wave: at the exit point in B the waves will recombine: the polarization form is changed from linear to circular due to the retardance. [6] In the same way a half-wave retarder will mirror the direction of the incident linear polarization around its axis because $\Delta\varphi_B = \lambda/2 \equiv 180°$.

In terms of Mueller matrix[7], the action of a generic retarder with retardance δ and with its fast axis at an angle θ with the $x-$axis, is equal to:

---

[6] If the incident light would have been circular it would have been transformed into linearly polarized.

[7] See Section 3.3 for details on the Mueller matrix formulation.

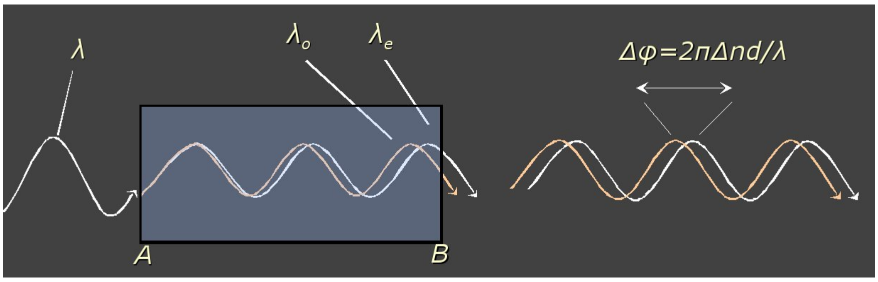

Figure 7.3: Birefringent phase shift.
Image source: SRON presentation on the 24 Nov. 2009.

$$M_{\text{ret}} = \begin{pmatrix} 1 & 0 & 0 & 0 \\ 0 & \cos^2 2\theta + \sin^2 2\theta \cos\delta & \cos 2\theta \sin 2\theta (1-\cos\delta) & -\sin 2\theta \sin\delta \\ 0 & \cos 2\theta \sin 2\theta (1-\cos\delta) & \sin^2 2\theta + \cos^2 2\theta \cos\delta & \cos 2\theta \sin\delta \\ 0 & \sin 2\theta \sin\delta & -\cos 2\theta \sin\delta & \cos\delta \end{pmatrix} \tag{7.9}$$

If the fast axis is aligned with the $x-$axis ($\theta = 0$):

$$M_{\text{ret\_hor}} = \begin{pmatrix} 1 & 0 & 0 & 0 \\ 0 & 1 & 0 & 0 \\ 0 & 0 & \cos\frac{2\pi\delta}{\lambda} & \sin\frac{2\pi\delta}{\lambda} \\ 0 & 0 & -\sin\frac{2\pi\delta}{\lambda} & \cos\frac{2\pi\delta}{\lambda} \end{pmatrix} \tag{7.10}$$

If we have a quarter-wave plate (QWP) with an horizontal fast axis ($\delta = -\frac{\lambda}{4}$):

$$M_{\text{QWP}} = \begin{pmatrix} 1 & 0 & 0 & 0 \\ 0 & 1 & 0 & 0 \\ 0 & 0 & 0 & -1 \\ 0 & 0 & 1 & 0 \end{pmatrix} \tag{7.11}$$

The same is for the half-wave plate (HWP) with an horizontal fast axis ($\delta = \frac{\lambda}{2}$):

$$M_{\text{HWP}} = \begin{pmatrix} 1 & 0 & 0 & 0 \\ 0 & 1 & 0 & 0 \\ 0 & 0 & -1 & 0 \\ 0 & 0 & 0 & -1 \end{pmatrix} \tag{7.12}$$

On the other hand if the axis of the retarder is $\theta = 45°$ as shown in Fig.7.2, the Mueller matrix becomes:

$$M_{\text{ret\_45}} = \begin{pmatrix} 1 & 0 & 0 & 0 \\ 0 & \cos\frac{2\pi\delta}{\lambda} & 0 & -\sin\frac{2\pi\delta}{\lambda} \\ 0 & 0 & 1 & 0 \\ 0 & \sin\frac{2\pi\delta}{\lambda} & 0 & \cos\frac{2\pi\delta}{\lambda} \end{pmatrix} \tag{7.13}$$

7.2.2 Polarizers

A **polarizer** is a device that allows the passage of only certain orientations of polarized light depending on the orientation of its own axis. For example, a polarizer with a vertical axis would allow only vertically polarized light, blocking (i.e. absorbing or reflecting) all the other polarization forms; if rotated by 90° it would allow only horizontally polarized light. In mathematical terms the action of a polarizer can be described by the following Mueller matrix:

$$M_\theta = \frac{1}{2}\begin{pmatrix} 1 & \cos 2\theta & \sin 2\theta & 0 \\ \cos 2\theta & \cos^2 2\theta & \sin 2\theta \cos 2\theta & 0 \\ \sin 2\theta & \sin 2\theta \cos 2\theta & \sin^2 2\theta & 0 \\ 0 & 0 & 0 & 0 \end{pmatrix} \tag{7.14}$$

where the angle θ^8 is the polarizer axis inclination with respect to the polarization direction of the incident light. If we have a linear polarizer with horizontal axis ($\theta = 0$) its action will be translated as:

$$M_{\mathrm{pol\_hor}} = \frac{1}{2}\begin{pmatrix} 1 & 1 & 0 & 0 \\ 1 & 1 & 0 & 0 \\ 0 & 0 & 0 & 0 \\ 0 & 0 & 0 & 0 \end{pmatrix} \tag{7.15}$$

Instead if the axis is oriented with a 45° angle, the Mueller matrix will be:

$$M_{\mathrm{pol\_45}} = \frac{1}{2}\begin{pmatrix} 1 & 0 & 1 & 0 \\ 0 & 0 & 0 & 0 \\ 1 & 0 & 1 & 0 \\ 0 & 0 & 0 & 0 \end{pmatrix} \tag{7.16}$$

7.2.3 Pre-optics

Fresnel Rhomb

The Fresnel Rhomb is the first component at the entrance of the modulator as shown in Fig.7.1. It is a quarter-wave retarder shaped in such a way that introduces retardance using total internal reflections [9]. Two total internal reflections can produce a retardance $\delta = \frac{\lambda}{4}$ as for the quarter-wave plate (i.e. the Rhomb's case), four total internal reflections produce a retardance $\delta = \frac{\lambda}{2}$ as for the half-wave plate.

The Fresnel Rhomb has a retardance equal to:

$$\delta(\lambda) = 2\arctan\left(-\frac{\cos\theta\sqrt{n(\lambda)\sin^2\theta - 1}}{n(\lambda)\sin^2\theta}\right) \tag{7.17}$$

The adavantage of the Fresnel Rhomb is that its retardance is not thermal dependent[10], as noticeable in Eq.7.17. The only dependence is on the wavelength through

---

[8] Not to be confused with the previously mentioned θ which represents the instrument viewing angle.

[9] The light that enters is reflected as many times as needed to generate phase shift in the reflected beam. Retarders using total internal reflection are called Fresnel Rhombs [Keller, 2002].

[10] Nonetheless temperature variations could still alter the rhomb's retardance [Snik et al., 2009]

the refractive index of the crystal. Furthermore, θ is the internal angle of incidence. The requirement to have total internal reflection is: $n(\lambda)\sin\theta > 1$ [Keller, 2002].

Athermal multiple-order retarder

Retarders are in general temperature dependent. The problem is that a variation in temperature will have an effect similar to a variation in the angle of linear polarization χ and therefore it will affect the whole modulation. It is clear that this dependence has to be reduced as much as possible.

An "athermal" retarder can be created combining two or more plates with different material and thicknesses: their thermal dependencies will cancel out (i.e. balance) while their retardances will not. The retardance variation with the temperature is defined as:

$$\gamma_i = \frac{1}{\delta_i}\frac{\mathrm{d}\delta}{\mathrm{d}T} = \frac{1}{d_i}\frac{\mathrm{d}(d_i)}{\mathrm{d}T} + \frac{1}{n_{e,i} - n_{o,i}}\frac{\mathrm{d}(n_{e,i} - n_{o,i})}{\mathrm{d}T} \tag{7.18}$$

where the two plates are indicated by $i = 1, 2$. Therefore the temperature balancing condition is described as:

$$\gamma_1\delta_1 - \gamma_2\delta_2 = 0 \tag{7.19}$$

The only requirement is that the two crystals need to have opposite birefringence (i.e. subtracting combination of retarders with $n_{e,1} > n_{o,1}$ and $n_{e,2} < n_{o,2}$), this explains the minus sign in Equation 7.19.

Thermal test have been performed by the Snik et al. [2008] yielding the combination of MgF_2-Al_2O_3 as the most appropriate one for the visible range 350 to 800 nm in which SPEX operates. According to these results the combined retarder will show an athermal behavior if the thickness ratio between the two plates is $d_1 : d_2 = 2.4$. The exact athermal behavior cannot be achieved for the whole visible range, but only for one unique wavelength. The maximum deviation of the angle of linear polarization χ is about $1.5 \cdot 10^2$ radians/°C [Snik et al., 2008, 2009].

Wollaston prism

The Wollaston prism is a beam-splitter polarizer with high extinction ratio (i.e. $\sim 10^{-4}$) [11]. It consists of two orthogonal prisms and, as the name says, it splits the light wave in two rays with different polarization state. As for the retarders, the optical axes of these prisms are the fast and slow axes, they are perpendicular to each other and orthogonal to the direction of the propagation of light. They are aligned to the Q and U directions respectively. The light that travels through the first prism is decomposed into $e-$ray and $o-$ray; at the entrance of the second prism these two directions get swapped: the $e-$ray becomes $o-$ray and viceversa generating thus a difference in directions as shown in Figure 7.4.

The difference in directions is due to Snell's law:

---

[11] A bad extinction ratio causes leaks in polarization and therefore decreases the modulation amplitude [Snik, 2008].

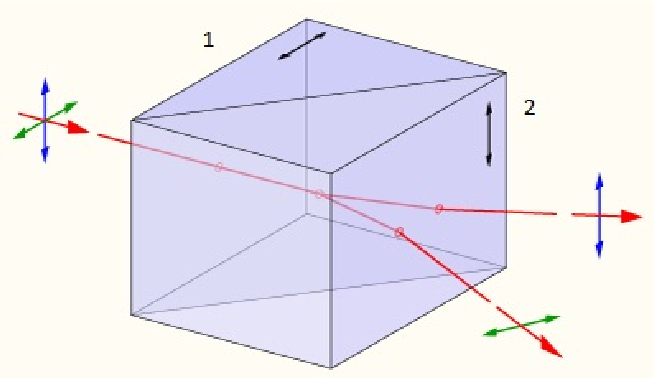

Figure 7.4: Wollaston prism.
Image source:
`http://upload.wikimedia.org/wikipedia/commons/d/d6/Wollaston-prism.png`

$$n_1 \sin\theta_1 = n_2 \sin\theta_2 \quad \rightarrow \quad \frac{n_1}{n_2} = \frac{\sin\theta_2}{\sin\theta_1} \tag{7.20}$$

where n_1 and n_2 are the indexes of refraction of two generic materials, while θ_1 is the angle of incidence and θ_2 is the angle of refraction. According to Snell's law, if a light wave moves from a less refractive material to a more refractive one (higher index of refraction, e.g. $n_2 > n_1$) the refracted light will bend closer to the normal as shown in Figure 7.5. The same is valid for the two crystals of the Wollaston prism, the indexes in Equation 7.20 can be seen as the refractive indexes of the crystals thus as n_e and n_o. If $n_e < n_o$, the final extraordinary ray is bent away from the normal: the two linear polarization parameters Q and U will show different directions at the Wollaston's exit.

7.2.4 Optical design

SPEX current design is optimized for the ExoMars mission to Mars. To sample the scattering phase angles 7 viewing angles (there are also 2 limb viewers) are required to obtain the desired spatial resolution for an orbital altitude of 300 km required for this mission. Each of these viewing angles needs to have its own pre-optic instruments as shown in Figure 7.6. The pre-optics instruments form the spectral modulator shown in Figure 7.7.

For one viewing angle the light enters the polarization pre-optics and is focused on a slit plane. All the 9 slit planes are combined into a single, larger, slit plane by a beam combiner. This slit plane passes a spherical mirror, a folding flat mirror, the transmission grating, and finally it is imagined onto a detector. The detector has 512×512 pixels each with a size of 25 μm^2 [12].

---

[12] Source:
`http://www.sron.nl/index.php?option=com_content&task=view&id=2376&Itemid=2094`

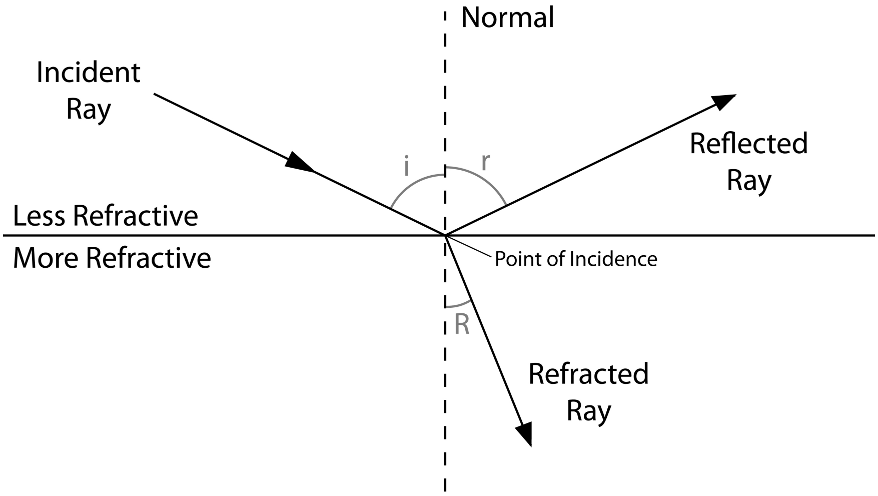

Figure 7.5: Snell's law of refraction. The law shows the behavior of the angle of incidence and the angle of refraction when a light ray passes from a less refractive media to a more refractive one: the refracted ray is bent closer to the normal. It is bent away from the normal if the second media has an index of refraction smaller than the first media.

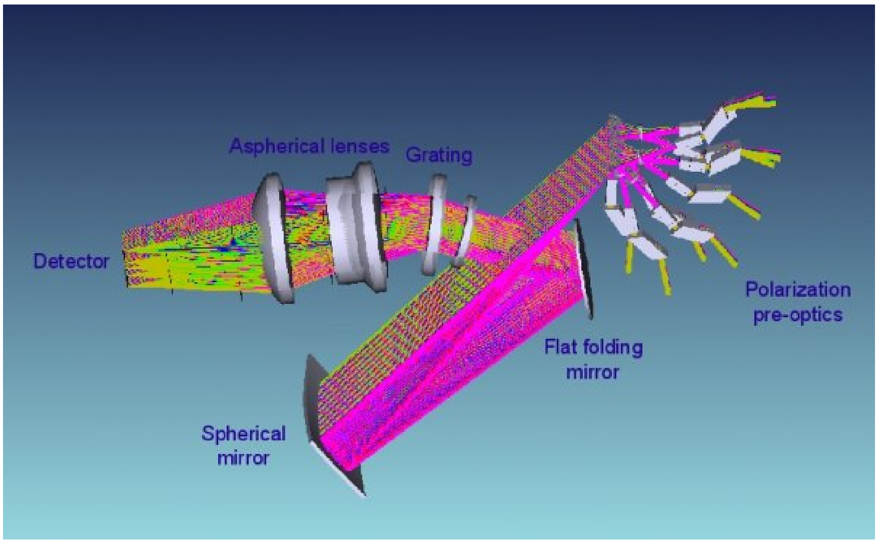

Figure 7.6: SPEX full optics design. Image adapted from SRON website.

7.3 Spectral modulation basic principle

In order to derive the modulated spectrum equation we started from Fig.7.1 where the configuration of retarders and polarizers for SPEX is shown. The first element of the optics train is the Fresnel Rhomb (quarter-wave retarder) with its axis oriented along the $\pm Q$ direction (x, y axes respectively). It is followed by the birefringent athermal multiple-order retarder made of a combination of MgF_2-Al_2O_3 with its axis at an angle of 45° with respect to the Fresnel Rhomb. Last component is the Wollaston

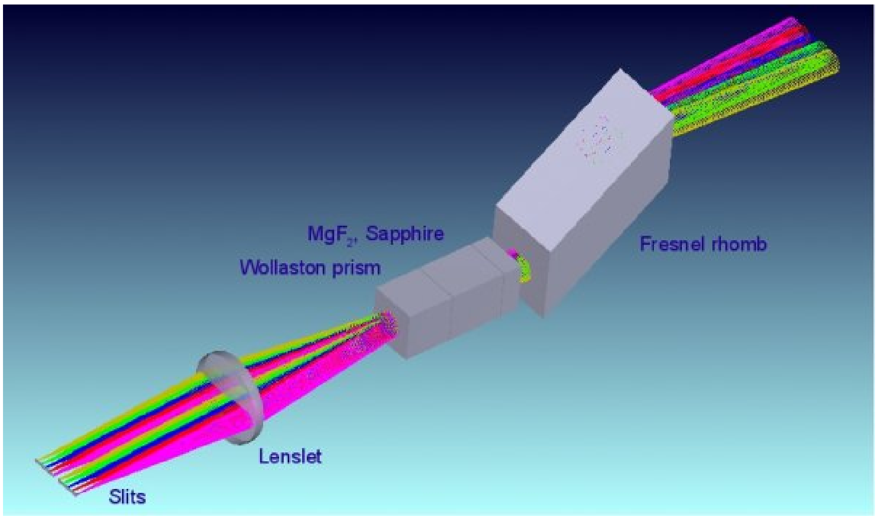

Figure 7.7: The spectral modulator is made by three optical elements that form the polarizing pre-optics. Image adapted from SRON website.

prism with its optic axis parallel to the Fresnel Rhomb's one. The orientation of the modulator components is shown in Figure 7.8(a). In Fig.7.8(b) the changes in the Poincare' sphere[13] are shown according to the steps taken inside the spectral modulator.

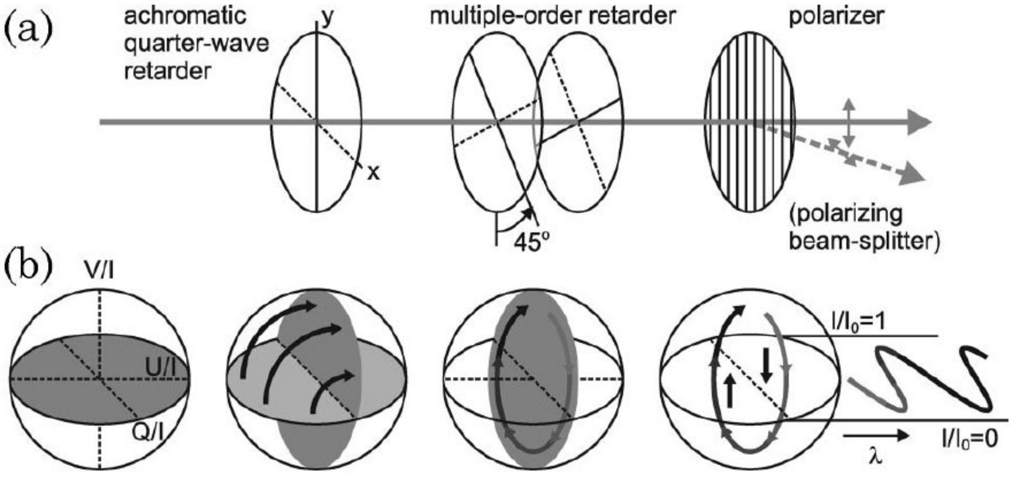

Figure 7.8: Modulator optics orientations (*a*) and Poincaré sphere (*b*). Image adapted from Snik et al. [2009].

Suppose that a polarized light wave is entering the modulator: what happens at each step?

To better understand the basic principle of polarimetric spectral modulation let's

---

[13] See Section 3.3 for details about the Poincarè sphere.

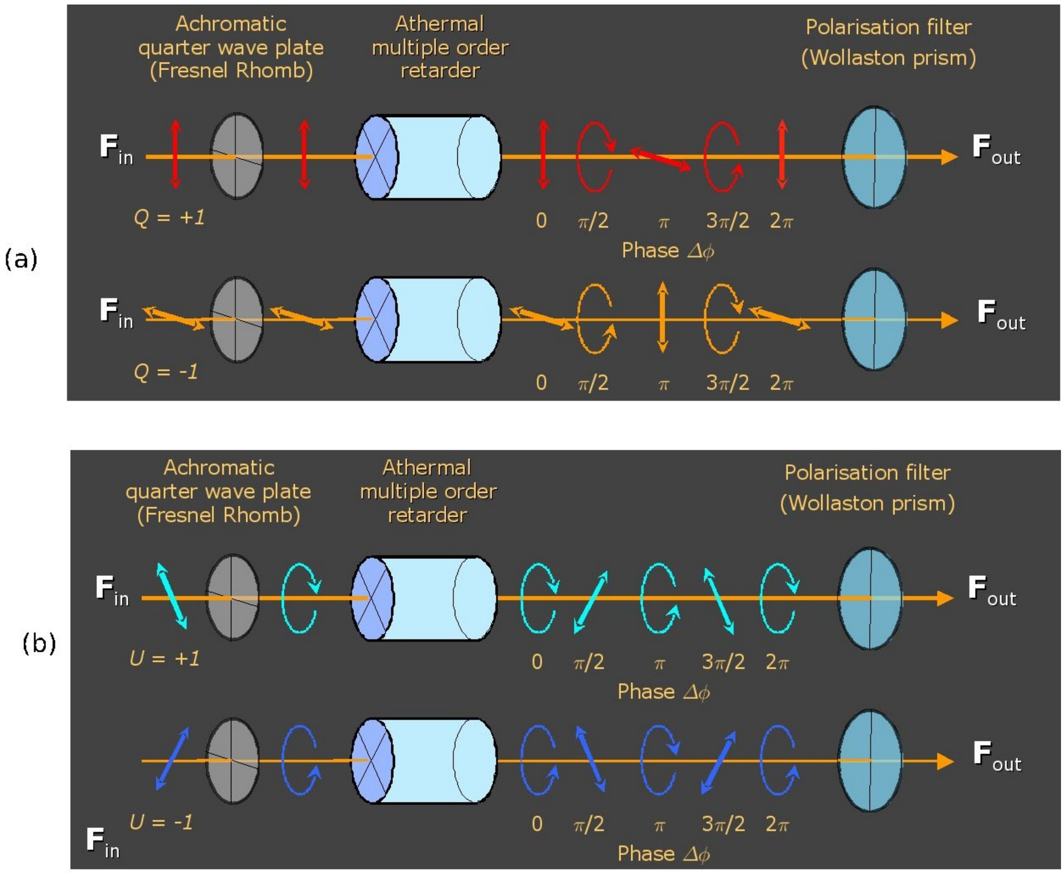

Figure 7.9: Figure (*a*) shows a $\pm Q$ polarized flux enetering the modulator optics and the possible changes in polarization status depending on the phase shift. Figure (*b*) shows the same but for a $\pm U$ polarized input.
Image source: SRON presentation on the 24 Nov. 2009.

keep an eye on Fig. 7.9 where some examples of polarized light modulation are presented.

1. Achromatic quarter-wave retarder - Due to its optical axis orientation the Fresnel Rhomb does not alter an incoming Stokes vector along the Q direction, but generates a phase shift of ±90° for the Stokes vector oriented along the U direction converting it into circular polarization. The plane $Q/I, U/I$ has been then converted to the $Q/I, V/I$ plane as shown in the Poincare' sphere in Fig. 7.8;

2. Athermal birefringent retarder - The crystals rotate the plane $Q/I, V/I$ of a certain amount around the U/I axis depending on the wavelength: longer is the wavelength (i.e. redder) less is the phase shift at the retarder exit. In fact in Fig.7.9 after the second stage there are several polarization state transformations according to the wavelength and the relative phase shift, see Eq.7.6.

3. Polarizer - The Wollaston prism at the end of the optics train separates the rays polarized along the Q direction from the ones polarized along the U direction: its main optical optical axis is along the Q/I direction, the other is orthogonal.

> These polarization states can be visualized on the Poincaré sphere as shown in Fig.7.8. The output intensity signal (or output spectrum) represents the projection of the relative polarization state in the Poincare' sphere on the Wollaston's axis Q/I. Basically it is thanks to the polarizer that the rotation in the Q, V plane is transformed into a sinusoidal signal as shown in Fig.7.8 and gives as result the two spectra shown in Eq.7.2.

After the polarizer the rays travel through the spectropolarimeter ending up eventually on the detector. The output signal we are referring to is the detector output spectra shown in Eq.7.2, the ± sign depends on the alignment of the output spectrum with respect to the Wollaston prism' optical axis: if the projection of the polarization on the Poincaré sphere is parallel to the Q/I direction, it will be represented by the '+' sign, otherwise by the '-' sign. If each of these two spectra is divided by the input spectrum, we get two different modulated signals that vary in the range $0 \leq \mathbf{S}/\mathbf{S}_0 \leq 1$ (i.e. one of these modulated signal is the input signal for the retrieval algorithm).

Let's clarify the dependence of the amplitude of modulated spectrum on the degree of polarization still shown in Eq.7.2. If after the Wollaston prism the "polarization" point is, for instance, on the surface of the Poincaré sphere, it means that the wave is fully polarized, the degree of polarization will be 1 and the signal amplitude will be maximum (i.e. 'deep' signal amplitude). The smaller is the degree of polarization, the smaller will be the sphere on which the status is visualized (concentric sphere), the 'shallower' will be the depth of the signal amplitude. The amplitude of the output spectra will change according to the degree of polarization variation producing 'deeper waves' for higher P values and 'shallower waves' for smaller P values.

In order to derive the modulated spectra shown in Eq.7.2, we should consider the Mueller matrices of each component paying attention at their relative orientation:

$$\mathbf{S}(\lambda) = M_{pol} \cdot M_{ret\_45} \cdot M_{QWP} \cdot \mathbf{S}_0(\lambda) = \tag{7.21}$$

$$= \frac{1}{2}\begin{pmatrix} 1 & 1 & 0 & 0 \\ 1 & 1 & 0 & 0 \\ 0 & 0 & 0 & 0 \\ 0 & 0 & 0 & 0 \end{pmatrix} \begin{pmatrix} 1 & 0 & 0 & 0 \\ 0 & \cos\frac{2\pi\delta}{\lambda} & 0 & -\sin\frac{2\pi\delta}{\lambda} \\ 0 & 0 & 1 & 0 \\ 0 & \sin\frac{2\pi\delta}{\lambda} & 0 & \cos\frac{2\pi\delta}{\lambda} \end{pmatrix} \begin{pmatrix} 1 & 0 & 0 & 0 \\ 0 & 1 & 0 & 0 \\ 0 & 0 & 0 & -1 \\ 0 & 0 & 1 & 0 \end{pmatrix} \cdot \mathbf{S}_0(\lambda) = \tag{7.22}$$

$$= \begin{pmatrix} \frac{1}{2} & \frac{1}{2}\cos\frac{2\pi\delta}{\lambda} & -\frac{1}{2}\sin\frac{2\pi\delta}{\lambda} & 0 \\ \frac{1}{2} & \frac{1}{2}\cos\frac{2\pi\delta}{\lambda} & -\frac{1}{2}\sin\frac{2\pi\delta}{\lambda} & 0 \\ 0 & 0 & 0 & 0 \\ 0 & 0 & 0 & 0 \end{pmatrix} \cdot \mathbf{S}_0(\lambda) \tag{7.23}$$

The input spectrum is supposed to be normalized with a degree of linear polarization P and an angle of linear polarization χ:

$$\mathbf{S}_0(\lambda) = \begin{pmatrix} 1 \\ P(\lambda)\cos 2\chi(\lambda, T) \\ P(\lambda)\sin 2\chi(\lambda, T) \\ 0 \end{pmatrix} \cdot I_0 \cdot t \tag{7.24}$$

where t is the instrument transmission factor. Then, taking into account just the intensity, the final modulated output intensity spectrum is equal to:

$$\mathbf{I}(\lambda) = \frac{1}{2}\mathbf{I}_0(\lambda) \cdot \left[1 + P(\lambda)\cos\left(\frac{2\pi \cdot \delta(\lambda, T)}{\lambda} + 2 \cdot \chi(\lambda)\right)\right] \tag{7.25}$$

Equation 7.25 is equivalent to the spectra in Eq.7.2, only the 'positive' intensity spectrum is shown. From one single modulated spectrum it is possible to obtain the degree of linear polarization P and its angle χ using a retrieval algorithm based on this equation [Snik et al., 2009].

Figure 7.10 presents an input spectrum representative for unpolarized incoming light and simulated for the Mars instrument set up. Figure 7.11 shows two possible modulated outputs. The one on the left side presents "deeper" sinusoidal amplitudes than the one on the right side. As mentioned before, this is an indication that the degree of polarization of the spectra on the left is higher than the one on the right side.

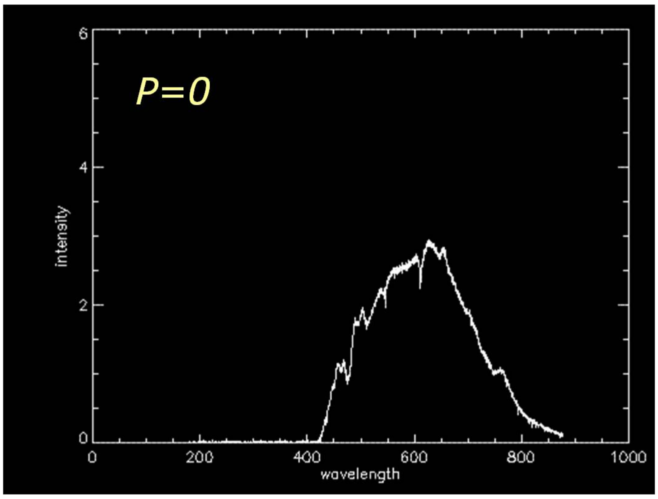

Figure 7.10: Example of unpolarized incoming light input spectrum for Mars.
Image source: SRON presentation on the 06 Nov. 2009.

7.4 Retrieval algorithm

The algorithm is modeled in such a way that it is able to retrieve the degree of linear polarization P and its direction χ from one unique SPEX measurement. The input signal for the retrieval algorithm is a normalized signal. It is obtained dividing the 'positive' (or 'negative') modulated spectra (Eq.7.25) by the input spectrum I_0 giving as result:

$$\mathbf{I}_{\text{norm}} = \frac{\mathbf{S}(\lambda)}{\mathbf{S}_0(\lambda)} = \frac{1}{2} + \frac{1}{2}P(\lambda)\cos\left(\frac{2\pi \cdot \delta(\lambda, T)}{\lambda} + 2 \cdot \chi(\lambda)\right) \tag{7.26}$$

The normalized spectrum in Eq. 7.26, in this case calculated for the 'positive' modulated intensity, is divided into a minimum number of 'windows' each of which is analyzed by the algorithm to find the best fit for both the degree of linear polarization

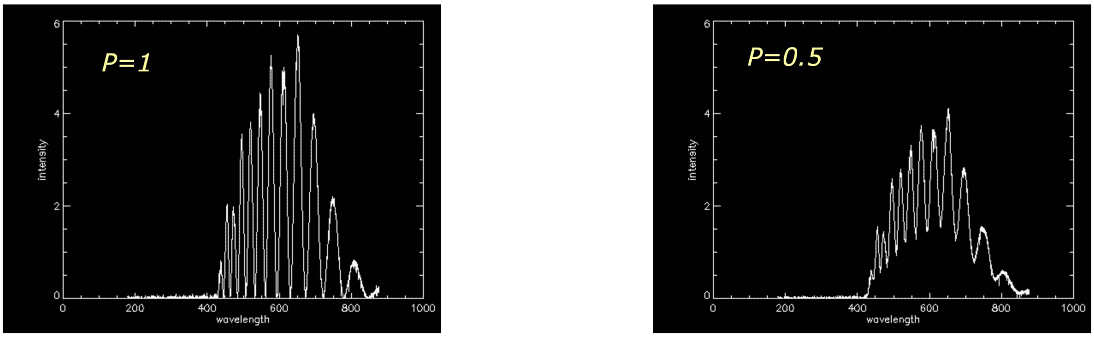

Figure 7.11: Example of output spectra for Mars. On the left side it is a fully polarized spectrum, the amplitude of the signal is at the maximum, on the right side the polarization is half (i.e. 'deeper' is the wave higher is the degree of polarization). See text for discussion.
Image source: SRON presentation on the 06 Nov. 2009.

and its direction. With the intention of obtaining a good first estimate of P, each discretized wavelength 'window' has to be big enough to contain at least one single modulation period in order to avoid any information loss. Since the modulation period is proportional to $1/\lambda$, for small λ (i.e. blue) we will have an higher periodicity of 'windows' than for large λ (the sampling has to be higher in the blue range than in the red range). To guarantee this higher sampling for shorter wavelengths, the 'windows' have to be smaller for small λ and bigger toward larger λ. The 'spectral windows' concept is mathematically represented by:

$$\Delta\lambda = \frac{\lambda^2}{\delta(1+\lambda^2/4\delta^2)} \tag{7.27}$$

where the retardance δ represents the modulation period of Eq.7.7. According to the thermal test's results of the athermal multiple-order retarder published by Snik et al. [2008] and described in Section 7.2.3, a total thickness $d = 4$ mm is optimal for SPEX. For this thickness the system will have a retardance $\delta \sim 27\mu$m which creates a modulation periodicity of ~20 nm in the red to ~5 nm in the blue. These values determine the size of the spectral windows inside which one full period of modulation is guaranteed (no information lost). Once the windows size is determined, the algorithm will analyze each window determining the minimum and maximum intensity. Subtracting these values and dividing them by the normalized signal, it is possible to obtain the variation in amplitude within that spectral window. As mentioned before the amplitude of the modulated signal is connected with the degree of linear polarization: we have a first estimate of P.

With the intention of having a first estimate of the direction of linear polarization χ, it is necessary to have a 'reference' instrument signal output obtained with an a-priori χ value (e.g $\chi = 0$). By cross-correlating the 'reference' signal output with the actual normalized intensity signal we can determine the eventual phase shift and thus a first estimate of the angle of linear polarization. Once we have the first estimate of the degree of linear polarization of both the degree of linear polarization and its orientation for each spectral windows, we can obtain the final values of P and χ thanks to a curve fit of these previously obtained values.

The retrieval algorithm can be summarized in the following steps:

1. Derive the spectral windows - the spectral 'windows' periodicity is higher in the blue range than in the red range, every window overlaps with the previous one: no loss of information because the presence of one modulation periodicity is guaranteed in each 'window'.

2. First estimate of P - one of the modulated intensity spectra output ('positive' or 'negative') divided by the input spectrum gives a normalized intensity spectrum input of the algorithm. At this point a first estimate of the degree of linear polarization P is possible by determining the minimum and maximum value of the intensity within each spectral window.

3. First estimate of χ - an artificial reference signal with $\chi = 0$ and $P = 1$ is created (i.e. fully polarized and in phase with the input spectrum). The reference signal gets cross-correlated with the normalized signal and a $cos^2(\lambda + \lambda_\chi)$ fit of the artificial signal. Thanks to this correlation a first estimate of the angle of linear polarization χ is obtained as:

   $$\chi_{\text{estimate}} = \frac{\pi \cdot \lambda_\chi}{\Delta\lambda(\lambda)} \tag{7.28}$$

   where λ_χ is the phase shift between the measurement and the reference signal, while $\Delta\lambda(\lambda)$ is the spectral window and depends on the retardance (see Eq. 7.27).

4. Retrieval of the final value - The procedure is repeated for each spectral window for the whole wavelength range. Once the first estimates of P and χ are obtained for each spectral window, a curve-fit of each normalized measurement in its own spectral window is performed according to Eq.7.2. For the curve-fit there are some obvious constraints on the periodicity: $0 \leq \chi \leq \pi$ and $0 \leq P \leq 1$. The curve fit will give us the final values of both the degree of linear polarization and its orientation.

Figure 7.12 shows that the Aolp and the DoLP are retrieved within the accuracy limits. These are the results of simulations done for the Martian atmosphere by Snik et al. [2008]. Once we have these values we can obtain the linear polarization parameters through Equation 3.9 and 3.10 and from them derive the microphysical properties of the aerosol particles in the atmosphere.

7.5 SPEX end-to-end simulator

The SPEX end-to-end simulator is a software tool currently under development at SRON. Its purpose is to fully describe all aspects of the SPEX instrument, measurements, and analysis for any space mission, which facilitates defining science and instrument requirements, assessing instrument performance, optimizing calibration routines and tracing potential system degradation. The simulator uses the concept of a traveling optical spectrum to calculate the final spectra measured by the focal plane array and subsequent electronics. This concept means that the evolution of an optical spectrum, incident on (one of the) apertures of SPEX, is calculated after it has passed

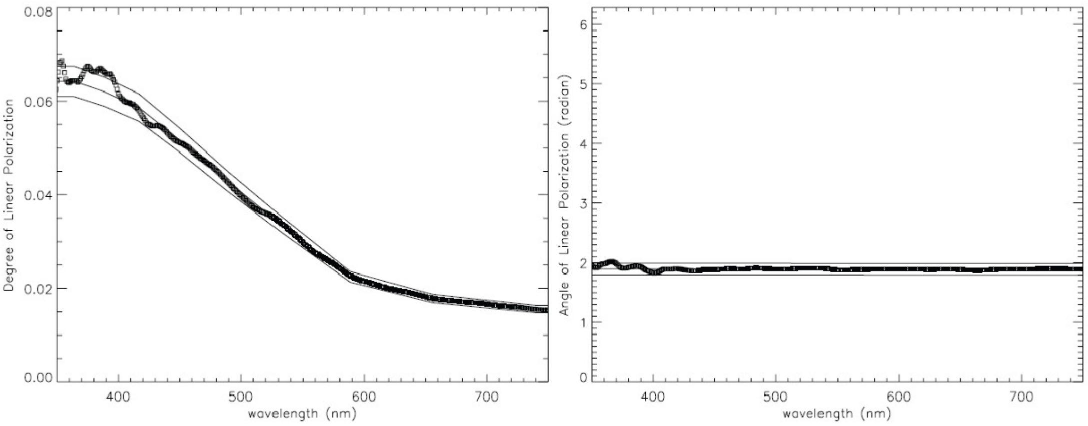

Figure 7.12: Curve fit results for atmospheric simulations for Mars. The lines represent the input signal and the margin from the accuracy requirements. The little square symbols represent the values obtained with the retrieval algorithm after a realistic instrument simulation. Image adapted from Snik et al. [2008].

each instrument component during its journey throughout the instrument. Components that interact with the optical spectrum are any kind of transmissive, reflective or diffractive optical materials. Both the effect of components on the intensity as well as on the polarization state of the spectrum is calculated using a Stokes-vector description of the spectrum and a Mueller matrix representation of each components. The input of the simulator are high-spectral resolution spectra of I, Q, and U (and possibly V), such as those calculated with our adding-doubling radiative transfer algorithm (see Section 5.2), for each of its viewing apertures. Each optical component of the instrument is modeled using appropriate Mueller matrices including wavelength dependent optical properties of the materials and field-of-view variations of the incident spectra. The modulated spectra at the end of the optical train are imaged on the focal plane array of the detector and binned. A wavelength dependent quantum efficiency, dark-current, read-, shot- and ADC-noise, are included in the calculation, while pixel-to-pixel variations in gain and offset, the effects of pixel cross-talk and detector non-linearity, and the contributions of thermal radiation and stray-light are ignored in the current version (they will be included in future versions). The demodulation of the measured spectra into spectra of the degree and angle of linear polarization is performed using the technique outlined by Snik et al. [2009]. As described in Section7.4, this technique involves fitting of one or more periods of the local modulation by the general formula (Eq.7.27) that describes the ideal behavior of the spectral modulation principle within each 'spectral window'. It is assumed that a spectral window covers a small wavelength region of the modulated radiance spectra across which P, χ, and the instrument's optical properties are assumed to be constant. Optimizing $\Delta\lambda$ in Eq.7.27 means optimizing the sampling frequency and therefore, the spectral resolution of P and χ. Note that we have not shown any spectra of χ; it is less sensitive to the atmospheric parameters than either I or P.

8 SPEX on Titan - End-to-End simulator results

In this chapter, we focus on a SPEX as payload for a balloon that floats through the Titan atmosphere as proposed to ESA's Cosmic Vision Programme in the Titan Saturn System Mission (TSSM) proposal [TSSM Study Final Report, 2009]. This hot-air balloon would float at an altitude of about 10 km, below the lowest haze layer with a velocity of 2 m/s (this equals the wind speed). SPEX as payload of this balloon would measure the radiance and state of polarization of sunlight that is scattered and transmitted through the haze layers.

SPEX on a balloon would not be the first polarimeter investigating Titan's atmosphere from the inside. The Descent Imager/Spectral Radiometer (DISR) [Tomasko et al., 1997] on the Huygens probe also performed polarimetric measurements and obtained valuable information on the shape and size of the aerosols at Huygens landing site [Tomasko et al., 2008]. The DISR instrument used two orthogonal polarization filters in combination with a blue and a red filter, thus four separate radiance measurements to determine the radiance and degree of polarization of the scattered sunlight and their broadband spectral variation. The errors resulting from the time differences and the differences in the optical properties of the filters will affect the retrieval of the microphysical properties of the haze particles.[1] Since SPEX would be able to measure the scattered radiance and the complete state of polarization simultaneously and continuously from 0.4 to 0.8 μm, and of course because it would float through the atmosphere as part of the balloon payload, it could add tremendously to our knowledge on Titan's haze particles.

8.1 Simulated SPEX' observations

The SPEX instrument has been described in details in Chapter 7. However, it might be useful to recall the main characteristics of the instrument and its novel technique before describing the results obtained with the SPEX' end-to-end simulator.

SPEX uses a novel spectropolarimetric technique which allows simultaneous measurements of the total radiance I, and the degree P and direction χ of polarization from 0.4 to 0.8 μm with a spectral resolution of 2 nm for the radiance to slightly larger for the polarization, without moving parts (current design). In addition to be-

---

[1] Note that because DISR used only two instead of three filters, it could not measure the full degree of polarization. Using two instead of three polarization filters can in principle be accounted for in the radiative transfer calculations in the retrieval, but the missing information will limit the accuracy of the retrievals.

ing robust, SPEX is small (< 5 kg) and uses little power [Snik et al., 2009]. SPEX' spectropolarimetric technique is based on spectral modulation: the radiance spectrum is sinusoidally modulated by the degree and direction of linear polarization of the incoming radiation (see Eq.7.2). The modulation is achieved by a carefully selected series of (passive) optical components. When leaving this pre-optics, the beam of light has been spectrally modulated and continues towards a spectrometer, where an off-the-shelf detector records the modulated spectrum with a 2 nm spectral resolution. The degree of linear polarization P and the direction of polarization χ can be derived from each of the modulated radiance spectra, using a demodulation algorithm. The spectral resolution of P and χ is on the order of the modulation, which depends on the choice of optical elements, in particular, for a given material of the retarder, on the length of the multiple-order retarder.

In this section, we show the accuracy of the demodulation algorithm and its spectral resolution using simulated Titan spectra shown in Chapter. 6, in combination with the SPEX end-to-end simulator described in Section 7.5.

We simulated radiance and polarization spectra for solar zenith angles θ_0 from 0° to 80°, and for instrument viewing zenith angles θ from 40° to 90°, for a difference in azimuth angle $\phi - \phi_0 =$ 0°, 180°, and for both DLA- and BPCA- particles. It is important to notice that the instrument zenith angles have been chosen taking into account the presence of the balloon on top of the gondola on which SPEX would be located. The spectral resolution depends mostly on the retardance, which in turn, is strictly connected with the length of the multiple-order retarder (see Eq.7.6). Our results are for different values of the retardance δ. We start with the value as chosen for SPEX on a Mars orbiter, namely $\delta \simeq 20$ μm (a crystal thickness of 4 mm), and then we optimize the value for SPEX on a Titan balloon.

The main difference between these two missions would be the spectral resolution with which the degree of linear polarization P is retrieved: while a Mars spectrum shows little to no spectral features across SPEX' wavelength region, a Titan spectrum is rich with methane absorption bands.

Figure 8.1 shows the retrieved P for the Mars-SPEX with $\delta \simeq 20$ μm and the errors in the retrieval, with our target error of at most 5 % (this error is based on retrieval algorithms for aerosol properties using polarization data [Hasekamp and Landgraf, 2007]. With $\delta \simeq 20$ μm, the spectral resolution of P is about 8 nm in the blue and about 32 nm in the red (cf. Eq. 7.27). The graphs in Fig. 8.1 show how arduous it is to fit the retrieved P to the original P. Clearly, this resolution is not good enough to resolve the methane band features.

In order to better resolve the methane band features[2], and to reach a retrieval accuracy within the target error, we have to increase the sampling frequency of the demodulation algorithm, hence to decrease the width of the spectral windows (cf. Eq. 7.27). This implies that we have to increase the retardance δ of our retarder, thus the thickness of the birefringent crystals (sticking with our choice of MgF_2-Al_2O_3 crystals). An optimal retrieval was found for a crystal thickness of 16 mm, four times as thick as in the original SPEX design (for a Mars mission), yielding a retardance

---

[2] An accurate retrieval of aerosol properties does not necessarily require complete resolving the methane bands, since the degraded resolution can be taken into account in the retrieval process. In general, however, the better the resolution, the more information can be retrieved.

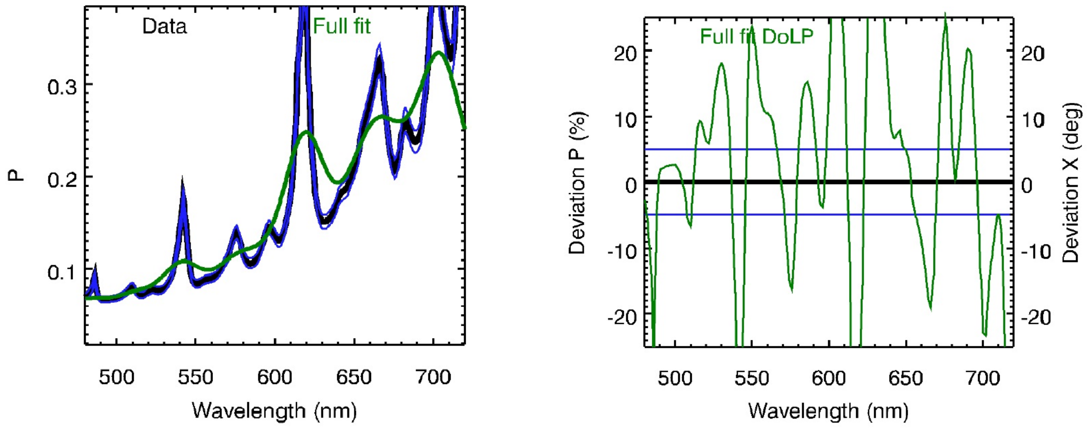

Figure 8.1: Retrieval of P_L using the demodulation algorithm of the SPEX end-to-end simulator: P (left) and the retrieval error with horizontal lines indicating a target error of at most 5 % (right). The retardance value used is equal to $\delta \simeq 20$ μm (top) as for the current design of SPEX. Note that 'DoLP' stands for 'Degree of Linear Polarization.'

$\delta \simeq 80$ μm. The optimized spectral resolution of the polarization spectra is 2 nm in the blue and 8 nm in the red (according to the wavelength dependency of Eq.7.27). It has to be pointed out that the athermal property of the multiple-order retarder is not changed. In order to be athermal, it is necessary to keep the thickness ratio between the two crystals constant (i.e. $d_1 : d_2 = 2.4$, see Section 7.2.3). For the current SPEX Mars design, experimental results of a prototype spectral modulator were obtained using a combination of 2.53 mm of MgF_2 and 1.10 mm of Al_2O_3 crystals [Snik et al., 2009]. For the Titan design, the thickness of the crystals should increase to 11.30 mm for the MgF_2 crystal and to 4.70 mm for the Al_2O_3 crystal in order to obtain a retardance of $\delta \simeq 80$ μm while keeping constant the thickness ratio of the crystals.

The spectrally improved retrieved P for a retardance of $\delta \simeq 80$ μm is shown in Fig. 8.2 together with the error in the retrieval. It is clearly noticeable how better the fitting is when compared to the Mars design retrieval of P in Fig.8.1. Note that in the deepest parts of the methane bands, the error can still exceed our target error. If we want to use these parts to retrieve aerosol properties (see Stam et al. [1999]), the instrument response should to be taken into account in the retrieval algorithm.

8.2 Designing SPEX for a Titan balloon

Here, we have presented SPEX's strengths as payload for the hot air balloon that is an intrinsic part of the Titan Saturn System Mission (TSSM). A detailed investigation of Titan's haze layer is key to expanding our the knowledge on the atmosphere's complex hydrocarbon cycle, which is one of the main goals of the TSSM. By measuring both the radiance and the degree of linear polarization of sunlight that has been scattered by the haze particles, SPEX allows the retrieval of the size, shape and composition of the haze particles and their vertical distribution.

SPEX has originally been designed as payload for a Mars orbiter, with 7 fixed downward viewing and 2 fixed limb-viewing apertures, parallel to the orbiter's ground

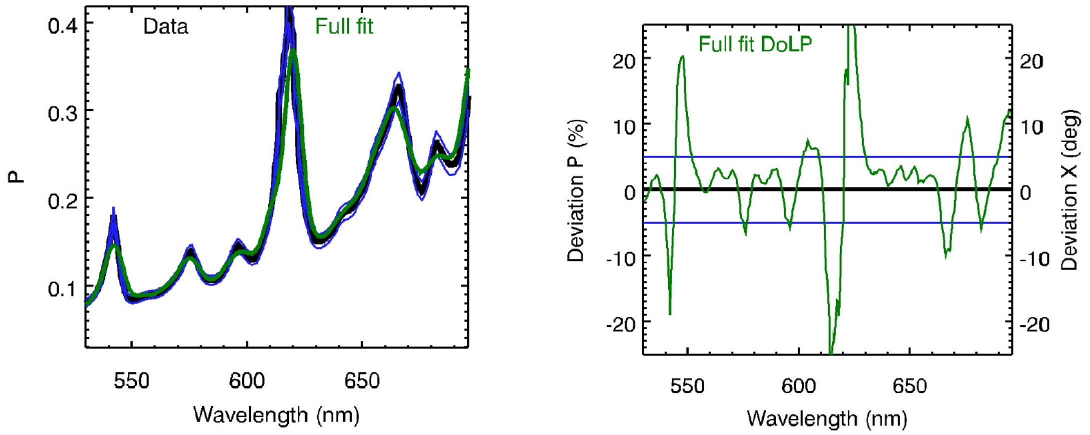

Figure 8.2: The same as in Fig.8.1, but with a retardance value of $\delta \simeq 80$ μm as optimized for the new design of SPEX for the balloon mission on Titan.

track. The main adaptations of SPEX to fly on a balloon mission through Titan's atmosphere would be the viewing geometries, and the spectral resolution. In this section we give an overview of the changes needed for the Titan design of SPEX which have been already partially presented in Section 8.1.

8.2.1 Viewing geometries

The mission plan is to have the TSSM balloon float at a nominal altitude of 10 km with a range between 6 and 12 km. As payload on the balloon, the interesting viewing angles for SPEX are looking upwards, towards the haze layer, and possibly downwards, towards the surface. Knowledge of the surface reflection and its spectral and angular variations is important for understanding the formation and evolution of Titan, and for identifying possible sources and sinks of methane. And it is also crucial for understanding SPEX' observations of scattered sunlight, because direct and diffuse sunlight will be reflected off the surface, back towards the atmosphere, where it can undergo more scatterings. Hence, the surface reflection has to be included in the retrieval process.

Our numerical simulations have shown the importance of sampling I but especially P at various viewing angles, so we foresee to use either a number of apertures (as in the Mars design), with fixed viewing zenith angles distributed like a hand-fan between $\theta \approx 50°$ and $130°$ (these angles would depend on the size of the balloon, the distance between SPEX and the balloon, and on the location of SPEX on the payload package), or a single aperture that scans up and down. If we keep SPEX as designed for the Mars orbiter, with fixed viewing angles, it could be placed on top of the gondola where the rest of the payload would be. The Mars design would force SPEX to look in one direction as shown in Fig.8.3 [tbd in delft] and measure only forward or only backward scattered light in Titan's atmosphere (depending on where the sun is with respect to the instrument).

To improve the scientific return, SPEX should also be able to rotate in the horizontal plane to sample a range of azimuthal angles $\phi - \phi_0$ and be able to take measurement of possible variations of P in the whole atmosphere around the balloon. This rotating would be taken care of if the balloon payload would rotate (although the rotation period should not be too long to avoid variations in the atmosphere). SPEX could be

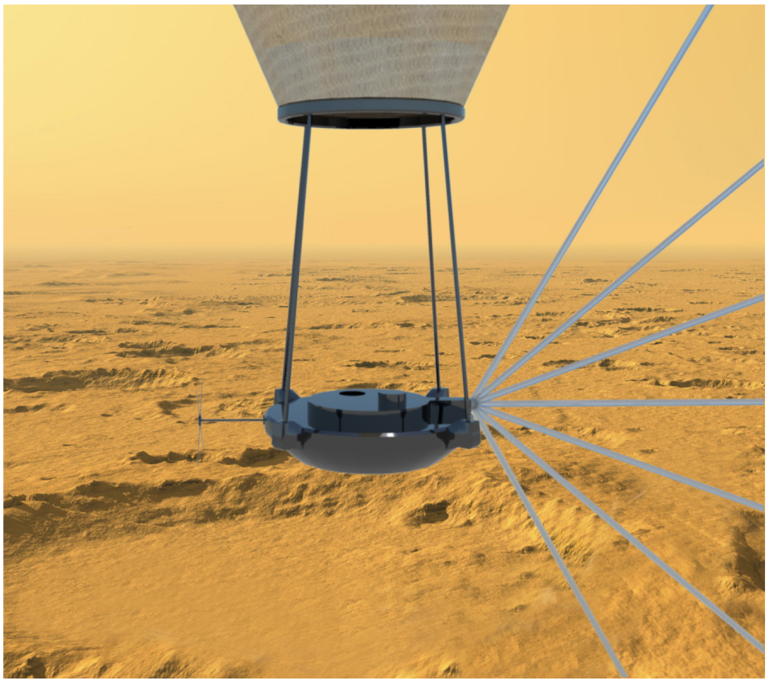

Figure 8.3: Artistic view of what SPEX, as designed for Mars orbiter, would look like when placed on the balloon for the TSSM. The grey beams are representative of the light direction as it would 'enter' SPEX's viewing apertures.

placed on top of the payload where it can rotate around a vertical axis, such as the connection between the payload and the balloon, but this would partially block both the upward and downward view, which would also be hampered by the presence of the eventual connections between the gondola and the balloon. Having SPEX below the payload would have the disadvantage of blocking the upward view.

An interesting solution that would allow the required angular sampling while limiting the number of moving elements, would be to have the detector part of the SPEX instrument on the gondola and have an extra rotating disk on the edge of a boom underneath the gondola where only the viewing apertures of the instrument will be. The disk should be inclined under an angle of 40° with respect to the vertical axis and with a number of apertures looking outward along the rim of the disk. This configuration, shown in Fig. 8.4 and 8.5, would allow measurements of scattered and transmitted light inside the atmosphere without blocking the upward nor the downward view. The length of the boom depends on the size of both balloon and gondola.

8.2.2 Spectral resolution

As already explained in Section 8.1, SPEX has been designed to measure I, P, and χ from the visible to the near-infrared. Across this wavelength spectrum, a Mars spectrum does not show significant high-spectral resolution features. A Titan spectrum, however, is rich in methane absorption band features. Clearly, as also shown in Chapter. 9, using the relatively low spectral resolution designed for the Mars-SPEX for the Titan-SPEX would result in too large errors in the retrieved values for P. To keep

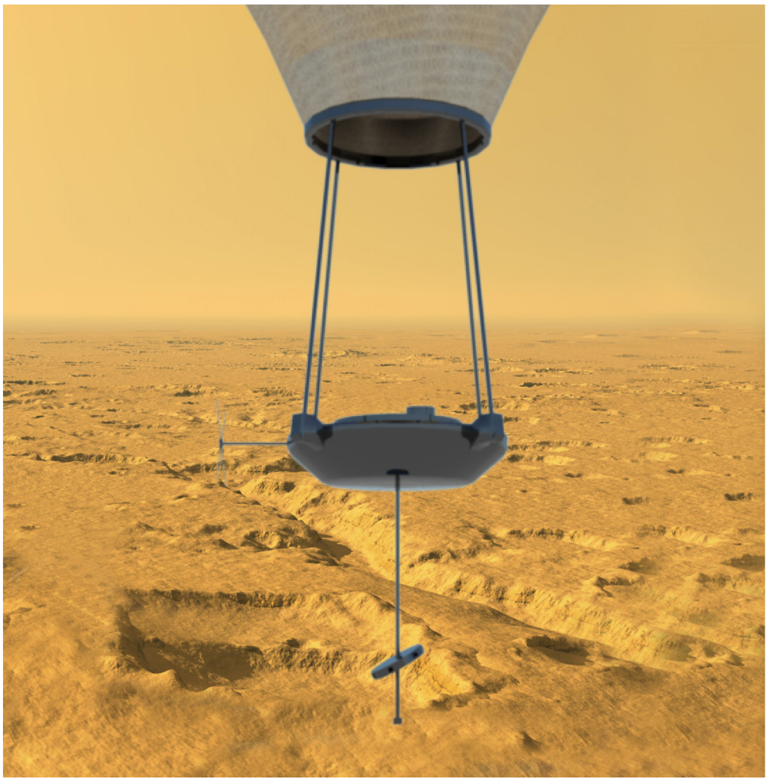

Figure 8.4: Artistic view of what SPEX, as designed for Titan, would look like when placed on the balloon for the TSSM. The only difference with the current design in Fig.8.3 stands in the viewing apertures which now are placed on the rim of a rotating disk underneath the gondola. The detector part of SPEX is still placed on the gondola as for the current design. See text for discussion.

the errors in P below 5 %, we have to increase the retardance, hence the thickness of the birefringent crystals from the original 4 mm for Mars to 16 mm for Titan.

Increasing the retardance and hence the modulation frequency, requires an increase of the sampling of the modulated radiance spectra. To allow for a much higher sampling of the spectra, not only the detector size can be increased, but also the wavelength range that is covered. For a Titan-SPEX, a wavelength coverage from 0.5 to 0.72 μm could be considered. Such a wavelength range would have the additional advantage that it excludes the deep methane band at 0.73 μm, which is especially difficult to fit with our current demodulation algorithm. Adapted demodulation algorithms, e.g. algorithms that distinguish between the continuum and the methane bands, could be considered if the inclusion of this deep band is interesting for scientific reasons.

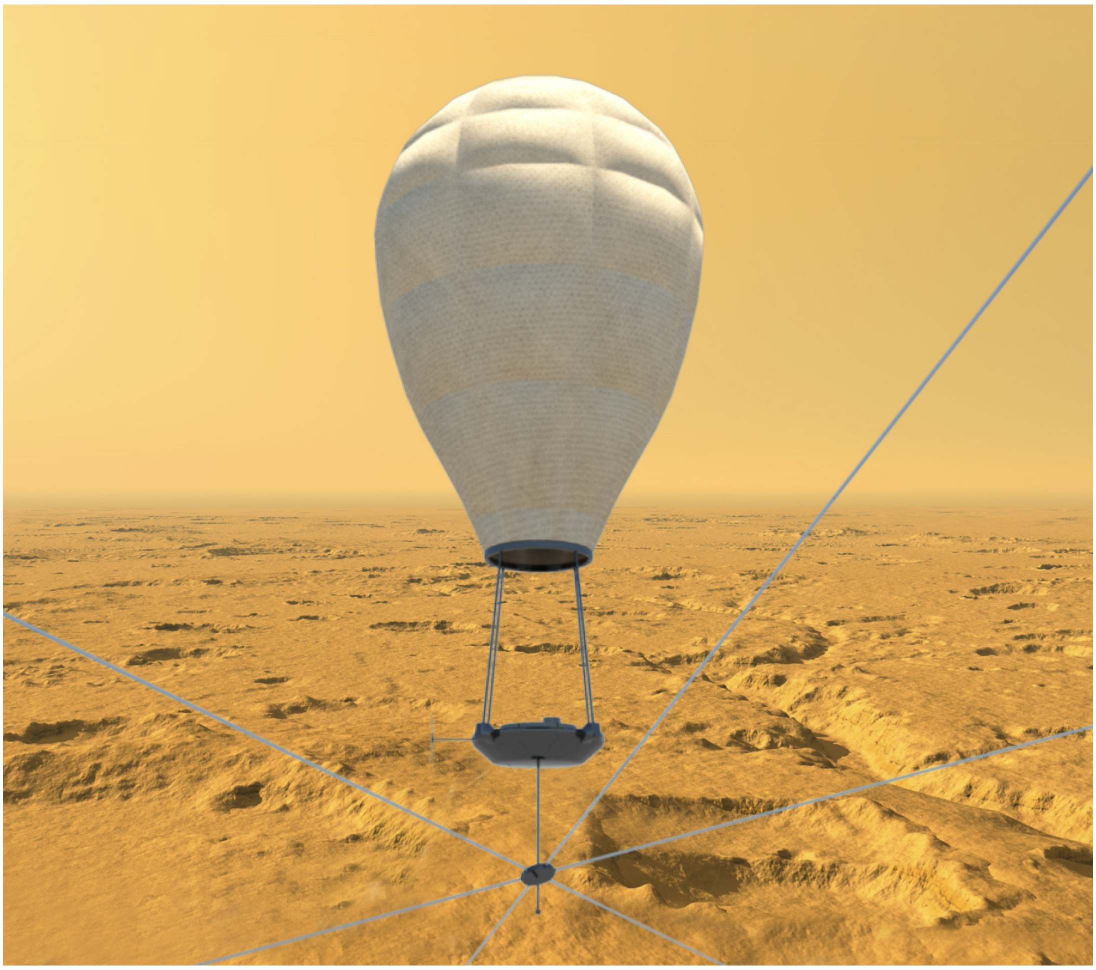

Figure 8.5: Artistic view of what the balloon for the TSSM would look like with SPEX as payload. The rotating disk beneath the gondola represents the innovation in the SPEX' design. The grey beams represent the light as it would be 'perceived' from the viewing apertures placed along the rim of the rotating disk. See text for discussion.

9 Conclusions and recommendations

This chapter presents conclusions based on the results achieved during the research. Then recommendations for the further research are given.

9.1 Conclusions

Saturn's moon Titan is covered by several haze layers. Information on the number density, the composition, size and shape of the haze aerosols as function of the altitude is key to understanding the atmosphere's complex hydrocarbon cycle. For an Earth-based observer or for a spacecraft instrument orbiting the moon, the highest haze layers hamper the view on lower layers. Instead, a hot-air balloon floating through Titan's thick atmosphere, as proposed in the Tandem/Titan Saturn System Mission (TSSM) to ESA, appears to be the ideal in-situ element for the desired science goals. The haze particles can be studied by a balloon instrument that measures scattered sunlight that has been diffusely transmitted through the haze layers.

In this report we have presented numerical simulations of the radiance I and degree of linear polarization P of sunlight that has been scattered in Titan's atmosphere, and of observations of this light as could be performed by the SPEX instrument as payload on the hot air balloon of the TSSM mission.

From this study we can conclude that:

1. *The degree of linear polarization of scattered sunlight is very sensitive to the microphysical properties of the scattering particles.*

   From the spectra we showed, it is clear that the spectral dependence of the degree of linear polarization of sunlight that is diffusively transmitted through Titan's atmosphere shows a stronger variation on the particle-type, than the radiance of this light. The latter does show variations, but the general shape of the spectra remains the same, while the continuum radiance is very dependent on the aerosol optical thickness and would thus not constrain particle type [Mishchenko and Travis, 1997]. Obviously, preferably, both the radiance and the polarization are measured.

2. *Floating in the atmosphere of Titan, SPEX novel spectropolarimetric technique would provide a valuable contribution to characterizing the famous hazes.*

The DISR instrument on the Huygens probe also had polarimetric capabilities for studying Titan's atmosphere at the Huygens site [Tomasko et al., 2008]. The disadvantage of the classical technique used by DISR is that the separate radiance measurements that are used to derive the degree of polarization of the observed light are not performed simultaneously, and through different optical systems. As a result, the degree of polarization P that is hence obtained can have an error of several percent, which is too large to use polarimetry to its full potential. SPEX (Spectropolarimeter for Planetary EXploration) measures the radiance I and degree of polarization P of scattered sunlight in the visible range, with 2 (I) to 20 nm (P) spectral resolution (current design). SPEX uses birefringent crystals to modulate the flux spectrum I with P. The main advantages of this novel technique are that I and P are measured simultaneously, and without moving parts. Since SPEX would be able to measure the scattered radiance and the (complete) state of polarization simultaneously and continuously from 0.4 to 0.8 μm, and of course because it would float through the atmosphere as part of the balloon payload, it could add tremendously to our knowledge on Titan's haze particles.

3. *Minor adaptations of the SPEX instrument as designed for placement on a Mars orbiter would be needed if SPEX were to fly on a Titan balloon.*

   SPEX has originally been designed as payload for a Mars orbiter, with 7 fixed downward viewing and 2 fixed limb-viewing apertures, parallel to the orbiter's ground track. We studied the accuracy of the demodulation algorithm and its spectral resolution using simulated Titan spectra in combination with the SPEX end-to-end simulator. The main difference between the Mars mission (SPEX current design) and the Titan mission (SPEX new design) would be the spectral resolution with which P is retrieved: while a Mars spectrum shows little to no spectral features across SPEX' wavelength region, a Titan spectrum is rich with methane absorption bands. In order to better resolve the methane band features and to reach a retrieval accuracy within the target error, we have to increase the sampling frequency of the demodulation algorithm. An optimal retrieval was found for a MgF_2-Al_2O_3 crystal thickness of 16 mm, four times as thick as in the current SPEX design (for a Mars mission), yielding a retardance $\delta \simeq 80$ μm. It is important to notice that, while increasing the total thickness of the MgF_2-Al_2O_3 crystal, its "athermal" property is preserved by keeping the thickness ratio between the two crystals equal to $d_1 : d_2 = 2.4$. For the new design of SPEX, the MgF_2 crystal thickness has to be of 11.30 mm, and the thickness of the Al_2O_3 crystal of 4.7 mm. For $\delta \simeq 80$ μm, the optimized spectral resolution of the polarization spectra is 2 nm in the blue and 8 nm in the red (respectively 8 nm and 32 nm for the Mars-SPEX). In addition, a wavelength coverage from 0.5 to 0.72 μm could be considered for the Titan-SPEX. Such a wavelength range would have the additional advantage that it excludes the deep methane band at 0.73 μm, which is especially difficult to fit with our current demodulation algorithm. Moreover the Mars design, with a number of fixed viewing apertures, would force SPEX to look in one direction and measure only forward scattered light in Titan's atmosphere, if, for example, the balloon is floating towards the sun. Our numerical simulations have shown the importance of sampling I but especially P at various viewing angles. An interesting solution that would allow the required angular sampling while limiting the number of moving elements, would be to have the detector part of the SPEX instrument on the balloon's gondola and have an extra rotating disk on the edge of a boom underneath the gondola on which only the viewing apertures of the instrument will be placed in. The disk should be inclined under an angle of 40° with respect to the vertical axis and with a number of apertures looking outward along the rim of the disk.

9.2 Recommendations

1. *The increase of the size of the aerosol particles in the numerical simulations.*

   Numerical simulations of radiative transfer taking place inside the atmosphere of Titan should be done using aerosol particles composed by $N \geq 3000$ monomers as suggested by Tomasko et al. [2008]. This means that the T-matrix code should be adapted to simulate single scattering for such large aggregates or simulations should be run using other means such as DDA-Scattering methods. On the other side, it is important to stress that using aggregates with only $N = 256$, as done for this study, is not pointless: big aggregates could be considered as formed by these smaller units.

2. *The variation in the composition of the aerosol particles.*

   We assumed that the aerosol particles are composed by nitrogen and methane in the proportion N_2:CH_4=98:2 according to Ramirez et al. [2002]. This composition was taken into account in the particles refractive index. Particles with different composition will have a different refractive index (different absorption properties) and will yield different single scattering properties. It would be interesting and useful to simulate radiative transfer taking place inside the atmosphere of Titan using aerosol particles with different compositions than ours and study how these changes would affect the results.

3. *The variation of the aerosol vertical profile.*

   In our simulations we considered the aerosol vertical profile retrieved with the DISR by Tomasko et al. [2008] during the Huygens descent. It would be recommendable to simulate altitude variations of the aerosols vertical profile, may be assuming different profiles for different locations in the atmosphere of Titan.

4. *To consider the presence of clouds.*

   Cloud microphysics should be taken into account since clouds could form during all Titan's year. Clouds should be formed also by methane aerosol particles and are of fundamental importance to further constrain the methane cycle taking place on Titan. SPEX, in fact, could be used to get information also about the clouds.

5. *To improve the error retrieval and to adapt the retrieval wavelength range.*

   It must be said that the SPEX simulator is still under development. We noticed that in the deepest parts of the methane bands, the error of our retrieved degree of polarization P can still exceed our target error. Therefore if we want to use these parts to retrieve aerosol properties (see Stam et al. [1999]), the instrument response has to be taken into account in the retrieval algorithm. Adapted demodulation algorithms, e.g. algorithms that distinguish between the continuum and the methane bands, could be considered if the inclusion of the deep band of 0.73μm is interesting for scientific reasons.

6. *To build a prototype of the Titan-SPEX.*

   The end-to-end simulator is a powerful tool to test the possible performances of SPEX, but a physical prototype of the Titan-SPEX could be more useful. In order to test the capability of SPEX' new design, the prototype could be tested on a tropospheric balloon for Earth-based experiments with the scope of retrieving the properties of the aerosols on Earth. Wavelength range and viewing apertures should be adapted consequently.

7. *To propose the Titan-SPEX for missions to other planets.*

   The Titan-SPEX design can be adapted for in-situ explorations of planets characterized by a thick atmosphere. An example is the planet Venus. An in-situ mission to Venus in fact, has been proposed within the ESA's Cosmic Vision Program with the name European Venus Explorer (EVE) [Chassefière et al., 2009]. The baseline EVE mission consists of an orbiter, a descent probe, but also of a balloon probe as planned for the TSSM. The EVE's balloon payload is focused on all aspects of cloud-level processes. One of the key instruments would be an optical spectrometer which should be able to characterize the cloud and haze particles composition, and measurement of dynamics, radiative balance, and their microphysical properties. Therefore SPEX, especially as designed for the TSSM balloon, could definitively contribute to the central theme of the EVE mission, which is to understand the evolution of Venus and its climate. Also in this case, as for the Earth-based missions, wavelength range and viewing apertures should be adapted consequently.

Bibliography

S.K. Atreya, E.Y. Adams, H.B. Niemann, J.E. Demick-Montelara, T.C. Owen, M. Fulchignoni, F. Ferri, and E.H. Wilson. Titan's methane cycle. *Planetary and Space Science*, 54(12):1177–1187, 2006.

S.K. Atreya, J.I. Lunine, H.B. Niemann, and T.C. Owen. Origin and Evolution of Titan's Nitrogen-Methane Atmosphere: A Cassini-Huygens Perspective. *AGU Fall Meeting Abstracts*, page 06, 2008.

A. Bar-Nun, V. Dimitrov, and M. Tomasko. Titan's aerosols: Comparison between our model and DISR findings. *Planetary and Space Science*, 56(5):708–714, 2008.

J.W. Barnes, R.H. Brown, L. Soderblom, B.J. Buratti, C. Sotin, S. Rodriguez, S. Le Mouèlic, K.H. Baines, R. Clark, and P. Nicholson. Global-scale surface spectral variations on Titan seen from Cassini/VIMS. *Icarus*, 186(1):242–258, 2007.

FA Berry, E. Bollay, and N.R. Beers. Handbook of meteorology. 1945.

M. Cabane, E. Chassefiere, and G. Israel. Formation and growth of photochemical aerosols in Titan's atmosphere. *Icarus*, 96(2):176–189, 1992.

M. Cabane, P. Rannou, E. Chassefiere, and G. Israel. Fractal aggregates in Titan's atmosphere. *Planetary and Space Science*, 41(4):257–267, 1993.

S. Chandrasekhar. *Radiative Transfer. Clarendon.* Oxford, 1950.

E. Chassefière, O. Korablev, T. Imamura, K.H. Baines, C.F. Wilson, D.V. Titov, K.L. Aplin, T. Balint, J.E. Blamont, C.G. Cochrane, et al. European Venus Explorer (EVE): an in-situ mission to Venus. *Experimental Astronomy*, 23(3):741–760, 2009.

A. Coustenis. Formation and Evolution of TitanŠs Atmosphere. *Space Science Reviews*, 116(1):171–184, 2005.

A. Coustenis, E. Lellouch, J.P. Maillard, and C.P. McKay. Titan's surface: composition and variability from the near-infrared albedo. *Icarus*, 118(1):87–104, 1995.

I. Dahl. How to measure the Mueller matrix of liquid-crystal cells. *Measurement Science and Technology*, 12(11):1938–1948, 2001.

J.F. De Haan, P.B. Bosma, and J.W. Hovenier. The adding method for multiple scattering calculations of polarized light. *Astronomy and Astrophysics (ISSN*, 183 (2):371–391, 1987.

I. de Pater and J.J. Lissauer. Planetary Sciences. *Planetary Sciences, by Imke de Pater and Jack J. Lissauer*, page 544, 2001.

W.A. De Rooij and C. Van der Stap. Expansion of Mie scattering matrices in generalized spherical functions. *Astronomy and Astrophysics (ISSN)*, 131(2):237–248, 1984.

F.M. Flasar, R.K. Achterberg, B.J. Conrath, P.J. Gierasch, V.G. Kunde, C.A. Nixon, G.L. Bjoraker, D.E. Jennings, P.N. Romani, A.A. Simon-Miller, et al. Titan's atmospheric temperatures, winds, and composition. *Science*, 308(5724):975, 2005.

A.D. Fortes. Surface Processes on Titan: A Review of the Literature, 1997. URL `http://www.es.ucl.ac.uk/research/planetary/undergraduate/dom/weathering_titan/tocf.htm`.

A. Fresnel. Memoire sur la diffraction de la lumiere. *da p. 339 a p. 475: 1 tav. ft; AQ 210*, 1819.

M. Fulchignoni, F. Ferri, F. Angrilli, AJ Ball, A. Bar-Nun, MA Barucci, C. Bettanini, G. Bianchini, W. Borucki, G. Colombatti, et al. In situ measurements of the physical characteristics of Titan's environment. *Nature*, 438(7069):785–791, 2005.

S.G. Gibbard, B. Macintosh, D. Gavel, C.E. Max, I. de Pater, H.G. Roe, A.M. Ghez, E.F. Young, and C.P. McKay. Speckle imaging of Titan at 2 microns: Surface albedo, haze optical depth, and tropospheric clouds 1996–1998. *Icarus*, 169(2):429–439, 2004.

C.A. Griffith, P. Penteado, K. Baines, P. Drossart, J. Barnes, G. Bellucci, J. Bibring, R. Brown, B. Buratti, F. Capaccioni, et al. The evolution of Titan's mid-latitude clouds. *Science*, 310(5747):474–477, 2005.

J.E. Hansen and L.D. Travis. Light scattering in planetary atmospheres. *Space Science Reviews*, 16(4):527–610, 1974.

O.P. Hasekamp and J. Landgraf. Retrieval of aerosol properties over land surfaces: capabilities of multiple-viewing-angle intensity and polarization measurements. *Applied optics*, 46(16):3332–3344, 2007.

E. Hecht. *Optics. Massachusetts.* Addison-Wesley, 1987.

M. Hirtzig, T. Tokano, S. Rodriguez, S. Le Mouélic, and C. Sotin. A review of TitanŠs atmospheric phenomena. *Astronomy and Astrophysics Review*, 17(2):105–147, 2009.

J.W. Hovenier and C.V.M. Van der Mee. Fundamental relationships relevant to the transfer of polarized light in a scattering atmosphere. *Astronomy and Astrophysics*, 128:1–16, 1983.

J.W. Hovenier, H.C. Van de Hulst, and C.V.M. Van der Mee. Conditions for the elements of the scattering matrix. *Astronomy and Astrophysics (ISSN*, 157(2):301–310, 1986.

J.W. Hovenier, C.V.M. Mee, and H. Domke. *Transfer of polarized light in planetary atmospheres: basic concepts and practical methods.* Kluwer Academic Publishers, 2004.

E. Karkoschka. Methane, Ammonia, and Temperature Measurements of the Jovian Planets and Titan from CCD–Spectrophotometry. *Icarus*, 133(1):134–146, 1998.

C.U. Keller. Instrumentation for astrophysical spectropolarimetry. *Astrophysical Spectropolarimetry*, pages 303–354, 2002.

H.U. Keller, B. Grieger, M. K
”uppers, S.E. Schr
”oder, Y.V. Skorov, and M.G. Tomasko. The properties of Titan's surface at the Huygens landing site from DISR observations. *Planetary and Space Science*, 56(5): 728–752, 2008.

P. Lavvas, R.V. Yelle, and V. Vuitton. The detached haze layer in Titan's mesosphere. *Icarus*, 201(2):626–633, 2009.

P. P. Lavvas, A. Coustenis, and I. M. Vardavas. Coupling photochemistry with haze formation in Titan's atmosphere, Part II: Results and validation with Cassini/Huygens data. *Planetary and Space Science*, 56:67–99, jan 2008. doi: 10.1016/j.pss.2007.05.027.

R.D. Lorenz and J.I. Lunine. Titan's snowline. *Icarus*, 158(2):557–559, 2002.

J.I. Lunine and S.K. Atreya. The methane cycle on Titan. *Nature Geoscience*, 1(3): 159–164, 2008.

D.W. Mackowski and M.I. Mishchenko. Calculation of the T matrix and the scattering matrix for ensembles of spheres. *Journal of the Optical Society of America A*, 13 (11):2266–2278, 1996.

T.B. McCord, G.B. Hansen, B.J. Buratti, R.N. Clark, D.P. Cruikshank, E. D'Aversa, C.A. Griffith, E.K.H. Baines, R.H. Brown, and C.M. etc. Dalle Ore. Composition of Titan's surface from Cassini VIMS. *Planetary and Space Science*, 54(15):1524–1539, 2006.

CP McKay, A. Coustenis, RE Samuelson, MT Lemmon, RD Lorenz, M. Cabane, P. Rannou, and P. Drossart. Physical properties of the organic aerosols and clouds on Titan. *Planetary and Space Science*, 49(1):79–99, 2001.

M.I. Mishchenko and L.D. Travis. Satellite retrieval of aerosol properties over the ocean using measurements of reflected sunlight: Effect of instrumental errors and aerosol absorption. *Journal of Geophysical Research*, 102(D12):13543, 1997.

M.I. Mishchenko, J.W. Hovenier, and L.D. Travis. *Light scattering by nonspherical particles: theory, measurements, and applications.* Academic Pr, 2000.

O. Mousis, D. Gautier, and D. Bockelée-Morvan. An Evolutionary Turbulent Model of Saturn's Subnebula: Implications for the Origin of the Atmosphere of Titan. *Icarus*, 156(1):162–175, 2002a.

O. Mousis, D. Gautier, and A. Coustenis. The D/H Ratio in Methane in Titan: Origin and History. *Icarus*, 159(1):156–165, 2002b.

H.B. Niemann, S.K. Atreya, S.J. Bauer, G.R. Carignan, J.E. Demick, R.L. Frost, D. Gautier, J.A. Haberman, D.N. Harpold, D.M. Hunten, et al. The abundances of constituents of Titan's atmosphere from the GCMS instrument on the Huygens probe. *Nature*, 438:779–784, 2005.

E.V. Petrova, V.P. Tishkovets, and K. Jockers. Polarization of light scattered by solar system bodies and the aggregate model of dust particles. *Solar System Research*, 38 (4):309–324, 2004.

S.I. Ramirez, P. Coll, A. Da Silva, R. Navarro-Gonzalez, J. Lafait, and F. Raulin. Complex refractive index of Titan's aerosol analogues in the 200-900 nm domain. *Icarus*, 156(2):515–529, 2002.

P. Rannou, M. Cabane, and E. Chassefière. Growth of aerosols in Titan's atmosphere and related time scales: A stochastic approach. *Geophysical Research Letters*, 20 (10), 1993.

P. Rannou, F. Hourdin, and C.P. McKay. A wind origin for Titan's haze structure. *Nature*, 418(6900):853–856, 2002.

P. Rannou, F. Montmessin, F. Hourdin, and S. Lebonnois. The latitudinal distribution of clouds on Titan. *Science*, 311(5758):201–205, 2006.

F. Raulin. Question 2: Why an Astrobiological Study of Titan Will Help Us Understand the Origin of Life. *Origins of Life and Evolution of Biospheres*, 37(4):345–349, 2007.

H. Roe. Titan's Methane Weather. In *American Astronomical Society, AAS Meeting# 214,# 219.05*, 2009.

S.V. Salinas, B. Grieger, W.J. Markiewicz, and H.U. Keller. A spherical model for computing polarized radiation in Titan's atmosphere. *Planetary and Space Science*, 51(14-15):977–989, 2003.

Y.V. Skorov, H.U. Keller, and A.V. Rodin. Optical properties of aerosols in Titan's atmosphere. *Planetary and Space Science*, 56(5):660–668, 2008.

F. Snik. Design study for spectral polarization encoders for SPEX. 2008.

F. Snik, T. Karalidi, C. Keller, E. Laan, R. ter Horst, R. Navarro, D. Stam, C. Aas, J. de Vries, G. Oomen, et al. SPEX: an in-orbit spectropolarimeter for planetary exploration. In *Proceedings of SPIE*, volume 7010, page 701015, 2008.

F. Snik, T. Karalidi, and C.U. Keller. Spectral modulation for full linear polarimetry. *Applied Optics*, 48(7):1337–1346, 2009.

D.M. Stam. Spectropolarimetric signatures of Earth-like extrasolar planets. *Astronomy and Astrophysics*, 482(3):989–1007, 2008.

D.M. Stam, J.F. De Haan, J.W. Hovenier, and P. Stammes. Degree of linear polarization of light emerging from the cloudless atmosphere in the oxygen A band. *Journal of Geophysical Research*, 104:16, 1999.

D.M. Stam, J.F. De Haan, J.W. Hovenier, and P. Stammes. A fast method for simulating observations of polarized light emerging from the atmosphere applied to the oxygen-A band. *Journal of Quantitative Spectroscopy and Radiative Transfer*, 64(2): 131–149, 2000.

V.P. Tishkovets, E.V. Petrova, and K. Jockers. Optical properties of aggregate particles comparable in size to the wavelength. *Journal of Quantitative Spectroscopy and Radiative Transfer*, 86(3):241–265, 2004.

G. Tobie, J.I. Lunine, and C. Sotin. Episodic outgassing as the origin of atmospheric methane on Titan. *Nature*, 440(7080):61–64, 2006.

G. Tobie, M. Choukroun, O. Grasset, S. Le Mouélic, JI Lunine, C. Sotin, O. Bourgeois, D. Gautier, M. Hirtzig, S. Lebonnois, et al. Evolution of Titan and implications for its hydrocarbon cycle. *Philosophical Transactions of the Royal Society A: Mathematical, Physical and Engineering Sciences*, 367(1889):617, 2009.

M.G. Tomasko, L.R. Doose, P.H. Smith, R.A. West, L.A. Soderblom, M. Combes, B. Bezard, A. Coustenis, C. de Bergh, E. Lellouch, et al. The Descent Imager/Spectral Radiometer Aboard Huygens. *Huygens: Science, Payload and Mission*, 1177:109, 1997.

M.G. Tomasko, B. Archinal, T. Becker, B. Bézard, M. Bushroe, M. Combes, D. Cook, A. Coustenis, C. De Bergh, L.E. Dafoe, et al. Rain, winds and haze during the Huygens probe's descent to Titan's surface. *Nature*, 438(7069):765–778, 2005.

M.G. Tomasko, L. Doose, S. Engel, L.E. Dafoe, R. West, M. Lemmon, E. Karkoschka, and C. See. A model of Titan's aerosols based on measurements made inside the atmosphere. *Planetary and Space Science*, 56(5):669–707, 2008.

MG Tomasko, LR Doose, LE Dafoe, and C. See. Limits on the size of aerosols from measurements of linear polarization in Titan?s atmosphere. *Icarus*, 2009.

B.N. Tran, M. Force, R.G. Briggs, J.P. Ferris, P. Persans, and J.J. Chera. Titan's atmospheric chemistry: Photolysis of gas mixtures containing hydrogen cyanide and carbon monoxide at 185 and 254 nm. *Icarus*, 2007.

TSSM Study Final Report. Titan Saturn System Mission Study Final Report on the NASA Contribution to a Joint Mission with ESA. 2009.

H.C. Van de Hulst. Light Scattering by Small Particles 1Wiley. *New York*, 425, 1957.

S. Vinatier, B. Bézard, C.A. Nixon, A. Mamoutkine, R.C. Carlson, D.E. Jennings, E.A. Guandique, N.A. Teanby, G.L. Bjoraker, F. Michael Flasar, et al. Analysis of Cassini/CIRS limb spectra of Titan acquired during the nominal mission. I: Hydrocarbons, nitriles and CO2 vertical mixing ratio profiles. *Icarus*, 2009.

J.H. Waite Jr, D.T. Young, T.E. Cravens, A.J. Coates, F.J. Crary, B. Magee, and J. Westlake. The process of tholin formation in Titan's upper atmosphere. *Science*, 316(5826):870, 2007.

J.M. Wallace and P.V. Hobbs. *Atmospheric science: an introductory survey.* Academic press, 2006.

O. Witasse, J.P. Lebreton, M.K. Bird, R. Dutta-Roy, W.M. Folkner, R.A. Preston, S.W. Asmar, L.I. Gurvits, S.V. Pogrebenko, I.M. Avruch, et al. Overview of the coordinated ground-based observations of Titan during the Huygens mission. *Journal of Geophysical Research*, 111(E07S01), 2006.

Appendix

Appendix A

Article presented at the IPPW-7

The work presented in this MSc Thesis report has been presented also at the 7^{th} International Planetary Probe Workshop (IPPW-7) that took place in Barcelona on June 14-18, 2010. I was selected to give an oral presentation (there were also poster presentations) and I won the first prize as ”Outstanding student oral presentation”.

CHARACTERIZING TITAN'S HAZE WITH A BALLOON-BORNE SPECTROPOLARIMETER SPEX

N. Silvestri^{1,2}**, D. M. Stam**^{1}**, J. M. Smit**^{1}**, and J. H. H. Rietjens**^{1}

^{1}*Earth and Planetary Science Division, SRON Netherlands Institute of Space Research, Sorbonnelaan 2, 3584 CA, Utrecht, The Netherlands*
^{2}*Astrodynamics & Space Missions Department, Faculty of Aerospace Engineering, Delft University of Technology, Kluyverweg 1, 2629 HS, Delft, The Netherlands - Email: nicoletta.silvestri@gmail.com, d.m.stam@sron.nl, j.m.smit@sron.nl, j.h.h.rietjens@sron.nl*

ABSTRACT

Saturn's moon Titan has a thick, hazy atmosphere. Knowing the properties of the hazes is crucial for understanding the existence and evolution of this atmosphere and the dynamical processes that take place. We present SPEX, the Spectropolarimeter for Planetary EXploration, as an instrument to retrieve information on the number density, composition, size and shape of the haze particles. As payload on a balloon that floats through Titan's atmosphere, SPEX would measure simultaneously the radiance and degree and direction of linear polarization of sunlight that has been scattered within Titan's atmosphere from 0.4 to 0.8 μm. In particular the degree of linear polarization of the scattered light is known to be very sensitive to the microphysical properties of the scattering particles. We show numerical simulations of radiance and polarization spectra of scattered sunlight and of radiance and polarization spectra as retrieved from the SPEX observations. The spectral resolution of the latter spectra depends on our choice of optical components for SPEX. In particular, in order to resolve the strong spectral features that are due to absorption by methane, the birefringent retarder should have a thickness of 16 mm.

Key words: Titan; aerosol; haze; atmosphere; balloon; spectropolarimetry.

1. INTRODUCTION

It has been known since the flybys of the Voyagers that Titan's atmosphere contains thick haze layers. The haze particles are most probably composed of various types of hydrocarbons which might be a sink for methane and its by-products [3, 4], and are thought to have fractal-like shapes [13, 17, 14]. Knowledge on the number density, the microphysical properties (size, shape, and composition) of the haze particles and the spatial and temporal variations therein is key to understanding the radiative, chemical and dynamical processes that take place in this unique atmosphere. Such knowledge can be obtained by measuring and analyzing the radiance and the state (i.e. the degree and direction) of polarization of sunlight that has been scattered by the haze particles. In particular the degree of (linear) polarization is known to be very sensitive to the particles' microphysical properties [1].

In the past decades there have been several planetary missions that carried instruments with polarimetric capabilities to study planetary atmospheres. Examples are Pioneers 10 and 11, Voyager 1 and 2, Pioneer Venus, the Galileo mission, and both the Saturn orbiter and the Huygens probe of the Cassini mission. The polarimetry with these instruments was and is based on measurements of the radiance of the scattered sunlight through polarisation filters in two or three positions (see Eqs. 1.5 and 1.6 of [1]). From combining these separate radiance measurements, the total radiance, the degree and direction of linear polarization can be obtained. The disadvantage of this polarimetric technique is that the separate radiance measurements are not performed simultaneously, and usually through different optical systems (e.g. different polarization filters). As a result, the degree of polarization that is hence obtained can have an error of several percent, which is too large to use polarimetry to its full potential. In addition, the polarimetry on previous and current planetary missions was and is limited to broadband measurements, while the degree of linear polarization shows at least as much spectral features as the radiance [2].

The SPEX instrument (Spectropolarimeter for Planetary EXploration) that we present in this paper, uses a novel polarimetric technique to simultaneously measure the radiance, the degree and the direction of linear polarization of scattered sunlight across the wavelength region from 0.4 to 0.8 μm, with the spectral resolution of the measured radiance spectra of about 2 nm, and that of the polarization spectra somewhat larger [5].

The SPEX instrument can be placed on an orbiter to measure the radiance and state of polarization of sunlight that has been reflected by Titan. This reflected sunlight will mainly contain information on Titan's outer haze layers. Here, we focus on a SPEX as payload for a balloon that floats through the Titan atmosphere as proposed to ESA's Cosmic Vision Programme in the Titan Saturn System Mission (TSSM) proposal [20]. This hot-air balloon would float at an altitude of about 10 km, below the lowest haze layer. SPEX as payload of this balloon would measure the radiance and state of polarization of sunlight that is scattered and transmitted through the haze layers.

SPEX on a balloon would not be the first polarimeter investigating Titan's atmosphere from the inside. The Descent Imager/Spectral Radiometer (DISR) [16] on the Huygens probe also performed polarimetric measurements and obtained valuable information on the shape and size of the aerosols at Huygens landing site [17]. The DISR instrument used two orthogonal polarization filters in combination with a blue and a red filter, thus four separate radiance measurements to determine the radiance and degree of polarization of the scattered sunlight and their broadband spectral variation. The errors resulting from the time differences and the differences in the optical properties of the filters (apart from the error in the polarization due to using only two instead of three radiance measurements per wavelength) will affect the retrieval of the microphysical properties of the haze particles. [1] Since SPEX would be able to measure the scattered radiance and the (complete) state of polarization simultaneously and continuously from 0.4 to 0.8 μm, and of course because it would float through the atmosphere as part of the balloon payload, it could add tremendously to our knowledge on Titan's haze particles.

This paper is structured as follows. In Sect. 2, we define the radiance and state of polarization as measured by SPEX. In Sect. 3, we describe the radiative transfer algorithm and the model planets that we use for our numerical simulations of scattered sunlight, and results of these simulations. In Sect. 4, we describe SPEX and explain its novel polarimetric technique, and present simulated SPEX observations. In Sect. 5, we discuss the adaptations of a SPEX instrument that was designed for a Mars mission to a Titan mission. Section 6 finally, contains the conclusions.

2. RADIANCES AND POLARIZATION

We describe the radiance and state of polarization of a beam of radiation by a Stokes vector **I** [6, 7], as follows

$$\mathbf{I}(\lambda) = \begin{bmatrix} I(\lambda) \\ Q(\lambda) \\ U(\lambda) \\ V(\lambda) \end{bmatrix}, \qquad (1)$$

with λ the wavelength of the radiation, I the total radiance of the beam, Q and U representing the linearly polarized, and V the circularly polarized radiance. All Stokes parameters have the dimension of W m^{-2} sr^{-1} μm^{-1}. Stokes parameters Q and U are defined with respect to a reference plane [1, 8]. For the simulations of light that has been singly scattered by a sample of aerosol particles, we will use the scattering plane, which contains both the direction of the incoming and that of the scattered beam of radiation, as the reference plane. For the simulations of sunlight that has been scattered in Titan's atmosphere, we will use the local meridian plane, which contains both the direction towards the zenith and the direction of propagation of the scattered light.

We define the degree of polarization of the beam of radiation as follows:

$$P(\lambda) = \frac{\sqrt{Q^2(\lambda) + U^2(\lambda) + V^2(\lambda)}}{I(\lambda)}. \qquad (2)$$

In planetary atmospheres, the circularly polarized radiance V is usually very small [1]. We will neglect V, and assume P is the degree of linear polarization of the sunlight that is scattered in Titan's atmosphere:

$$P(\lambda) = \frac{\sqrt{Q^2(\lambda) + U^2(\lambda)}}{I(\lambda)}. \qquad (3)$$

For incident unpolarized light that has been singly scattered by a sample of aerosol particles, U equals zero, and we will use the following definition of the degree of polarization that includes information on the polarization direction

$$P_\mathrm{S} = -\frac{Q}{I}. \qquad (4)$$

If P_S is positive (negative), the light is polarized perpendicular (parallel) to the scattering plane.

For the sunlight that has been scattered in Titan's atmosphere, the direction of (linear) polarization with respect to the reference plane is represented by the angle:

$$\chi(\lambda) = \frac{1}{2} \arctan \frac{U(\lambda)}{Q(\lambda)}, \qquad (5)$$

where the value of χ that should be chosen is the one which makes $\cos 2\chi$ have the same sign as Q [1]. When $\chi = 90^\circ$ ($\chi = 0^\circ$), the direction of polarization is perpendicular (parallel) to the reference plane.

From SPEX measurements, we can derive the total radiance I, the degree of linear polarization P, and the direction of polarization χ of light, as functions of λ. Note that in order to derive the absolute total radiance, we will have to calibrate SPEX, e.g. by using an internal reference light source. No such calibration is required for deriving P and χ, since these are relative measures.

3. CALCULATING SCATTERED SUNLIGHT

3.1. Our radiative transfer algorithm

For our numerical simulations of sunlight that is scattered in Titan's atmosphere, we use an adding-doubling algo-

---

[1] Using two instead of three polarization filters can in principle be accounted for in the radiative transfer calculations in the retrieval, but the missing information will limit the accuracy of the retrievals.

rithm that fully includes multiple scattering and polarization [8, 9]. The algorithm is monochromatic, i.e. every wavelength is treated separately.

The algorithm (for details of the calculations, see [8]) assumes a model atmosphere that consists of a stack of horizontally homogeneous layers that can differ from each other, and that is bounded below by a horizontally homogeneous surface. The surface reflects Lambertian (i.e. isotropic and completely depolarizing) with a (wavelength dependent) albedo $A_{\rm S}$. Each atmospheric layer contains gaseous molecules and, optionally, aerosol particles. For each layer, we have to specify for each type of particles, their column number density (in $\rm m^{-2}$), and for each wavelength λ, their extinction cross-section σ, single scattering albedo $\tilde{\omega}$ and single scattering matrix $\mathbf{F}$.

The (total) optical thickness of a layer due to a certain type of particles and at a given wavelength is calculated by multiplying the column number density of the particles with their extinction cross-section at the given wavelength. The optical thickness b of a layer is thus given by

$$\begin{aligned} b(\lambda) &= b_{\rm m}(\lambda) + b_{\rm a}(\lambda) \\ &= b_{\rm msca}(\lambda) + b_{\rm mabs}(\lambda) + b_{\rm asca}(\lambda) + b_{\rm aabs}(\lambda) \end{aligned} \quad (6)$$

with $b_{\rm m}$ and $b_{\rm a}$ the optical thicknesses of the gases and the aerosol particles, respectively, which are the sums of the scattering and the absorption optical thicknesses of the gases and the aerosol particles, $b_{\rm msca}$, $b_{\rm mabs}$, $b_{\rm asca}$, and $b_{\rm aabs}$, respectively. Obviously, $b_{\rm msca} = \tilde{\omega}_{\rm m}\; b_{\rm m}$, and $b_{\rm asca} = \tilde{\omega}_{\rm a}\; b_{\rm a}$. The single scattering albedo $\tilde{\omega}$ of the mixture of gases and particles in a layer is given by

$$\tilde{\omega}(\lambda) = \frac{b_{\rm msca}(\lambda) + b_{\rm asca}(\lambda)}{b_{\rm m}(\lambda) + b_{\rm a}(\lambda)}. \quad (7)$$

The single scattering matrix $\mathbf{F}$ of the gases and particles in a layer is given by

$$\mathbf{F}(\Theta, \lambda) = \frac{b_{\rm msca}(\lambda)\mathbf{F}_{\rm m}(\Theta, \lambda) + b_{\rm asca}(\lambda)\mathbf{F}_{\rm a}(\Theta, \lambda)}{b_{\rm msca}(\lambda) + b_{\rm asca}(\lambda)} \quad (8)$$

where Θ is the single scattering angle ($0^\circ \leq \Theta \leq 180^\circ$, $\Theta = 0^\circ$ implies forward scattering), and $\mathbf{F}_{\rm m}$ and $\mathbf{F}_{\rm a}$ are the single scattering matrices of the gaseous molecules and the aerosol particles, respectively [8]. Each scattering matrix is normalized such that the average of the single scattering phase function, i.e. element F_{11} of each matrix, over all scattering angles equals one, as follows

$$\frac{1}{4}\int_0^{4\pi} F_{11}(\Theta, \lambda) d\Omega = 1, \quad (9)$$

where $d\Omega$ is an element of solid angle. If incident light is unpolarized, the degree of linear polarization of the light that is singly scattered by the gases and particles can be written as $P_{\rm S} = -F_{12}/F_{11}$ (cf. Eq. 4).

Apart from the properties of the surface and atmosphere, the radiative transfer depends on the illumination and viewing geometries. We specify the solar zenith angle θ_0 (the angle between the direction towards the sun and the upward vertical), the instrument zenith viewing angle θ (the angle between the direction of propagation of the observed light and the downward vertical), and the azimuthal angles ϕ_0 and ϕ that are measured between an arbitrary vertical plane and the directions of propagation of, respectively, the incoming and observed beams of radiation. Since our model atmosphere and surface are horizontally homogeneous, only $\phi - \phi_0$ is relevant. When $\phi - \phi_0 = 0^\circ$, the instrument is looking in the direction towards the sun. When $\phi - \phi_0 = 180^\circ$, it has the sun 'in its back.'

Since we assume that SPEX will be payload on a balloon floating below Titan's lowest haze layer, it will observe sunlight that has been transmitted through the atmosphere. With our adding-doubling algorithm, we calculate the transmission matrix $\mathbf{T}$ of the atmosphere-surface system, and obtain the Stokes vector of the transmitted light using [1]

$$\mathbf{I}(\lambda, \theta_0, \theta, \phi - \phi_0) = \cos\theta_0 \mathbf{T}(\lambda, \theta_0, \theta, \phi - \phi_0)\mathbf{F}_0(\lambda), \quad (10)$$

where $\mathbf{F}_0$ is the Stokes vector of the incoming solar radiation, with πF_0 the solar flux at the top of the atmosphere, measured perpendicularly to the direction of incidence. The solar radiation is assumed to be unidirectional and unpolarized, and is thus given by $\mathbf{F}_0 = F_0\mathbf{1}$, with $\mathbf{1}$ the unit column vector. Note that P and χ of the scattered sunlight are independent of F_0.

3.2. The model atmosphere and surface

To describe the reflection of sunlight by Titan's surface, we use a surface albedo equal to 0.04, which is representative for Titan's dark terrain [12].

We model Titan's atmosphere from 0 km to 400 km with 34 layers. We calculate the molecular scattering optical thickness $b_{\rm msca}$ of each layer as described in [8], using the values of [10] for the ambient pressure and temperature at the bottom and top of each layer. Across SPEX' wavelength region, the main gaseous absorption bands are due to methane. We calculate the molecular absorption optical thickness $b_{\rm mabs}$ of each layer as described in [8], using the methane mixing ratio profile from [19] and the methane absorption coefficients from [18].

Apart from gaseous molecules, each atmospheric layer also contains haze aerosol particles. For the simulations presented in this paper, we use the same type of aerosol throughout the atmosphere. We assume that the aerosol optical thickness $b_{\rm a}$ varies with altitude as described by [17], with the total atmospheric $b_{\rm a}$ at λ =550 nm, equal to 8.10. The cumulative $b_{\rm a}$ at $\lambda = 550$ nm as a function of altitude is shown in Fig.1.

The actual wavelength dependence of $b_{\rm a}$, as well as $\tilde{\omega}_{\rm a}$ and $\mathbf{F}_{\rm a}$ of the aerosol particles depends on the particles' microphysical properties (size, shape, composition). We

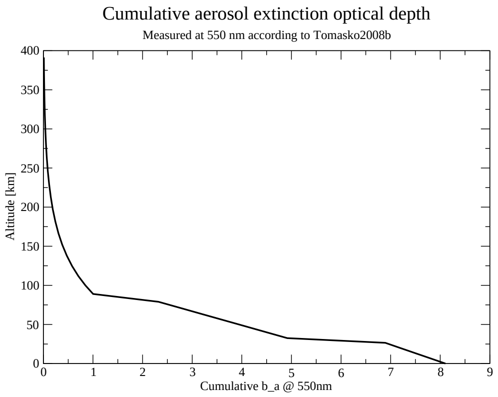

Figure 1. The cumulative optical thickness of the haze aerosol in our model atmosphere as a function of the altitude at $\lambda = 550$ nm (from [17]).

assume aggregate, fractal-type particles that consist of clusters of spherical monomers. In our simulations, we consider particles that formed through Ballistic Particle-Cluster Aggregation (BPCA), and particles that formed through Diffusion-Limited Aggregation (DLA). The difference between the two aggregation processes is that with ballistic aggregation, the monomers move along straight lines before colliding with the aggregate, while with the diffusion limited aggregation, the monomers are subject to Brownian motions. According to [13], BPCA should be more common in the higher, thinner layers of the atmosphere, while DLA is more appropriate for the lower, denser layers.

We calculated the optical properties of the two types of fractal aerosol particles across SPEX' wavelength region using the 3-D positions of the monomers provided by dr. Y.V. Skorov [13] as input for the super-position T-matrix code [15], adopting the refractive index values of [11]. Both our BPCA and our DLA particles consist of 256 monomers, with the monomer's radius equal to 0.05 μm in accordance with [14]. We combined the calculated optical properties of the aggregate particles and their mirror particles. Including the mirror particles removed the negative branch of polarization that [13] found in their single scattering simulations and that did not agree with the DISR observations.

Figure 2 illustrates the shapes of the fractal-type aerosol particles that we used in our model atmosphere. The BPCA-particle is characterized by a compact core that is surrounded by 'arms' of monomers. The DLA-particle lacks the extended arms of monomers. The different shapes of the two types of particles yield different scattering behaviours. In Fig. 3 we show the calculated [15] phase functions and degree of linear polarization $P_{\rm S}$ of unpolarized incident light that is singly scattered by the two types of particles for $\lambda = 0.47$ μm and $\lambda = 0.83$ μm, respectively.

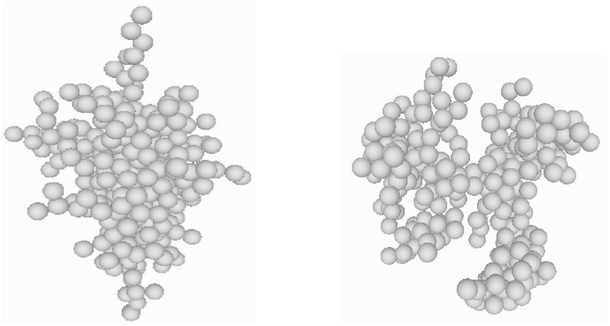

Figure 2. Graphs illustrating the structure of the BPCA-particles (on the left) and the DLA-particles (on the right). Both particle types consist of 256 monomers.

The phase functions for both types of particles clearly show forward scattering behaviour (see Fig. 3). The strength of the forward scattering peak is significantly stronger for both types of particles for the shorter wavelength ($\lambda = 0.47$ μm). With the shorter wavelength, the phase functions for both types of particles also show more angular features. These angular features are much less obvious for $\lambda = 0.83$ μm. Such features are usually due to interference between light that has been scattered by different, similarly sized particles [1]. Apparently, when the light has a short wavelength compared to the fractal particles, the light scattered by the different monomers that make up the fractal particle will interfere and give rise to the angular features [23]. With increasing λ, the light will increasingly be scattered by the fractal particle as a whole, and the interference patterns disappear due to the different scales of the macroscopic particle. Since the DLA-particle is more compact and thus somewhat smaller than the BPCA-particle, its phase function is the more symmetric one at $\lambda = 0.83$ μm.

The degree of linear polarization $P_{\rm S}$ of the light that is singly scattered by the two types of particles (see Fig. 3) shows the bell-shape that is characteristic for light that is scattered by particles that are small with respect to the wavelength [1]. Apparently, this polarization signal is dominated by that of light that is scattered by the monomers. An effect of the macroscopic shape of the particles on $P_{\rm S}$ is found in the strength of the maximum of the polarization curve: with increasing λ, the maximum $P_{\rm S}$ increases more for the compact DLA-particles than for the fluffier BCPA-particles.

3.3. Sunlight that is scattered in Titan's atmosphere

Here, we present results of numerical simulations of the radiance I (Eq. 10) and degree of linear polarization P (Eq. 3) of sunlight that has been scattered in Titan's atmosphere and that emerges at the bottom of the atmosphere. We'll show spectra for different amounts of aerosol particles, for different illumination and viewing geometries, and for the two types of particles. We assume that the incoming solar flux equals π, i.e. $F_0 = 1$ in Eq. 10. In our

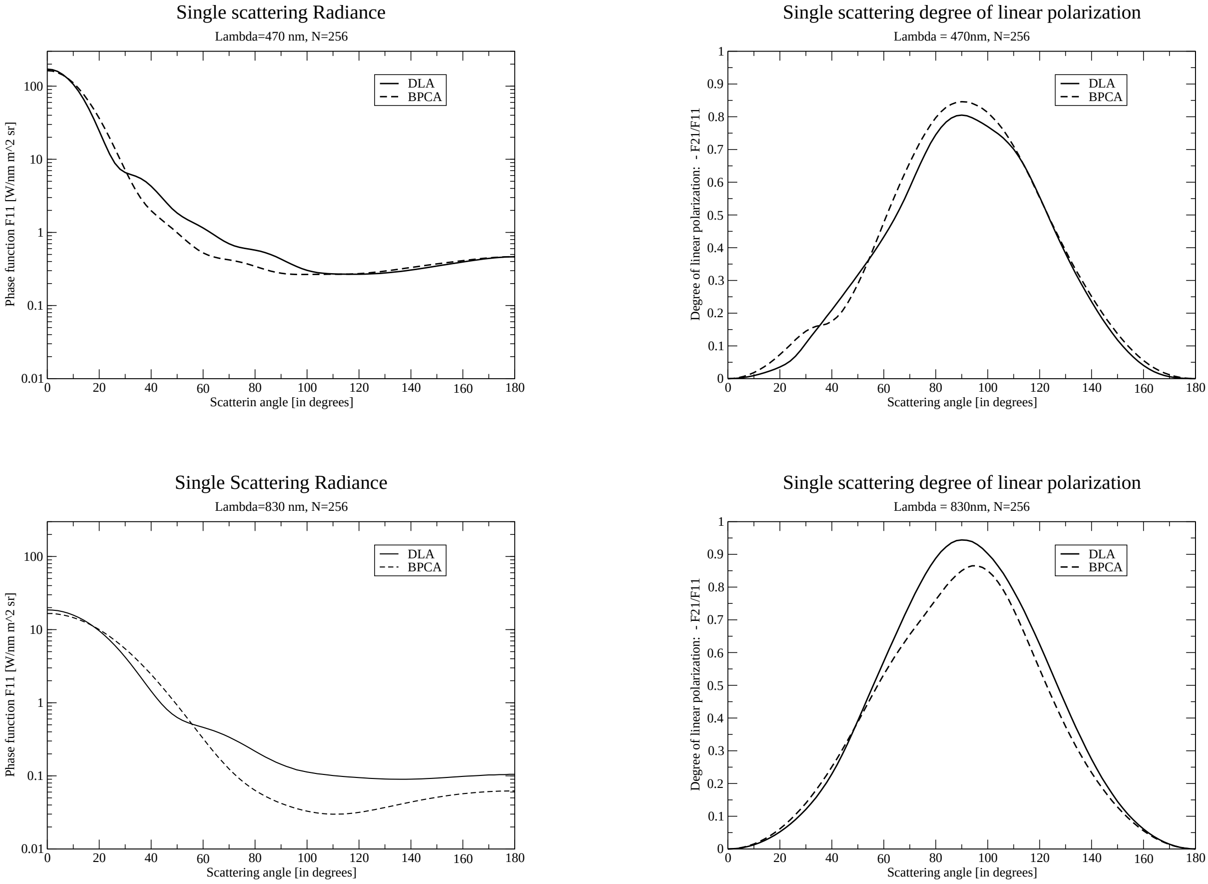

Figure 3. The phase function (left) and degree of linear polarization P_S (right) of unpolarized incident light that is singly scattered by the BPCA-particles (dashed lines) and the DLA-particles (solid lines) as functions of the single scattering angle Θ, for $\lambda = 0.47$ μm (top) and $\lambda = 0.87$ μm (bottom).

discussion of the results, we will focus on the continuum radiances and polarization.

Figure 4 shows I and P as functions of the wavelength λ from 0.3 to 0.9 μm (SPEX' spectral range is somewhat shorter, namely from 0.4 to 0.8 μm). The solar zenith angle θ_0 is 0° (the sun is thus in the zenith), and the viewing angle θ ranges from 0° (looking towards the zenith) to 60°. For $\theta_0 = 0°$, the azimuthal angle $\phi - \phi_0$ is undefined. The aerosol optical thickness profile as shown in Fig. 1 is used, with a total optical thickness of 8.1 at $\lambda = 0.55$ μm, and the aerosol particles are of the DLA-type.

As can be seen in Fig. 4, the scattered radiance spectra show strong absorption lines that are due to the methane in the atmosphere. With increasing λ, the continuum radiance of each spectrum increases steadily because of the decrease of the atmospheric optical thickness (gas + aerosol). The continuum radiance is highest for $\theta = 0°$ and decreases with increasing θ, because of the forward scattering behaviour of the phase function of the aerosol particles (see Fig. 3), and because of the increase of the effective atmospheric optical thickness with increasing θ (the sun is in the zenith).

The scattered polarization spectra (Fig. 4) can, like the radiance spectra, be thought of as to consist of a continuum with super-imposed spectral features that are due to absorption of light by methane. The continuum degree of polarization is small at the smallest wavelengths, because at those wavelengths, the optical thickness b of the atmosphere is relatively large. The multiple scattering of light in an optically thick atmosphere will usually decrease P. With increasing λ, b decreases, the multiple scattering decreases, and the continuum P increases. The continuum P will also depend on the single scattering P_S of the gas molecules and aerosol particles in the atmosphere. For example, at the longest wavelengths, P will be mostly determined by low order scattering by aerosol particles. The values of the continuum P at $\lambda = 0.9$ μm for each value of θ compare very well with those in Fig. 3 for the corresponding single scattering values of Θ (i.e. $\theta_0 = 0°$ and $\theta = 60°$ correspond to $\Theta = 60°$).

From $\lambda \approx 0.4$ to 0.5 μm, the continuum P is low for all values of θ. This is called a 'neutral' point of polarization, and it is due to interference of the polarization signatures of single and second or higher order scattered light. In the methane absorption bands, P generally increases with increasing absorption band strength. This is explained by a decrease of multiple scattering with increasing absorption, and hence an increase of P. However, to fully explain the changing shape of P across gaseous absorption bands, one also has to take into account the single scattering properties of the atmospheric molecules and aerosol particles. In the different parts of the absorption band, the transmitted light has been scattered in different regions of the atmosphere, and will carry the polarization signature of the mixture of aerosol particles and gases in those regions.

Figure 5 is similar to Fig. 4, except that the model atmosphere contains twice the amount of aerosol particles (the vertical profile has the same shape). Comparing the radiance spectra in Figs. 5 and 4, we see that doubling $b_{\rm a}$ leaves the general shape of the radiance spectra untouched, while it lowers the absolute radiance values across the continuum for $\theta = 0°$ and 20°, and increases the absolute radiance values across the continuum for $\theta = 40°$ and 60°. Apparently, increasing $b_{\rm a}$ from 8.1 to 16.2 (at $\lambda = 0.55$ μm), makes the sky brightness more homogeneous.

The polarization spectra in Fig. 5 are very similar in shape to those in Fig. 4, except that at the longer wavelengths, doubling $b_{\rm a}$ has led to a significant decrease of the continuum P, which is due to an increase of multiple scattering. At the shorter wavelengths, the amount of multiple scattering hasn't changed much and P seems rather insensitive to the doubling of $b_{\rm a}$ from 8.1 to 16.2 (at $\lambda = 0.55$ μm), probably because scattering of light by the gas molecules is the most important process at those wavelengths. Interestingly, the neutral points of polarization seem to have shifted towards longer wavelengths with the increase of $b_{\rm a}$.

Figure 6 is similar to Fig. 4, except that the solar zenith angle θ_0 is 30° and 60°, respectively. The azimuthal angle $\phi - \phi_0 = 0°$. For $\theta_0 = 30°$, the viewing angles $\theta = 20°$ and 40° are close (10°) to looking into the direction of the sun, which results in a large continuum radiance at the longest wavelengths, where the forward scattering by the aerosol particles is important. At the longest wavelengths and for $\theta = 60°$, the scattered continuum radiance is larger than for $\theta = 0°$, which means that in the red, the horizon is brighter than the zenith sky. At the shortest wavelengths, where scattering by gas molecules is most important, the horizon ($\theta = 60°$) is darker than the zenith sky. For $\theta_0 = 60°$, the viewing angle of 60° is looking straight into the direction of the sun. At the longest wavelengths, the forward scattering by aerosols makes this direction of the sky very bright (note that the spectra only include the scattered light), while the zenith sky is darkest. At the shortest wavelengths, the direction towards the sun is darkest.

The continuum P for $\theta_0 = 30°$ looks very different from that when $\theta_0 = 0°$. In particular, the viewing directions $\theta = 20°$ and 40°, which are closest to looking directly into the sun yield very low degrees of polarization ($< 2\%$), because this is mostly forward scattered light which has a low degree of polarization (see Fig. 3). The curves for $\theta = 0°$ and 60° pertain to similar single scattering angles (i.e. 30°), yet their shapes are quite different because of the interplay between the degree of polarization of singly scattered light at $\Theta = 30°$ and the ratio of single to multiple scattering. The latter depends strongly on the effective atmospheric optical thickness, which increases with the viewing angle. In particular, for $\theta = 60°$, this results in a broad region where P is about zero (a neutral point), which is absent for $\theta = 0°$. For $\theta_0 = 60°$ (Fig. 6), this low degree of polarization is seen for $\theta = 60°$, while for $\theta = 40°$, which is close towards the direction of the sun, the continuum P is low, too.

Figures 7 and 8 show the effects having BPCA instead of DLA-particles, with the same aerosol optical thickness at 0.55 μm, on the transmitted radiance and degree of polarization. The solar zenith angle is 0° (Fig. 7) or 60° (Fig. 8) and results are shown for $\theta = 0°$ and 60° (with $\phi - \phi_0 = 0°$). As can be seen from the radiance spectra in Fig. 7, the DLA-particles show a stronger forward scattering behaviour than the BPCA-particles. For the polarization, and $\theta = 60°$, we see in Fig. 7 that at the shorter wavelengths, there is little difference between DLA and BPCA, while at the longer wavelengths, there is a large difference (just like we would expect based on Fig. 3). With the sun at 60° (Fig. 8), we can again see the single scattering polarization features (Fig. 3) back in the multiple scattering behaviour. In this geometry, both the DLA- and the BPCA-particles give rise to neutral points at certain wavelengths, especially the DLA-particles. What permits to discern the two spectra, is the location of the neutral points. In Fig.8 for a viewing zenith angle of 60°, the DLA-particle presents neutral points at $\lambda \approx 0.8$ μm that the BPCA-particle does not show. The DLA-particles also give rise to inverted polarization in some of the methane absorption bands.

From the spectra we showed, it is clear that the spectral dependence of the degree of linear polarization of sunlight that is transmitted through Titan's atmosphere shows a stronger variation on the particle-type, than the radiance of this light. The latter does show variations, but the general shape of the spectra remains the same, while the continuum radiance is very dependent on the aerosol optical thickness and would thus not constrain particle type [21]. Obviously, preferably, both the radiance and the polarization are measured.

4. THE SPEX INSTRUMENT

4.1. SPEX' novel spectropolarimetric method

In planetary observations, linear polarimetry of a beam of radiation is traditionally done by measuring the beam's radiance in three different polarization directions, e.g. through a single rotatable polarization filter, or through

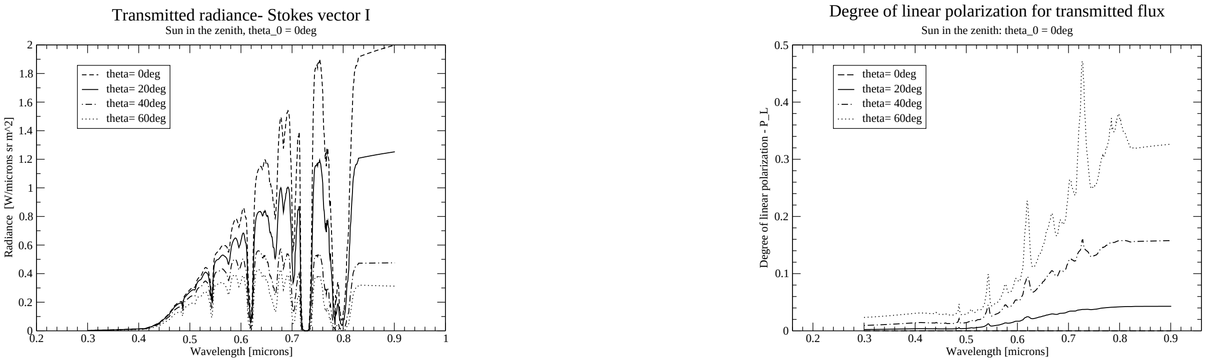

Figure 4. Numerically calculated radiance (on the left) and polarization (right) spectra of sunlight that is scattered in and transmitted through Titan's atmosphere. The solar zenith angle $\theta_0 = 0°$, and the viewing zenith angles are: 0° (solid lines), 20° (dashed lines), 40° (dot-dashed lines), and 60° (dotted lines). Note that for $\theta = 0°$, P equals zero at all wavelengths. The aerosol profile is as shown in Fig. 1 and the aerosol particles are of the DLA-type.

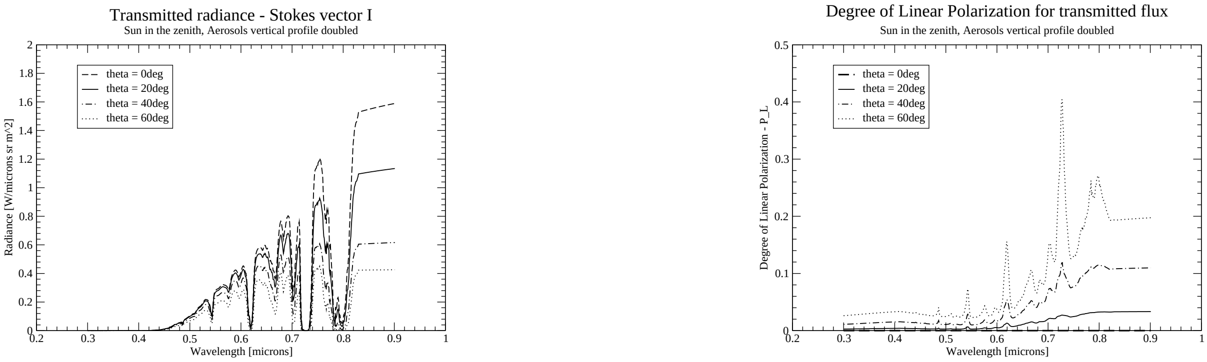

Figure 5. Similar to Fig. 4, except for twice the amount of aerosol particles.

three polarization filters with different orientation angles in a filter wheel. The three radiance measurements are combined to yield the beam's total radiance I, and the linearly polarized radiances Q and U (see [1]). Note that DISR measured only two linearly polarized radiances, hence it could only provide a partial degree of linear polarization, for example, only Q/I, instead of $\sqrt{Q^2 + U^2}/I$ (Eq. 3). The main disadvantages of these traditional polarimetric methods are 1. time differences, hence differences in observed scenes and illumination geometries, between the separate radiance measurements, which can cause errors of several percent in the derived degree of polarization, and/or 2. differences in the optical properties of the optical systems, e.g. filters, through which the separate radiance observations are done. In addition, most traditional polarimeters use rotating filters or filter wheels, which carry the risk of getting stuck, while polarimeters that have three (sometimes two) inert optical systems for the radiance measurements are too heavy for a planetary mission (an example is the APS polarimeter on NASA's Earth observing Glory mission that will be launched at the end of this year).

SPEX uses a novel spectropolarimetric technique which allows simultaneous measurements of the total radiance I, and the degree P and direction χ of polarization from 0.4 to 0.8 μm with a spectral resolution of 2 nm for the radiance to slightly larger for the polarization, without moving parts. In addition to being robust, SPEX is small (< 5 kg) and uses little power. Details on SPEX' polarimetric technique can be found in [5]. Here, we will summarize the main characteristics of the technique.

SPEX' spectropolarimetric technique is based on spectral modulation: the radiance spectrum is sinusoidally modulated by the degree and direction of linear polarization of the incoming radiation. The modulation is achieved by a carefully selected series of (passive) optical components. When leaving this pre-optics, the beam of light has been spectrally modulated and continues towards a spectrometer, where an off-the-shelf detector records the modulated spectrum with a 2 nm spectral resolution. The pre-optics consists of an achromatic quarter-wave plate, an athermal multiple-order retarder, and a polarizing beam-splitter, the effects of which we will explain below.

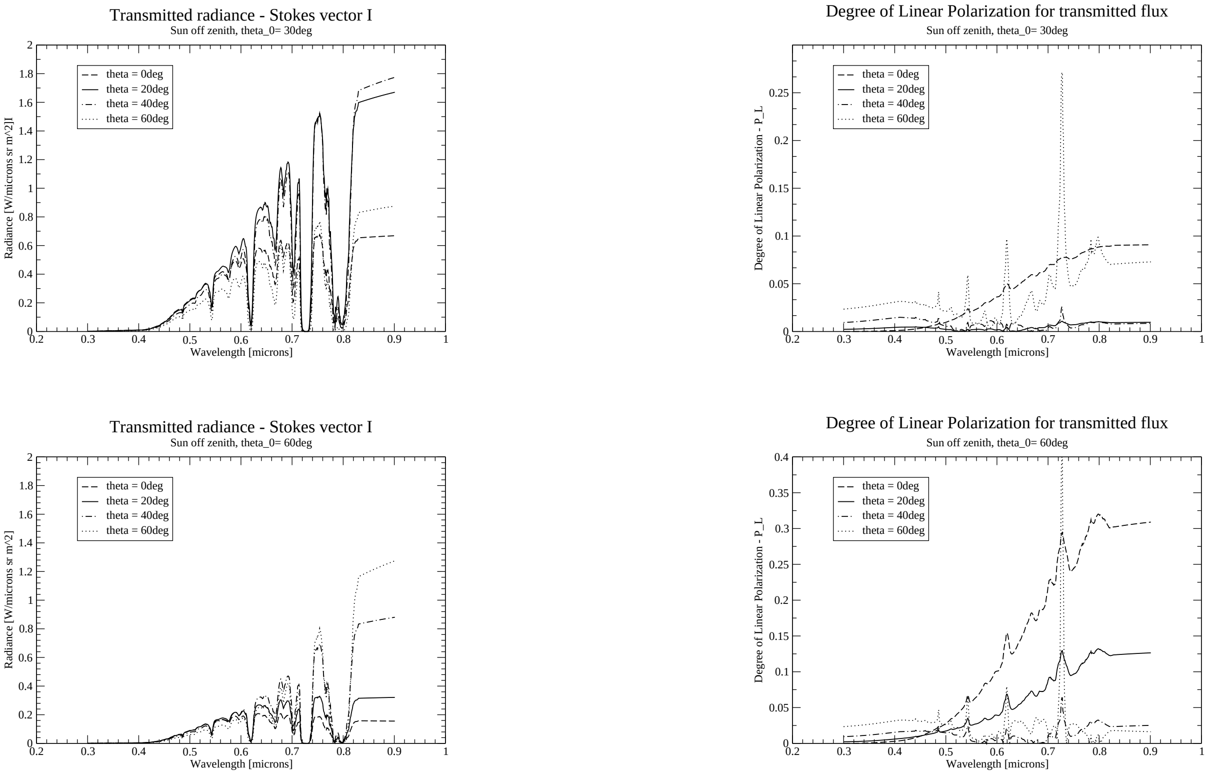

Figure 6. Similar to Fig. 4, except for $\theta_0 = 30^\circ$ (top) and 60° (bottom) instead of 0°. The azimuthal angle $\phi - \phi_0 = 0^\circ$.

1. The achromatic quarter-wave plate
This element has its optical axes oriented such (at 0° and 90°) that Stokes parameter Q passes untouched, while parameter U is converted into circular polarization V (we assume that the light that enters the instrument has $V = 0$). We have chosen a Fresnel rhomb as SPEX' achromatic quarter-wave plate.

2. The athermal multiple-order retarder
This element is the core of the SPEX instrument. A retarder induces a phase difference between two polarization components of a beam of light due to the fact that its indices of refraction have different values for different polarization directions (this is called 'birefringence'). The retarder changes the ellipticity of the light that is incident on it, depending on the wavelength of the light, since the retardance is very achromatic. As an example, light with a wavelength independent degree of linear polarization that is incident on the retarder will leave the optical element with a state of polarization that varies between linear to circular as a function of the wavelength. The axes of our retarder are at 45° and 135°. It consists of MgF_2-Al_2O_3, which has been chosen because its retardance is insensitive to temperature changes.

3. The polarizing beam-splitter
A Wollaston prism is used as a polarizing beam-splitter to filter two orthogonal directions of linear polarized light out of the beam of light that leaves the retarder. Both of the filtered beams have a modulated radiance spectrum with a phase difference of π between them. The modulation is described by the following equations [5]

$$S_\pm(\lambda) = \frac{1}{2} S_0(\lambda) \left[1 \pm P(\lambda) \cos\phi(\lambda)\right], \qquad (11)$$

where the phase is given by

$$\phi(\lambda) = \frac{2\pi\delta(\lambda)}{\lambda} + 2\chi(\lambda), \qquad (12)$$

with δ the retardance of the multiple-order retarder (in m), and χ the angle of polarization. In Eq. 11, S_0 is the incoming (unmodulated) radiance spectrum, P the degree of linear polarization of the incoming light, and $S_\pm$ the detected (modulated) radiance spectrum with either a 'positive' modulation (indicated by the + sign) or a 'negative' modulation (with the - sign). With SPEX, we detect both the S_+ and the S_- spectrum, and it is clear that by adding these two modulated spectra, the incoming radiance spectrum S_0 is obtained with the spectral resolution with which $S_\pm$ are measured. The degree of linear polarization P and the direction of polarization χ can be derived from each of the modulated radiance spectra, using a demodulation algorithm. The spectral resolution of P and χ is on the order of the modulation, which depends on the choice of optical elements, in particular, for a given material of the retarder, on the length of the multiple-order retarder.

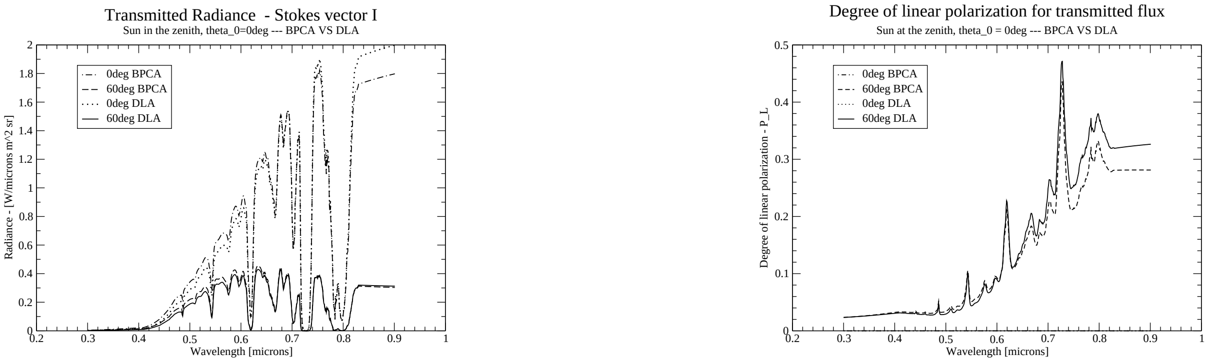

Figure 7. Similar to Fig. 4, except only for the viewing angles $\theta = 0°$ and 60°, and it also includes curves for BPCA-particles instead of DLA-particles (b_a at 0.55 μm is 8.1 for both aerosol types). Note that at $\theta = 0°$, $P = 0$ at all the wavelengths for both BPCA-particle and DLA-particle (see Fig.4).

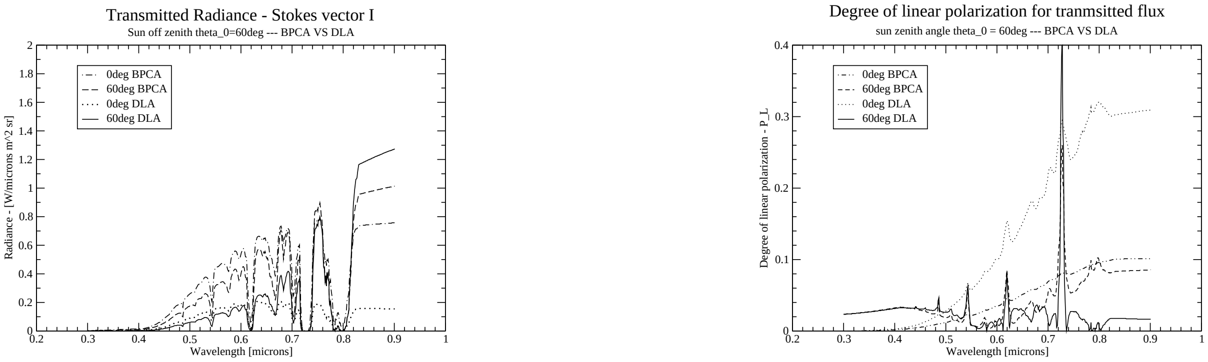

Figure 8. Same as for Fig.7, except for $\theta_0 = 60°$.

4.2. SPEX end-to-end simulator

The SPEX end-to-end simulator is a software tool that fully describes the SPEX instrument, its measurements, and the data analysis for missions to different planets. This tool (which is still under development) facilitates defining the science and instrument requirements, assessing the instrument performance, optimizing calibration routines and tracing potential system degradations during a mission.

The input of the simulator are high-spectral resolution spectra of I, Q, and U (and possibly V), such as those calculated with our adding-doubling radiative transfer algorithm (see Sect. 4). Each optical component of the instrument is modeled using appropriate Mueller matrices including wavelength dependent optical properties of the materials and field-of-view variations of the incident spectra. The modulated spectra at the end of the optical train are imaged on the focal plane array of the detector and binned. A wavelength dependent quantum efficiency, dark-current, read-, shot- and ADC-noise, are included in the calculation, while pixel-to-pixel variations in gain and offset, the effects of pixel cross-talk and detector non-linearity, and the contributions of thermal radiation and stray-light are ignored in the current version (they will be included in future versions).

While the radiance spectrum of the observed light is simply obtained adding S_+ and S_-, the derivation of P and χ and especially their spectral resolution depends on the demodulation algorithm for a given set of optical components. For the demodulation of the measured, modulated radiance spectra S_+ and S_- (see Eq. 11) into spectra of P and χ, we use the technique outlined in [5]. This technique involves fitting of one or more periods of the local modulation. The fitting is applied on each 'spectral window' determined as:

$$\Delta\lambda = \frac{\lambda^2}{\delta(1+\lambda^2/4\delta^2)}, \tag{13}$$

where $\Delta\lambda$ represents a spectral 'window' and δ is the retardance (see Eq.11) across that window. A spectral window covers a small wavelength region of the modulated radiance spectra across which P, χ, and the instrument's optical properties are assumed to be constant. Optimizing $\Delta\lambda$ means optimizing the sampling frequency and therefore, the spectral resolution of P and χ. Note that we have not shown any spectra of χ; it is less sensitive to the atmospheric parameters than either I or P.

4.3. Simulated SPEX' observations

Here, we show the accuracy of the demodulation algorithm and its spectral resolution using simulated Titan spectra shown in Sect. 4 ($0° \leq \theta_0 \leq 80°$, $40° \leq \theta \leq 90°$, $\phi - \phi_0 = 0°, 180°$, and DLA- particles), in combination with the SPEX end-to-end simulator.

The spectral resolution depends mostly on the retardance. We will present results for different values of the retardance δ, starting with the value as chosen for SPEX on a Mars orbiter, namely $\delta \simeq 20\ \mu$m (a crystal thickness of 4 mm), and then optimizing the value for SPEX on a Titan balloon. The main difference between these two missions would be the spectral resolution with which P is retrieved: while a Mars spectrum shows little to no spectral features across SPEX' wavelength region, a Titan spectrum is rich with methane absorption bands.

Figure 9 shows the retrieved P for the Mars-SPEX with $\delta \simeq 20\ \mu$m and the retrieved P optimized for the Titan-SPEX, in which case $\delta \simeq 80\ \mu$m. It also shows the errors in the retrieval, with our target error of at most 5 $\%$ (this error is based on retrieval algorithms for aerosol properties using polarization data [24]. With $\delta \simeq 20\ \mu$m, the spectral resolution of P is about 8 nm in the blue and about 32 nm in the red (cf. Eq. 13). The top graphs in Fig. 9 show how arduous it is to fit the retrieved P to the original P. Clearly, this resolution is not good enough to resolve the methane band features.

In order to better resolve the methane band features[2], and to reach a retrieval accuracy within the target error, we have to increase the sampling frequency of the demodulation algorithm, hence to decrease the width of the spectral windows (cf. Eq. 13). This implies that we have to increase the retardance δ of our retarder, thus the thickness of the birefringent crystals (sticking with our choice of MgF_2-Al_2O_3 crystals). An optimal retrieval was found for a crystal thickness of 16 mm, four times as thick as in the original SPEX design (for a Mars mission), yielding a retardance $\delta \simeq 80\ \mu$m. The optimized spectral resolution of the polarization spectra is 2 nm in the blue and 8 nm in the red. The spectrally improved retrieved P is shown at the bottom of Fig. 9 together with the error in the retrieval. Note that in the deepest parts of the methane bands, the error can still exceed our target error. If we want to use these parts to retrieve aerosol properties (see [8]), the instrument response has to be taken into account in the retrieval algorithm.

5. DESIGNING SPEX FOR A TITAN BALLOON

Here, we have presented SPEX's strengths as payload for the hot air balloon that is an intrinsic part of the Titan Saturn System Mission (TSSM). A detailed investigation of Titan's haze layer is key to expanding our the knowledge on the atmosphere's complex hydrocarbon cycle, which is one of the main goals of the TSSM. By measuring both the radiance and the degree of linear polarization of sunlight that has been scattered by the haze particles, SPEX allows the retrieval of the size, shape and composition of the haze particles and their vertical distribution. In addition, SPEX is small (about 1 liter volume), uses little power and its novel polarimetric technique requires no moving parts.

SPEX has originally been designed as payload for a Mars orbiter, with 7 fixed downward viewing and 2 fixed limb-viewing apertures, parallel to the orbiter's ground track. The main adaptations of SPEX to fly on a balloon mission through Titan's atmosphere would be the viewing geometries, and the spectral resolution. These will be discussed below.

5.1. Viewing geometries

The mission plan is to have the TSSM balloon float at a nominal altitude of 10 km with a range between 6 and 12 km. As payload on the balloon, the interesting viewing angles for SPEX are looking upwards, towards the haze layer, and possibly downwards, towards the surface. Knowledge of the surface reflection and its spectral and angular variations is important for understanding the formation and evolution of Titan, and for identifying possible sources and sinks of methane. And it is also crucial for understanding SPEX' observations of scattered sunlight, because direct and diffuse sunlight will be reflected off the surface, back towards the atmosphere, where it can undergo more scatterings. Hence, the surface reflection has to be included in the retrieval process.

Our numerical simulations have shown the importance of sampling I but especially P at various viewing angles, so we foresee to use either a number of apertures (as in the Mars design), with fixed viewing zenith angles distributed like a hand-fan between $\theta \approx 50°$ and $130°$ (these angles would depend on the size of the balloon, the distance between SPEX and the balloon, and on the location of SPEX on the payload package), or a single aperture that scans up and down. SPEX should also be able to rotate in the horizontal plane to sample a range of azimuthal angles $\phi - \phi_0$. This rotating would be taken care of if the balloon payload would rotate (although the rotation period shouldn't be too long to avoid variations in the atmosphere). Better would be to have SPEX on top of the payload where it can rotate around a vertical axis, such as the connection between the payload and the balloon. Having SPEX below the payload would have the disadvantage of blocking the upward view.

---

[2] An accurate retrieval of aerosol properties does not necessarily require complete resolving the methane bands, since the degraded resolution can be taken into account in the retrieval process. In general, however, the better the resolution, the more information can be retrieved

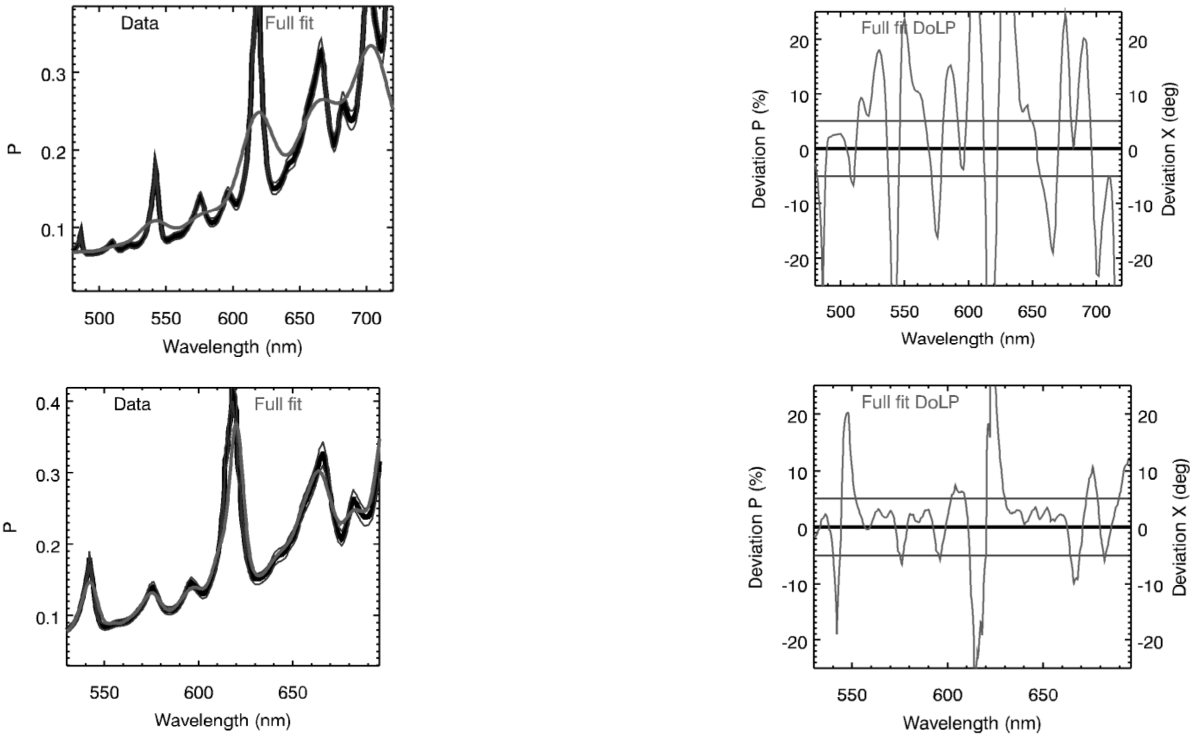

Figure 9. Retrieval of P using the demodulation algorithm of the SPEX end-to-end simulator: P (left) and the retrieval error with horizontal lines indicating a target error of at most 5 $\%$ (right). Two different values for the retardance δ of the multiple-order retarder were used: $\delta \simeq 20$ μm (top) and 80 μm (bottom). Note that 'DoLP' stands for 'Degree of Linear Polarization.'

An interesting solution that would allow the required angular sampling while limiting the number of moving elements, would be to have a rotating disk inclined under an angle of 40° with respect to the vertical axis, with a number of apertures looking outward along the rim of the disk.

5.2. Spectral resolution

SPEX has been designed to measure I, P, and χ from the visible to the near-infrared. Across this wavelength spectrum, a Mars spectrum does not show significant high-spectral resolution features. A Titan spectrum, however, is rich in methane absorption band features. Clearly, as also shown in Sect. 6, using the relatively low spectral resolution designed for the Mars-SPEX for the Titan-SPEX would result in too large errors in the retrieved values for P. To keep the errors in P below 5 $\%$, we have to increase the retardance, hence the thickness of the birefringent crystals from the original 4 mm for Mars to 16 mm for Titan.

Increasing the retardance and hence the modulation frequency, requires an increase of the sampling of the modulated radiance spectra. To allow for a much higher sampling of the spectra, not only the detector size can be increased, but also the wavelength range that is covered. For a Titan-SPEX, a wavelength coverage from 0.5 to 0.72 μm could be considered. Such a wavelength range would have the additional advantage that it excludes the deep methane band at 0.73 μm, which is especially difficult to fit with our current demodulation algorithm. Adapted demodulation algorithms, e.g. algorithms that distinguish between the continuum and the methane bands, could be considered if the inclusion of this deep band is interesting for scientific reasons.

6. CONCLUSIONS

We have presented numerical simulations of the radiance and degree of linear polarization of sunlight that has been scattered in Titan's atmosphere, and of observations of this light as performed by the SPEX instrument as payload on the hot air balloon of the TSSM mission. In particular the degree of linear polarization of scattered sunlight is known to be very sensitive to the microphysical properties of the scattering particles. Floating in the atmosphere of Titan, SPEX novel spectropolarimetric technique would provide a valuable contribution to characterizing the famous hazes. Minor adaptations of the SPEX instrument as designed for placement on a Mars orbiter would be needed if SPEX were to fly on a Titan balloon: the viewing directions and the spectral range and spectral resolution. The latter is necessary to better resolve the methane absorption bands.

ACKNOWLEDGMENTS

We are grateful to dr. Y.V. Skorov, dr. S. Ramirez, dr. R. de Kok, and dr. M. Min for their help in developing our research.

REFERENCES

[1] Hansen J.E. and Travis L.D., Light scattering in planetary atmospheres, *Space Sci. Revs.*, **16**, 527-610, 1974.

[2] Aben I., Helderman F., Stam D. M., and Stammes P., Spectral fine-structure in the polarization of skylight, *Geophys. Res. Lett.*, **26**, 591-594, 1999.

[3] Waite Jr. J.H., et al. The process of tholin formation in Titan's upper atmosphere, *Science*, **316**, 870-875, 2007.

[4] Lunine J.I. and Atreya S.K., The methane cycle on Titan, *Nature Geoscience*, **1**, 159-164, 2008.

[5] Snik F., Karalidi T. and Keller C.U., Spectral modulation for full linear polarimetry, *Appl. Optics*, **48**, 1337-1346, 2009.

[6] Chandrasekhar S., Radiative transfer, *Oxford Univ. Press*, 1950.

[7] Hovenier J.W. and Van der Mee C.V.M., Fundamental relationships relevant to the transfer of polarized light in a scattering atmosphere, *Astron. Astrophys.*, **128**, 1-16, 1983.

[8] Stam D.M., De Haan J.F., Hovenier J.W., Stammes P., Degree of linear polarization of light emerging from the cloudless atmosphere in the oxygen A band, *J. Geophys. Res.*, **104**-D14, 16843-16858, 1999.

[9] De Haan J., Bosma P., Hovenier J., The adding method for multiple scattering calculations of polarized light, *Astron. Astrophys.*, **183**, 371-391, 1987.

[10] Flasar F.M. et al., Titan's atmospheric temperatures, winds, and composition, *Science*, **308**, 975, 2005.

[11] Ramirez S.I. et al., Complex refractive index of Titan's aerosol analogues in the 200-900 nm domain, *Icarus*, **156**, 515-529, 2002.

[12] McCord T.B. et al., Composition of Titan's surface from Cassini VIMS, *Planet. Space Sci.*, **54**, 1524-1539, 2006.

[13] Skorov Y.V., Keller H.U., Rodin A.V., Optical properties of aerosols in Titan's atmosphere, *Planet. Space Sci.*, **56**, 660-668, 2008.

[14] Tomasko M.G., Doose L.R., Dafoe L.E., See C., Limits on the size of aerosols from measurements of linear polarization in Titan's atmosphere, *Icarus*, **204**, 271-283, 2009.

[15] Mishchenko M.I., Travis L.D., Mackowski D.W., T-matrix computations of light scattering by nonspherical particles: a review., *J. Quant. Spectrosc. Radiat. Transfer*, **55**, 535-575, 1996.

[16] Tomasko M.G, et al., The Descent Imager/Spectral Radiometer Aboard Huygens , *Huygens: Science, Payload and Mission*, 1997.

[17] Tomasko M.G, et al., A model of Titan's aerosols based on measurements made inside the atmosphere, *Planet. Space Sci.*, **56**, 669-707, 2008.

[18] Karkoschka E., Spectrophotometry of the jovian planets and Titan at 300-to 1000-nm wavelength: The methane spectrum, *Icarus*, **111**, 174-192, 1994.

[19] Niemann H.B. et al., The abundances of constituents of Titan's atmosphere from the GCMS instrument on the Huygens probe, *Nature*, **438**, 779–784, 2005.

[20] Titan Saturn System Mission Study Final Report on the NASA Contribution to a Joint Mission with ESA, *Task Order NMO710851*, 30 January 2009.

[21] Mishchenko M.I., and Travis L.D., Satellite retrieval of aerosol properties over the ocean using measurements of reflected sunlight: Effect of instrumental errors and aerosol absorption, *Journal of Geophysical Research*, **102**-D12, 13543, American Geophysical Union 1997.

[22] Snik F., and Karalidi T., Trade-off study for the polarimetric principle of SPEX, *SRON private property*, 2008.

[23] Tishkovets V.P., Petrova E.V., Jockers K., Optical properties of aggregate particles comparable in size to the wavelength, *J. Quant. Spectrosc. Radiat. Transfer*, **86**, 241–265, 2004.

[24] Hasekamp O., and Landgraf J., Retrieval of aerosol properties over land surfaces: capabilities of multiple-viewing-angle intensity and polarization measurements, *Appl. Opt.*, **46**, 3332-3344, 2007.

Appendix B

Titan facts and figures

A table with the inforamation regarding the orbit and some physical characteristics of Titan is presented.

Table 9.1: Titan's characteristics [1]

Description	Value
Date of discovery	1655
Mass (kg)	1.35 x 10^{23}
Mass (Earth=1)	0.022
Equatorial radius (km)	2575
Equatorial radius (Earth=1)	0.403
Mean density (gm/cm^3)	1.88
Mean distance from Saturn (km)	1,221,850
Rotational period (days)	15.945
Orbital period (days)	15.945
Mean orbital velocity (km/sec)	5.58
Orbital eccentricity	0.0292
Orbital inclination[2] (deg)	0.33
Escape velocity (km/sec)	2.64
Visual geometric albedo	0.21
Magnitude (Vo)	8.28
Mean surface temperature (° C)	-178
Atmosphere pressure(bar)	1.5

One Titan year is the same as one Saturn year. Saturn's orbital period is 29.7 terrestrial years, a season should change every 7.25 years. Therefore we can make a table for the past and future Titan's changes in season for the Southern hemisphere. Table 9.2 can be useful to know which was the season on Titan at the time of a certain observation/measurement. The decimals indicate the terrestrial months in which the change should take place. They indicate approximately the start of each season.

---

[2] With respect to Saturn's orbit, which in turn is inclined of 26.73° with respect to its own orbit.

Table 9.2: Titan seasons for the Southern Hemisphere from 1980 to 2038. In bold is the current season at the South pole.

Season	Year
Autumn equinox	1980.75
Winter solstice	1988.00
Spring equinox	1995.25
Summer solstice	2002.50
Autumn equinox	**2009.75**
Winter solstice	2017.00
Spring equinox	2024.25
Summer solstice	2031.50
Autumn equinox	2038.75

Appendix C

Cassini Huygens instrumentation

The Cassini orbiter is equipped with 12 science instruments and the Huygens probe has 6 [1]. The set of instruments includes optical and microwave sensing as cameras (able to collect images in many varying conditions and light spectra; from visible light to the infrared[2]), spectrometers, radar and radio instruments that are able to measure magnetic fields, mass, electrical charges and densities of atomic particles. They also measure the quantity and composition of dust particles, the strengths of plasma (electrically charged gas), and radio waves [2].

Cassini's scientific instruments are [1]:

- **Cassini Plasma Spectrometer** (CAPS) explores plasma (highly ionised gas) within and near Saturn's magnetic field.
- **Cosmic Dust Analyser (CDA)** studies ice and dust grains in and near the Saturn system.
- **Composite Infrared Spectrometer (CIRS)** measures infrared energy from the surfaces, atmospheres and rings of Saturn and its moons to study their temperature and compositions.
- **Ion and Neutral Mass Spectrometer (INMS)** examines neutral and charged particles near Titan, Saturn and moons to learn more about their extended atmospheres and ionospheres.
- **Imaging Science Subsystem (ISS)** takes pictures in visible, near-ultraviolet and near-infrared light.
- **Dual-Technique Magnetometer (MAG)** studies Saturn's magnetic field and its interactions with the solar wind, the rings and the moons of Saturn.
- **Magnetospheric Imaging Instrument (MIMI)** images Saturn's magnetosphere and measures interactions between the magnetosphere and the solar wind, a flow of ionised gases streaming out from the Sun..
- **Cassini Radar (RADAR)** maps surface of Titan using radar imager to pierce veil of haze. Also used to measure heights of surface features.
- **Radio and Plasma Wave Spectrometer (RPWS)** investigates plasma waves (generated by ionised gases flowing out from the Sun or orbiting Saturn), natural emissions of radio energy and dust.

- **Radio Science Subsystem (RSS)** searches for gravitational waves in the Universe; studies the atmosphere, rings and gravity fields of Saturn and its moons by measuring telltale changes in radio waves sent from the spacecraft.
- **Ultraviolet Imaging Spectrograph (UVIS)** measures ultraviolet energy from atmospheres and rings to study their structure, chemistry and composition.
- **Visible and Infrared Mapping Spectrometer (VIMS)** identifies the chemical compositions of the surfaces, atmospheres and rings of Saturn and its moons by measuring colours of visible light and infrared energy emitted or reflected.

Huygens probe instruments are [1]:

- **Aerosol Collector and Pyrolyser (ACP)** collected aerosols for chemical-composition analysis. After extension of the sampling device, a pump drew the atmosphere through filters which capture aerosols. Each sampling device can collect about 30 micrograms of material.
- **Descent Imager/Spectral Radiometer (DISR)** can take images and make spectral measurements using 14 sensors covering a wide spectral range. A few hundred meters before impact, the DISR switched on its lamp in order to acquire spectra of the surface material. The DISR consists of 14 sensors; Three imagers, four solar aureole cameras, two imagers covering the visible spectrum, two imagers in the near infrared, two violet photometers, and a sun sensor.
- **Doppler Wind Experiment (DWE)** used radio signals to deduce atmospheric properties. The probe drift caused by winds in Titan's atmosphere induced a measurable Doppler shift in the carrier signal. The swinging motion of the probe beneath its parachute and other radio-signal-perturbing effects, such as atmospheric attenuation, may also be detectable from the signal.
- **Gas Chromatograph and Mass Spectrometer (GCMS)** is a versatile gas chemical analyser designed to identify and quantify various atmospheric constituents. It is also equipped with gas samplers which were filled at high altitude for analysis later in the descent when more time was available.
- **Huygens Atmosphere Structure Instrument (HASI)** comprises sensors for measuring the physical and electrical properties of the atmosphere and an on-board microphone that sent back sounds from Titan.
- **Surface Science Package (SSP)** is a suite of sensors to determine the physical properties of the surface at the impact site and to provide unique information about its composition. The package includes an accelerometer to measure the impact deceleration, and other sensors to measure the index of refraction, temperature, thermal conductivity, heat capacity, speed of sound, and dielectric constant of the (liquid) material at the impact site.

---

[1] `http://www.esa.int/SPECIALS/Cassini-Huygens/SEMMD2HHZTD_0.html`

[2] `http://saturn.jpl.nasa.gov/overview/index.cfm`

Appendix D

Aerosols vertical mixing ratio profiles

Titan's atmosphere is famous for its complex coupling between radiative balance, chemistry and dynamics. The atmosphere is mainly composed of Nitrogen (N_2) and Methane (CH_4). Due to photodissociation in the mesosphere, these two molecules recombine to form hydrocarbons and nitriles that can react to create complex molecules and produce aerosols. Molecules and aerosols have a strong impact on the radiative forcing and on temperature distribution which in turn, affect the dynamics. It is important to see which kind of methane-nitrogen compounds can be present in the atmosphere of Titan.

Here a description of the most important compounds is presented. The data are retrieved from CIRS observations during the Cassini nominal mission at 9 latitudes between 56° S and 80° N between February 2005 and May 2008. At the time of the observations the winter season was in the northern hemisphere, during these three years the temperatures and abundances are expected not to vary significantly. Over the same time span longitudinal variations are negligible .

The altitude range of the retrieval is between 130-500 km. Photochemical models predict that molecular vertical mixing ratio profiles increase with height as the molecules are formed in the upper layer, diffuse downwards and generically condense in the lower stratosphere. Further details can be found in the article published by Vinatier et al. [2009] and in the references therein.

Hydrocarbons are mentioned in Table 9.3, while nitriles are mentioned in Table 9.4.

In conclusion, we can see that all the molecules except C_2H_6,C_3H_8 and CO_2, have an higher mixing ratio at lower altitudes due to the downwelling branch of the winter hemisphere. Moreover, most of the minima take place at 80° N and at 300km of altitude.

Table 9.3: Titan hydrocarbons compounds present in the atmosphere between 130 and 500 km. They are ordered with respect to their abundance in the stratosphere. Note that: TY = Titan year, TD = Titan day, uniform = within the error bars.

Compound	**Chemical name**	**Mixing ratio** (ppm)	**Vertical abundance**	**Latitudinal variation**	**Lifetime** @ 300 km
Ethane	C_2H_6	10	uniform	weak increase winter hem.	24 TY
Acetylene	C_2H_2	2 (80°S-30°N) 6 (85°N)	strong variation	increase winter hem.	0.3 TY
Propane	C_3H_8	0.5-0.8	uniform	uniform	10 TY
Ethylene	C_2H_4	2.5x10^{-7} (85°S-30°N)	decreasing 56°S-46°N constant 54°N-76°N	increases winter hem.	0.04 TY
Methylacetylene	CH_3C_2H	1x10^{-8}	-	-	0.03 TY
Diacetylene	C_4H_2	1.5 ppb 80°S-40°N	strong variation	increase summer hem.	0.6 TY
Benzene	C_6H_6	0.5-5 (0.5 mbar)	increase with altitude	increase winter hem.	0.3 TD

Table 9.4: Titan Nitrile compounds present in the atmosphere between 130 and 500 km. They are ordered with respect to their abundance in the stratosphere. Note that: TY = Titan year, TD = Titan day, uniform = within the error bars.

Compound	**Chemical name**	**Mixing ratio** (ppm)	**Vertical abundance**	**Latitudinal variation**	**Lifetime** @ 300 km
Hydrogen cyanide	HCN		@ 1-mbar steep gradients	strong variation	1.5 TY
Cyanoacetilene	HC_3N	-	strong	-	0.03 TY